Control and Power Management of Photovoltaic Systems with Plug-in Hybrid Electric Vehicles as Energy Storage

Yuchuan Zhang

B.Eng. (Hons), University of Tasmania, 2014

Supervised by:

Dr. Bernardo A. León de la Barra

Dr. Sarah Lyden

Dr. Md Enamul Haque

A thesis submitted in fulfillment of the requirements for the degree of Master of Engineering Science

University of Tasmania

October 2017

This page intentionally left blank.

Declaration and Statements

Declaration of Originality

This thesis contains no material which has been accepted for a degree or diploma by the University or any other institution, except by way of background information and duly acknowledged in the thesis, and to the best of my knowledge and belief no material previously published or written by another person except where due acknowledgement is made in the text of the thesis, nor does the thesis contain any material that infringes copyright.

……..

Yuchuan Zhang

Date: 19th October 2017

Authority of Access

This thesis may be made available for loan and limited copying and communication in accordance with the Copyright Act 1968.

……..

Yuchuan Zhang

Date: 19th October 2017

This page intentionally left blank.

Statement of Co-Authorship

The following people and institutions contributed to the publication of the work undertaken as part of this thesis:

1. *Yuchuan Zhang, Master by research candidate*
   School of Engineering and ICT, University of Tasmania
2. *Dr. Bernardo A. León de la Barra, Primary supervisor*
   School of Engineering and ICT, University of Tasmania
3. *Dr. Sarah Lyden, Co-supervisor*
   School of Engineering and ICT, University of Tasmania
4. *Dr. Md Enamul Haque, Co-supervisor*
   School of Engineering, Deakin University

Author details and their roles:

Paper 1, A Genetic Algorithm Approach to Parameter Estimation for PV Modules:
Located in chapter 2
Candidate was the primary author contributed approximately 75% to the planning execution and preparation of the research project and draft significant parts of the paper. Dr. Sarah Lyden contributed approximately 10% to the simulation program development, the paper formation and refinement, and guidance in academic writing. Dr. Bernardo A. León de la Barra (7.5%) and Dr. Md Enamul Haque (7.5%) contributed to paper refinement and guidance in academic writing.

Paper 2, Optimization of Tremblay's Battery Model Parameters for Plug-in Hybrid Electric Vehicle Applications:
Located in chapter 5
Candidate was the primary author contributed approximately 75% to the planning execution and preparation of the research project and draft significant parts of the paper. Dr. Sarah Lyden contributed approximately 10% to the simulation program development, the paper formation and refinement, and guidance in academic writing. Dr. Bernardo A. León de la Barra (7.5%) and Dr. Md Enamul Haque (7.5%) contributed to paper refinement and guidance in academic writing.

We the undersigned agree with the above stated “proportion of work undertaken” for each of the above published (or submitted) peer-reviewed manuscripts contributing to this thesis:

Signed:

Dr. Bernardo A. León de la Barra
Primary Supervisor
School of Engineering and ICT
University of Tasmania

Associate Professor Leonie Ellis
Deputy Head of School
School of Engineering and ICT
University of Tasmania

Date: 19th October 2017

Acknowledgement

First and foremost, I am incredibly grateful for the continuous, invaluable and dedicated guidance, supports and inspirations provided by my co-supervisor, Dr. Sarah Lyden, right from the start towards the completion of my candidature. She is a stunning, caring and very helpful lady who continually helped me with administrative and technical problems as well to maintain a positive mental state throughout my candidature. She took time to explain concepts and new research directions for me. She also inspired me to come up with new research ideas and help me to step off some of the dark periods during times of difficulty. At last, she guided me to organize an appropriate project schedule and the ways to combine different parts of my work into a complete story.

I would like to express my appreciation to Dr. Enamul Haque (Deakin University) for his continued support and guidance on my research project.

I would also like to thank Dr. Bernardo A. León de la Barra for his continued support on time management, reference management skills and aspirations that make a successful accomplishment of the final thesis. He helped me so much on correcting and formatting the conference papers and thesis. He also motivated me to stay focused on the upcoming research tasks when I experienced the most challenging part of the project.

Thirdly, I deeply appreciate all the academic staff members and postgraduate students who create a nice, friendly, cordial, academic environment.

Fourthly, I would like to thank my friends Jeana and David for their companionship at some stage of my candidature, as well as my family members for their continuous encouragement during my candidature.

Additionally, I would like to express my sincere thanks to Jon Rodden for his fault detection for the PV characteristics measurement experimental setup and his efforts to make the entire circuit working.

Finally, I would like to thank faithfully all my supervisors for their continuous encouragement and guidance during my candidature, as sometime working individually in an unknown field, it is very easy to place myself on the horns of a dilemma.

Yuchuan Zhang

This page intentionally left blank.

Abstract

The distribution network has experienced an increasing level of photovoltaics (PVs) and plug-in hybrid vehicles (PHEVs) integration in recent years. Investigating the potential influence of integrating these sources into distribution networks is difficult and requires the development of a suitable system simulation model for a grid-tied PV system with energy storage. The major objective of this thesis is modelling, control and power management of a grid-connected PV system with PHEVs as energy storage. The parameters of the PV array and Tremblay's battery models integrated within the whole system simulation model are estimated using the parameter estimation techniques. The simulation models developed throughout the thesis are implemented in MATLAB/SimPowerSystems environment. Experimental testing of BP 380 PV modules is conducted to validate the effectiveness of the PV module model. A suitable control and charging strategy is also developed to control the charging and discharging processes of the PHEV battery.

The major novelty of the work described in the thesis lies in three aspects: (1) parameter identification of PV modules using a genetic algorithm (GA) approach to improve the accuracy of the model parameters; (2) parameter identification of Tremblay's battery model using a novel quantum-behaved particle swarm optimization (QPSO) parameter estimation technique; (3) development of a charging strategy for PHEVs to optimally coordinate the power flow among the system based on the State of Charge (SOC) scenario of a day.

This thesis begins with a study of modelling approaches for a PV cell and selects the single diode model (SDM) to model the PV array. A critical review of three parameter estimation techniques for the SDM is presented. A novel GA approach to parameter estimation for the SDM is also proposed. Simulation results are presented to show the advantages of the GA approach over Villalva's iterative method [1]. Experimental testing of a BP 380 PV module is conducted to validate the effectiveness of the SDM in

modelling the experimental current-voltage (I-V) and P-V characteristics. A PV array simulation model is developed using the SDM calibrated through parameter estimation.

Secondly, the thesis presents overviews of MPPT techniques, DC-DC converter topologies, and grid-tied PV inverter topologies for MPPT applications. A review of the input voltage control of DC-DC converters is presented, especially on the voltage mode control (VMC) and current mode control (CMC). This leads to the development of a proportional-integral-derivative (PID) controller. This controller is used to transform the PV array voltage tracking error into the duty cycle to control the operation of the boost converter interfacing the PV array. Four cases are developed based on whether the effect of the DC link capacitor is considered, and different linear models are selected for modelling a PV array. According to the assumptions given in the four cases, the small signal model of the boost converter is developed by adoption of the PWM model in each case. Consistently with the derived small signal model, four different control-to-input voltage transfer functions are developed and the corresponding parameter sets of the PID controller are determined. To investigate the performance of different parameter sets of the PID controller, a single-phase grid-tied PV system model is employed. Four case studies have been conducted to analyse the effects of different tuning settings of the PID controller on the PV array voltage response. The most appropriate PID controller parameter settings are selected leading to the fastest rise time and zero steady state error of the PV array voltage response among the four different cases.

Thirdly, the thesis provides a review of existing parameter estimation techniques used to parameterize Tremblay's battery model for PHEV batteries. These existing techniques include: particle swarm optimisation (PSO), GA, and simulated annealing (SA). A QPSO is proposed in the thesis to estimate the model parameters of Tremblay's model and the resultant discharge curve is compared to those generated by GA and PSO approaches. The simulated battery discharge curves obtained from GA, PSO, and QPSO parameter estimation techniques are compared to the experimental data together with the simulated discharge curve obtained from Tremblay's parameter estimation method. Results of the comparison indicate that the QPSO parameter estimation technique converges to acceptable solutions with fewer iterations than the GA and the PSO techniques. The

QPSO parameter estimation technique also needs less tuning effort than the GA and the PSO techniques since there is only one tuning parameter involved in the QPSO approach.

Finally, this thesis also develops control and charging management strategies for controlling the charging operation of a PHEV battery. The PHEV battery can be charged from the PV array during the daytime when solar power is sufficient, and from the grid at night. The charging power is determined in such a way that the actual SOC of the PHEV battery follows a pre-set SOC reference when the PHEV battery is charging from the grid. The charging power reference is set to the power difference between the PV array and the local load when the PHEV battery is charging from the PV array. Results show that the charging management strategies can achieve the objectives of charging using the PV array power when solar energy is available, and using the grid power at night time.

Table of Contents

List of Figures

List of Tables

List of Symbols

The following is a list of frequently appeared symbols used in this thesis. Other symbols are defined and described within the text where they first appear.

I_{pv}	PV Array Current	(A)
I_{dc}	DC Bus Current	(A)
I_{mpp}	Current at the MPP of the PV cell	(A)
I_{sc}	Short circuit current of PV module	(A)
K_i	Current temperature coefficient of PV module	$(A/°C)$
K_v	Voltage temperature coefficient of PV module	$(V/°C)$
N_{par}	Number of parallel-connected modules in a PV array	
N_s	Number of series-connected cells in a PV module	
N_{ser}	Number of series-connected modules in a PV array	
P_B	Actual power output of the PHEV battery	(W)
P_B^*	Power reference of the PHEV battery	(W)
P_{dc}	DC Bus Power	(W)
$R_{p,array}$	Parallel Resistance of the PV array	(Ω)
R_p	Parallel Resistance of the PV cell	(Ω)
$R_{s,array}$	Series Resistance of the PV array	(Ω)
$R_{s,mod}$	Series Resistance of the PV module	(Ω)
R_s	Series Resistance of the PV cell	(Ω)
SOC_B^*	SOC reference of the PHEV battery	$(\%)$
V_{pv}	PV Array Voltage	(V)
V_{pv}^*	PV Array Voltage Reference	(V)
V_{dc}	DC Bus Voltage	(V)
V_{mpp}	Voltage at the MPP of the PV cell	(V)
V_{oc}	Open circuit voltage of PV module	(V)
NOCT	Normal Operating Cell Temperature	(°C)

This page intentionally left blank.

List of Abbreviations

ACMC	Average Current Mode Control
ANN	Artificial Neural Network
BESS	Battery Energy Storage System
BEV	Battery Electric Vehicle
BMS	Battery Management System
BOT	Beginning of Test
CCM	Continuous Conduction Mode
CMC	Current Mode Control
CSI	Current-source Inverter
DER	Distributed Energy Resources
DG	Distributed Generation
DNO	Distribution Network Operator
DOD	Depth of Discharge
EOT	End of Test
EV	Electric Vehicle

FCEV	Fuel Cell Electric Vehicle
GA	Genetic Algorithm
GMPP	Global Maximum Power Point
GMPPT	Global Maximum Power Point Tracking
HC	Hill Climbing
HCMC	Hysteresis Current Mode Control
HESS	Hybrid Energy Storage System
HEV	Hybrid Electric Vehicle
HF	High Frequency
IC	Incremental Conductance
ICT	Internal Combustion Engine
IGBT	Insulated-gate bipolar transistor
MPP	Maximum Power Point
MPPE	Maximum Power Point Estimation
MPPT	Maximum Power Point Tracking
P&O	Perturb & Observe
PCMC	Peak Current Mode Control

PF	Power Factor
PHEV	Plug-in Hybrid Electric Vehicle
PID	Proportional, Integral and Derivative
PSC	Partial Shading Condition
PSO	Particle Swarm Optimisation
PV	Photovoltaic
PVA	Photovoltaic Array
QPSO	Quantum-behaved Particle Swarm Optimization
SA	Simulated Annealing
SEPIC	Single-ended Primary-inductor Converter
SMC	Sliding Mode Control
SOC	State of Charge
STC	Standard Test Condition
TNM	Total number of modules in a PV array
V2G	Vehicle-to-grid
VMC	Voltage Mode Control
VSI	Voltage-source Inverter

This page intentionally left blank.

Thesis Related Publications

Conference papers given as follows have been generated as the outcome of this research.

Conference Papers:

1 Y. Zhang, S. Lyden, B. A. León de la Barra, and M. E. Haque, "A genetic algorithm approach to parameter estimation for PV modules," in *2016 IEEE Power and Energy Society General Meeting (PESGM)*, 2016, pp. 1–5.

2 Y. Zhang, S. Lyden, B. A. León de la Barra, and M. E. Haque, "Optimization of Tremblay's Battery Model Parameters for Plug-in Hybrid Electric Vehicle Applications," in *2017 Australasian Universities Power Engineering Conference (AUPEC)*, 2017.

3 Y. Zhang, S. Lyden, B. A. León de la Barra, and M. E. Haque, " Design and Control of a Grid Connected PV system with MPPT" (under preparation to submit to IEEE Transactions on Power Electronics).

4 Y. Zhang, S. Lyden, B. A. León de la Barra, and M. E. Haque, "Review of Maximum Power Point Tracking Techniques and Power Electronic Systems for Grid-connected Photovoltaic Systems" (under preparation to submit to IEEE Transactions on Sustainable Energy).

This page intentionally left blank.

Chapter 1
Introduction

1.1 Background

Due to environmental concerns and rising fuel prices, there has been a striving impetus towards transportation electrification. Electric vehicles (EVs) such as battery electric vehicles (BEVs), hybrid electric vehicles (HEVs), plug-in hybrid electric vehicles (PHEVs) and fuel cell electric vehicles (FCEVs) are more fuel efficient and environmental friendly compared to conventional vehicles propelled by an internal combustion engine (ICT) [1]. PHEVs stand out from the electric vehicle market due to several advantages. These advantages are that they are mainly powered by an on-board energy storage system and can be recharged from a power utility grid as well as renewable energy sources [2]. PHEV batteries act as energy storage to counter the intermittency of renewable energy sources as well as to supply power back to the grid via the vehicle-to-grid (V2G) technology [2]. PHEVs provide a way of using clean energy in transportation sectors and could provide further energy savings if equipped with regenerative braking.

Among all the renewable energy sources, solar is clean, inexhaustible and widely accessible. The problems for solar energy are that solar power varies rapidly with respect to ever-changing environmental conditions. The maximum power generated by photovoltaic (PV) system does not happen at the time when there is a peak load demand. Thus, the value to the system may be enhanced if the energy harvested by PV panels can be stored in energy storage systems and released to cover the peak load at different times. Fig. 1.1 demonstrates the total PV installations in Australia from April 2001 to June 2017. Up to July 2017, the number of PV installations in Australia exceeds 1.7 million, with an aggregated capacity of over 6.2 gigawatts [3].

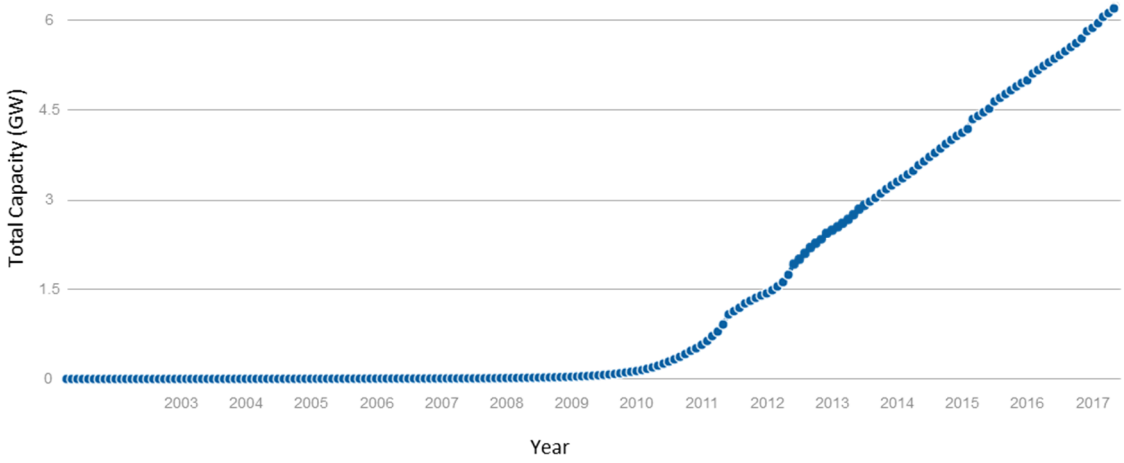

Fig. 1.1: Australian PV installations from April 2001 to June 2016 [3].

Two major configurations of PV generation systems are stand-alone systems or off-grid systems and grid-connected systems. Stand-alone PV systems are designed to operate without a connection to the utility grid and are often installed in remote areas where extreme weather often happens [4]. Energy storage integration is necessary when an uninterruptible electricity supply is required [5]. Grid-connected PV systems provide a connection between the PV system and the grid via inverters. Grid-connected PV systems are often equipped with maximum power point tracking (MPPT) techniques to extract as much power as possible from the sun and deliver electricity to the grid for a reasonable tariff. The purpose of implementing MPPT techniques is to ensure that the PV array always operates at its maximum power point (MPP). This is accomplished by controlling the duty cycle to determine the on/off state of the IGBT switch within the converters interfaced with the PV array.

PV material recycling is another problem associated with PV generation [6]. The normal lifetime of a PV module is 25 years. A PV module needs to be decommissioned and recycled at the end of its lifetime [7] for environmental and economic purposes. It is estimated that about 80 metric tons of waste will be generated from 1 MW of end-of-life PV modules [6].

PHEVs can be a good choice to implement energy storage as they provide an eco-friendly medium of transportation. The V2G technology enables the onboard energy storage system of the vehicle to supply power to the grid when the load demand is high. V2G technology can be defined as a system that provides a controllable, bi-directional power

flow between a vehicle and the grid. A PHEV can be recharged from the grid when its battery's state of charge (SOC) is low, whereas a PHEV can supply power to the grid when there is an imbalance of generation and load. The power management unit (PMU) is used to implement V2G technology. Although there is no such vehicle designed to incorporate PMU in its energy storage system, the potential for V2G technology is significant. Research shows that vehicles are not in use for transportation up to 95% of the time, when the energy storage system can be utilized to stabilize the electricity network without compromising its primary transportation function [8].

The distribution networks were initially constructed for a centralized generation paradigm [9]. Power generated from the central power plant is transmitted to the end users through the transmission line [10]. With an increasing number of distributed generation resources (DGRs) such as solar, wind, biomass and fuel cell integrated into the network, some instability issues and operational challenges may arise in the distribution network [11], [12]. These challenges include but are not limited to: bidirectional power flow [13], poor power quality [12], dysfunction of protection equipment, reactive power shortage, and steady-state voltage rise [12]. These challenges can be mitigated by the integration of energy storage systems. Energy storage systems are able to store excessive energy for further use and supply power to local loads and the grid at night time. They can also improve the distribution network reliability by mitigation of the aforementioned challenges. PHEV energy storage systems are one of the cost-effective energy storage technologies, and provide an effective approach to solar energy utilization for PHEV batteries charging. With an increasing penetration of PHEVs in the transportation sector, the operational challenges attributed to DGRs can be significantly reduced and power system reliability and security can be maintained or improved.

There is increasing attention being paid to the electric vehicle market, as PHEVs and HEVs have significantly lower carbon emissions, less operational costs and consume less fuels compared to the vehicles propelled by internal combustion engines [14]. DERs can be used to charge PHEVs with low fuel costs. During the time when DERs are abundant, such as strong wind and high solar irradiance, the energy generated from these DERs can be stored into the energy storage system of PHEVs. The utilization of PHEVs could improve the coordination of the DERs connected to the distribution grid and increase the penetration level of DERs [15]. However, the massive usage of PHEVs may lead to

several potential issues for power systems. One problem could be that charging large numbers of PHEVs simultaneously cause some technical problems in maintaining the reliability and security of power systems. These technical problems include huge power losses [16], voltage deviations at some local buses and peak loads of distribution transformers at a particular time of a day [17].

PHEVs and PV systems both have a positive influence on the environment with decreasing carbon emissions and low fuel consumption. Increasing PV penetrations without integration with PHEVs (or similar energy storage facilities) may lead to voltage and frequency instability of the power system, whereas connecting PHEVs into the network without any PV system integration could cause considerable increased power losses and voltage deviations. Grid-connected PV systems integrated with PHEVs utilizing appropriate energy management strategies can neutralize their negative effects on the power system.

1.2 Problem Statement and Motivation

Environmental effects of fossil fuels on various aspects of human life require developing some low-carbon-emission strategies. It is reported that greenhouse gases emissions in the U.S. is largely attributed to human activities such as electricity generation from coal and other fossil fuels, heat and transportation [18]. PV power generation converts sunlight into electricity with zero carbon emissions. This advantage has led to a great development in the PV industry in recent years. The solar PV market had reached a total global operating capacity over the $300\ GW$ milestone in 2016, with a total of $75\ GW$ newly installed capacity [19] and China, being the global leader of the PV market, has installed another $34.2\ GW$ during the year 2016. A PV panel is easily installed on the roof of a residential house and can be embedded within the fabric of individual buildings [20]. It reduces the power generation from conventional power plants and increases the total power generation within the entire electricity network.

Grid-connected PV systems integrated with PHEVs as energy storage have been receiving much academic attention over recent years due to large-scale installations of rooftop PV panels and the increasing interest in the green commuting concept. The energy

sources within the system are controlled by associated power electronics converters that perform like a power regulation interface system. Grid-connected PV systems inject power to the grid when excessive solar energy is generated during the daytime and receives power from the grid when off-peak demand occurs. This means that the overall power system losses could be reduced, and frequency and voltage variations could be minimized.

With an increasing penetration of PHEVs and PVs, distribution network operators (DNOs) should understand whether a premature update of the transformer and auxiliary facilities are required to tackle the load peaks resulted from charging the PHEVs [21] and the high reverse power flow caused by PV generation during the daytime. There are several distinct issues observed in the network operation. First, the power flow on the distribution network becomes bidirectional as end users could supply electrical power to the network via the V2G technology and on-roof PV generation [13], [22]. Second, distribution transformers will sustain an increasing dynamic load that may cause problems such as accelerated aging, insulation failures between transformer windings, increased power losses and harmonic issues [21].

As the predominant concerns for the electricity utility companies are still to ensure a reliable and safe operation of the network [14], the consequences arising from the integration of PHEVs and PVs and their impacts on the distribution networks needed to be addressed. It is necessary to adopt proper power management strategies to control the power flow within the network for a safe and efficient operation, since it is obvious to find that PV arrays supply excessive energy to the network in the daytime and the charging period of a PHEV often starts at around 17:00 in the evening [23].

1.3 Aims and Contributions of This Research

The overall objective of this project is modelling, control and power management of a grid-connected PV system with a PHEV battery as energy storage under various temperature and irradiance conditions. This grid-connected PV system can extract the maximum power from the PV array via MPPT techniques, charge the PHEV battery from the PV array during the daytime and from the grid during the night when solar energy is

not available. The parameters of the PV modules in the PV array and the PHEV battery model are estimated using parameter estimation algorithms. Finally, the estimation results for the parameters of PV modules and the PHEV battery are incorporated in the simulation model for the grid-connected PV system with a PHEV battery as energy storage.

The main aims of this research include:

- Development and experimental validation of a simulation model for the BP 380 PV modules under uniform environmental conditions.
- Development of an improved parameter estimation technique for parameter estimation of PV modules.
- Development of an enhanced parameter estimation technique for parameterization of Tremblay's battery model.
- Development of a control and charging algorithm for a grid-tied PV system with PHEVs as energy storage.

The main contributions presented in the these are:

- Development of a novel genetic algorithm (GA) approach to parameter estimation of PV modules to improve the model parameters' accuracy.
- Development of a quantum-behaved particle swarm optimization (QPSO) parameter estimation technique to estimate the parameters of Tremblay's battery model.
- Development of a control and charging algorithm for a grid-tied PV system with a PHEV battery as energy storage to control the charging power of the PHEV battery based on the SOC scenario of a day.

1.4 Thesis Outline

The thesis is organized as follows:

- Chapter 1 includes background theories, problem statement and motivation, aims and scopes of the project, describes the components of the grid-connected PV systems with PHEVs as an energy storage.
- Chapter 2 provides the theoretical backgrounds on the PV effect, conventional PV cell modelling techniques, such as single diode model (SDM) and double diode model (DDM), and PV cell technologies. This chapter applies a GA approach to parameter estimation of a developed SDM to improve the accuracy of the model parameters. Experimental testing of a BP 380 PV module is also conducted to compare between the experimental and simulated PV characteristics and validate the performance of the developed SDM. The developed SDM will be used throughout the thesis.
- Chapter 3 investigates various MPPT techniques, including conventional techniques for uniform environmental conditions, such as perturb and observe (P&O) and incremental conductance (IC), and stochastic search algorithms for non-uniform environmental conditions, such as SA and PSO. The second part of this chapter provides a brief review of various DC-DC converters, DC-AC inverters and filters topologies for PV applications.
- Chapter 4 derives the small signal models of a boost converter fed by a PV array using the PWM switch model approach. Then, the four control-to-input voltage transfer functions of a boost converter are derived based on four different assumptions. Four case studies are conducted based on four different assumptions on the boost converter and the associated frequency responses are plotted. The parameter settings of a digital PID controller are determined based on the four control-to-input voltage transfer functions and simulations have been conducted using a detailed non-linear simulation model for the single-phase grid-connected PV system to investigate PV array voltage responses.

- Chapter 5 provides a brief literature review on the charging level of PHEVs and Tremblay's battery model. This chapter also proposes a QPSO parameter estimation technique to estimate the model parameters of Tremblay's battery model. Simulations results presented in this chapter show that the QPSO parameter estimation technique generates similar discharge characteristics when compared to the GA and PSO parameter estimation techniques with only one tuning parameter.

- Chapter 6 develops the simulation model of the grid-connected PV system with the PHEV energy storage integration in *Matlab/SimpowerSystems*. The PV module model developed in Chapter 2 and the parameter estimation results of Tremblay's battery model developed in Chapter 5 are utilized in this simulation model. A control and charging strategy is developed to charge the vehicle from the PV array during the daytime and from the grid at night.

- Chapter 7 provides a summary of the whole project and highlights some potential future directions.

Chapter 2
Modelling of Photovoltaic Cells

2.1 Introduction

This chapter provides a brief discussion on the photovoltaic (PV) effect, types of PV technologies, and various modeling methods for a PV cell. The Single Diode Model (SDM) is fully illustrated to describe the characteristics of a PV cell. A review of three parameter estimation techniques of a SDM model will be presented. One of the three parameter estimation techniques is known as Villalva's iterative approach that was proposed in [24]. This technique is analyzed and its parameter estimation results are compared to the results obtained from a novel genetic algorithm (GA) approach mentioned in [25] in modeling four different types of PV modules. The novel GA approach to parameter estimation of a PV cell is fully explained and its simulation results are obtained to compare with the other three parameter estimation techniques.

2.2 PV Effect

In 1839, Becquerel first discovered that solar energy can be converted into electricity by means of the PV effect [26]. This PV effect can be realized in a sufficiently pure semiconductor material that achieves a certain cell efficiency. The principle of operation of a PV cell is based on the PV effect illustrated in Fig. 2.1. A semiconductor material consists of a large number of p-n junctions built by doping intrinsic silicone with an element such as Phosphorus to create a free electron, and Boron to produce a hole. Holes and electrons are the charge carriers of the semiconductor material. The material is called n-type when the extrinsic silicone contains mostly free electrons, whereas it is called p-type when the material contains mostly free holes. A p-n junction is created by joining the p-type and n-type materials together and their boundary is called the depletion region where all the charge carriers are annihilated. An electric potential is established by each

side of the depletion region with abundant free charge carriers. This potential provides the open circuit voltage of a PV cell.

When there is no solar irradiance, the electrical characteristic of a PV cell is similar to a normal diode characteristic [27], as shown in Fig. 2.2. When the PV cell is illuminated, the electrical potential of the depletion region is strengthened and more charge carriers are induced by the semiconductor material, which shifts the dark characteristics downward by a short circuit current I_{sc} to create the illuminated characteristics.

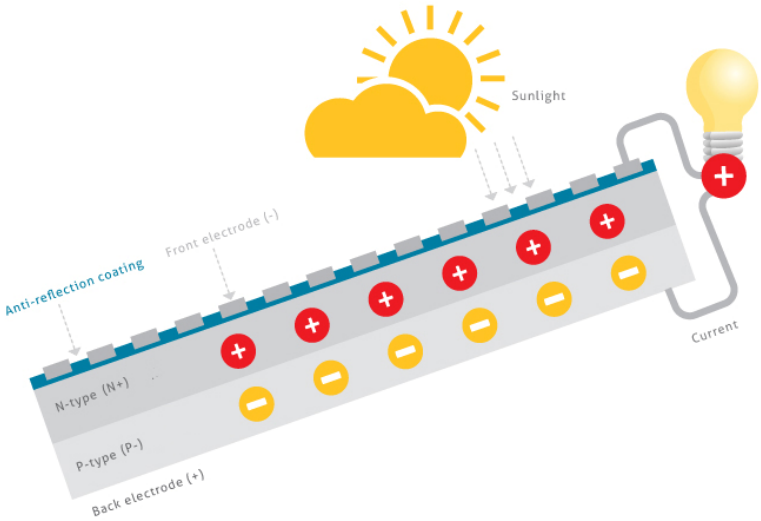

Fig. 2.1: An illustration of the PV effect [28].

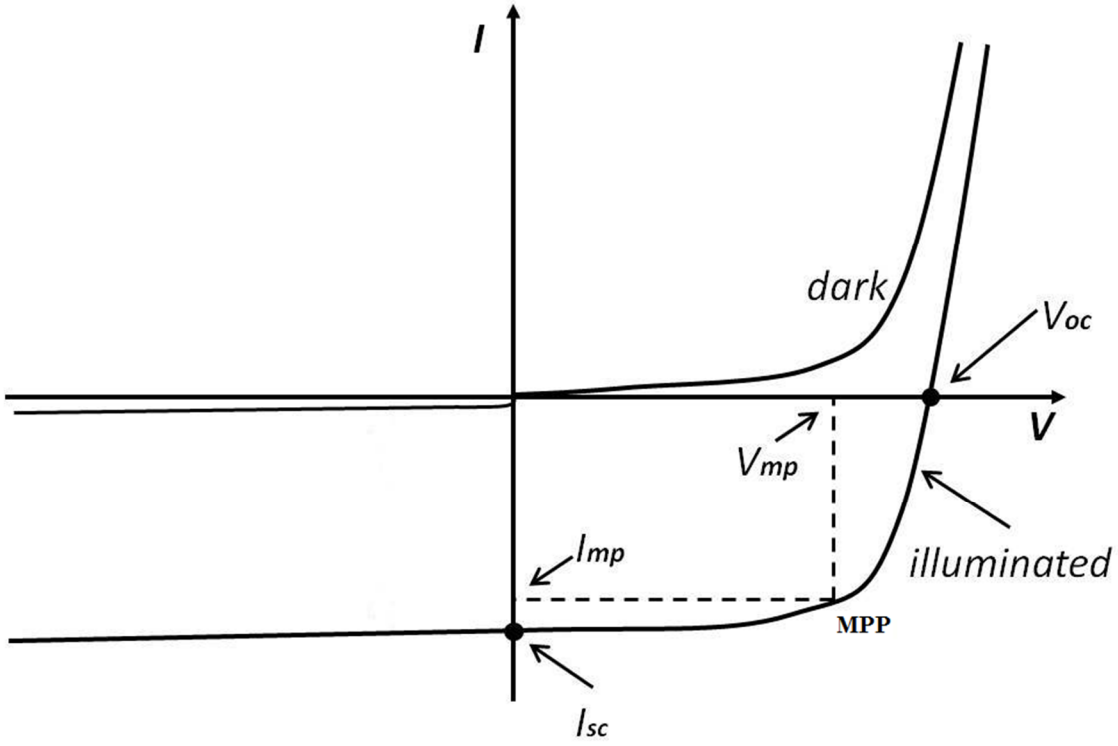

Fig. 2.2: Current-voltage characteristics of a dark PV cell and an illuminated PV cell with short circuit current I_{sc} and open circuit voltage V_{oc} identified.

2.3 Review of PV Cell Technologies

A wide range of PV cell technologies are available commercially with the major difference being in the module efficiency. C-Si-based technology is the first generation of PV technology [5] that currently dominates the PV market. Two major types of c-Si-based PV technologies are monocrystalline silicon (mono-c-Si) and multi-crystalline silicon (multi-c-Si) [29]. Table 2.1 shows a performance review of commercial solar PV cell technologies. It can be seen that PV modules have the advantage of a long lifetime. Most PV manufacturers claim that their PV technologies have long lifetimes that are approximately 25 years [30]. Module efficiency is the major concern for the PV manufacturing industry to determine the type of PV technology adopted for manufacturing [29]. A mono-c-Si type PV cell has the highest efficiency among the common PV cell technologies. A six-monthly review of the current highest confirmed efficiencies for a range of PV cell technologies was reported in the journal *Progress in*

Photovoltaics: Research and Applications. The most recent version, *Solar cell efficiency tables (version 48)*, published online in November 2016, had indicated the maximum efficiency of all considered cells measured from a monocrystalline silicon cell is $26.3 \pm 0.5\%$ [31]. The efficiency of a crystalline silicon cell recorded in the latest version was slightly improved by 0.7% comparing to the value reported in the last version in 17 June 2016 [32]. This version indicated that a large-area crystalline module had a new highest efficiency record of 24.4% measured by Advanced Industrial Science and Technology (AIST) with a marginal increase by 0.6% compared to the value reported in the last version [32]. An increase to 19.9% in module efficiency for a large-area multi-crystalline silicon module manufactured by Trina Solare is also presented in the latest version [31], with an increase by 0.4% compared to the last version [32]. From the above evidence, it can be concluded that researchers have paid added attention to improve the efficiency of PV cells and modules in recent years.

The disadvantages of crystalline silicon technologies are significant as they consume enormous amounts of energy during the manufacturing process and cannot adapt to low light conditions such as partial shading. These disadvantages had been addressed as thin film (TF) technologies arose in the second generation of PV technology. TF technologies have a much simpler yet energy-efficient manufacturing process, so they are much cheaper to produce. TF technologies commanded 18% of the total solar panel sales with the trend of increasing in 2011 [33]. The flexibility and ultra-thinness of an individual cell make TF technologies suitable for a variety of applications, such as consumer electronics for items such as a solar calculator or solar watch and building-integrated PVs (BIPVs). TF PV modules also have the benefit that they have high temperature resistance and are less susceptible to partial shading effects. Amorphous silicon (a-Si) and microcrystalline silicon (μc-Si) are two TF technologies based on silicon, which dominates the TF PV market. Other common materials adopted for TF technologies include Copper Indium Diselenide (CIS), Titania (titanium dioxide), Cadmium Telluride (CdTe) and Copper Indium Gallium Selenide (CIGS). These materials are not commonly used as the PV cells constructed from these technologies need more installation area and hardware.

A PV cell is basically a large area PN diode illuminated with sunlight [34]. The electricity generated by a PV cell is highly dependent on a quantifying factor known as the bandgap energy of the semiconductor material E_g. A typical value of E_g for multi-crystalline silicon is $1.12\ eV$ at 25 ℃. The bandgap energy is defined as the required energy level for the normal operation of a PV cell, i.e., the PV cell starts to generate a flow of electrons across the PN diode [34]. Semiconductors with lower bandgaps take advantage of a larger radiation spectrum, but generate lower voltages [35]. In order to make full utilisation of the available solar spectrum, multi-junction solar cells have been developed to extract solar energy from a wider spectrum. Multi-junction solar cells have comparatively higher module efficiencies and higher output voltages compared to single junction cells. An example of a multi-junction cell, InGaP/GaAs/InGaAs, shown in [31], has a module efficiency of 37.9 ± 1.2 % that is much higher than that of a mono-crystalline silicon PV cell, and an open circuit voltage of $3.605\ V$.

Table 2.1: Performance of commercial solar PV technologies [29].

PV technology		Module Efficiency (%)	Record lab efficiency (%)	Record commercial efficiency (%)	Area/kW (m^2/kW)	Lifetime (Years)
c-Si	Mono-c-Si	13-19	24.7	22	7	25
	Multi-c-Si	11-15	-	20.3	8	25
TF	a-Si	4-8	10.4	7.1	15	25
	a-Si/µc-Si	7-9	13.2	10	12	25
	CI[G]S	7-12	20.3	12.1	10	25
	CdTe	10-11	16.5	11.2	10	25

2.4 PV Characteristics

An individual cell only generates about $0.5\ V$ [36], which is too low for most applications. The fundamental building block of a large-scale PV system is a PV module that consists of a number of PV cells connected in series. Typical values of the number of series-connected cells within a commercial PV module are 36, 54, and 72. Several modules connected in series form a PV string, several PV strings connected in parallel create a PV array. A PV array output voltage is affected by the number of series-connected PV modules in one string whereas the output power is dependent on the number of parallel-connected PV strings within the PV array. A PV array is constructed by connecting a bunch of PV modules in a series-parallel combination. It is commonly known that a series

connection of PV modules will increase the output voltage of a PV array whereas a parallel configuration of PV modules will increase the current capacity, respectively.

A BP 380 PV module can be taken as an example to show the output characteristics of a PV array under various temperature and irradiance conditions. The output characteristics of a PV array consisting of 66 strings of 5 series-connected BP 380 PV modules at different environmental conditions are plotted in Figs. 2.3 to 2.6 for demonstration purposes.

From Figs. 2.3 to 2.4, the output characteristics of a BP 380 PV array are plotted with increasing irradiance levels, the blue circles in the plots represent the MPPs of the PV module/array under different irradiance conditions. The characteristic of one module is presented in Fig. 2.3 whereas the PV array characteristic is plotted in Fig. 2.4. From Figs. 2.3 to 2.4, it can be seen that the MPP moves up as the solar irradiance increases. This is partly because an increase in solar irradiation results in a corresponding increase in the photo-generated current, which consequently leads to a corresponding increase in the short circuit current [24], [37]. Note that the number of free charge carriers within a PV cell is highly affected by solar irradiance [5], [38].

Fig. 2.5 shows the I-V and P-V curves of the PV array with respect to module temperature variation. The module temperature can be calculated from the ambient temperature using the Nominal Operating Cell Temperature (NOCT) as follows [39]:

$$T_m = T_{amb} + \frac{NOCT-20}{800} S \tag{2.1}$$

where T_m is the module temperature, T_{amb} is the ambient temperature, S is the solar irradiance in W/m^2 and NOCT is the nominal operating cell temperature. The NOCT is defined as the temperature within the PV module in an open circuit condition under the environmental conditions of solar irradiance of $800\ W/m^2$; wind speed of $1\ m/s$ and ambient temperature of 20°C. It can be seen that at lower module temperature, the array produces a high power whereas the output power is reduced when the array experiences high temperatures. Thus, it is undesirable to operate the PV array under high ambient temperature conditions. It is worth noting that the array output current increases as the temperature increases, which is unnoticeable when compared to the change in the array output voltage as the effect of module temperature variation.

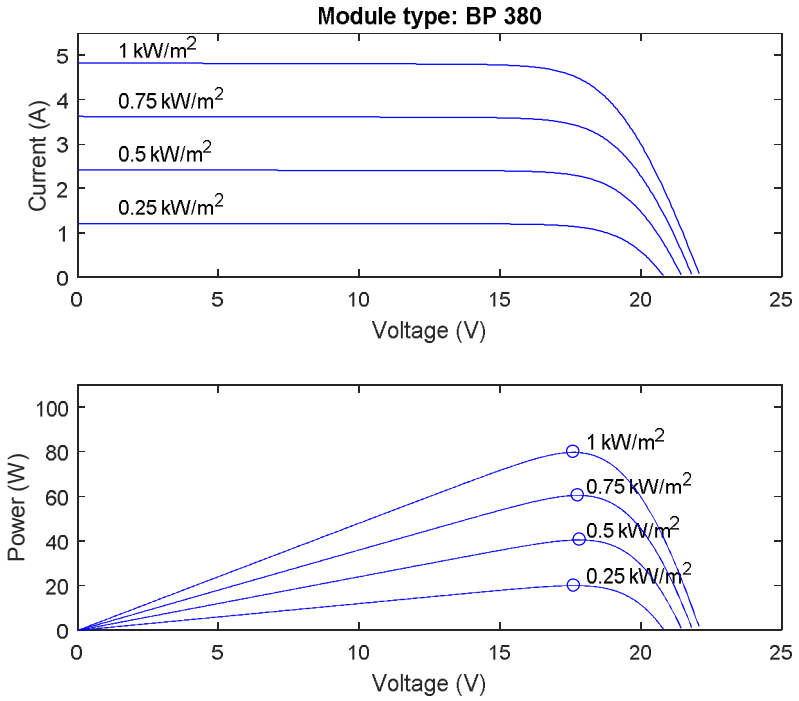

Fig. 2.3: I-V and P-V characteristics of a BP380 PV module with different irradiance levels.

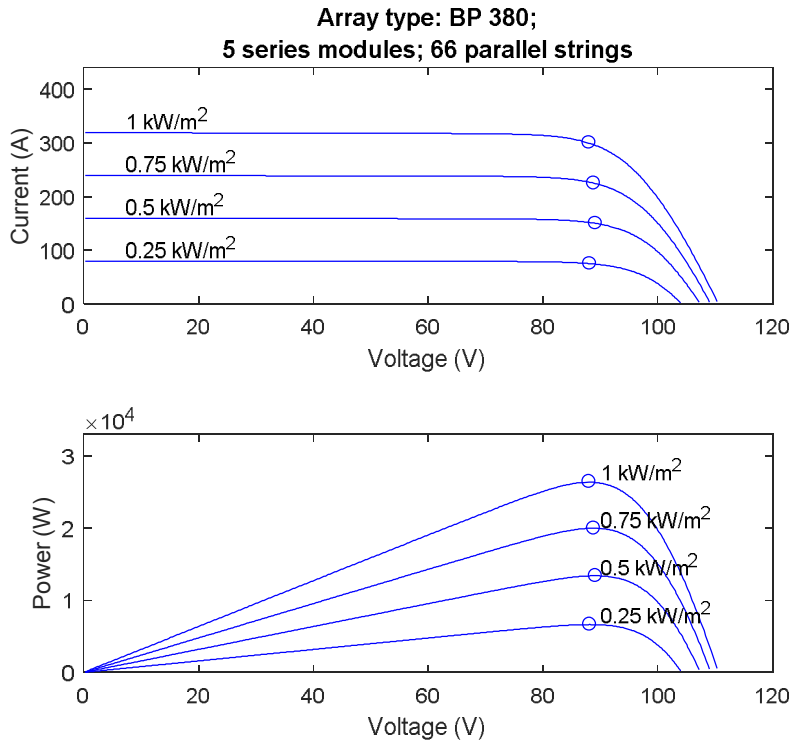

Fig. 2.4: I-V and P-V characteristics of a BP 380 PV array with different irradiance levels.

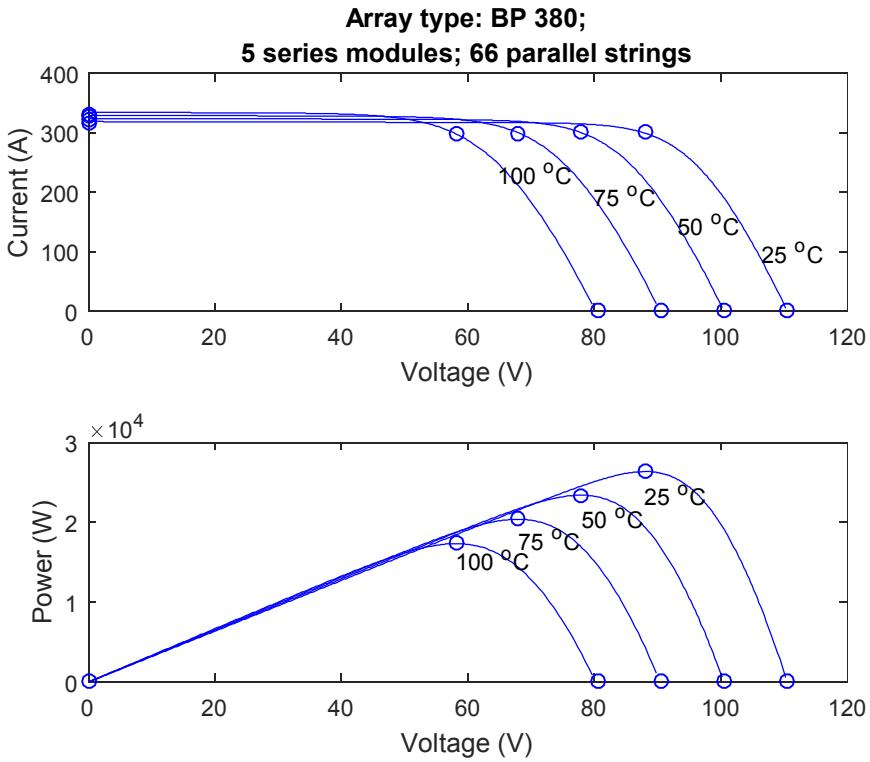

Fig. 2.5: I-V and P-V characteristics of a BP 380 PV array with different module temperature levels.

One concept that can be derived from the I-V curves is the dynamic resistance. The dynamic resistance of a PV cell is defined as the ratio of the voltage deviation to the current deviation [40], representing the reciprocal of the slope of an I-V curve. This is shown in (2.2). The value of r_{pv} is negative and time-variant since PV cells provide electricity to the network under ever-changing environmental conditions.

$$r_{pv} = \frac{dv_{pv}}{di_{pv}} \tag{2.2}$$

Note that v_{pv} symbolizes the PV cell output voltage and i_{pv} represents the PV cell output current, respectively.

The output characteristics from Figs. 2.3 to 2.5 are obtained when the PV array experiences uniform environmental conditions, that is constant irradiance and temperature levels for each cell. Partial shading conditions arise due to passing clouds, or the shadow of obstacles such as trees, houses and tall buildings [22], [41]. When the PV array is partially shaded, it is observed that the I–V curves look like a staircase while the P–V curves are characterized by multiple peaks [42]–[46]. In the case of non-uniform

conditions for three series-connected BP 380 modules, the corresponding I-V and P-V characteristics are shown in Fig. 2.6. Three local maxima are observed in the PV characteristics whereas only one local maximum is the global maximum power point (GMPP) of the PV array. It is desirable to ensure that the PV array always works at its GMPP with appropriate global maximum power point tracking (GMPPT) techniques. Power losses are introduced when the PV array operates at other local MPPs except for the GMPP.

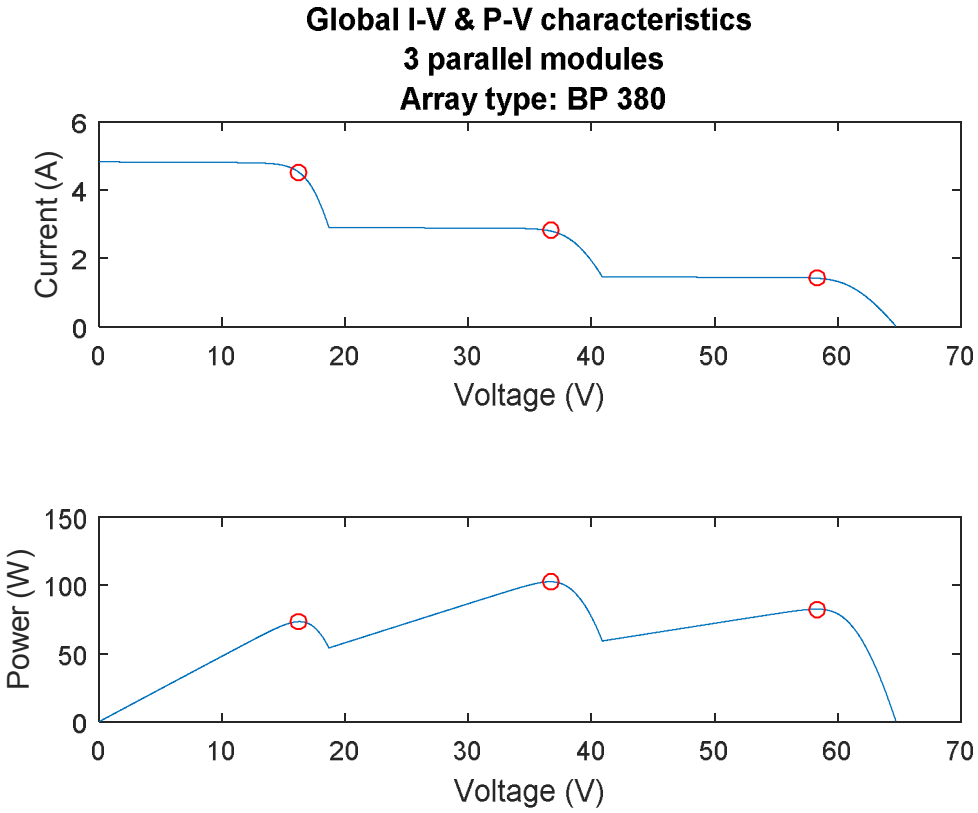

Fig. 2.6: I-V and P-V characteristics under a certain partial shading condition, where the irradiances for the modules are 1000 W/m^2, 300 W/m^2 and 600 W/m^2, with the three local MPPs identified.

One approach to improving the overall efficiency of a PV array experiencing partial shading is known as distributed MPPT (DMPPT) [47]–[51], which utilizes power electronic converters that are connected at the output of each module within a PV array. The maximum power of each module is tracked separately by its interface power electronic converter using conventional MPPTs. PV arrays equipped with DMPPT have a high-power yield with the disadvantage of an increase in the cost of system components.

2.5 Modeling of PV Cells

A variety of modeling methods has been proposed in the literature to model a PV cell. Some of the advanced modeling approaches adopt artificial neural networks [52]–[54], however as these models need training datasets, their applications are limited to proprietary PV systems. Two important current flows within a PV cell resulting from the movement of charge carriers need to be considered. One of the current flows is called recombination current. This current takes place at the external circuit of a PV cell when an electron and hole pair recombines anywhere within the p-n junction [55]. The other current flow is known as diffusion current, which happens across the p-n junction as a result of the charge carrier concentration difference. The diffusion current is formed where electrons from the n-type material diffuse into the p-type and holes from the p-type material diffuse into the n-type [56].

A lumped parameter equivalent circuit model is well known to emulate a PV cell characteristic under different operating conditions [57]. The basic principle of a lumped parameter equivalent circuit model is to represent the effects of the diffusion and recombination currents using conventional diodes, which is more convenient when compared to other modelling techniques as their models' parameters cannot be easily estimated based on the data provided in manufacturers' datasheets. Fig. 2.7 displays four typical diode-based models, which are known as Ideal Single Diode Model (ISDM), Simplified Single Diode Model (SSDM), Single Diode Model (SDM) and Dual Diode Model (DDM). A 3-diode equivalent circuit model mentioned in [58] models a PV cell with large leakage current and mainly focuses on the multi-crystalline silicon (Mc-Si) type of solar cells. SDM and DDM are the two modeling approaches commonly used in grid-connected PV system simulations. A detailed explanation of SDM and DDM is presented in Sections 2.5.1 and 2.5.2, respectively.

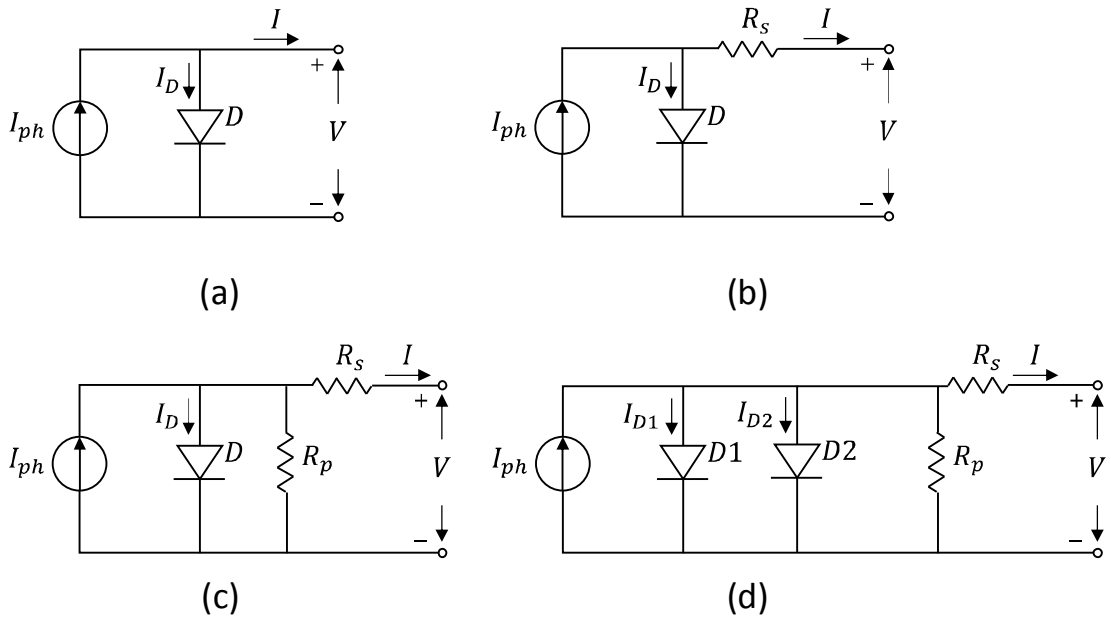

Fig. 2.7: The conventional diode-based PV cell models: (a) *ISDM,* (b) *SSDM,* (c) *SDM,* (d) *DDM.*

2.5.1 SDM

The circuit diagram of the SDM is shown in Fig. 2.7 (c). It is known to provide a good compromise between model accuracy and simplicity [24], [37], [59]–[62]. The performance of an SDM depends on the values of five key parameters, namely photo-generated current I_{ph}, diode saturation current I_o, diode's ideality factor A, series resistance R_s and parallel resistance R_p. The values of these parameters are provided indirectly by PV manufacturers in terms of three remarkable points [24], which are the open circuit voltage $(V_{oc}, 0)$, the short circuit current $(0, I_{sc})$ and the MPP (V_{mpp}, I_{mpp}). The values of the five key parameters could be accurately estimated using the parameter estimation algorithms mentioned in Section 2.6.

Due to the fact that the diffusion and recombination currents of a PV cell are linearly independent, it is reasonable to use a single diode with a constant diode's ideality factor to represent a PV cell [56].

An SDM of a PV cell has the characteristic equation between the output voltage and current that is given as follows:

$$I = I_{ph} - I_o\left[e^{\frac{q(V+IR_S)}{AkT}} - 1\right] - \frac{V+IR_s}{R_p} \tag{2.3}$$

where I and V are the PV cell output current and voltage, respectively. q is the charge of an electron ($1.6 \times 10^{-19}\ C$), k is the Boltzmann constant ($1.38 \times 10^{23}\ J/K$), T is the cell temperature on the absolute scale (K) and A is the diode's ideality factor. The current of a PV cell can be solved using iterative algorithms, e.g., Newton-Raphson, Bisection, Gauss-Seidel, etc. [37], [63], [64].

The thermal voltage of a PV cell is defined as follows [24], [37]:

$$V_t = \frac{kTA}{q} \tag{2.4}$$

In an SDM, the photo-generated current depends on both solar irradiance and ambient temperature, whereas the diode saturation current and thermal voltage are only influenced by ambient temperature [59].

In [65], [66], the series and parallel resistances in the SDM are left out for simplicity. A method to calculate the diode saturation current at Standard Test Condition (STC), that is 25 ℃, $1000\,W/m^2$, and the diode's ideality factor (A) are given as follows:

$$\begin{bmatrix} \ln(I_{o,n}) \\ \frac{q}{AkT} \end{bmatrix} = \begin{bmatrix} 1 & V_{mpp,n} \\ 1 & V_{oc,n} \end{bmatrix}^{-1} \cdot \begin{bmatrix} \ln(I_{sc,n} - I_{mpp,n}) \\ \ln(I_{sc,n}) \end{bmatrix} \tag{2.5}$$

where $I_{sc,n}$, $I_{mpp,n}$ and $I_{o,n}$ symbolise the short circuit current, the current at the MPP and the diode saturation current of the PV cell at STC, respectively. $V_{oc,n}$ and $V_{mpp,n}$ stand for the open circuit voltage and voltage at the MPP of the PV cell at STC, respectively.

Equation (2.3) demonstrates an implicit relation between the PV cell output current and voltage. Some numerical iterative methods, such as Newton-Raphson method, are adopted to produce the PV characteristics by solving for the output current at a given value of the output voltage. In terms of modeling a larger PV structure, such as a PV array or a PV system, a large number of system equations are needed to describe the operation of each individual PV module, especially when the system experiences partial shading. Convergence issues and substantial computational errors may arise as the system equations become more complicated. An alternative approach developed in [67] could be

used to convert (2.3) to an explicit form in (2.6), where the output voltage could be expressed using the Lambert-W function.

$$V = R_p \cdot (I_{ph} + I_o) - (R_s + R_p) \cdot I - A \cdot W\left\{\frac{R_p I_o}{A} e^{\frac{R_p(I_{ph}+I_o-I)}{A}}\right\} \tag{2.6}$$

where, $W\left\{\frac{R_p I_o}{A} e^{\frac{R_p(I_{ph}+I_o-I)}{A}}\right\}$ is the Lambert-W function and its input is the PV cell output current. The basic introduction to the Lambert-W function can be referred to [68].

A simplification method presented in [69], [70] reduces the number of parameters that need to be estimated and simplifies the SDM from an engineering perspective. The basic simplification steps are listed below:

- As R_p is much larger compared to the other terms, the term $(V + IR_s)/R_p$ can be neglected in (2.3).
- Assume the load resistance is relatively small, so $I_{ph} \approx I_{sc}$.

Thus, the PV cell output characteristic equation is described as:

$$I = I_{sc}\left\{1 - C_1\left[e^{\frac{V}{C_2 V_{oc}}} - 1\right]\right\} \tag{2.7}$$

where C_1 and C_2 affect the amplitudes of the voltage and current of the PV cell [69], and are shown to be given by:

$$C_1 = \left(1 - \frac{I_{mpp}}{I_{sc}}\right) e^{\left(-\frac{V_{mpp}}{C_2 V_{oc}}\right)} \tag{2.8}$$

$$C_2 = \left(\frac{V_{mpp}}{V_{oc}} - 1\right) / \ln\left(1 - \frac{I_{mpp}}{I_{sc}}\right) \tag{2.9}$$

The PV cell power output can be expressed in terms of the PV cell voltage by:

$$P(V) = V I_{sc}\left\{1 - C_1\left[e^{\frac{V}{C_2 V_{oc}}} - 1\right]\right\} \tag{2.10}$$

The values of the model parameters of an SDM at STC, deviate from those of the model parameters at actual environmental conditions [37], [71], [72]. In order to quantify the

effects of temperature and irradiance variations on the model parameters, the following equations from (2.11) to (2.14) are used to express the relationships between the values of the model parameters at STC and at different environment conditions.

$$I_{sc} = I_{sc,n} \cdot \frac{S}{S_n}(1 + a \cdot \Delta T) \tag{2.11}$$

$$V_{oc} = V_{oc,n} \cdot \ln(e + b \cdot \Delta S) \cdot (1 - c \cdot \Delta T) \tag{2.12}$$

$$I_{mpp} = I_{mpp,n} \cdot \frac{S}{S_n}(1 + a \cdot \Delta T) \tag{2.13}$$

$$V_{mpp} = V_{mpp,n} \cdot \ln(e + b \cdot \Delta S) \cdot (1 - c \cdot \Delta T) \tag{2.14}$$

$$\Delta S = (S/S_n - 1) \tag{2.15}$$

$$\Delta T = (T - T_n) \tag{2.16}$$

where e is the natural logarithm base. $I_{sc,n}$, $V_{oc,n}$, $I_{mpp,n}$, $V_{mpp,n}$ represent the PV cell parameters at STC. S symbolizes the solar intensity at a given environmental condition whereas S_n stands for the solar irradiance at STC, which is $1000\,W/m^2$. T symbolises an arbitrary cell temperature whereas T_n stands for the cell temperature at STC, which is $25\,℃$. Typical values of the parameters a, b and c can be selected as $0.025/℃$, $0.5/(W/m^2)$, and $0.0028/℃$, respectively [69].

2.5.1.1 Constructing PV modules and arrays

The characteristic equation for a PV module composed of N_s series-connected cells is expressed as follows:

$$I_{mod} = I_{ph} - I_o\left[e^{\frac{q\left(V_{mod}+I_{mod}R_{s,mod}\right)}{N_sAkT}} - 1\right] - \frac{V_{mod}+I_{mod}R_{s,mod}}{R_p} \tag{2.17}$$

where I_{mod} and V_{mod} represent the current and voltage of the PV module, respectively, N_s stands for the number of series-connected PV cells in the module. $R_{s,mod}$ denotes the series resistance of the PV module. Comparing (2.3) and (2.17), it can be noted that series resistance of the PV module and its constituent PV cells have the relation $R_{s,mod} = N_sR_s$. Analogous to (2.4), the thermal voltage of a PV module is given as follows:

$$V_{t,module} = N_s \cdot V_t \tag{2.18}$$

The parameters of a PV array can be estimated using multipliers that are determined by N_{ser} and N_{par} with the assumptions that identical characteristics of individual modules are employed and the operating conditions for all the modules are exactly the same. The parameters of a PV array can be calculated on the basis of the parameters of its constituent PV modules, which are provided in the following equations [38]:

$$I_{ph,array} = N_{par} \cdot I_{ph} \tag{2.19}$$

$$I_{o,array} = N_{par} \cdot I_o \tag{2.20}$$

$$R_{s,array} = (N_{ser}/N_{par}) \cdot R_{s,mod} \tag{2.21}$$

$$R_{p,array} = (N_{ser}/N_{par}) \cdot R_p \tag{2.22}$$

$$V_{t,array} = N_{ser} \cdot V_{t,module} \tag{2.23}$$

where the parameters $I_{ph,array}$, $R_{s,array}$, $R_{p,array}$, $V_{t,array}$ and $I_{o,array}$ have the same physical meanings as those given in (2.3) and (2.4) for a PV cell but are now applied to a PV array.

The I-V characteristics for a PV array composed of $N_{ser} \times N_{par}$ modules with uniform environmental conditions are given by:

$$I_{array} = I_{ph,array} - I_{o,array}\left[e^{\frac{(V_{array}+I_{array}R_{s,array})}{V_{t,array}}} - 1\right] - \frac{V_{array}+I_{array}R_{s,array}}{R_{p,array}} \tag{2.24}$$

where I_{array} and V_{array} stand for the current and voltage of the PV array.

2.5.2 DDM

The DDM represents diffusion and recombination currents separately with the introduction of two diodes with different ideality factor values. The adoption of two diodes in the DDM is due to the fact that the equivalent diode's ideality factor varies as a function of the voltage across the device [73]. There are seven parameters involved in a DDM [57], which are the photo-generated current I_{ph}, diode diffusion current I_{o1}, diode

recombination current I_{o2}, diffusion diode's ideality factor A_1, recombination diode's ideality factor A_2, series resistance R_s and parallel resistance R_p. The values of these parameters could also be estimated using the parameter estimation algorithms mentioned in [57].

From Fig. 2.7 (d), the output voltage and current relationship of a DDM is given by:

$$I = I_{ph} - I_{o1}\left[e^{\frac{q(V+IR_S)}{A_1 kT}} - 1\right] - I_{o2}\left[e^{\frac{q(V+IR_S)}{A_2 kT}} - 1\right] - \frac{V+IR_s}{R_p} \quad (2.25)$$

Here, all the parameters have the same physical meanings as those of an SDM.

2.6 Parameter Estimation of a Single Diode Model

2.6.1 Introduction

The simulation model developed in the succeeding chapters utilizes the SDM to develop the model of the PV array. The five key parameters in a SDM cannot be found directly in manufacturers' datasheets [74]. The basic information provided by a PV manufacturer's datasheet is P_{max}, V_{oc}, I_{sc}, V_{mpp}, I_{mpp}, K_V, and K_I [24], [37], [75]. This information is provided when the PV module is under STC. Since the actual values of P_{max}, V_{oc}, I_{sc}, V_{mpp} and I_{mpp} vary with respect to actual environmental conditions, such as ambient temperature and solar irradiance variations, the information provided by a PV manufacturer's datasheets can be used to estimate the five parameters within an SDM at STC using parameter estimation techniques.

A number of parameter estimation techniques are mentioned in the literature to transform the information of the remarkable points provided by a manufacturer's datasheet into the values of model parameters [24], [37], [76], [77]. General techniques include least-squares optimization, iterative techniques, analytical equations and artificial intelligence [24], [77]–[79]. The neuro-fuzzy-based modeling approach proposed in [54] requires an abundance of measured data or historical data that may not be available at existing PV plants. In the following sections, three parameter estimation techniques proposed in the literature are thoroughly explained, these techniques are Chatterjee's iterative approach in [37], Villalva's iterative method in [24], and the ideal single diode model (ISDM)

approach in [76]. A novel GA approach to parameter estimation is developed in [25] to enhance the performance of Villalva's iterative method in [24]. This approach formulates the PV module parameter estimation problem as a search and optimization problem and refines the parameters R_s and A obtained in Villalva's iterative method, which in turn improves the accuracy of the resultant PV characteristics. This approach is fully analysed and the results for this approach and Villalva's iterative method are compared and tabulated in modelling four different types of PV modules.

2.6.2 Chatterjee's iterative approach

Chatterjee's iterative approach in [37] uses five system conditions to generate five system equations and uses the Gauss-Seidel method to solve for the five unknowns parameters. The first three equations, (2.26) to (2.28), are generated by substitution of the three remarkable points into (2.3).

$$I_{sc} = I_{ph} - I_o \cdot e^{\frac{qIR_s}{AkT}} - \frac{I_{sc}R_s}{R_p} \tag{2.26}$$

$$I_{mpp} = I_{ph} - I_o \cdot e^{\frac{q(V_{mpp}+I_{mpp}R_s)}{AkT}} - \frac{V_{mpp}+I_{mpp}R_s}{R_p} \tag{2.27}$$

$$0 = I_{ph} - I_o \cdot e^{\frac{qV_{oc}}{AkT}} - \frac{V_{oc}}{R_p} \tag{2.28}$$

The term "-1" in (2.3) is neglected for simplicity, the last two equations are derived from the slopes of the V-I and V-P curves, respectively. Evaluating the derivative of the V-P curve at the MPP, we get

$$\left.\frac{dP}{dV}\right|_{\substack{V=V_{mpp}\\I=I_{mpp}}} = 0 \tag{2.29}$$

Evaluating the derivative of the V-I curve at the short circuit current, we have

$$\left.\frac{dI}{dV}\right|_{\substack{V=0\\I=I_{sc}}} = -\frac{1}{R_p} \tag{2.30}$$

The drawback of this analytical method is the introduction of computational errors generated by the assumptions and omissions made in the algebraic manipulations and related simplifications.

2.6.3 Villalva's iterative approach

The numerical method discussed in [24] is an iterative technique based on the relationship between the series resistance and the parallel resistance derived from matching the experimental MPP with the MPP estimated from the PV model. This method is referred to as "Villalva's iterative method" in [80]. This method assumes that there is only one (R_s,R_p) pair leading to the following key relationship:

$$P_{max,m} = P_{max,e} = V_{mpp}I_{mpp} \tag{2.31}$$

where $P_{max,e}$ represents the maximum power obtained from the datasheet at the MPP and $P_{max,m}$ denotes the maximum power estimated from the SDM. Substituting (2.27) into (2.31) and rearranging the resultant equation, the relationship between the series and parallel resistance of a SDM can be expressed as [24]:

$$R_p = \frac{V_{mpp}(V_{mpp}+I_{mpp}R_s)}{I_{ph}V_{mpp}-I_oV_{mpp}\left[e^{\frac{q(V_{mpp}+I_{mpp}R_s)}{AkTN_s}}-1\right]-P_{max,e}} \tag{2.32}$$

where N_s is the number of series-connected cells of a PV module. The value of A can be arbitrarily chosen between 1 and 1.5, and is nominally selected as 1 [41]. A may be given other values when a negative value of R_p is obtained. The value of A can be later modified to improve the curve fitting since the value of A is found in [81] based on empirical analysis and slightly affects the shape of the PV module characteristic [24].

The iterative process is conducted by starting with the initial value of R_s equal to zero, calculating the value of R_s using (2.17), and then generating the PV characteristic curve and locating the maximum power. The value of the located maximum power is compared with the value obtained from the manufacturer datasheet. If the difference between the two values is within the chosen tolerance, the iterative process stops and returns the resultant (R_s,R_p) pair. If the difference is larger than the tolerance, Villalva's iterative method increments R_s until a suitable (R_s,R_p) pair is obtained.

The value of I_{ph} is assumed to be equal to I_{sc} during the iterative process. After the (R_s,R_p) pair is obtained using the iterative approach, the values of parameters I_{ph} and I_o can be calculated using the following two equations:

$$I_{ph} = \frac{R_s+R_p}{R_p} \cdot I_{sc} \tag{2.33}$$

$$I_o = \frac{I_{sc}}{e^{\frac{qV_{oc}}{AkT}}-1} \tag{2.34}$$

From the sensitivity analysis of the I-V and P-V characteristics to variations in the five key parameters of a SDM presented in [22], the diode's ideality factor (A) and the series resistance (R_s) are the two most promising parameters that can be tuned to improve the model fit to the experimental data. To further refine the values of these parameters, an extension method is developed in [25], which utilises a GA approach to perform parameter estimation for a SDM. This method will be fully explained in Section 2.6.5.

2.6.4 Ideal single diode model approach

This method uses the ISDM shown in Fig. 2.7 (a) to avoid the complexity given in (2.3) [76]. The current and voltage relationship of an ISDM is expressed as follows:

$$I = I_{ph} - I_o\left[e^{\frac{q(V+IR_S)}{AkT}} - 1\right] \tag{2.35}$$

An ISDM has three model parameters (I_{ph}, I_o, and A) [76]. I_{ph} can be represented as follows:

$$I_{ph} = G(I_{sc} + K_I\Delta T) \tag{2.36}$$

where G is the solar intensity (kW/m^2), ΔT is the difference between the actual temperature and the temperature at STC ($T - T_o$). This method assumes $I_{ph} = I_{sc}$ when the PV cell is under STC.

An expression for I_o is derived by first setting

$$V_{oc}(G,T) - V_{oc}(G,T_o) = -|K_V|\Delta T \tag{2.37}$$

where $V_{oc}(G,T)$ and $V_{oc}(G,T_o)$ are the open circuit voltage at an arbitrary temperature (T) and at the temperature at STC (T_o), respectively. The values of $V_{oc}(G,T)$ and $V_{oc}(G,T_o)$ can be calculated separately by substituting $I = 0$ in (2.35), which gives

$$V_{oc}(G,T) = \frac{KTA}{q}\ln\left(\frac{G(I_{sc}+K_I\Delta T)}{I_o}+1\right) \tag{2.38}$$

$$V_{oc}(G,T_o) = \frac{KT_oA}{q}\ln\left(\frac{GI_{sc}}{I_{o_{ref}}}+1\right) \tag{2.39}$$

where $I_{o_{ref}}$ represents the saturation current at STC and can be calculated as follows:

$$I_{o_{ref}} = \frac{I_{sc}}{e^{\frac{qV_{OC}}{AKT_o}}-1} \tag{2.40}$$

Substituting (2.38) and (2.39) into (2.37), and rearranging it to solve for the parameter I_o, we have

$$I_o = \frac{e^{\frac{|K_V|\Delta Tq}{AKT}}G(I_{sc}+K_I\Delta T)}{\left(\frac{GI_{sc}}{I_{o_{ref}}}+1\right)^{\frac{T_o}{T}}-e^{\frac{|K_V|\Delta Tq}{AKT}}} \tag{2.41}$$

The value of A can be calculated by first substituting the MPP into (2.35), the resultant equation becomes:

$$I_{mpp} = I_{sc} - I_{o_{ref}}\left[e^{\frac{qV_{mpp}}{AKT_o}}-1\right] \tag{2.42}$$

Then, the value of the diode's ideality factor A can be derived by substituting (2.40) into (2.42) and solving for A using the Newton-Raphson iterative approach as the resultant equation is transcendental in nature.

The advantage of this method is to avoid the use of a numerical solver to determine the value of I at the given value of V [76], which reduces the overall simulation time compared to the curve-fitting method.

2.6.5 GA approach

A novel GA approach to parameter estimation [25] is developed to improve the accuracy of the model parameters compared to that of Villalva's iterative method described in

Section 2.6.3. The aim of the GA approach is to optimize the values of the series resistance and diode's ideality factor to minimize the root mean square error (RMSE) between the three estimated remarkable points, $(0,I_{sc,e})$, $(V_{oc,e},\ 0)$ and $(I_{mpp,e},V_{mpp,e})$ obtained from the SDM, and the three remarkable points, $(0,I_{sc})$, $(V_{oc},0)$ and (I_{mpp},V_{mpp}) obtained from the manufacturer's datasheets [25]. It formulates the PV module parameter estimation as a search and optimization problem. The problem variables R_s and A are represented using a 20-bit string (10 bits for each variable). Fig. 2.8 shows an example of a problem solution represented by a 20-bit chromosome.

Fig. 2.8: An example of a 20-bit chromosome representing a solution for R_s and A.

The RMSE between the estimated and extracted remarkable points is used as the cost function of the GA and can be expressed as follows:

$$RMSE = \sqrt{\frac{(I_{sc}-I_{sc,e})^2+(V_{oc}-V_{oc,e})^2+(I_{mpp}-I_{mpp,e})^2+(V_{mpp}-V_{mpp,e})^2}{4}} \qquad (2.43)$$

where, $RMSE$ is defined as the index for measuring the average magnitude of the error between the actual data sets and the estimated data sets based on the square root of the sum of the relevant quadratic terms [82].

This method is an extension of Villalva's iterative method. It employs (2.32) to calculate R_p at a given value of R_s, which reduces the number of parameters requiring estimation. The values of I_{pv} and I_o are determined in the same manner than for Villalva's iterative method using (2.33) and (2.34), respectively.

The flowcharts for the GA approach to parameter estimation technique are shown in Fig. 2.9. It consists of two parts: GA and cost function evaluation. Fig. 2.9 shows the cost function evaluation and Fig. 2.10 shows the calculating procedures for the GA. The entire process starts with initialization of the parameters of the GA, including crossover, mutation and elite rates, the number of generations and the size of the chromosome

population, it generates the initial solutions for R_s and A represented as strings of ones and zeroes. Then, chromosomes fitness evaluation is conducted based on the cost function specified in (2.43). Thirdly, the GA randomly selects two parental chromosomes based on the selection strategy to form two offspring chromosomes by crossover and mutation techniques. In this case, roulette wheel selection is used for chromosome selection. The entire algorithm will run iteratively until the number of iterations specified by the user is satisfied.

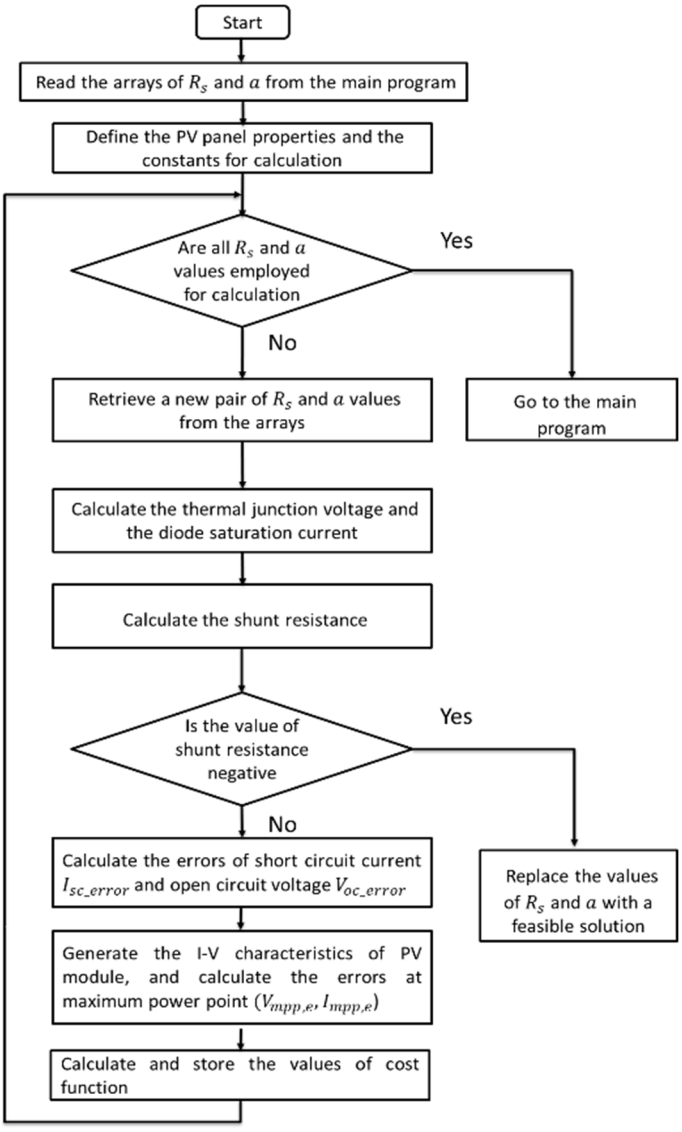

Fig. 2.9: Flowchart of the cost function evaluation.

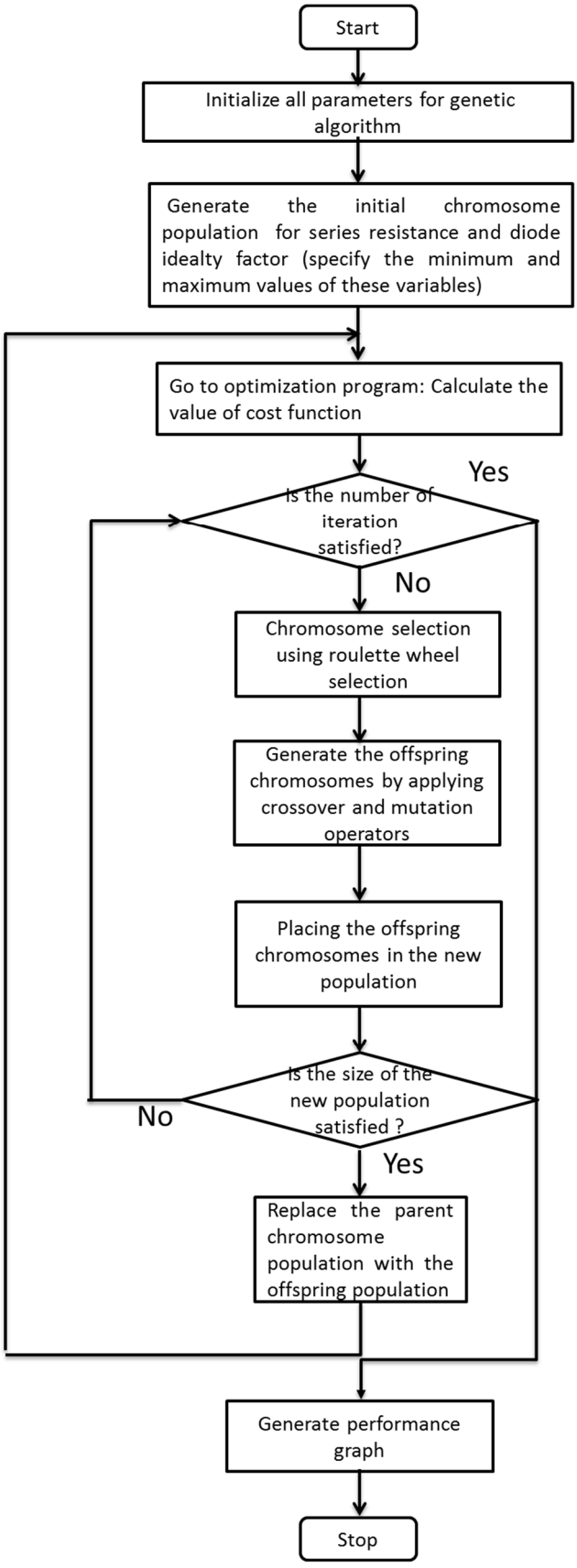

Fig. 2.10: Flowchart of the GA.

2.6.6 Simulation results

Four different commercial PV modules are investigated to compare the performance of the four parameter estimation techniques. The results are compared in terms of the relative errors in maximum power (P_{max}), short circuit current (I_{sc}), open circuit voltage (V_{oc}), current (I_{mpp}) and voltage (V_{mpp}) at the MPP, respectively. These five indexes illustrate the performance of each parameter estimation technique. One parameter estimation technique estimates the parameters of a SDM more precisely that the others when a lower index value is observed. The parameters of the four PV modules at STC are shown in Table 2.2.

Table 2.2: Parameters of the four PV modules at STC.

Parameters	BP3175	BP380	Solarex MSX-60	Kyocera KC200GT
Rated maximum power (P_{max})	175 W	80 W	60 W	200 W
Voltage at the MPP (V_{mpp})	36 V	17.6 V	17.1 V	26.3 V
Current at the MPP (I_{mpp})	4.9 A	4.55 A	3.5 A	7.61 A
Short circuit current (I_{sc})	5.3 A	4.8 A	3.8 A	8.21 A
Open circuit voltage (V_{oc})	44.2 V	22.1 V	21.1 V	32.9 V
Temperature coefficient of I_{sc}	(0.065±0.015) %/℃	(0.065±0.015) %/℃	(0.065±0.015) %/℃	3.18×10-3 A/℃
Temperature coefficient of V_{oc}	-(160±20) mV/℃	−(80±10) mV/℃	−(80±10) mV/℃	-1.23×10-1 V/℃
Number of cell (N_s)	72	36	36	54

In Tables 2.3 to 2.6, the results for the four parameter estimation techniques are displayed. The first six rows show the values of the parameters involved in an SDM and the last five rows demonstrate the relative errors in terms of the remarkable points.

In Figs. 2.11 to 2.15, the values of the relative errors are displayed graphically using bar charts and compared among the four types of PV modules. Fig. 2.11 shows the results of the relative errors in P_{max}. Fig. 2.12 displays the results of the relative errors in I_{sc}. Fig. 2.13 shows the results of the relative errors in V_{oc}. Fig. 2.14 shows the results of the relative errors in I_{mpp}. Fig. 2.15 shows the results of the relative errors in V_{mpp}. Among the parameter estimation techniques evaluated, Chatterjee's iterative approach is seen to

have the best overall performance regarding the relative errors in maximum power, short circuit current, open circuit voltage and the current and voltage at the MPP.

From Figs. 2.11 to 2.15, it can be seen that the relative errors for the GA approach are much smaller than those for Villalva's iterative approach using the four PV modules in all five indexes, which validates that the GA approach can significantly improve the model accuracy when compared to Villalva's iterative approach. It is also interesting to note that the relative errors in P_{max} obtained from the GA approach have the lowest values among the four parameter estimation techniques using the four PV modules. This information reveals that the SDM estimated by the GA approach has the highest accuracy in estimating the PV module output power among the four parameter estimation techniques.

It is worth mentioning that the results generated by the analytical method have the smallest relative errors when compared against the other methods using the four types of PV modules except for the relative errors in P_{max}. This suggests the possibility of using the analytical method as the benchmarking method for the other three methods, as the analytical method takes the least amount of simulation time and obtains fairly accurate results. The accuracy of the results obtained using Villalva's iterative approach varies with different values of A. Changing the value of A can significantly affect R_s, which will assist in improving the model fit to the PV characteristic. The general relationship between A and R_s suggests that the value of R_s will increase with a decrease in A. A method of determining the value of A in Villalva's iterative approach is incrementing A by, say, 0.1 at each simulation iteration in such a way that the calculated value of R_s is approximately equal to the value obtained in Chatterjee's iterative approach.

The advantages of the ISDM approach are that it can estimate the open circuit voltage and short circuit current of a PV module with zero error and finish each iteration in a very short duration. The drawback of this approach is that it has the highest estimation error in the power at the MPP except for the modelling of the Solarex MSX-60 PV module.

Table 2.3: Results comparison of parameter estimation techniques in modelling a BP 3175 PV module.

	Chatterjee's iterative approach	Villalva's iterative approach	ISDM Approach	GA Approach
V_t	0.0379 V	1.8506 V	-	1.8506 V
R_s	0.2085 Ω	0.3390 Ω	-	0.2567 Ω
R_p	1917.5 Ω	235.43 Ω	-	480.96 Ω
I_o	0.49631 µA	12.029 nA	4.7356 µA	0.19907 µA
I_{ph}	5.3006 A	5.3076 A	5.3 A	5.3028 A
A	1.4762	1.2	1.7148	1.3970
$P_{max,error}$	0.0080	0.0021	0.0082	8.4513e-04
$I_{sc,error}$	4.6674e-08	2.8234e-09	0	2.5997e-08
$V_{oc,error}$	0	0.0018	0	0.0011
$I_{mpp,error}$	9.7868e-08	0.0111	0.0056	0.0065
$V_{mpp,error}$	0	0.0053	0.0058	5.5556e-04

Table 2.4: Results comparison of parameter estimation techniques in modelling a BP 380 PV module.

	Chatterjee's iterative approach	Villalva's iterative approach	ISDM Approach	GA Approach
V_t	0.0238 V	0.9253 V	-	0.9253 V
R_s	0.4317 Ω	0.3940 Ω	-	0.4667 Ω
R_p	39397 Ω	282.64 Ω	-	719.16 Ω
I_o	30.926 pA	14.316 pA	2.3928 µA	1.9007 pA
I_{ph}	4.8001 A	4.8067 A	4.8	4.8031 A
A	0.9269	0.9	1.6459	0.8364
$P_{max,error}$	0.001	0.0026	0.0077	6.0805e-04
$I_{sc,error}$	6.5732e-11	2.5880e-11	0	6.7566e-12
$V_{oc,error}$	0	9.0498e-04	0	4.5249e-04
$I_{mpp,error}$	1.1308e-09	0.0097	0.0265	3.9849e-05
$V_{mpp,error}$	0	0.0114	0.0341	5.6818e-04

Table 2.5: Results comparison of parameter estimation techniques in modelling a Solarex MSX-60 PV module.

	Chatterjee's iterative approach	Villalva's iterative approach	ISDM Approach	GA Approach
V_t	0.0378 V	0.9253 V	-	0.9253 V
R_s	0.1387 Ω	0.1690 Ω	-	0.1970 Ω
R_p	1157.8 Ω	154.13 Ω	-	352.97 Ω
I_o	0.68938 µA	21.226 nA	5.7992 µA	87.883 nA
I_{ph}	3.8005 A	3.8042 A	3.8 A	3.8021 A
A	1.4695	1.2	1.7027	1.2970
$P_{max,error}$	0.0025	0.0028	0.0023	5.5521e-04
$I_{sc,error}$	8.5913e-08	4.3696e-09	0	2.0013e-08
$V_{oc,error}$	0	0.0019	0	9.4787e-04
$I_{mpp,error}$	1.9039e-07	0.0097	0.0056	1.3848e-04
$V_{mpp,error}$	0	0.0152	0.0058	0.0029

Table 2.6: Results comparison of parameter estimation techniques in modelling a Kyocera KC200GT PV module.

	Chatterjee's iterative approach	Villalva's iterative approach	ISDM Approach	GA Approach
V_t	0.0353 V	1.3879 V	-	1.3879 V
R_s	0.2068 Ω	0.2290 Ω	-	0.2076 Ω
R_p	1743.5 Ω	174.14 Ω	-	1390.7 Ω
I_o	0.25706 µA	21.651 nA	17.812 µA	0.25023 nA
I_{ph}	8.2110 A	8.2208 A	8.2100	8.2112 A
A	1.3720	1.2	1.8177	1.3697
$P_{max,error}$	7.1503e-04	0.0018	0.0022	1.9448e-04
$I_{sc,error}$	4.5064e-08	5.5098e-09	0	4.4215e-08
$V_{oc,error}$	0	0.0012	0	3.0395e-04
$I_{mpp,error}$	3.1456e-08	0.0064	0.0143	5.2015e-04
$V_{mpp,error}$	0	0.0076	0.016	0

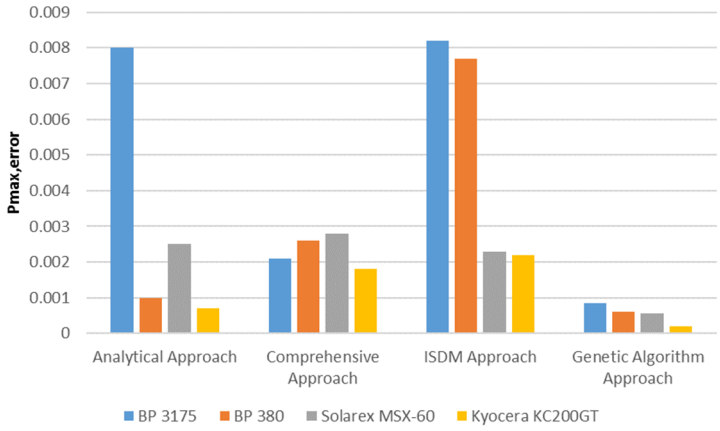

Fig. 2.11: Comparison of the relative errors in P_{max}.

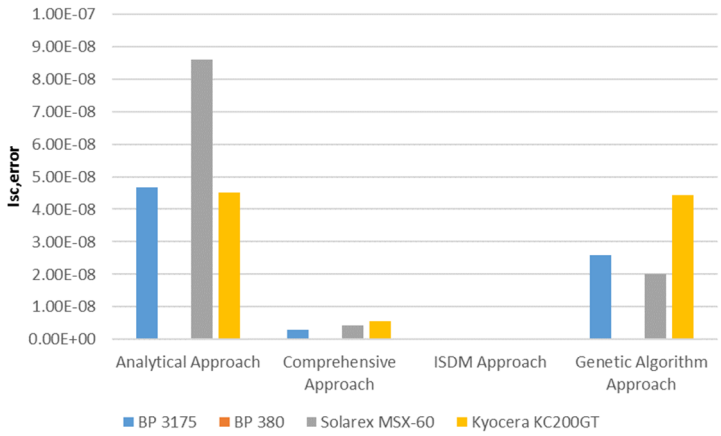

Fig. 2.12: Comparison of the relative errors in I_{sc}.

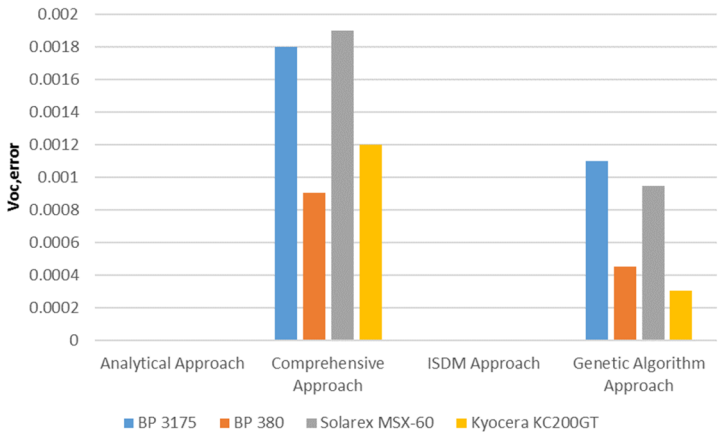

Fig. 2.13: Comparison of the relative errors in V_{oc}.

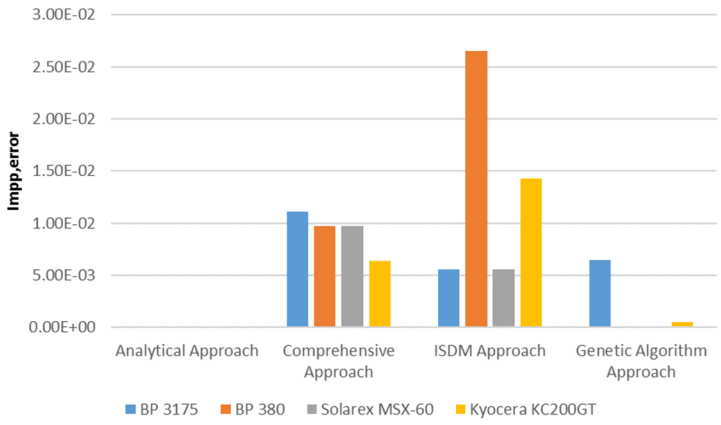

Fig. 2.14: Comparison of the relative errors in I_{mpp}.

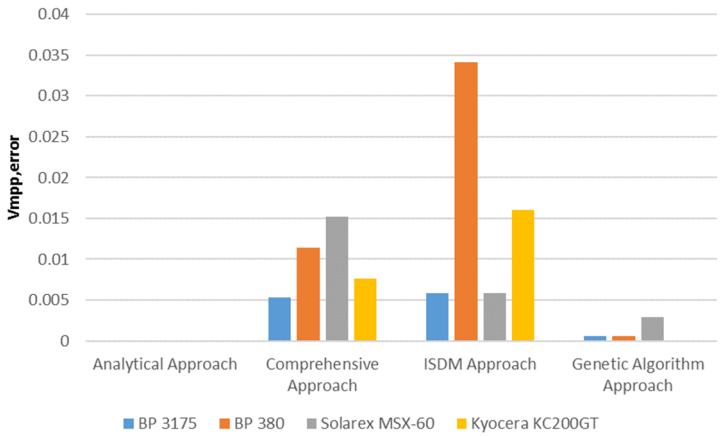

Fig. 2.15: Comparison of the relative errors in V_{mpp}.

2.7 Experimental Testing of a BP 380 PV Module

In order to validate the effectiveness of the SDM and measure the experimental I-V and P-V characteristics, experimental measurement of a BP380 PV module characteristics was conducted. The BP380 PV module was set up on the roof of the School of Engineering and ICT building and a ramp signal was applied to the duty cycle of the boost converter to enable the PV module voltage to be swept from approximately 22 V to 3 V. The irradiance was measured using the Kimo SL200 solarimeter [83] whereas the temperature was sampled via a thermocouple mounted on the back of the BP380 PV panel. The data for the PV module voltage, current and power at different tilt angles were collected through a NI data acquisition unit and logged in a LabVIEW interface. The experimental setup is shown in Fig. 2.16.

Fig. 2.16: Experimental Setup.

2.7.1 Development of the PV module model

A PV module model is developed in the *MATLAB/SimPowerSystems* environment using the SDM modelling approach. Fig. 2.17 shows the simulation model for a BP 380 PV module characteristics tracing. The *Matlab* function inside the PV module sub-model (as shown in Fig. 2.18) implements the SDM mathematical equations mentioned in Section 2.5.1. The detailed script of the *Matlab* function in Fig. 2.18 implementing the SDM can be found in Appendix A. In the succeeding chapter, this model will be extended to the PV array model that used in the entire simulation model for the single-phase grid-tied PV system. The parameters of the PV module model are estimated using Chatterjee's iterative approach described in [37]. The parameters of the BP380 PV module are shown in the second column of Table 2.2. The parameters of the PV module model are also provided in the column 'Chatterjee's iterative approach' of Table 2.4.

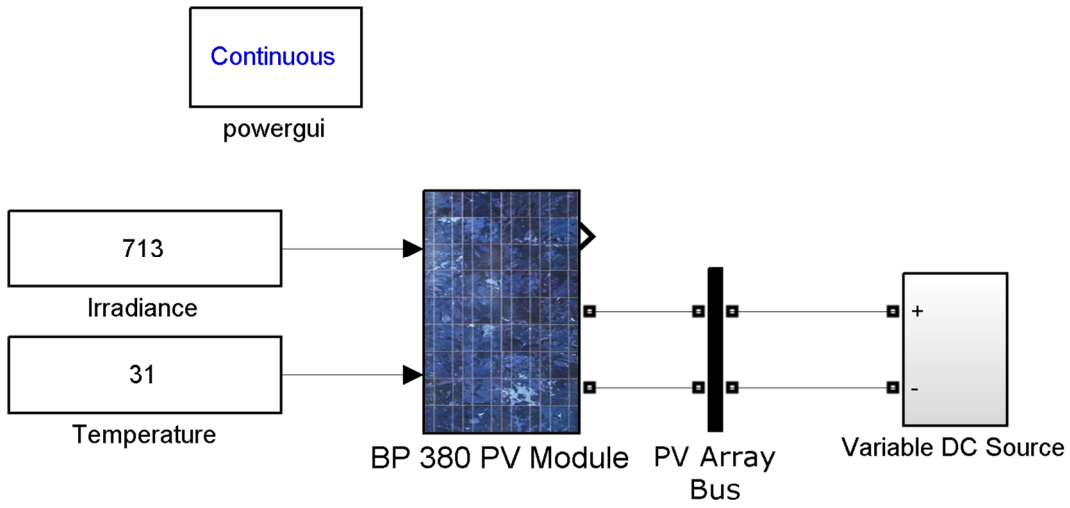

Fig. 2.17: The simulation model for the BP 380 PV module characteristics tracing.

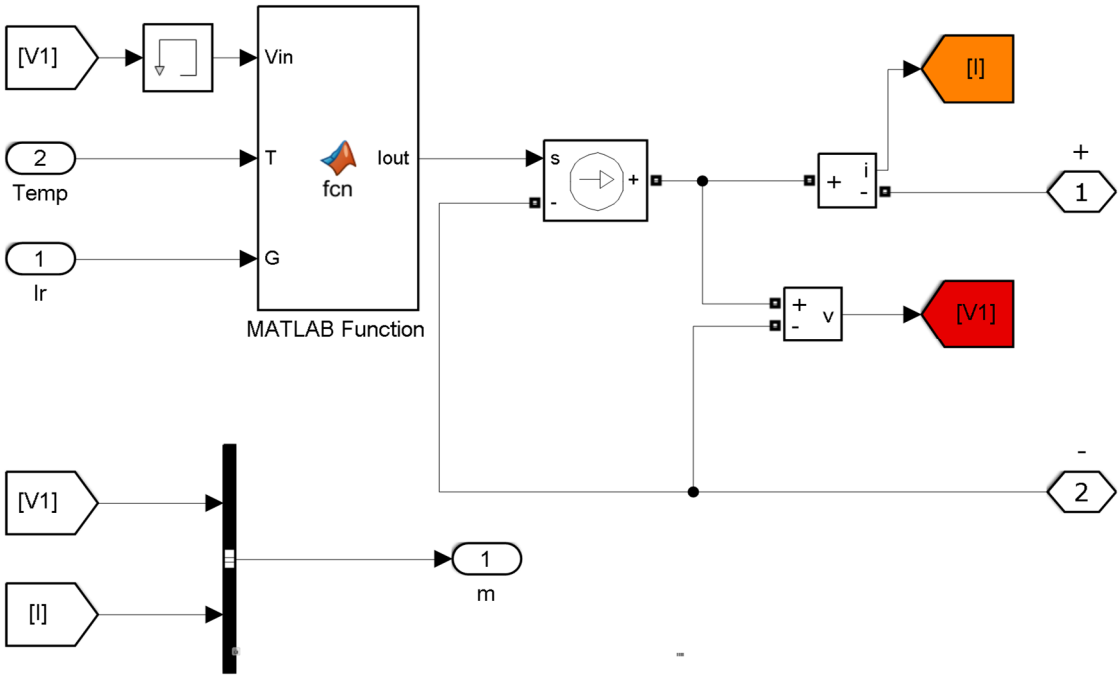

Fig. 2.18: Subsystem model of the PV module.

2.7.2 Validation of the PV module model

To validate the utility of the developed PV module model in modeling the BP 380 PV module, a PV module characteristics tracker composed of a boost converter and a resistive load is used to sample the characteristics of the BP380 PV module. The circuit diagram of the boost converter and sensor circuitry is shown in Fig. 2.19.

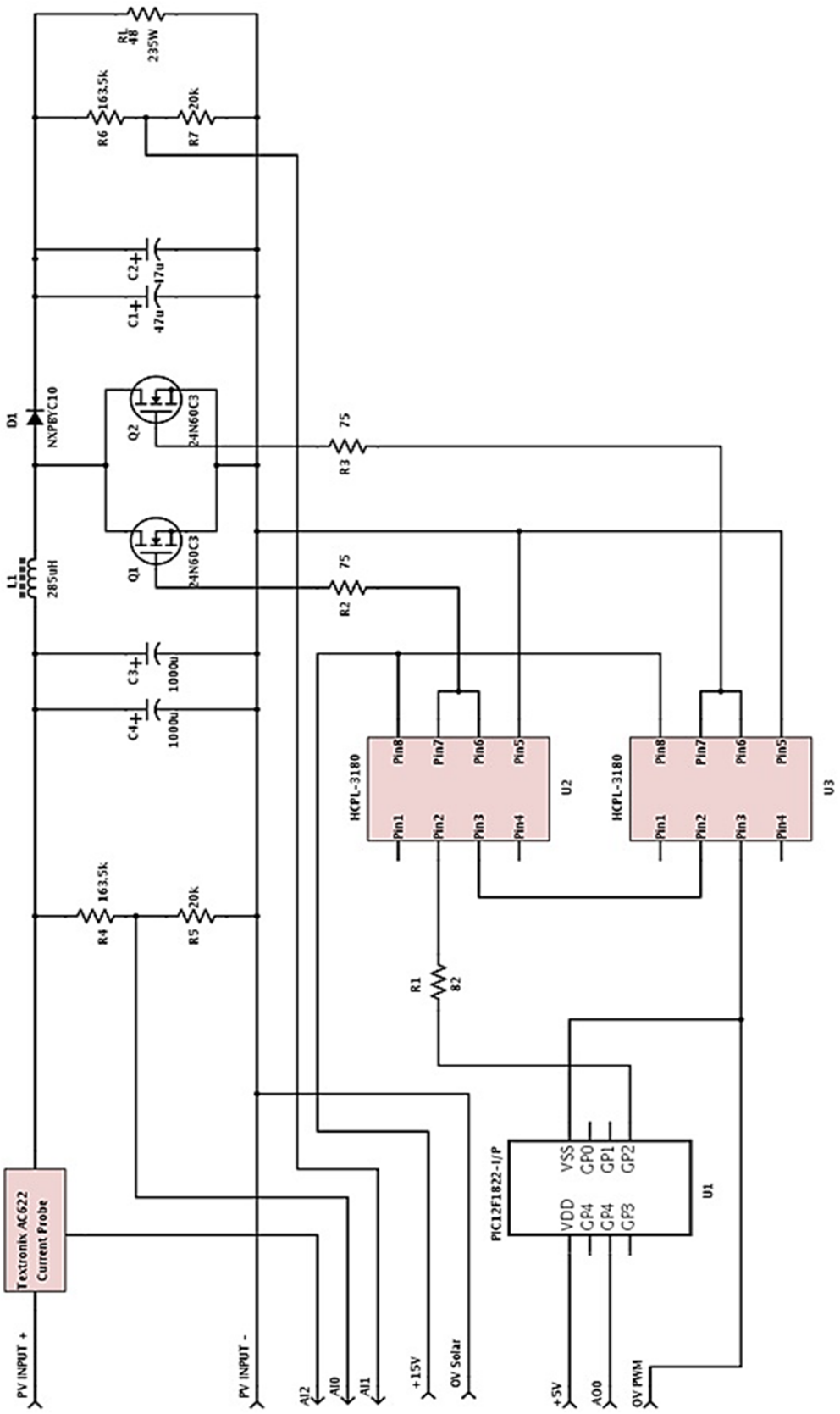

Fig. 2.19: Circuit diagram of the boost converter with voltage and current sensor circuitry [22].

For the experimental measurement of the BP380 PV module characteristics, a total number of ten P-V and I-V curve traces were measured. With experimental uncertainties at each test, the measurements of irradiance and temperature may have slight errors. One source of errors for the irradiance measurement is that the solar cell of the Kimo SL200 solarimeter may not be in line with the test BP380 PV module and the solarimeter may produce inconsistent data. The accuracy of irradiance recordings is low since the Kimo Solarimeter samples irradiance for one-minute increments [83], [84]. Proper calibration must be done prior to tracing each characteristic curve.

Another factor affecting measurement accuracy is that the temperature and irradiance levels slightly vary during the test period. Inaccurate irradiance measurement may also result from a time delay in running the test LabVIEW program to extract the PV module characteristics after temperature and irradiance measurements. These critical influences contribute to some of the differences between the experimental and measured characteristics of the PV module. The acceptable tolerances for the irradiance and temperature records are considered to be no more than 5 W/m^2 and 2 ℃, respectively. To improve the fitting of the PV module model, additional 5 W/m^2 and 2 ℃ are added to the actual values of temperature and irradiance in the simulations, respectively.

Two samples of I-V and P-V characteristics for the BP380 PV module with additional correction values added to the actual temperature and irradiance levels under similar environmental conditions are shown in Fig. 2.21 and Fig. 2.20, respectively. These two sample measurements are labelled as Case A and Case B. The relative errors (in percentage) of the three remarkable points in the experimental I-V and P-V characteristics are presented in Table 2.7. One can easily see that a reasonable match between the experimental and simulated P-V and I-V characteristics is shown in Figs. 2.20 and 2.21. Generally, the simulated characteristics preserve the overall shape of the experimental characteristics. In Table 2.7, it can be seen that the simulated curves match closely the experimental curves in terms of the voltage at the MPP (about 1.1% of relative error) and open circuit voltage (about 1% of relative error). For MPP power matching, the PV module model produces a poor prediction (about 6% of relative error), indicating that the PV module model tends to overestimate the power at the MPP together with the characteristics in Figs. 2.20 to 2.21. There is a slight deviation between the short circuit

current predicted by the PV module model and that measured in the experiment. The PV module model has a better prediction of the BP 380 PV module voltage than that of the current (about 7% of relative error in current compared with 1% in voltage).

Table 2.7: Percentage errors of the three remarkable points in the experimental measurements.

	Case A	Case B
$P_{max,error}$	6.05%	5.01%
$I_{sc,error}$	7.23%	6.14%
$V_{oc,error}$	0.93%	0.83%
$I_{mpp,error}$	7.23%	6.14%
$V_{mpp,error}$	1.09%	1.05%

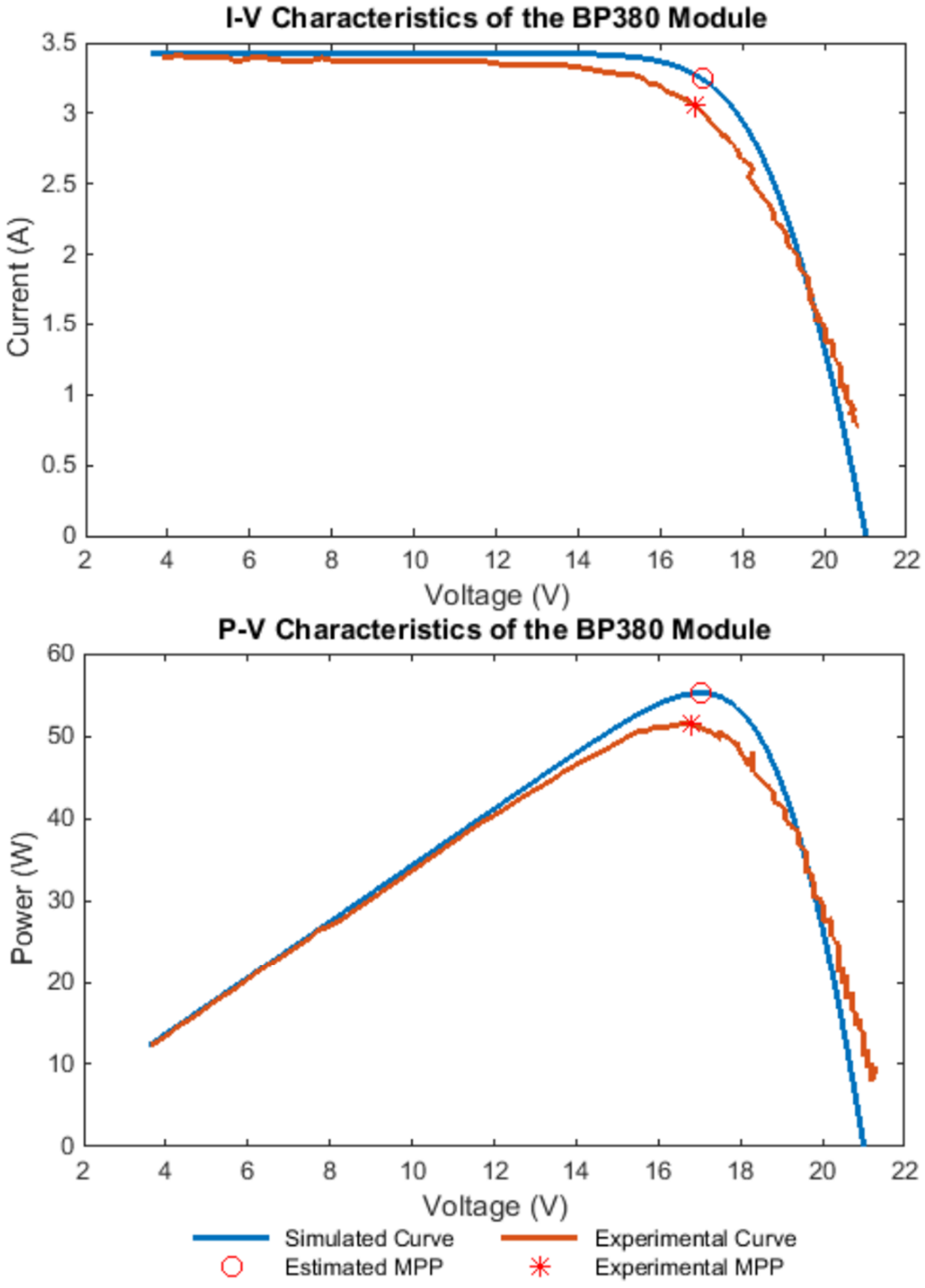

Fig. 2.20: Case A - the simulated and experimental I-V and P-V characteristics at irradiance of $715\ W/m^2$ *and temperature* $32.86\ ℃$.

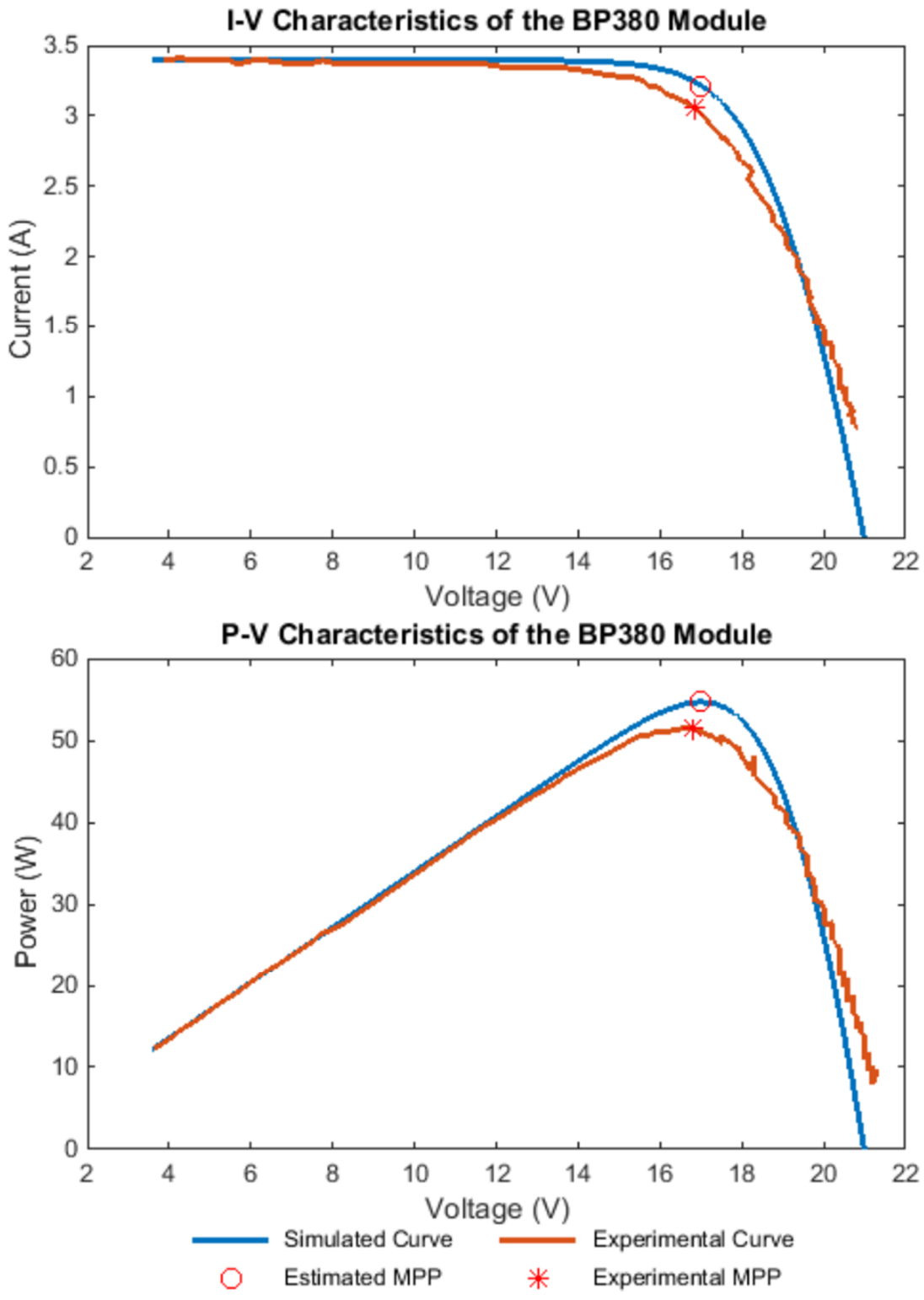

Fig. 2.21: Case B - the simulated and experimental I-V and P-V characteristics at irradiance of $708\ W/m^2$ *and temperature* $33\ ℃$.

2.8 Conclusion

In this chapter, a review of the available PV technologies is presented. PV characteristics under uniform and non-uniform environmental conditions and their dependences on the ambient temperature and irradiance have been investigated. Several conventional diode-based PV cell models in modelling a PV cell have been elaborated. Among these PV cell models, the SDM has been explored in detail due to its simplicity and low computational requirement. Three parameter estimation techniques of a SDM in literature have been thoroughly explored. A novel GA approach to parameter estimation of a SDM is proposed to improve the model accuracy when compared to Villalva's iterative method. Comparison between the experimental and simulated characteristics of the BP 380 PV module under uniform environmental conditions has been provided. The experimental results show that the developed PV module can actually replicate the PV module characteristics measured in the experiment with slight errors in predicting the power at the MPP and short circuit current.

Chapter 3
Review of Maximum Power Point Tracking Techniques and Power Electronic Interfaces for Photovoltaic Systems

3.1 Introduction

Photovoltaic (PV) systems exhibit non-linear characteristics and the maximum power point (MPP) is ever-changing with respect to temperature and irradiance variations. It is important to track the MPP in real time to ensure PV systems operate in an efficient manner [22], [85]. Maximum power point tracking (MPPT) is the process of matching the output voltage or current of a PV device with its maximum operating point based on the environmental conditions [86]. The general classification of various MPPT methods is based on whether the technique could distinguish between the global MPP (GMPP) and the local MPPs of the PV characteristics. Conventional MPPT methods are only capable of tracking the MPP of a PV system under uniform environmental conditions, where only one MPP is observed in the P-V characteristic. Conventional MPPT techniques require less computational power and are easily implemented in cheap programmable microcontrollers such as field-programmable gate array (FPGA) [87]. One key factor that affects the PV system performance is partial shading, when PV array is exposed to non-uniform environmental conditions, the output characteristics of PV array may exhibit multiple peaks [41], [88]–[90]. There is only one GMPP on the P-V curve of the PV array that experiences partial shading. A PV array with non-uniform irradiance conditions can provide the maximum power output if its operating point is located at its GMPP. Global (GMPPT) techniques are able to distinguish the GMPP among all the local MPPs especially when PV arrays experience partial shading. Partial shading can be attributed to several factors, such as cloud passing, the shadow from surrounding objects, dust or dirt on the PV panel surface and mismatch of PV cells [22], [41]. GMPPT techniques usually suffer from significant power losses and the techniques itself needs to be tailored for different PV systems [91].

In general terms, a variety of MPPT techniques can also be classified on the basis of the control variable adopted [85]:

1) PV array output voltage.
2) PV array output current.
3) Duty cycle signal in DC/DC converters.

The first two options require a digital controller to convert a voltage or current signal to a duty cycle signal that controls the operation of the switch in the DC/DC converter. The digital controller can be a proportional-integral (PI) or proportional-integral-derivative (PID) controller depending on the changing pattern of the control variable, or a hysteresis controller [92].

The criteria for assessing various MPPT techniques for uniform and non-uniform environmental conditions are shown as follows [22], [90], [93]:

- Distinguish between the GMPP and the local MPPs, or capable of tracking the GMPP.
- Time taken to the vicinity of the GMPP.
- Response time to abrupt changes in environmental variables, such as temperature and solar irradiance.
- Hardware requirements, for example, the number of sensors required.
- Dependence on the PV array parameters.

The instrumentation involved for different MPPT techniques are vastly different [94]. Only one current sensor used for shaping the buck–boost inductor current as well as for MPPT, and one voltage sensor for the PV array voltage measurement are required in the MPPT method mentioned in [94]. This MPPT method does not require an inductor current measurement, and is applicable to any single-phase single-stage grid-connected PV inverter operating in continuous conduction mode (CCM). The PV array output power is estimated from the PV array voltage and the inductor current amplitude. The inductor current is determined using the principle of correlation between the reference inductor current and the PV array output current. A MPPT technique proposed in [95] only requires voltage measurements of the PV array. A suitable capacitive load connected at the output

of the PV array is used to estimate the PV array output power. The position of the MPP is identified by considering the second-order derivative of the squared capacitive load voltage. A complex noise filtering technique is also implemented in this MPPT method to reduce the noise component in the second-order derivative of the squared capacitive load voltage. These methods highlight the reduction of the sensor requirements for the MPPT operation.

Measurement noise could have a significant impact on the performance of MPPT techniques [96]. In practical PV systems, the voltage and current of a PV array contain measurement noise. Although measurement noise is insignificant when compared to its corresponding signal, it can contribute significantly to the difference between two or more consecutive measurements [97]. Some conventional MPPT techniques such as P&O and IC methods, utilize the differences between several voltage or current measurements to determine the direction of tracking, which are particularly susceptible to measurement noise. Neglecting measurement noise could lead to poor tracking performance or even divergence from the MPP in some circumstances [98].

In real environmental conditions, the ambient temperature and solar irradiance under which PV arrays operate changes instantaneously with time [5]. The sampling rate of the MPPT controller is required to be fast enough to track intermittent variations of irradiance and temperature.

3.2 Conventional MPPT Techniques

Conventional MPPT techniques can be further classified into two categories, which are indirect (*quasi seeking*) and direct (*true seeking*) methods [99]. Some examples of indirect methods are curve fitting [100]–[102], look-up table [103], fractional open circuit voltage [104]–[107] and fractional short circuit current [108]–[110]. Some examples of direct methods are P&O [111]–[124], IC [125]–[129].

In this section, some of the conventional MPPT methods will be concentrated on as listed below:

- Fractional open-circuit voltage method;

- Fractional short-circuit current method;
- P&O method;
- IC method.

These conventional MPPT methods are most commonly used in various PV systems. This is largely due to their simplicity and ease of implementation [85].

3.2.1.1 Maximum power point estimation techniques

Various maximum power point estimation (MPPE) techniques [107], [130]–[132] are proposed in the literature to estimate the operating point of a PV array. These techniques depend on measured parameters of the PV array [133] and predefined relationships to estimate the MPP location. Empirical relationships adopted by MPPE techniques are developed under uniform environmental conditions, so these relationships are no longer valid when the PV array is partially shaded [22]. The estimation accuracy may decrease with time as the characteristic of the PV array varies due to cell degradation [41].

Two common MPPE techniques that will be introduced in the following sections are fractional open-circuit voltage method and fractional short-circuit current method respectively. These methods only rely on one measured variable and regulate the current or voltage of a PV array to implement the MPPT.

3.2.1.1.1 Fractional open-circuit voltage method

Fractional open-circuit voltage method estimates the MPP via measuring the open circuit voltage of a PV array. The operating voltage of the PV array can be determined by the following linear relationship:

$$V_{mpp} = k_1 V_{oc} \tag{3.1}$$

where k_1 represents the constant of proportionality. The values of k_1 is computed through determining the empirical relation between V_{oc} and V_{mpp} for the specific PV array. A useful rule of thumb is that k_1 takes a value between 0.71 and 0.78 [133].

The measurement of V_{oc} can be achieved by periodically opening the switch with the DC-DC converter connected at the output of the PV array. During the switch opening period, the power supply from the PV array is temporarily interrupted. The periodical measurement of the open circuit voltage is used to calculate the operating voltage of the PV array.

A sample&hold used in [134], [135] consisting of external passive elements is to periodically sample the open circuit voltage of a PV array with a fixed sampling rate. The method in [135] dynamically changes the sampling period (T) and sampling time (ξ) of the fractional open circuit voltage MPPT controller to control the operation of the DC-DC converter using pulse frequency modulation (PFM).

The pilot cell tracking method in [136] assumes a constant proportionality between the open circuit voltage of a pilot cell and that of the PV array. It also assumes a constant ratio within the PV array between the voltage at MPP and the open circuit voltage. A pilot cell is a small-scale PV device that is the same type and is in the same placement with the PV array. Measuring the open circuit voltage of a pilot cell is easily implemented when compared to that of the PV array as the pilot cell is electrically separated from the PV array. The operating voltage of the PV array is regulated to a fixed multiple of the open circuit voltage of the pilot cell.

3.2.1.1.2 Fractional short-circuit current method

This method is similar to fractional open circuit voltage method as mentioned before. It locates the MPP of a PV array via measuring its short circuit current. Fractional short-circuit current method regulates the operating current of the PV array to a fixed multiple of its short circuit current [133].

As with the fractional open circuit voltage method, the proportional constant between the current at the MPPT of the PV array and its short circuit current can be expressed as follows:

$$I_{mpp} = k_2 I_{sc} \tag{3.2}$$

where k_2 is a proportionality constant, the value of k_2 is normally selected from 0.78 and 0.92 [133]. Similar to fractional open circuit voltage method, the value of k_2 is influenced by several factors such as PV technology, fill factor and meteorological conditions [137].

The measurement of I_{sc} can be achieved in a similar manner to that of V_{oc} in fractional open-circuit voltage method. The PV array is momentarily shorted by means of closing the switch within the DC-DC converter. Power supply of the PV array becomes unavailable during the switch closing period. Hall-effect sensors and resistive shunts are commonly used to obtain the measurement of short circuit current [138]. For high short circuit current conditions, such as the measurement of the short circuit current of a PV array, pilot cell tracking can be used to determine the short circuit current on the basis of the measurement of the output of a pilot cell.

3.2.1.2 P&O method

The P&O method is the most commonly implemented MPPT technique due to its ease of implementation [5], [139]. It perturbs the control variable based on the slope of the P-V curves of interest. The control variable could be either voltage [133], [140], current [94], [141], [142] or duty cycle [143]–[145]. P&O method utilises the fact that the slope of the P-V curve is negative on the right-hand side of the MPP, zero at the MPP, and positive on the left-hand side of the MPP [139], [146]–[148]. This is summarized using the following mathematical equations:

$$\frac{\partial P}{\partial V} > 0 \qquad \text{Left-hand side of the MPP} \tag{3.3}$$

$$\frac{\partial P}{\partial V} = 0 \qquad \text{At the MPP} \tag{3.4}$$

$$\frac{\partial P}{\partial V} < 0 \qquad \text{Right-hand side of the MPP} \tag{3.5}$$

The P&O method is implemented discretely in practical applications, the slope of P-V characteristics can be expressed in the discrete form as follows [149]:

$$\nabla_{P\&O} = \frac{P_k - P_{k-1}}{V_k - V_{k-1}} = \frac{\Delta P}{\Delta V} \tag{3.6}$$

where $\nabla_{P\&O}$ represents the slope of the two consecutive samples points in discrete form. The sign of $\nabla_{P\&O}$ determines the perturbation direction of the control variable. V_k and P_k symbolise the voltage and power values at the kth (current) sampling instant, respectively, whereas V_{k-1} and P_{k-1} are the voltage and power values at the (k-1)th (previous) sampling instant, respectively.

P&O method operates by perturbing the control variable periodically and comparing the power difference between the current and previous perturbation cycles [150]. If the power difference is positive, the method maintains the same perturbation direction, otherwise changes to the opposite perturbation direction [22]. The flowchart of the P&O method using voltage as the control variable is shown in Fig. 3.1.

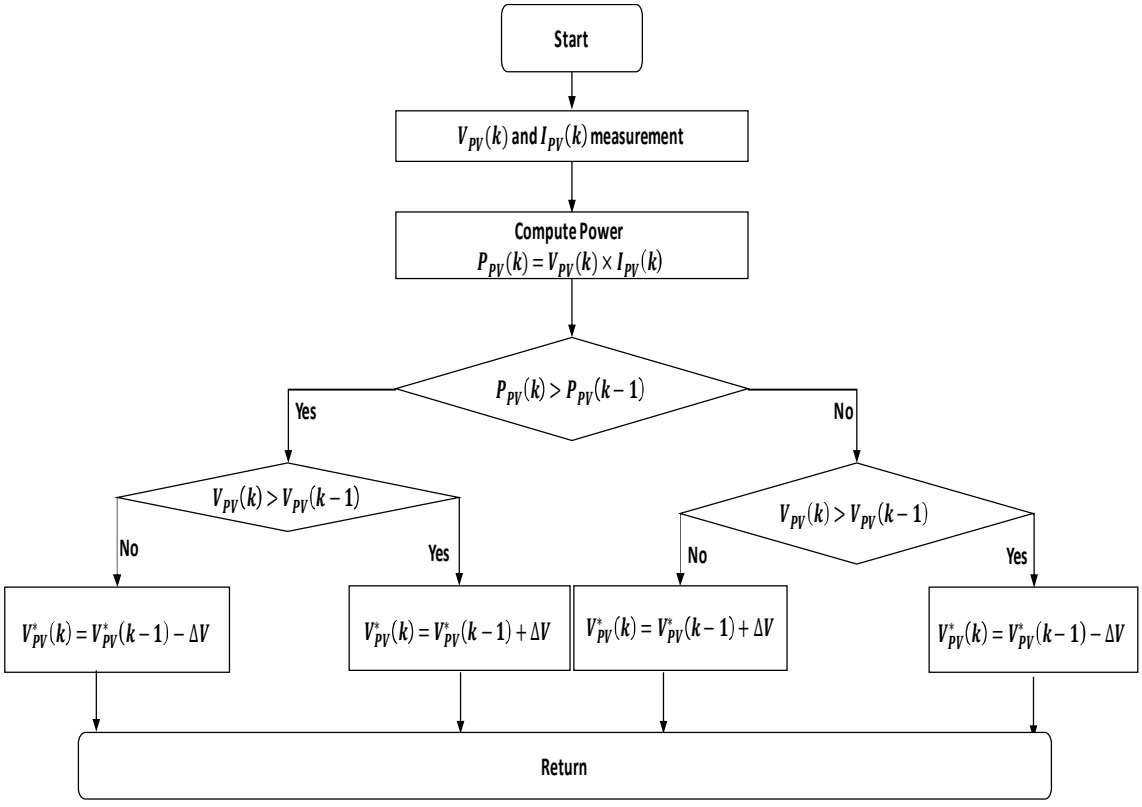

Fig. 3.1: Flowchart of P&O method adapted from [22].

A drawback of the P&O method is the introduction of the steady-state oscillation around the MPP leading to unnecessary power consumption [22]. This can be mitigated by selecting a small duty cycle perturbation and a high sampling period for the P&O algorithm [139]. A small duty cycle perturbation may however reduce the tracking speed.

Thus, there is a trade-off between the steady-state oscillation around the MPP and the tracking speed of the algorithm. Another disadvantage of the P&O method is that it cannot manage rapid solar irradiance variations [151]–[153]. When the solar irradiance changes abruptly, the P&O method may track to a suboptimal MPP location or totally lose track of the MPP.

For the traditional P&O method, the step size of the control variable is fixed and affected by the requirements of tracking accuracy and efficiency. Lower step size will cause lower convergence towards the MPP whereas higher step size will generate oscillations in power around the MPP. A variety of variable step size P&O methods are employed to improve the convergence speed to the MPP and reduce the steady-state power losses. Two examples of variable step-size P&O methods are shown in [144] and [70], respectively. These two examples use duty cycle and PV array voltage as the control variables respectively. The control variable update equation in [144] uses the following expression to change the duty cycle:

$$D(k+1) = D(k) - N\frac{\Delta P}{\Delta I} \tag{3.7}$$

where $D(k+1)$ denotes the duty cycle at the next perturbation cycle while $D(k)$ symbolises the value at the current perturbation cycle. $\frac{\Delta P}{\Delta I}$ represents the changes in the PV array output power with respect to its current. N is known as the scaling factor that is highly dependent on the specifications of each individual PV array and must be tuned at the design process [144], [152].

The PV array output voltage is regulated in [70] and the reference PV voltage is given by:

$$V_{ref}(k) = V_{ref}(k-1) + N \cdot \frac{dP}{dV} \tag{3.8}$$

where $V_{ref}(k)$ represents the reference voltage of the PV array in the current perturbation cycle and $V_{ref}(k-1)$ symbolises the reference voltage in the preceding perturbation cycle. N is the scaling factor and $\frac{dP}{dV}$ is the derivative of the PV array power to voltage.

3.2.1.3 IC method

The IC technique [85], [154] uses the same basic principle as the P&O method as provided in (3.3) to (3.5). It uses the instantaneous conductance ($\frac{dI}{dV}$) and incremental conductance ($\frac{I}{V}$) to determine the perturbation direction of the MPPT controller.

$$\frac{dI}{dV} > -\frac{I}{V} \qquad \text{Left-hand side of the MPP} \qquad (3.9)$$

$$\frac{dI}{dV} = -\frac{I}{V} \qquad \text{At the MPP} \qquad (3.10)$$

$$\frac{dI}{dV} < -\frac{I}{V} \qquad \text{Right-hand side of the MPP} \qquad (3.11)$$

A comparative analysis between P&O and IC methods is included in [85], [150]. In [149], the IC and P&O methods are considered as equivalent methods in terms of their basic theories and mathematical background, but different in discrete implementation. The discrete implementation of the IC method is given in (3.12). In practice, both methods are discretised with different sampling frequencies, usually ranging from 1 Hz to.20 Hz [65], [155]. The IC method has advantages of better noise rejection and less off-track of the MPP of the PV array owing to system dynamics [156].

$$\nabla_{IC} = \frac{I_k - I_{k-1}}{V_k - V_{k-1}} + \frac{I_k}{V_k} = \frac{\Delta I}{\Delta V} + \frac{I_k}{V_k} \qquad (3.12)$$

where ∇_{IC} represents the sum of the instantaneous conductance and incremental conductance for two consecutive samples in discrete form. The perturbation direction of the IC method is dependent on the sign of ∇_{IC}. I_k and I_{k-1} symbolise the current values at the current and previous sampling instants, respectively.

The relationship between ∇_{IC} for the IC method and $\nabla_{P\&O}$ for the P&O method shown in (3.13) is investigated in [149]. The analytical expression between ∇_{IC} and $\nabla_{P\&O}$ is given as follows:

$$\nabla_{IC} = \frac{\nabla_{P\&O}}{V_k} + \frac{\Delta I}{V_k} = \frac{\nabla_{P\&O}}{V_k} + \varepsilon \qquad (3.13)$$

where ε represents the error between the P&O and IC methods in discrete implementations. The signs of ∇_{IC} and $\nabla_{P\&O}$ can be potentially different with the introduction of ε in a certain situation, which means that the P&O and IC methods could perturb in different directions with the same environmental condition [149]. This situation can be further explained where the operating point moves across the MPP with the step perturbation. Equation (3.13) also illustrates the tracking direction differences between the P&O and IC methods in discrete implementations. The drawbacks of the IC method are relatively similar to those of the P&O method. The disadvantages of the IC method include the trade-off between steady-state oscillations and tracking speed, and the inability to distinguish between the local MPPs and the GMPP [22].

Using the PV array voltage as the control variable, the flowchart for the IC method is shown in Fig. 3.2. The algorithm checks whether the voltage difference between two consecutive samples is zero. This must be done before evaluating the incremental conductance and instantaneous conductance since a division by zero occurs if the voltage difference is zero. A check for the current difference is required when the voltage difference is zero. The PV array must operate at its MPP if both the voltage and current differences are equal to zero.

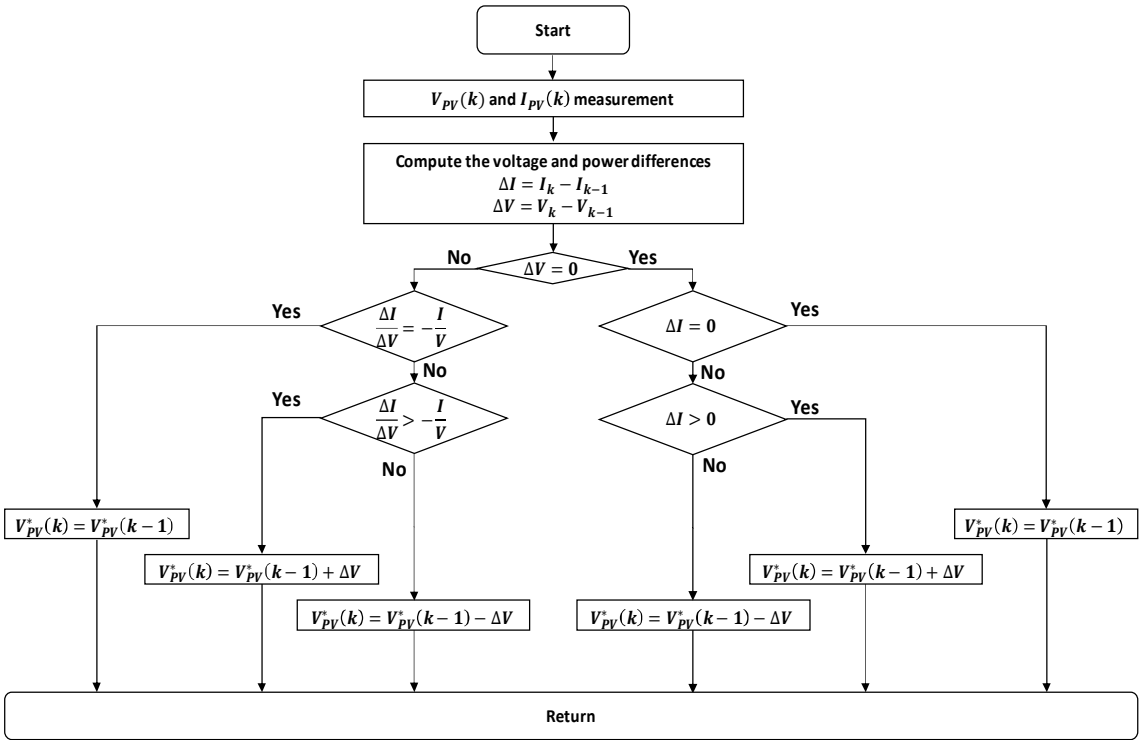

Fig. 3.2: Flowchart of the IC method adapted from [22], [157].

3.3 GMPPT Algorithms

This section will address techniques which have been specifically designed to handle tracking the GMPP under non-uniform environmental conditions. These techniques are capable of distinguishing the GMPP from multiple local MPPs under partial shading conditions (PSCs). These techniques include line search with Dividing Rectangle (DIRECT) [158], Fibonacci sequence [159], [160], PSO and SA. One drawback of some of the GMPPT techniques such as PSO and SA, is that reinitialization conditions are needed to re-initialize the algorithms when a sudden change in solar irradiance occurs. This change may be attributed to a change in the shading pattern of PV systems, which is mostly likely a consequence of passing clouds over PV systems. If the reinitialization conditions fail to detect a sudden change in solar irradiance, the algorithms are not able to track the new GMPP. Thus, some of the GMPPT algorithms are unable to perform a continuous tracking, which can be resolved by combining the algorithms with a conventional MPPT technique such as P&O and IC, to form a two-stage method to ensure the continuous operation of a PV system at GMPP. PSO and SA GMPPT algorithms are our main focuses in this section since they are belonged to the category of artificial intelligent algorithms and are able to provide good performances in tracking to the GMPP under both uniform and non-uniform conditions [90]. These GMPPT algorithms will be fully explained in the following subsections.

3.3.1.1 Particle swarm optimisation

PSO MPPT algorithms are suitable for tracking the GMPP with the presence of multiple local peaks [92], [161]–[163]. PSO is an intelligent, stochastic and metaheuristic evolutionary computation algorithm [164], established by Eberhart and Kennedy in 1995 [165]. This optimization technique is inspired by the social behaviour of birds flocking and fish schooling. Compared to other evolutionary computation algorithms, such as GA and Artificial Bee Colony (ABC) [166], [167], it has advantages that only some primitive mathematical operators are required to converge to the final solution and the algorithm itself has memory [165]. The classical PSO algorithm is initialized with a population of random solutions. Instead of representing the solutions in chromosomes as for a GA, the potential solutions are called particles. A numerical example illustrating a vector for

particles' positions with N_p particles using voltage as the control variable can be written as follows:

$$x^k = \left[V_1^k, V_2^k, \cdots, V_i^k, \cdots, V_{Np}^k\right] \tag{3.14}$$

Correspondingly, the vector for particles' velocities is given as follows:

$$v^k = \left[V_1^k - V_1^{k-1}, V_2^k - V_2^{k-1}, \cdots, V_i^k - V_i^{k-1}, \cdots, V_{N_p}^k - V_{N_p}^{k-1}\right] \tag{3.15}$$

The position of a particle is influenced by two factors, one is the local best particle in a neighbourhood P_{best} and the other is the global best particle found by all the particles in the entire population G_{best} [92]. The classical PSO algorithm updates an individual particle's position x_i and velocity $\emptyset_i$ in each iteration using (3.16) and (3.17), respectively, where ω is the inertia weight, c_1 and c_2 are the acceleration coefficients, r_1 and r_2 are random numbers between 0 and 1. $P_{best,i}$ is the best position of particle i, and G_{best} is the best position of all particles in the population [90]. k is the current iteration index.

$$x_i^{k+1} = x_i^k + \emptyset_i^{k+1} \tag{3.16}$$

$$\emptyset_i^{k+1} = \omega\emptyset_i^k + c_1 r_1\left(P_{best,i} - x_i^k\right) + c_2 r_2(G_{best} - x_i^k) \tag{3.17}$$

A reinitialization condition described in [164] can be added to the classical PSO algorithm to enable it to track a time-varying GMPP. The time varying nature of GMPP may be attributed to change in solar irradiations or load variations with respect to time. The particles are reinitialized when the reinitialization condition, as shown in (3.18), is satisfied.

$$\frac{|P_{PV,new} - P_{PV,last}|}{P_{PV,last}} \geq \Delta P(\%) \tag{3.18}$$

where $P_{PV,new}$ is the current PV array power at steady state and $P_{PV,last}$ is its final power when the last PSO MPPT algorithm terminates. $\Delta P(\%)$ is the power threshold in percentage. The flowchart of the PSO GMPPT technique is shown in Fig. 3.3.

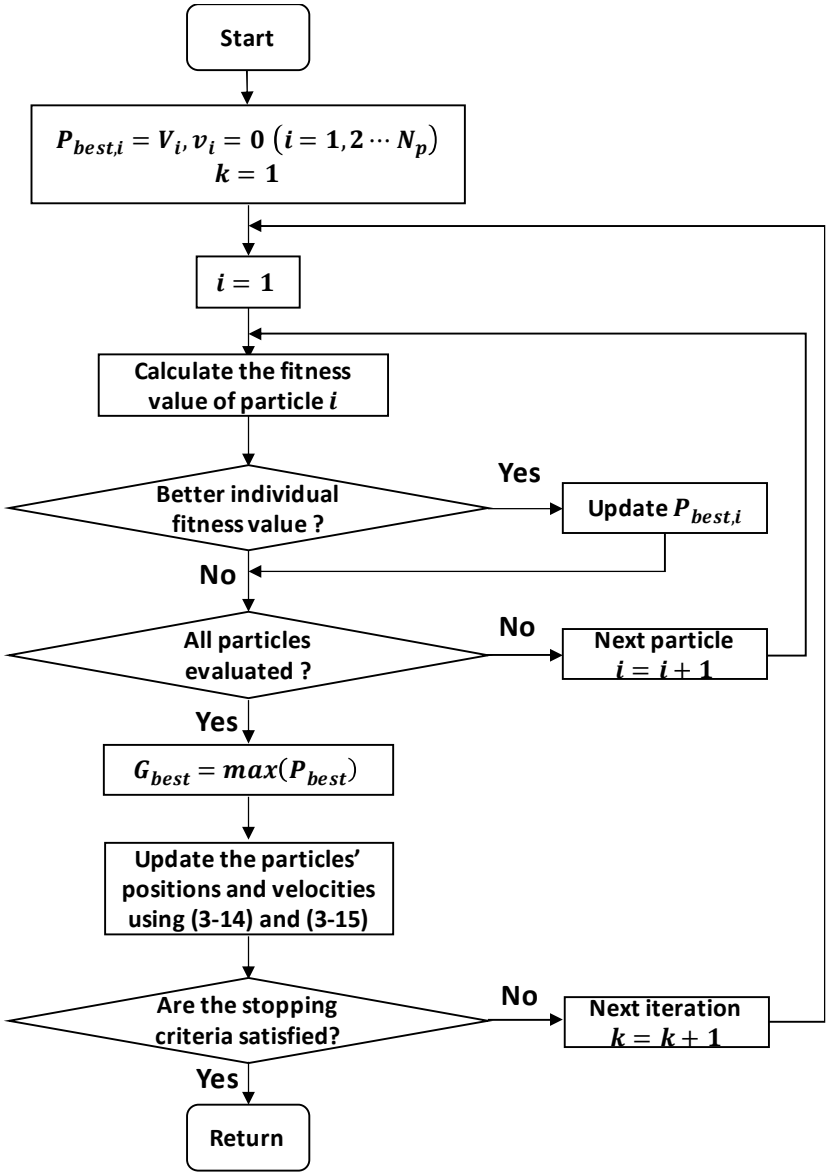

Fig. 3.3: Flowchart of the PSO MPPT technique adapted from [168].

A deterministic PSO (DPSO) algorithm is proposed in [169] to improve the performance in tracking to the GMPP. It utilizes the direct duty cycle control method, that is, the position of an individual particle represents one possible value of the duty cycle that is used to track the GMPP of the PV array. One problem resulting from the classical PSO algorithm is that a large number of iterations is needed for the algorithm to reach its final solution when there is a small difference in duty cycle between two successive iterations. Another problem is that a large change in the velocity vector may happen during the exploration process; this might lead to particles escaping from the vicinity of the GMPP. These problems can be resolved using the DPSO approach by eliminating the randomness

in (3.17) and constraining the particles' velocities between 0 and V_{max}, which leads to a deterministic velocity update equation given as follows:

$$\emptyset_i^{k+1} = \omega\emptyset_i^k + \left(P_{best,i} + G_{best} - 2x_i^k\right) \quad (3.19)$$

$$\text{for } 0 < \emptyset < V_{max}$$

Several advantages are associated with the DPSO approach: first, the particles follow a deterministic behavior with the absence of the random factors in (3.17). Second, only one parameter, i.e., inertia weight, needs to be tuned. Finally, the algorithm can adapt to rapid variations in ambient temperature and solar irradiance by limiting the velocity vector to a certain range.

The overall MPPT algorithm described in [169] comprises of two search stages: the first stage utilizes the DPSO approach to perform a coarse search for the GMPP and moves the operating point to the vicinity of the GMPP. This stage is activated when the PV array experiences partial shading. After the region of the GMPP is located, the MPPT algorithm switches to the second stage when a Hill Climbing (HC) method with variable step-size perturbation is employed to take the operating point to the exact GMPP.

A hybrid PSO and Artificial Neural Network (PSO-ANN) algorithm is proposed in [170] to improve the tracking efficiency to the range of 92.7% – 99.7% and effectively track the GMPP under PSCs. The ANN algorithm is used to initialize the optimal PV array current values at different solar irradiance levels. These initial PV array current values are fed into the PSO algorithm to constrain the search range of the GMPP in a sufficiently small region, which drastically shortens the overall computational time.

A two-stage PSO algorithm combined with the shuffled frog leaping algorithm (SFLA) is proposed in [171] to partition the entire search space into multiple sectors. Each sector is initialized with an independent micro particle swarm. The local best particle is obtained by the PSO algorithm in the first stage whereas the global best particle in the entire swarm is selected from all the local best particles by the PSO algorithm in the second stage, respectively. This method offers faster and more accurate local searching capability compared to the classical PSO algorithm.

The particles' initial locations are critical in terms of tracking speed of the PSO technique to the GMPP. An inadequate initialization of particles' positions can result in an unnecessary exploration of the P-V curve, which consequently leads to energy dissipation and a reduced MPPT efficiency. A two-phase initialization process is proposed in [92] to initialize the new particles' positions based on the previous particles' positions. In this PSO MPPT technique, direct duty cycle control is employed and the three duty cycles ($d_i, i = 1, 2, 3$) are represented by three particles. In the first phase, the new particles' positions are updated using an approximate linear correlation, shown in (3.20), based on the previous positions and the change in the PV array output power; The second phase is to perturb the new particles d_1 and d_3 obtained from the first phase in positive and negative directions by a factor of K_2, respectively. The value of d_2 remains unchanged in the second phase.

$$d_{i,new}^{1} = d_{i,old} - \frac{1}{K_1}(P_{old} - P) \tag{3.20}$$

$$d_{1,new}^{2} = d_{1,new} - K_2 \tag{3.21}$$

$$d_{3,new}^{2} = d_{3,new} + K_2 \tag{3.22}$$

where $d_{i,new}^{1}$ is the new duty cycle obtained in the first phase and $d_{i,old}$ is the previous duty cycle representing the previous GMPP, respectively. P is the PV array power at the current iteration whereas P_{old} is the PV array power at the previous iteration, respectively. K_1 is the slope of the linear segment approximating the quadratic relationship between the PV array global maximum power and the corresponding duty cycle. $d_{1,new}^{2}$ and $d_{3,new}^{2}$ are the first and the third duty cycles calculated from the second phase, respectively. K_2 is the perturbation factor.

3.3.1.2 Simulated annealing

SA is a metaheuristic optimization algorithm [172] that emulates the physical processes involved in the annealing process that is used in metallurgy [88]–[90]. This algorithm was proposed by Kirkpatrick et al. [173] and Černý [174] to solve the travelling salesman problem in 1983 and 1985, respectively. SA mathematically mimics the cooling of a set of atoms to a state of minimum energy to solve an optimization problem. The SA

algorithm has been applied to MPPT applications under uniform environmental conditions in [175] and partial shading condition in [89]. A SA MPPT technique is shown to have a good global searching behavior to locate the GMPP rather than a local MPP under PSCs [88]. An artificial temperature parameter is incorporated in the optimization process with an initial temperature T_{max} and a final temperature T_{min}. The temperature parameter starts with T_{max} and is progressively reduced to T_{min} during the optimization process. A cooling function is employed to control the temperature decrease during the optimization process. Several cooling functions could be used and an optimised cooling function is preferred to improve the performance of the SA algorithm. A common cooling function for SA algorithms is the geometric cooling function [176]–[178] given in (3.23) where T_k is the new temperature and T_{k-1} is the previous temperature, respectively. At high temperature values, the SA algorithm performs a coarse search to explore a wide search space to find the region where the GMPP lies. At low temperature values, the exploration is restricted to a local region to exactly track the GMPP.

$$T_k = \alpha T_{k-1} \tag{3.23}$$

where α is the geometric cooling constant that is a positive number less than 1.

The SA MPPT technique perturbs the PV array operating point (voltage) for several iterations to measure the corresponding energy (power) [88]. If the power obtained in the new operating point is larger than the previous power, the new operating point will be accepted. If the new operating point generates less power than that of the previous operating point, the new operating point may still get accepted depending on the acceptance probability specified in the following formula [88]–[90], [179]:

$$Pr = \exp\left(\frac{P(k)-P(k-1)}{T(k)}\right) \tag{3.24}$$

where, $P(k)$ is the measured power at the new operating point and $P(k-1)$ is the measured power at the previous operating point, respectively. $T(k)$ is the current temperature used in the SA algorithm. Pr symbolizes the probability that the SA algorithm accepts the new operating point with a worse output power.

A two-stage method combining a P&O method and an SA technique was proposed in [179] to utilize the merit of a P&O method for a continuous tracking operation and the advantage of an SA technique to locate the GMPP under PSC. This technique employs a decision criterion to determine whether a global search is required. Power variations are usually small when the P&O method operates to perform a global exploration [179]; Thus, a large power difference between the current measurement and the last measurement will trigger a global search implemented by the SA MPPT technique.

The parameters of a SA algorithm can have a significant impact on its performance. Key parameters involved in the SA algorithm described in [180] are listed as follows:

- Initial temperature;
- Cooling rate;
- Cooling frequency;
- Acceptance probability threshold;
- Neighborhood size;
- Stopping temperature;
- Cooling function;
- Stopping criterion.

A proper design for these parameters will significantly improve the performance of a SA algorithm, such as the time taken to converge to the GMPP and the accuracy of the results obtained. A methodology for assessing their impact on a SA algorithm's performance was also proposed in [180] and the results highlight the selection of suitable parameters in the SA algorithm for MPPT applications.

3.4 Power Electronic Interfaces for PV Systems

3.4.1 Introduction

Power converters are commonly used in grid-connected PV systems to control the operating point of the PV array to its MPP and to ensure an efficient conversion of energy

from the PV array side to the grid side. There are two common configurations employed in grid-tied PV systems design, which are single-stage and double-stage configurations [181]. The single-stage configuration, as illustrated in Fig. 3.4 (a), provides a reliable and cost-effective approach to supply electricity to the grid by connecting PV arrays directly to a grid-tied PV inverter. The inverter is controlled by two control schemes: MPPT control and Voltage Oriented Control (VOC). The MPPT control varies the DC link voltage reference to regulate the DC link voltage and ensures that the PV array operates at its MPP. The VOC is used to control the active and reactive power injected into the grid. One disadvantage of a single-stage configuration is that the minimum DC link voltage must be larger than the peak AC grid voltage to avoid the over-modulation operation of the grid-tied inverter [182]. Operating the inverter in the over-modulation region leads to a clipped capacitor voltage waveform, which consequently will result in a distorted inverter output voltage waveform [183]. Another shortcoming of a single-stage configuration is that galvanic isolation is not provided between the PV array and the grid. Thus, double-line frequency voltage ripple is significant at the DC link, which results from the double-line frequency of the AC grid power ripple [182]. The efficiency of MPPT techniques implemented in a PV inverter is low since the PV array output voltage fluctuates significantly. This issue can be mitigated by connecting a DC-DC converter at the output of the PV array to form a double-stage configuration.

A double-stage configuration can effectively address the disadvantages of a single-stage configuration by adding an additional power link. This power link can be either a high frequency (HF) AC link or a DC link. Depending on the type of link used, a double-stage configuration can be further classified into two categories: DC-link and HF-link topologies [66], as shown in Fig. 3.4 (b) and (c), respectively. A DC-link topology converts the variable and intermittent output voltage of a PV array to a regulated and stabilized DC link voltage via a DC-DC converter [5]. MPPT control is usually implemented in the DC-DC converter to optimize the performance of the PV array under a wide operational range [184]. The regulated DC link voltage is then converted to the AC grid voltage for AC load utilization via a grid-tied PV inverter. The advantages of a DC-link topology are that a stable DC input voltage for the grid-tied PV inverter is maintained and multiple control objectives such as MPPT and anti-islanding protection can be implemented [185]. Decoupling is provided through the inserted DC-DC converter;

as a result, the AC grid power ripple cannot directly affect the PV array voltage. Energy storage systems can be connected to the DC link to store the excess energy generated by the PV array when the solar irradiance is abundant during the daytime and to supply energy to the grid when the power output of the PV array is deficient. A HF-link topology uses a HF DC-AC inverter to boost the PV array voltage to the HF AC link voltage and convert the HF AC link voltage to a low frequency (LF) grid voltage via an AC-AC frequency converter. Although the efficiency of the grid-tied PV inverter is reduced in a two-stage configuration, the efficiency of the entire grid-tied PV system may improve due to an increase in MPPT efficiency [186].

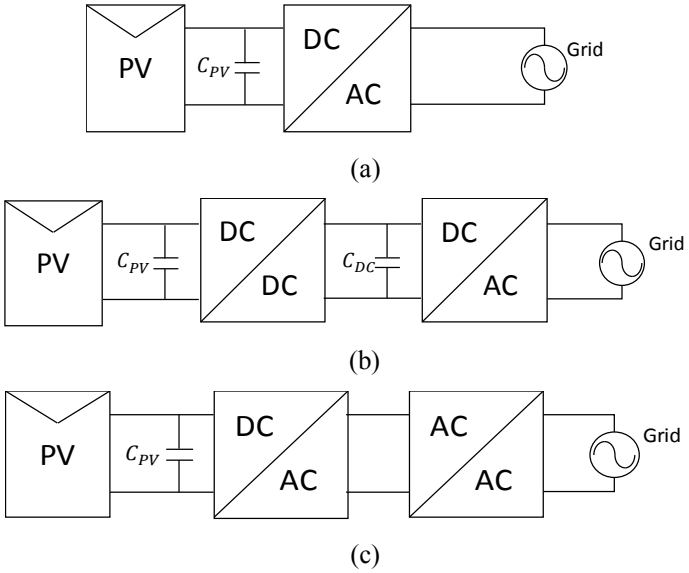

Fig. 3.4: Fundamental configurations of grid-tied PV systems: (a) single-stage configuration, (b) double-stage configuration with a DC link, (c) double-stage configuration with a HF link.

The capacitors used in grid-tied PV systems are of significant importance as they can minimize voltage ripple and balance the power difference between the instantaneous power and the average power [187]. The capacitor connected at the output of a PV array is known as the input filter capacitor (C_{PV}) whereas the capacitor connected at the input of the grid-tied PV inverter is known as the DC-link capacitor (C_{DC}), respectively. The selection and operation of these capacitors are presented in detail in Chapter 4.

3.4.2 DC-DC converters

DC-DC converters are commonly used in the DC-DC power stage of a two-stage grid-tied PV system as illustrated in Section 3.4.1. Based on whether there is a galvanic isolation between the input and output, DC-DC converters can be generally classified as non-isolated and isolated converters. Non-isolated DC-DC converters are frequently used in PV applications due to high conversion efficiency [188]. DC-DC converters are capable of controlling the PV array current output in real-time to ensure MPPT operation, therefore DC-DC converters need to draw a smooth input current from the PV array [157] and avoid the suboptimal operation around the MPP [182]. Since the PV array often experiences varying environmental conditions, its output voltage is intermittent and ever-changing. A DC-DC converter can maintain a constant output voltage irrespective of environmental changes [5], which provides a stable operating point for the grid-tied inverter. The input voltage of DC-DC converters may step up or step down depending on the input voltage requirement of the grid-tied PV inverter. In general terms, a DC-DC converter turns the MPPT for a PV array into an impedance matching problem. This problem states that the MPPT operation is achieved when the output impedance of the PV array equals to a DC-DC converter input impedance that can be adjusted by changing the duty cycle [189]. Converter topology is one of the main considerations in designing a DC-DC converter for PV applications. Low input current ripple is the main selection criterion to determine the topology of a DC-DC converter for MPPT operation [190]. Some of the common DC-DC converter topologies are buck, boost, buck-boost, SEPIC, Ćuk and Zeta. A properly selected DC-DC converter topology can optimize the performance of a PV system [191]. A comparative study of three different DC-DC converter topologies (buck converter, boost converter and buck-boost converter) for grid-tied PV system applications is presented in [192] through modelling and simulation studies. A comparison analysis between buck converter and boost converter topologies for interfacing PV arrays is illustrated in [193] and results show that a boost converter topology has several benefits over a buck one. These advantages include small capacitance for input capacitors, well-damped response characteristics and blocking diodes to avoid reverse current flowing back to the PV array. A brief review of various converter topologies is presented in the following subsections.

3.4.2.1 Boost converter

A boost converter can provide an output voltage greater than the input voltage. The schematic of a boost converter is shown in Fig. 3.5. The simplicity and cost-effectiveness of this topology make boost converters a preferable solution for MPPT applications since there is only one inductor in this topology. A boost converter has an additional advantage that it does not need an additional diode in series with the PV module to prevent reverse current flow [194]. However, when compared with a Ćuk or Zeta converter, a boost converter presents high ripple in the output current.

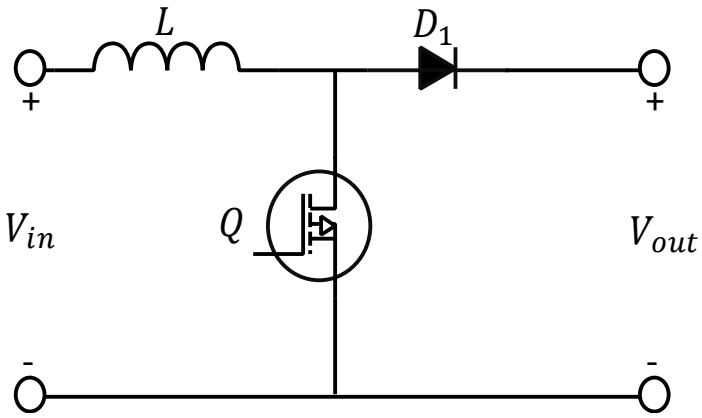

Fig. 3.5: Schematic of a boost converter.

The relationship between the input and output voltages is given as follows:

$$\frac{V_{out}}{V_{in}} = \frac{1}{1-D} \tag{3.25}$$

where D is the duty cycle to control the operation of the converter.

3.4.2.2 SEPIC converter

The input and output voltages of a SEPIC converter are decoupled by a coupling capacitor. With this capacitive isolation, the output grid-tied inverter is protected when failure of the power switch occurs [5]. A SEPIC converter is able to prevent reverse current flow without an additional diode, which is the same for a boost converter. The schematic of a SEPIC converter is shown in Fig. 3.6. It is similar to the topology of a buck-boost converter but with the advantage of a non-inverted output. The input current ripple of a SEPIC converter can be reduced if a coupled dual-winding inductor is used instead of two

uncoupled separate inductors. Better efficiency, more robust control-loop characteristics and a reduction on the footprint can be realized when a coupled dual-winding inductor is used instead of two separate inductors [195].

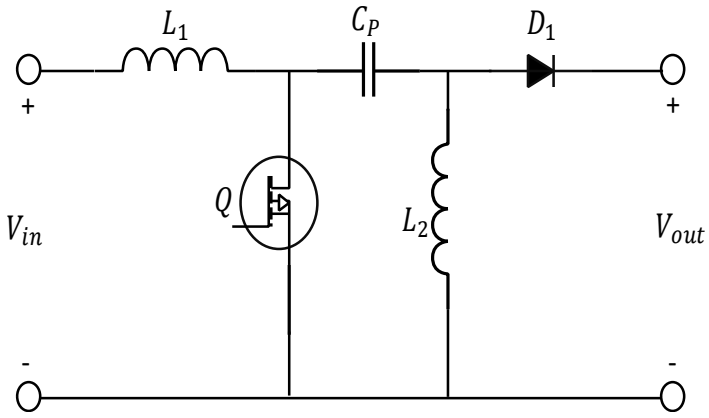

Fig. 3.6: Schematic of a SEPIC converter.

3.4.3 DC-AC inverters

The primary function of DC-AC inverters is to convert DC power from PV arrays to AC power injected to the power utility grid [5]. The magnitude and frequency of inverter output voltage is synchronized with the grid voltage. DC-AC inverters can be either single-phase or three-phase depending on the power rating, a single-phase inverter can supply up to approximately $5 - 6\ kW$ [196]. Apart from DC-AC conversion, inverters for PV applications also have several other functionalities, including MPPT, anti-islanding for grid-tied PV systems, grid synchronization and data logging [5].

Anti-islanding is an important feature that grid-connected PV inverters need to incorporate. Grid-connected PV inverters must disconnect from the grid when the grid voltage and frequency are beyond the steady-state voltage and frequency limits stipulated by the grid codes. Islanding occurs when the utility grid is tripped due to fault conditions and the grid-connected PV system still supplies power to the utility. Unintentional islanding is hazardous to personal and equipment and may violate the assumption that the grid is fully de-energized. Anti-islanding protection system must detect islanding and immediately disconnect the PV inverter from the grid [184], [196], [197].

DC-AC inverters can be categorized into three types based on their topologies, which are voltage-source inverter (VSI), current-source inverter (CSI) and Z-source inverter [183], [198]. VSI is able to control its output voltage waveform that is independent from load changes with small or negligible input impedance. The input DC voltage of a VSI must be higher than the output AC voltage to avoid the over-modulation operation [182]. Therefore, a proper voltage boosting stage is necessary for VSIs used for grid-connected PV applications. An appropriate filter is required to be connected at the output of a VSI to ensure a sinusoidal AC voltage with harmonic content suppressed. A CSI controls its output square-wave current waveform that is able to boost the PV array voltage to the AC voltage without an intermediate boost DC-DC conversion stage. CSIs can also provide a unidirectional current flow via series diodes and bidirectional voltage blocking capabilities [198]. One limitation of a CSI is that it must be supplied by a stiff DC voltage source with high impedance, thus a DC link voltage control scheme is required for VSIs to regulate the DC link voltage [184]. Another drawback is that the AC output voltage must be higher that the DC link voltage. In other words, a VSI can only boost up the DC link voltage to the AC output voltage. Z-source inverter is a new promising architecture for PV applications that overcomes some of the drawbacks of the VSI and CSI. Compared to the VSI and CSI, it provides buck-boost voltage capability with only single-stage conversion [199].

DC-AC inverters can also be categorised based on whether a HF transformer is used in the inverter topology. Inverters with a HF transformer offer good galvanic isolation at the expense of complexity in control and low conversion efficiency. Transformerless inverters are more common and relatively simpler in structure and control than their transformer-based counterparts [30]. Transformerless inverters can be further classified into two-level and multilevel inverters. A typical example of two-level inverters is full-bridge inverter. Fig. 3.7 demonstrates a three-phase full-bridge inverter with its input connected to a DC link capacitor.

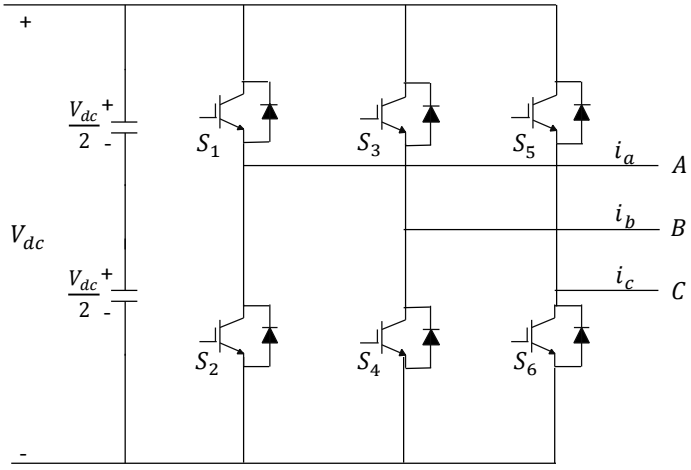

Fig. 3.7: A three-phase full-bridge inverter adapted from [196].

Each phase of the three-phase full-bridge inverter is controlled by two switches in a leg. These two switches never conduct simultaneously to avoid shoot-through fault. There are six active switching states and two zero switching states. The six active switching states represent one switching cycle that has a 60° interval for each state. There are two types of control signals that can be applied to the switches. One is 180-degree conduction, in which each switch conducts for 180° to generate a three-level $(V_{dc}, -V_{dc}, 0)$ phase-to-phase inverter output voltage. The other is 120-degree conduction, in which each switch turns on for 120° to produce a three-level $\left(\frac{V_{dc}}{2}, -\frac{V_{dc}}{2}, 0\right)$ phase-to-neutral inverter output voltage. Three switches are in ON state for 180-degree conduction, while only two switches are in ON state for 120-degree conduction at any instant of time. The switching sequence for a three-phase full-bridge inverter in 180-degree conduction is shown in Table 3.1.

Table 3.1: Switching sequence for a three-phase full-bridge inverter in 180-degree conduction.

Switching Sequence	State No.	Switch States	v_{ab}	v_{bc}	v_{ca}
S_1, S_2 and S_6 are on and S_4, S_5 and S_3 are off	1	100	V_{dc}	0	$-V_{dc}$
S_2, S_3 and S_1 are on and S_5, S_6 and S_4 are off	2	110	0	V_{dc}	$-V_{dc}$
S_2, S_3 and S_4 are on and S_1, S_4 and S_5 are off	3	010	$-V_{dc}$	V_{dc}	0
S_3, S_4 and S_5 are on and S_1, S_2 and S_6 are off	4	011	$-V_{dc}$	0	V_{dc}
S_1, S_2 and S_3 are on and S_4, S_5 and S_6 are off	5	001	0	$-V_{dc}$	V_{dc}
S_1, S_5 and S_6 are on and S_2, S_3 and S_4 are off	6	101	V_{dc}	$-V_{dc}$	0
S_1, S_3 and S_5 are on and S_2, S_4 and S_6 are off	7	111	0	0	0
S_2, S_4 and S_6 are on and S_1, S_3 and S_5 are off	8	000	0	0	0

Multilevel inverters are capable of handling high voltage and power due to their cascaded structure. This feature makes them suitable for interfacing renewable energy sources such as PV array, fuel cell and geothermal power plant to the utility. They can overcome some of the drawbacks of two-level inverters such as high harmonic content, high switching losses and lack of reactive power compensation [200]. The voltage stress on each semiconductor switch of a multilevel inverter is significantly reduced compared to that of a two-level inverter. The output voltage of a multilevel inverter comprises several levels that syntheses a sinusoidal waveform. Several examples of multilevel inverters are multilevel inverter with cascaded DC sources, diode-clamped multilevel inverter and flying capacitor multilevel inverter [200].

The relevant Australia standard for grid-connected PV inverters is AS4777 for *Grid connection of energy systems via inverters.* Part I of this standard addresses the installation requirements of PV inverters, whereas Part II and Part III clarify PV inverter power quality requirements and grid protection requirements, respectively. Some key requirements for grid-connected inverters such as power factor, harmonic currents, voltage fluctuations and flicker, impulse protection, transient voltage limits and direct

current injection are covered in Part II of this standard [201]. These requirements are used to ensure the reliability and sustainability of grid-tied PV inverters [202].

3.4.4 Filters

In order to ensure a sinusoidal output current injected into the grid, a suitable filter is connected at the output of the grid-tied PV inverter to satisfy the power quality requirements of the utility. Filters can be generally classified as passive and active filters. Passive filters are commonly used due to their simplicity and low cost. Although active filters provide a better performance than passive filters in terms of reactive power compensation capability, they comprise active power sources that are expensive and require regular maintenance [203]. There are three basic topologies of passive filters, namely L filter, LC filter and LCL filter as shown in Fig. 3.8.

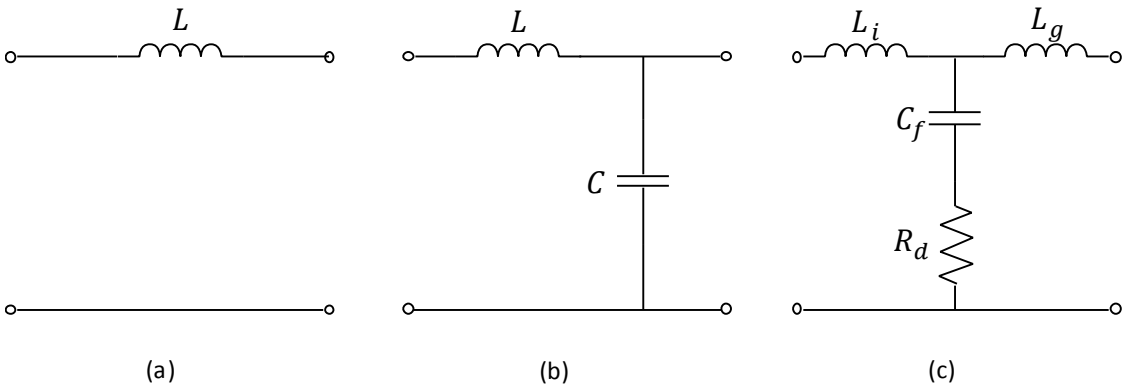

Fig. 3.8: Three basic passive filter topologies: (a) L filter, (b) LC filter and (c) LCL filter.

L filter is a first order filter that consists of only one inductor in series with the grid. It is the most efficient option among passive filters due to its simplicity. The drawback of L filters is that bulky inductors are required to attenuate the harmonics in the inverter output voltage to satisfy the power quality requirements. LC filters can suppress the disturbance generated by specific harmonics, but the resonance frequency of a LC filter highly depends on the grid impedance. This problem can be alleviated by the adoption of a LCL filter since the resonance frequency is determined by the filter parameters itself [196]. LCL filter is a third order filter, which has a good current attenuation performance and is widely used to interface renewable energy sources with the utility grid [204], [205]. It has

more degree of freedom in design compared to L and LC filters. The inclusion of the damping resistor (R_d) in a LCL filter is necessary since R_d can mitigate the effect of filter resonances and ensure a stable current control loop, especially when the grid impedance is unknown [206]. The instability of the undamped current control loop and the effect of R_d in reducing the resonant peak have been investigated in [207]. The LCL filter topology will be selected in designing the single-phase grid-connected PV system described and simulated in Chapter 4.

3.5 Conclusion

This chapter has reviewed a selection of conventional MPPT techniques and GMPPT algorithms in locating the MPP of a PV array. The criteria for performance evaluation of various conventional and global MPPT techniques have also been highlighted. Power electronic interfaces including DC-DC converters and DC-AC inverters, and filters for grid-connected PV applications have been presented. These components in a single-phase grid-connected PV system are design, analysed and simulated in Chapter 4 to investigate the performance of PV array voltage response under different parameter settings of a digital PID controller.

Chapter 4
Control, Design and Analysis of a Single-phase Grid-tied Photovoltaic System

4.1 Introduction

Many research articles have investigated the output voltage control of DC-DC converters [208]–[214]. Little attention has been paid to the input voltage control [215]. The control of the input voltage of a DC-DC converter is necessary for grid-connected photovoltaic (PV) applications. For most grid-tied PV applications, the output voltage of a DC-DC converter is maintained constant due to the DC link capacitor and the PV inverter DC link voltage control, while its input voltage is regulated by the MPPT operation. To track the MPP of a PV array with fast dynamic response and zero steady-state error, a digital PID controller is employed to dynamically adjust the duty cycle at a given PV array voltage error to increase or decrease the PV array voltage to meet the MPPT requirement. To optimize the performance of the digital PID controller, a well-tuned PID controller parameters setting is necessary. The PID controller parameters setting is determined based on the control-to-input voltage transfer function of the boost converter to achieve a desired PV array voltage response.

In this chapter, a boost converter is used to control the voltage of a PV array for MPPT operation. Firstly, a brief review of closed-loop control techniques for DC-DC converters is presented, concentrating on voltage-mode control and peak current-mode control schemes. This is followed by a brief review of small signal models for a PV array, PWM generator and a boost converter. Secondly, four cases are developed based on whether the effect of the DC link capacitor is considered and different linear models selected for modelling a PV array. The control-to-input voltage transfer function of the boost converter is derived under each case. Thirdly, the boost converter design is presented and the corresponding frequency response is analysed. Finally, based on the derived four different control-to-input voltage transfer functions, four different parameter settings of a digital PID controller are determined. Simulation studies are carried out using the four

different parameter settings of the PID controller to assess their influences on the performance of a grid-tied PV system through its non-linear simulation model.

4.2 Closed-loop Control Schemes for DC-DC Converters

The input voltage control of a DC-DC converter is necessary for PV systems to ensure that they often operate at the MPP. A feedback control loop is always used in modern pulse-width modulation (PWM) converters for voltage regulation [200]. There are two common closed-loop control schemes, namely voltage mode control (VMC) and current mode control (CMC) [5], [216]–[218]. The working principles of these two closed-loop control schemes will be briefly outlined in the following subsections.

4.2.1 Voltage mode control

Fig. 4.1 demonstrates the VMC of a boost converter fed by a PV array. The PV array current (I_{pv}) and voltage (V_{pv}) are measured and sent to the MPPT controller to generate the PV array voltage reference (V_{pv}^{*}) for the boost converter. Then, V_{pv} is compared with V_{pv}^{*} using an error amplifier [5], where an optimal dynamic response of the feedback loop can be achieved by the compensating network around the error amplifier [219]. The error between V_{pv}^{*} and V_{pv} is amplified by a PID controller and converted into a duty cycle signal (d). This signal is then fed to the PWM generator to generate a PWM waveform to drive the semiconductor switch of the boost converter. The input voltage of the DC-DC converter can be regulated by adjusting the duty cycle to compensate for any variations in the DC-DC converter input or output currents. The advantage of VMC is that only one single feedback loop is employed with voltage as the control variable, which makes the design and implementation easy [5], [220]. The shortcoming of VMC lies in its slow response [220]. In other words, any changes in input and output currents must first be translated into the changes in input and output voltages and then compensated by the feedback loop. For PV MPPT applications, V_{pv}^{*} is characterized by fast dynamic changes due to the intermittent nature of environmental conditions.

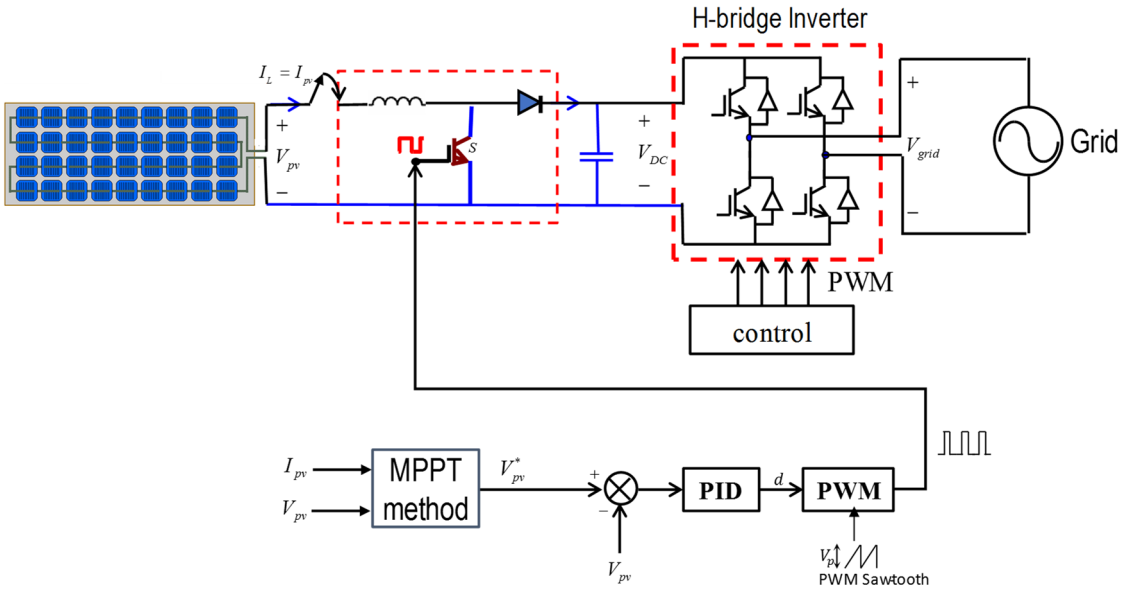

Fig. 4.1: Functional circuit diagram of the VMC of a boost converter fed by a PV array adapted from [221].

4.2.2 Current mode control

In order to overcome the deficiency of VMC, CMC is developed by adding an inner current loop to control the inductor current. The adoption of the inductor current as the second control variable significantly improves the load transient response [5], [222] and over-current protection capability [223]. This consequently improves the performance of the closed-loop control of PWM switching DC-DC converters. There are two control loops in the CMC scheme: outer voltage and inner current loops. The inner current loop implements a cycle-by-cycle control, which responds much faster than the outer voltage loop, resulting a speed difference between the two control loops [224]. CMC schemes can be broadly classified into two main categories, namely fixed-frequency methods and variable-frequency methods [225]. Fixed-frequency methods are preferred with a fixed-frequency PWM waveform since electromagnetic interference (EMI) generated by DC-DC converters can be limited [226]. Fixed-frequency methods have evolved into three variants that are peak current-mode control (PCMC) [222], [227]–[230], average current-mode control (ACMC) [231]–[233] and charge control [234], [235] approaches. A brief description of PCMC scheme is presented in the subsection below.

4.2.2.1 Peak current mode control

Fig. 4.2 shows the peak current-mode control (PCMC) of a boost converter controlled PV array. The objective of the inner current loop is to control the instantaneous peak inductor current (I_L) to a pre-defined set-point (I_L^*) [236]. This setpoint is determined by comparing V_{pv} with V_{pv}^* as shown in Fig. 4.2. The inner current loop implements a cycle-by-cycle control technique that controls the inductor current in each switching cycle, which provides a much faster transient response than that of the outer voltage control loop. One drawback of the PCMC scheme is that it suffers from instability when the duty cycle rises above 0.5 [237]. Fig. 4.3 demonstrates the effect of a perturbation in the inductor current waveform at the beginning of a switching cycle when D is less than 0.5. In Fig. 4.3, the solid line represents the inductor current waveform at the steady state whereas the dash line denotes the waveform with a small perturbation at the beginning of a switching cycle. The steady-state inductor current increases with a rising slope of M_1 during the turn-on period of the semiconductor switch, and decreases with a failing slope of M_2 during the turn-off period. The inductor current perturbations at the start of and at the end of the switching cycle are represented as $\Delta i_L(0)$ and $\Delta i_L(T)$, respectively. The relationship between the slopes of the inductor current and the duty cycle is given in a linear fashion in (4.1). The perturbation at the end of the switching cycle can be determined using (4.2) based on the perturbation at the beginning of the switching cycle.

$$\left|\frac{m_2}{m_1}\right| = \left(\frac{D}{1-D}\right) \tag{4.1}$$

$$\Delta i_L(T) = \left(\frac{D}{1-D}\right) \cdot \Delta i_L(0) \tag{4.2}$$

As can be seen in (4.2), the initial perturbation will be attenuated at the end of the switching cycle and eventually eliminated when D is less than 0.5 (shown in Fig. 4.3), while the initial perturbation could be amplified when D is larger than 0.5 (shown in Fig. 4.4). The instability occurs when $D > 0.5$ is known as subharmonic oscillation [238], [239]. To resolve this instability issue, slope compensation is developed by adding a compensating sawtooth waveform into the inner current loop, as seen in Fig. 4.2. With slope compensation, the steady-state inductor current waveform and its perturbed waveform are shown in Fig. 4.5. The slope of the compensating sawtooth signal must be

greater than one-half of the down slope of the current waveform to guarantee current loop stability [223], [225].

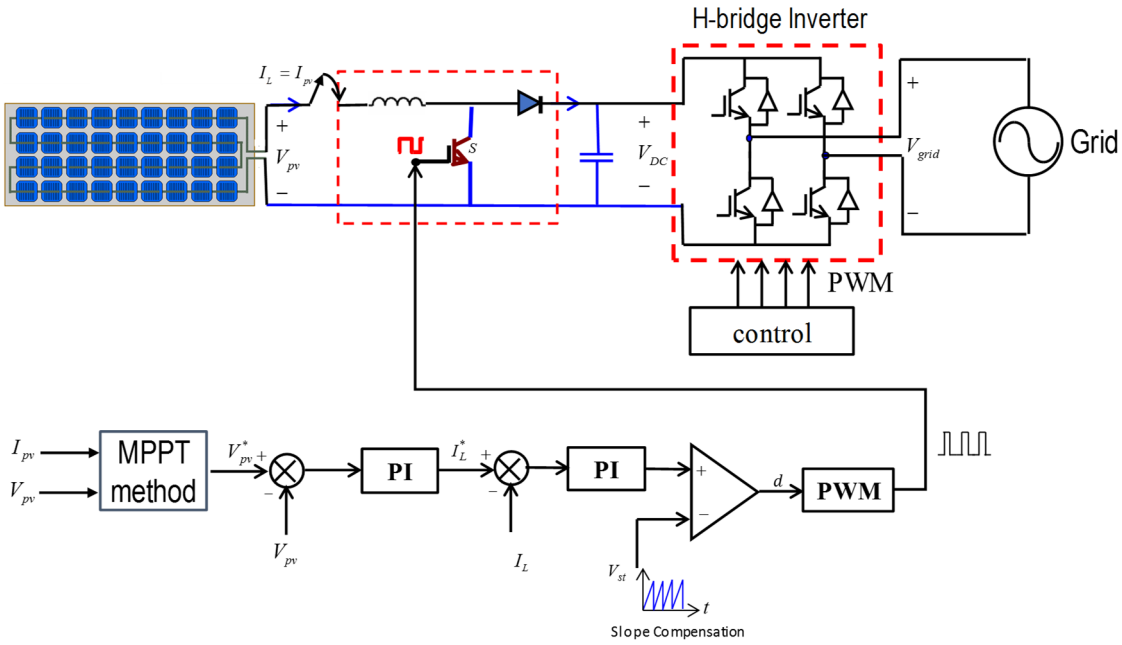

Fig. 4.2: Functional circuit diagram of the PCMC of a boost converter controlled PV array adapted from [221].

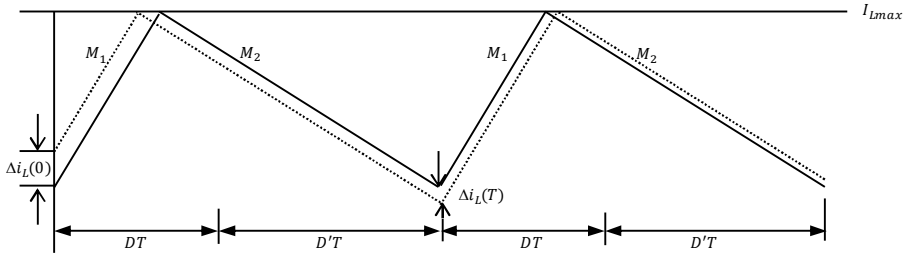

Fig. 4.3: Propagation of a current perturbation in PCMC when $D < 0.5$.

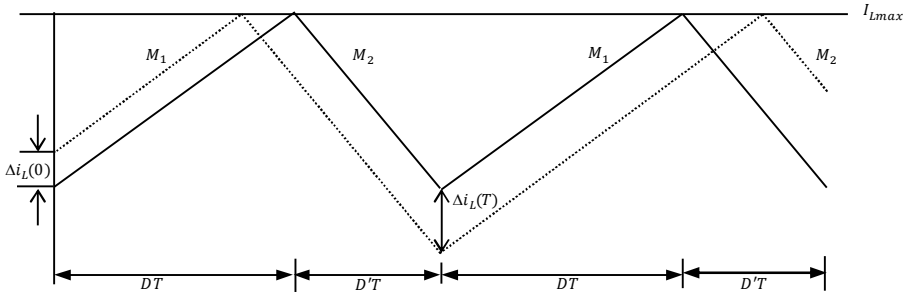

Fig. 4.4: Propagation of a current perturbation in PCMC when $D > 0.5$.

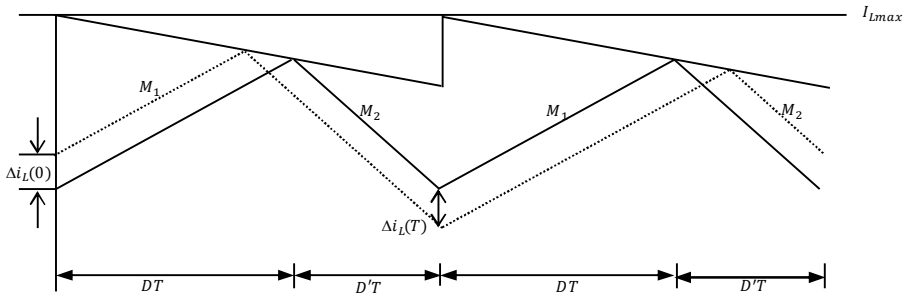

Fig. 4.5: Propagation of a current perturbation in PCMC with slope compensation.

Another disadvantage of the PCMC is its poor noise immunity [236]. A current spike is initialized when the semiconductor switch turns on, which may momentarily trigger the comparator [240]. As a result, the output PWM pulses could have a very low duty cycle. This problem can be mitigated by a "leaking edge blanking" technique applied to the comparator [241]. This technique adds a small "blanking period" at the beginning of each switching cycle where the amount of blanking period overlaps the period when a current spike occurs.

4.3 Input Voltage Control of the Boost Converter Fed by a PV Array

In this section, a linear model for the PV array and boost converter is developed for control system analysis. This linear model is used to study the PV array voltage response with different parameter setting of the digital PID controller. This linear model neglects all the parasitic resistances of the inductors and capacitors in the boost converter. Voltage-mode control is employed to control the PV array voltage for MPPT operation. Fig. 4.6 shows the block diagram of the feedback control of the input voltage of a boost converter fed by a PV array. This voltage feedback control loop consists of a PID controller C_{PID}, a PWM generator and a boost converter fed by a PV array. The output signal of the digital PID controller V_{PID} is fed into a PWM generator to produce switching pulses to drive the semiconductor switch in the boost converter. The control-to-input voltage transfer function of the boost converter is represented as G_{vd}. For the PV array voltage control, V_{PV}^* denotes the reference of the PV array voltage whereas V_{PV} symbolises the measured

PV array voltage. C_{PID} represents the transfer function of a digital PID controller that has the following parallel form:

$$C_{PID}(z) = K_p + K_i T_s \frac{1}{z-1} + K_d \cdot \frac{1}{T_s} \frac{z-1}{z} \tag{4.3}$$

where K_p, K_i, and K_d represent the proportional, integral and derivative gains, and T_s is the sampling time of the digital controller. T_s has a much larger value than the sampling time of the simulation model of a single-phase grid-tied PV system. To derive the control-to-input voltage transfer function, four case studies will be conducted in Section 4.3.4 under four different assumptions regarding whether the DC link capacitor or the equivalent Thévenin's resistance is taken into consideration. The control-to-input voltage transfer function of the boost converter is also determined under each case in Section 4.3.4.

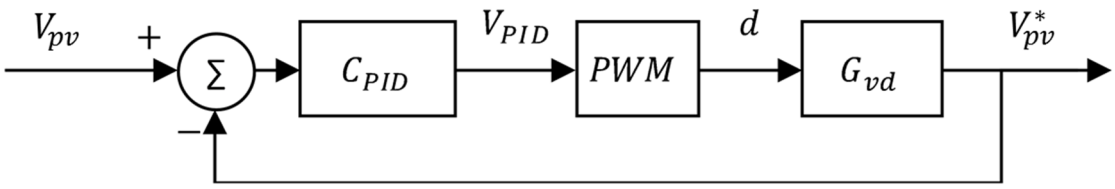

Fig. 4.6: Block diagram of the input voltage control loop of a boost converter.

4.3.1 Small signal model for a PV array

A simple approach to derive the small signal model for a PV array is to use an ideal constant DC current source to simulate PV arrays as shown in Fig. 4.7. For small signal analysis, $\hat{v}_{pv}$ and $\hat{i}_{pv}$ are defined as the small signal increments of the PV array voltage and current, respectively. These small increments are relative to the steady-state values of the corresponding variables that are represented by V_{pv} and I_{pv}, respectively. The small signal model shown in Fig. 4.7 assumes that the PV array always operates at its MPP in steady state conditions [181].

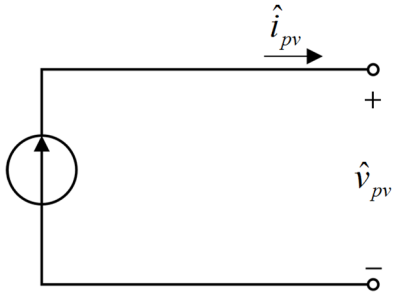

Fig. 4.7: Small signal model for a PV array using an ideal constant DC current source.

A common two-piecewise-linear model is presented in [217], [218], which divides the PV array I-V curve into two linear segments. The equivalent circuit of the two-piecewise-linear model and its two piecewise-linear I-V curves are shown in Fig. 4.8 (a) and (b), respectively.

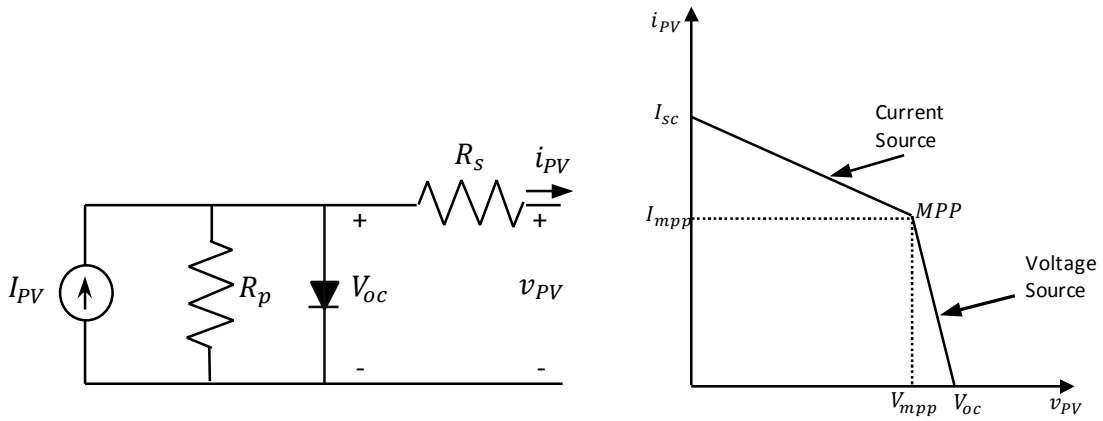

(a) (b)

Fig. 4.8: (a) Equivalent circuit of the two-piecewise-linear model for a PV array and (b) its piecewise-linear I-V curves adapted from [218].

Note that i_{PV} and v_{PV} symbolize the full output current and voltage of the PV array, respectively. I_{PV} stands for the PV array current whereas V_{oc} symbolizes the open circuit voltage of the PV array. R_s and R_p stand for the series and parallel resistance of the PV array, respectively. The information provided in manufacturer's datasheets can be used to compute the parameters of the two-piecewise-linear model shown in Fig. 4.8 (b). This information includes: the open circuit voltage (V_{oc}), the short circuit current (I_{sc}), the

voltage at the MPP (V_{MPP}) and the current at the MPP (I_{MPP}). The parameters of the two-piecewise-linear model can be determined as follows [217], [218]:

$$R_s = \frac{V_{oc} - V_{MPP}}{I_{MPP}} \quad , \quad R_p = \frac{V_{MPP}}{I_{sc} - I_{MPP}} - R_s \tag{4.4}$$

$$I_{PV} = I_{sc} \frac{R_s + R_p}{R_p} \tag{4.5}$$

There are two linear segments in the PV array I-V curve shown in Fig. 4.8 (b), each segment can be represented by its corresponding equivalent circuit model shown in Fig. 4.9.

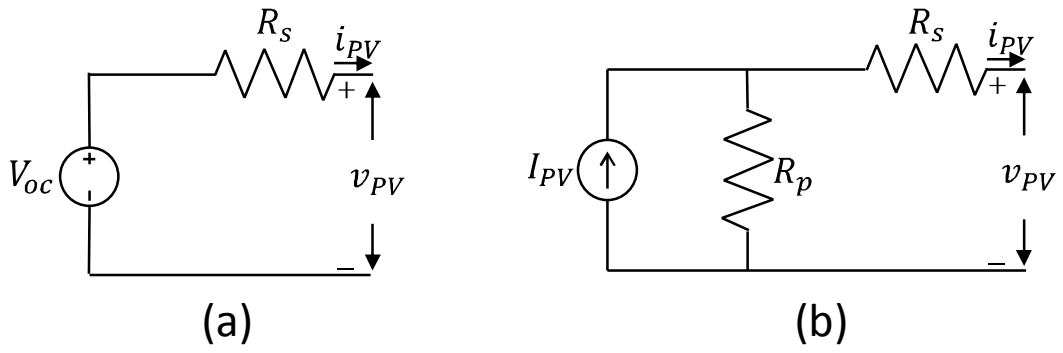

Fig. 4.9: Two equivalent circuit models of a PV array: (a) Voltage source and (b) Current source [218].

If an equivalent Thévenin's circuit is used to represent the PV array, the equivalent voltage V_{eq} and equivalent resistance R_{eq} can be calculated based on the type of equivalent circuit model employed.

If the current source model (Fig. 4.8 (b)) is adopted, we have:

$$V_{eq} = I_{PV} R_p \qquad R_{eq} = R_p + R_s \tag{4.6}$$

If the voltage source model (Fig. 4.8 (a)) is adopted, we have:

$$V_{eq} = V_{oc} \qquad R_{eq} = R_s \tag{4.7}$$

The authors of [40] proposed a piecewise linear model that approximates the PV array output characteristics in four separate regions, namely, the current source region, power

zone I, power zone II and voltage source region. These four regions are illustrated in Fig. 4.10 to approximate an I-V curve of a PV array. When a PV array works in the current source region, the control to PV array voltage transfer function of the plant consisting of a PV array and a boost converter exhibits a slightly damped frequency response. This damped response imposes some control issues on the plant and produces considerable power losses [40].

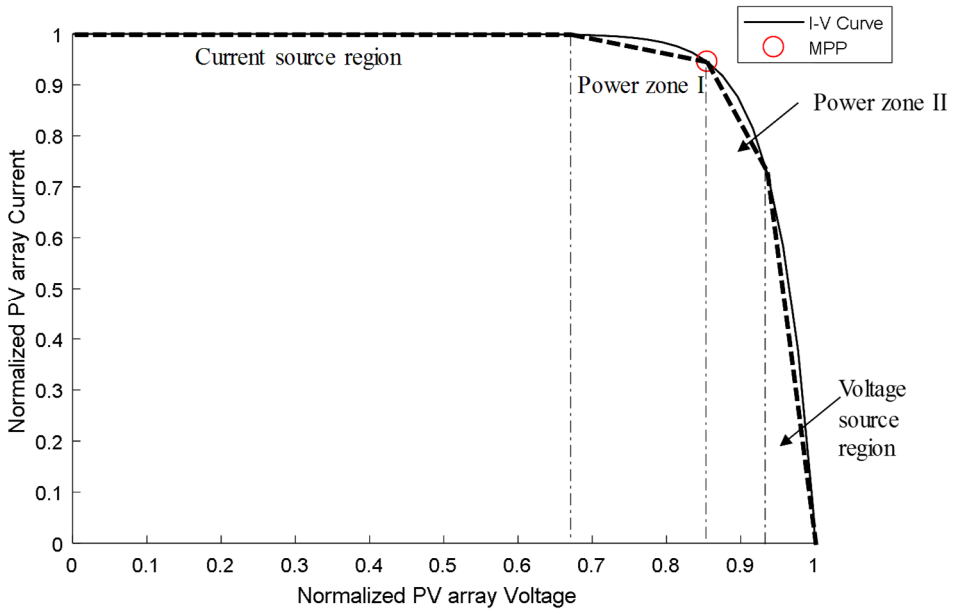

Fig. 4.10: A four-pieces linear approximation of an I-V curve.

4.3.2 Transfer function of a PWM generator

A PWM generator converts duty cycle into a constant-frequency PWM signal to control the on/off states of a semiconductor device [242]. This constant-frequency PWM signal is generated by comparing a sawtooth waveform with an amplitude V_p with the output signal of a PID controller v_c [243]. The output of a PWM generator is at high level when V_c is higher than the sawtooth and is at low level when V_c is lower than the sawtooth [242]. The transfer function of a PWM generator derived from a linear relation is given as follows:

$$\frac{d(s)}{V_{PID}(s)} = \frac{1}{V_p} \tag{4.8}$$

The transfer function is constant, meaning only a constant gain is added to the overall voltage control loop. In the subsequent derivation of the control-to-input voltage transfer function of a boost converter, V_p is assumed to be 1, indicating a unity gain for the overall voltage control loop.

4.3.3 PWM switch model

To design appropriate control strategies for the DC-DC converter, small signal analysis is needed to determine the control-to-input transfer function of the system consisting of a PV array with its associated DC-DC converter. An ideal constant voltage source with an magnitude of V_{dc} is assumed to connect at the output of the DC-DC converter [218]. The system schematics is shown in Fig. 4.11.

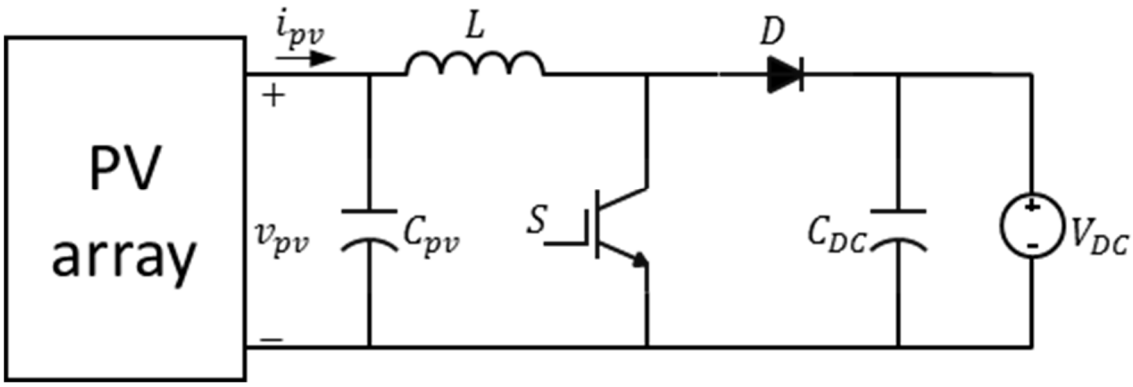

Fig. 4.11: Schematics of the boost converter fed by a PV array.

There are two analytical approaches used to derive the small signal model of the PV system, which are [40], [181], [244]–[246]:

- State-space averaging
- PWM switch model

The state-space averaging approach derives the state space model of the system from the differential equations describing the dynamics of the DC-DC converter based on the state variables [247]. The state variables for the model are the inductor current and capacitor voltage [181]. The drawback of this approach is that it describes the system in a more complex matrix structure with a high number of state variables, especially when the converter topology has more than two passive elements, such as for the Ćuk and SEPIC.

An alternative approach to derive the small signal model is by adoption of the PWM model developed by Vorpérian [244] in 1986. The advantage of this approach is that it converts the derivation problems of small signal models of DC-DC converters into simple circuit analysis problems and solves them using fundamental circuit laws such as KCL and KVL. This approach lumps all the active switches (IGBT, MOSFET, etc.) and passive switches (diodes) within the converter together in a three-terminal nonlinear device shown in Fig. 4.12. For representation reasons, a, p and c symbolise the active, passive and common terminals of the PWM switch model, respectively [244]. The instantaneous variables of input current, output current, input voltage and output voltage of the PWM switch network are designated as $\hat{i}_a$, $\hat{i}_c$, $\hat{v}_{ap}$, and $\hat{v}_{cp}$, respectively. d symbolises the instantaneous value of the duty cycle of the converter.

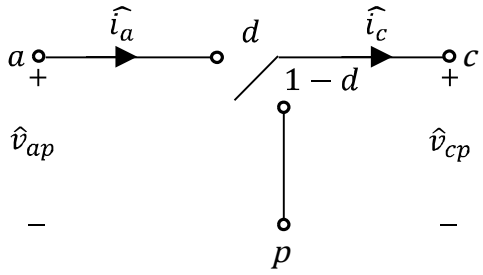

Fig. 4.12: PWM switch model.

The instantaneous values of the circuit variables of the PWM switch model can be obtained by superposition with the steady state portion and perturbation portion of the variables, which form the DC and small signal models of the PWM switch, respectively. The DC and small signal models of a PWM switch are shown in Fig. 4.13 (a) and (b), respectively.

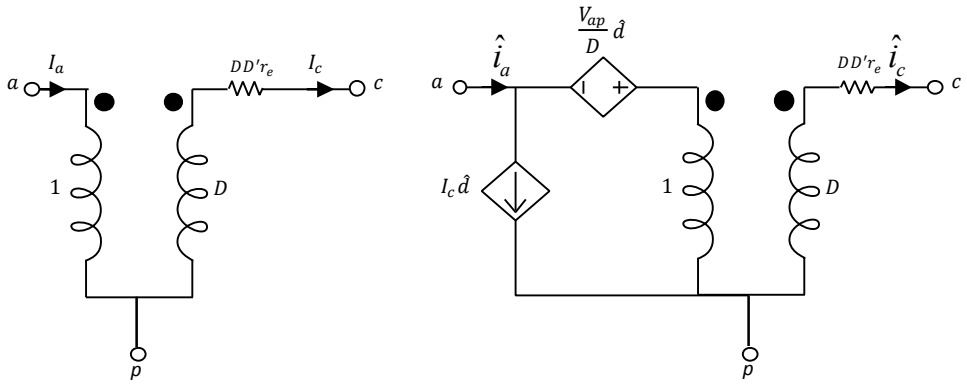

(a) (b)

Fig. 4.13: DC and small signal models of a PWM switch: (a) DC model and (b) small signal model.

For DC analysis, the relationships between the DC variables of the PWM switch are:

$$I_a = DI_c \tag{4.9}$$

$$V_{cp} = D(V_{ap} - I_c r_e D'), \qquad D' = 1 - D \tag{4.10}$$

where V_{cp}, V_{ap}, I_a and I_c represent the corresponding DC quantities of the circuit at its equilibrium point. D stands for the duty cycle at steady state and r_e is influenced by the equivalent series resistance (ESR) of capacitors and the equivalent load resistance, which depends on the converter topology [244]. For boost and buck-boost converters, the value of r_e can be calculated by:

$$r_e = \frac{r_{C_o} \cdot R}{r_{C_o} + R} \tag{4.11}$$

where r_{C_o} symbolises the ESR of the output capacitor and R represents the load resistance.

Let us define that the perturbation portions of the input current, output current, input voltage and output voltage of the PWM switch network are represented by $\hat{i}_a$, $\hat{i}_c$, $\hat{v}_{ap}$, and $\hat{v}_{cp}$, respectively. For small signal analysis, the V-I relations in Fig. 4.13 (a) can be expressed using perturbation variables as follows:

$$\hat{i}_a = D\hat{i}_c + I_c\hat{d} \tag{4.12}$$

$$\hat{v}_{ap} = \frac{\hat{v}_{cp}}{D} + \hat{i}_c r_e D' - V_D \frac{\hat{d}}{D} \tag{4.13}$$

where

$$V_D = V_{ap} + I_c(D - D')r_e \tag{4.14}$$

In the following analysis of the closed-loop control of PV array voltage, an ideal DC/DC converter is considered, which does not include the ESRs of inductor and capacitors. The modelling of parasitic resistances of inductors and capacitors in a DC/DC converter circuit arises out of the research scope of the project and could be targeted as further research. Thus, the ESR of the capacitors are not considered in the subsequent analysis, in other words, r_e is neglected in the small signal model for the PV system.

4.3.4 Development of the control-to-input voltage transfer functions of the PV system

As the small signal model of a PWM switch is developed, we can derive the small signal model of the PV system by substituting the small signal model of the PWM switch into the PV system circuitry shown in Fig. 4.11. By changing the directions of the circuit variables and representing the variables in the PWM switch using the state variables (inductor current and capacitor voltage), the small signal model of the PV system is obtained. Four different cases are considered in the following subsections. These four cases are developed based on whether the equivalent Thévenin's resistance of the PV array (R_{eq}) or the DC link capacitor (C_{dc}) is taken into consideration in the small signal model of the PV system. Four different control-to-input voltage transfer functions are derived in the four case studies and will be used in subsequent analysis of frequency response of the PV system and tunning of the digital PID controller.

4.3.4.1 Case 1

This case ignores the effects of both C_{dc} and R_{eq}, and uses an ideal constant DC current source to represent the PV array. The small signal model of the PV system is shown in Fig. 4.14.

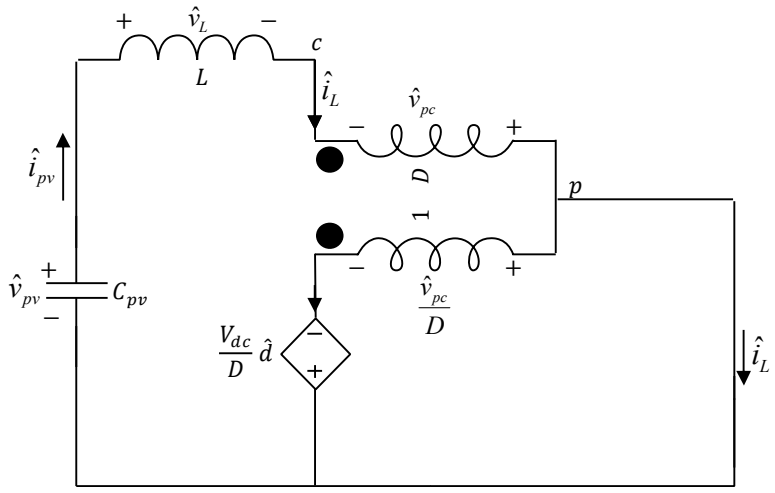

Fig. 4.14: Small signal model of the PV system in Case 1.

Applying KVL to the equivalent circuit, we have:

$$\hat{v}_{pv} - \hat{v}_L + \hat{v}_{pc} = 0 \tag{4.15}$$

$$\frac{\hat{v}_{pc}}{D} = \frac{V_{dc}}{D}\hat{d} \tag{4.16}$$

The voltage-current relations of the inductor and input filter capacitor are given as follows:

$$\hat{v}_{pv} = -\frac{\hat{i}_L}{sC_{pv}} \tag{4.17}$$

$$\hat{v}_L = sL\hat{i}_L \tag{4.18}$$

Substituting (4.16), (4.17) and (4.18) into (4.15), we have:

$$\left(-\frac{1}{sC_{pv}} - sL\right)\hat{i}_L + V_{dc}\hat{d} = 0 \tag{4.19}$$

The control-to-inductor current transfer function can be derived as follows:

$$\frac{\hat{i}_L(s)}{\hat{d}(s)} = \frac{V_{dc}}{\frac{1}{sC_{pv}} + sL} = \frac{sV_{dc}C_{pv}}{1 + s^2LC_{pv}} \tag{4.20}$$

Thus, the control-to-input voltage transfer function in Case 1 is given as follows:

$$G_{vd,1}(s)=\frac{\hat{v}_{pv}(s)}{\hat{d}(s)}=-\frac{1}{sC_{pv}}\cdot\frac{\hat{i}_L(s)}{\hat{d}(s)}=-\frac{V_{dc}}{1+s^2LC_{pv}} \tag{4.21}$$

4.3.4.2 Case 2

This case ignores the effect of C_{dc} and uses the equivalent Thévenin's circuit model to represent the PV array. The small signal model of the PV system is shown in Fig. 4.15.

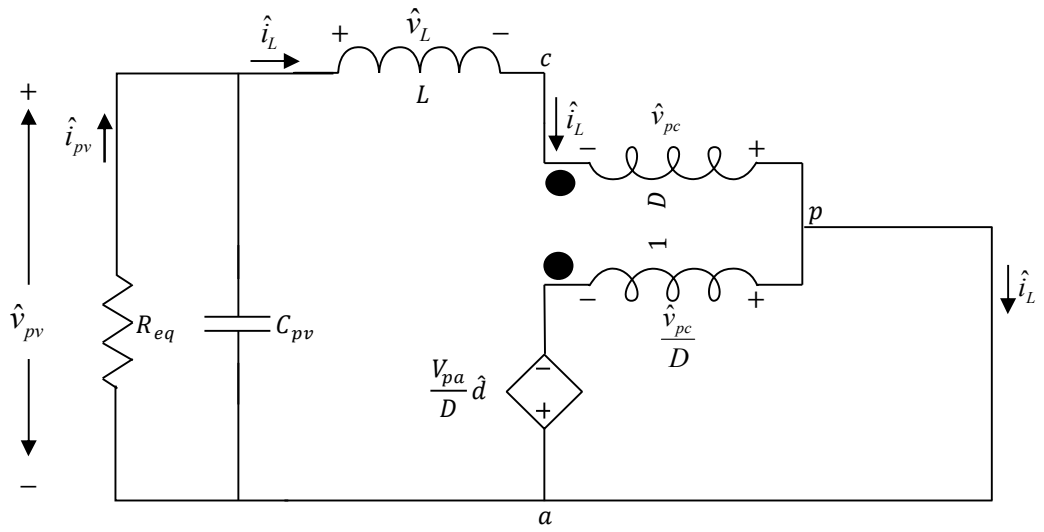

Fig. 4.15: Small signal model of the PV system in Case 2.

Using the same derivation procedures as those for case 1, the control-to-input voltage transfer function in case 2 can be derived as follows:

$$G_{vd,2}(s)=\frac{\hat{v}_{pv}(s)}{\hat{d}(s)}=-\frac{R_{eq}V_{dc}}{LC_{pv}R_{eq}s^2+Ls+R_{eq}} \tag{4.22}$$

Equation (4.22) can be re-written in the prototype second-order system form as follows [139]:

$$G_{vd,2}(s)=\frac{\hat{v}_{pv}(s)}{\hat{d}(s)}=-\frac{\mu\omega_n^2}{s^2+2\xi\omega_n s+\omega_n^2} \tag{4.23}$$

where $\mu=-V_{dc}$, $\omega_n=1/\sqrt{LC_{pv}}$ and $\xi=\sqrt{L}/(2\cdot R_{eq}\cdot\sqrt{C_{pv}})$. ξ can be any positive value depending on the parameters of the boost converter. In this case, (4.22) indicates a second-order system with two complex poles in the LHP.

In [40], modelling of the PV system is achieved by using the state-space averaging approach described in Section 4.3.3. The control-to-input voltage transfer function is given as follows:

$$G_{vd,2}(s) = \frac{\hat{v}_{pv}(s)}{\hat{d}(s)} = -\frac{K_o}{s^2+2\xi_i\omega_i s+\omega_i^2} \tag{4.24}$$

where

$$K_o = \frac{V_{dc}+V_{FW}}{LC_{pv}} \tag{4.25}$$

$$\omega_i = \sqrt{\frac{R_{eq}+R_L}{R_{eq}LC_{pv}}} \tag{4.26}$$

$$\xi_i = \frac{R_{eq}R_LC_{pv}+L}{2R_{eq}LC_{pv}\omega_i} \tag{4.27}$$

V_{FW} and R_L symbolise the diode forward voltage drop and the equivalent series resistance of the inductor, respectively. If both V_{FW} and R_L are neglected, (4.24) becomes exactly the same as (4.23).

4.3.4.3 Case 3

This case considers the effect of C_{dc} and ignores the effect of R_{eq} to represent the PV array. The small signal model of the PV system is shown in Fig. 4.16.

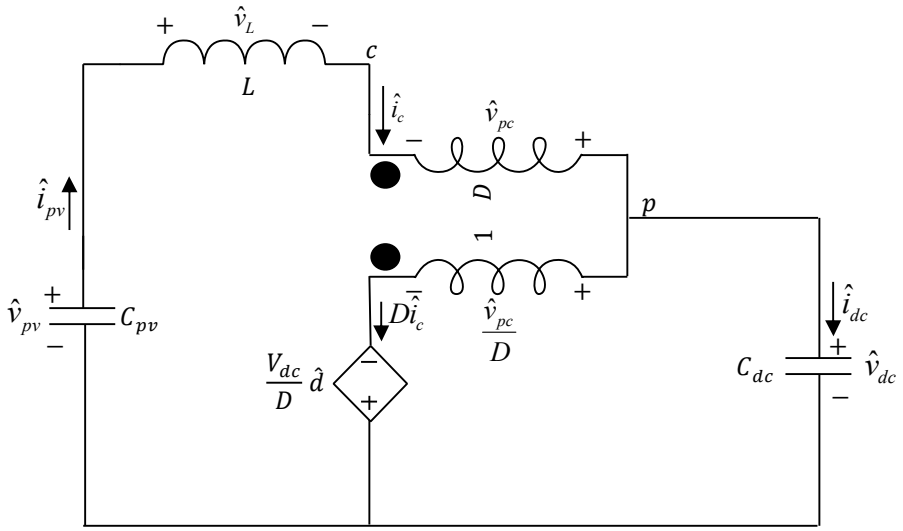

Fig. 4.16: Small signal model of the PV system in Case 3.

Applying KVL to the circuit, we have:

$$\hat{v}_{pv} - \hat{v}_L + \hat{v}_{pc} - \frac{\hat{v}_{pc}}{D} + \frac{V_{dc}\hat{d}}{D} = 0 \tag{4.28}$$

$$\frac{\hat{v}_{pc}}{D} = \frac{V_{dc}\hat{d}}{D} + \hat{v}_{dc} \tag{4.29}$$

Substituting (4.29) into (4.28) and rearranging it, we have:

$$\hat{v}_{pv} - \hat{v}_L + \left(1 - \frac{1}{D}\right)\left(D\hat{V}_{dc} + V_{dc}\hat{d}\right) + \frac{V_{dc}}{D}\hat{d} = 0 \tag{4.30}$$

Applying KCL at node p, we have:

$$\hat{i}_L = D\hat{i}_L + I_{pv}\hat{d} + \hat{i}_{dc} \tag{4.31}$$

The I-V relations of the passive elements within the equivalent circuit are given by:

$$\hat{v}_{pv} = -\frac{\hat{i}_{pv}}{sC_{pv}} \tag{4.32}$$

$$\hat{v}_L = sL\hat{i}_{pv} \tag{4.33}$$

$$\hat{v}_{dc} = \frac{\hat{i}_{dc}}{sC_{dc}} \tag{4.34}$$

Using the I-V relations given by (4.32) to (4.34), (4.30) can be rewritten as follows:

$$-\frac{\hat{i}_{pv}}{sC_{pv}} - sL\hat{i}_{pv} + \left(1-\frac{1}{D}\right)\left(D\frac{\hat{i}_{dc}}{sC_{dc}} + V_{dc}\hat{d}\right) + \frac{V_{dc}}{D}\hat{d} = 0 \tag{4.35}$$

From Fig. 4.16, we have:

$$\hat{i}_{pv} = \hat{i}_L \tag{4.36}$$

Equations (4.31) and (4.35) are two simultaneous equations. The control-to-input current transfer function of the boost converter can be calculated by substitution of variables:

$$\frac{\hat{i}_{pv}(s)}{\hat{d}(s)} = \frac{C_{dc}C_{pv}V_{dc}s + C_{pv}D'I_{pv}}{C_{dc}C_{pv}Ls^2 + C_{pv}(D')^2 + C_{dc}} \tag{4.37}$$

Therefore, the control-to-input voltage transfer function can be expressed as follows:

$$G_{vd,3}(s) = \frac{\hat{v}_{pv}(s)}{\hat{d}(s)} = -\frac{\hat{i}_{pv}(s)}{sC_{pv}\hat{d}(s)} = -\frac{C_{dc}V_{dc}s + D'I_{pv}}{C_{dc}C_{pv}Ls^3 + (C_{pv}(D')^2 + C_{dc})s} \tag{4.38}$$

From the above control-to-input voltage transfer function, it can be seen that the plant is an open loop marginally stable system with one zero in the LHP, one integrator and two poles on the imaginary axis.

4.3.4.4 Case 4

This case considers the effect of both C_{dc} and R_{eq} in the small signal model. The small signal model of the PV system is redrawn in Fig. 4.17.

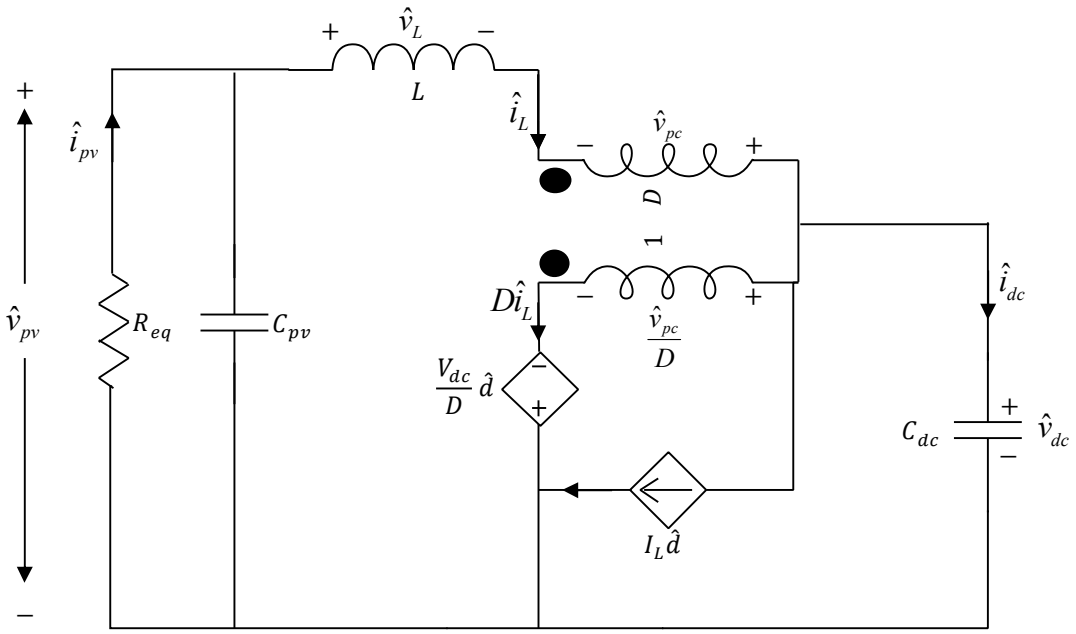

Fig. 4.17: Small signal model of the PV system in Case 4.

Using the same derivation procedures as those for Case 3, the control-to-input current transfer function can be derived as follows:

$$\frac{\hat{i}_{pv}(s)}{\hat{d}(s)} = \frac{C_{dc}C_{pv}R_{eq}V_{dc}s^2 + (C_{dc}V_{dc} + C_{pv}D'I_{pv}R_{eq})s + D'I_{pv}}{C_{dc}C_{pv}LR_{eq}s^3 + C_{dc}Ls^2 + (C_{pv}R_{eq}(D')^2 + C_{dc}R_{eq})s + (D')^2} \tag{4.39}$$

Therefore, the control-to-input voltage transfer function can be expressed as follows:

$$G_{vd,4}(s) = \frac{\hat{v}_{pv}(s)}{\hat{d}(s)} = -\frac{C_{dc}R_{eq}V_{dc}s + D'I_{pv}R_{eq}}{C_{dc}C_{pv}LR_{eq}s^3 + C_{dc}Ls^2 + (C_{pv}R_{eq}(D')^2 + C_{dc}R_{eq})s + (D')^2} \tag{4.40}$$

From the above transfer function, it can be seen that the plant has one zero in the left-half plane, which defines an open-loop unstable system.

4.4 Design of the Single-phase Grid-Tied PV System

The single-phase grid-tied PV system consists of a 3 kW PV array, a boost converter, a H-bridge inverter, a LCL filter and a single-phase grid. The design of the PV array, the boost converter, the LCL filter and single-phase grid will be discussed in Sections 4.4.1, 4.4.3, 4.4.4 and 4.4.5, respectively. The boost converter is used to maximize the energy

harvest from a PV array using a MPPT controller. Voltage oriented control (VOC) is implemented to control the operation of PV inverter to regulate the DC link voltage to 400 V. The purpose of using the LCL filter is to reduce output voltage harmonics and minimize the current distortion injected into the utility grid. Fig. 4.18 shows the schematic diagram of the single-phase grid-tied PV system. The design of the PV array, the boost converter, the LCL filter and the single-phase grid will be discussed in the following subsections.

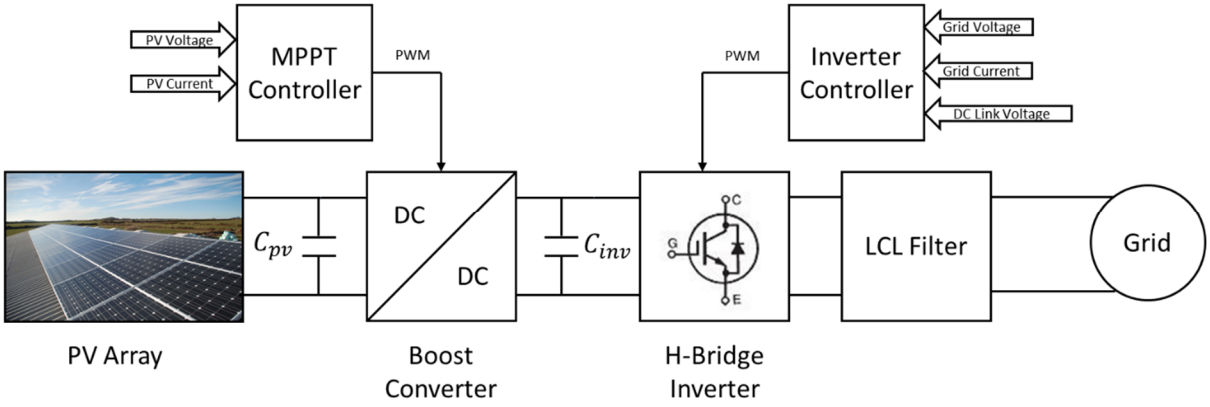

Fig. 4.18: Schematic diagram of the single-phase grid-tied PV system.

4.4.1 PV array design

The PV array is designed based on the BP 380 solar panel. The specifications of a BP 380 solar panel have been tabulated in Table 2.2. The maximum power output of the grid-tied PV system is specified as 3 kW. To achieve a total power rating that is slightly higher than 3 kW, two parallel-connected PV strings of 19 series-connected BP 380 PV modules are used to construct the PV array. The maximum total power output of the PV array (P_{max_array}) at STC is calculated as follows:

$$P_{max\_array} = V_{mpp\_module} \cdot I_{mpp\_module} \cdot TNM = 17.6 \times 4.55 \times 38 = 3043.04\ W \qquad (4.41)$$

where TNM stands for the total number of modules in a PV array, V_{mpp_module} and I_{mpp_module} represent the voltage and current at the MPP in a module, respectively. These parameters will also be used in Section 4.4.2 to determine the voltage and current operating points of the boost converter that is fed by the PV array.

4.4.2 DC analysis of the PV system

DC operating point analysis is necessary to determine the input and output parameters of the boost converter when the PV system operates at steady state. DC analysis is conducted with the assumption that the PV array always operates at its MPP in steady-state conditions. The specifications of the PV array have been provided in Section 4.4.1. According to the parameters of the PV module in Table 2.2, the input voltage, current and power of the boost converter can be calculated as follows:

$$V_{in} = V_{mpp\_module} \times 19 = 17.6 \times 19 = 334.4\ V \tag{4.42}$$

$$I_{in} = I_{mpp\_module} \times 2 = 9.1\ A \tag{4.43}$$

$$P_{in} = P_{max,\_array} = 3043.04\ W \tag{4.44}$$

The two-piecewise-linear model shown in Fig. 4.8 (a) is used to model a BP 380 solar panel. According to (4.4) and (4.5), the parameters of the two-piecewise-linear model in modelling the BP 380 PV module are calculated as follows:

$$R_s = \frac{V_{oc} - V_{mpp}}{I_{mpp}} = \frac{22.1 - 17.6}{4.55} = 0.989\ \Omega \tag{4.45}$$

$$R_p = \frac{V_{mpp}}{I_{sc} - I_{mpp}} - R_s = \frac{17.6}{4.8 - 4.55} - 0.989 = 69.41\ \Omega \tag{4.46}$$

$$I_{PV} = I_{sc} \cdot \frac{R_s + R_p}{R_p} = 4.8 \times \frac{0.989 + 69.41}{69.41} = 4.8684\ \text{A} \tag{4.47}$$

Using the current source model shown in Fig. 4.9 (b), the equivalent Thévenin's resistance of the PV array is calculated as follows:

$$R_{eq} = \left(R_p + R_s\right) \cdot \frac{N_{ser}}{N_{par}} = (69.41 + 0.989) \times \frac{19}{2} = 668.8\ \Omega \tag{4.48}$$

where N_{ser} symbolizes the number of PV modules per string and N_{par} stands for the number of parallel-connected strings in the PV array.

As the DC link voltage is regulated at 400 V, the DC link current can be calculated by:

$$I_{dc} = \frac{P_{mpp}}{V_{dc}} = \frac{3043.04\ kW}{400\ V} = 7.6\ A \tag{4.49}$$

The steady-state duty cycle value can be calculated by using the relationship between input and output voltages for the boost converter:

$$D = 1 - \frac{V_{in}}{V_{dc}} = 1 - \frac{334.4\ V}{400\ V} = 0.164 \tag{4.50}$$

The parameters of the PV system in steady-state analysis are tabulated in Table 4.1.

Table 4.1: Parameters of the PV system in DC analysis.

Parameter	Value
Boost converter input voltage (V_{in})	$334.4\ V$
Boost converter input current (I_{in})	$9.1\ A$
Boost converter input power (P_{in})	$3043.04\ W$
Equivalent Thévenin's resistance (R_{eq})	$668.8\ \Omega$
DC link current (I_{dc})	$7.6\ A$
DC link voltage (V_{dc})	$400\ V$
Steady-state duty cycle (D)	0.164

4.4.3 Boost converter design

The primary use of a boost converter is to extract power from the PV array using MPPT techniques. In this design, the boost converter is assumed to always operate in continuous conduction mode (CCM). It is always desirable to have a DC-DC converter with high switching frequency since the size of both the inductors and capacitors can be reduced. Effect of PV array voltage ripple can be mitigated with high switching frequency. However, power loss in the switches is increased with high switching frequency, which reduces the overall efficiency of the converter and may require a large heat sink to dissipate the excessive heat generated by the switches [248]. Therefore, it is better to select the switching frequency that compromises between components size and the converter efficiency [200]. In this design, the boost converter is assumed to always operate in CCM and the switching frequency is selected as $10\ kHz$.

4.4.3.1 Determination of the minimum inductance for CCM

The selection of the inductance for a boost converter is based on the value of the duty cycle and the maximum allowed ripple current. If the allowable ripple current is too high, the electromagnetic interference (EMI) is significant whereas an unstable PWM operation may occur when the allowable ripple current is too low [249]. Initially, the output current of the boost converter is calculated by:

$$I_o = \frac{p_{pv}}{V_{dc}} = \frac{3043.04}{400} = 7.6\ A \tag{4.51}$$

A rule of thumb is that the inductor ripple current ΔI_L is selected as 30% of the maximum input current, which is calculated by:

$$\Delta I_L = 30\% \times I_{in} = 2.73\ A \tag{4.52}$$

Thus, the minimum inductance of the boost converter is calculated as:

$$L = \frac{V_{mpp} \times D}{f \times \Delta I_L} = \frac{334.4 \times 0.164}{10000 \times 2.73} = 2\ mH \tag{4.53}$$

Therefore, the actual inductance value is selected as 2 mH.

4.4.3.2 Power decoupling capacitors design for the grid-tied PV system

The two power decoupling capacitors connected at the input and output terminals of the boost converter make a key contribution to the system's power stability and voltage regulation. The capacitor connected at the input terminal is known as the input filter capacitor (C_{pv}) whereas the capacitor connected at the output is known as the DC link capacitor (C_{dc}). These two capacitors are shown in Fig. 4.18 in Page 95.

4.4.3.2.1 Calculation of the DC link capacitance

The DC link capacitor is used as a load-balancing energy storage device between the DC link and the AC grid side [182]. This component is connected in parallel with the inverter to maintain a stable and fixed DC voltage. This component is also known as the power decoupling capacitor as it decouples the PV array and the grid. Bulk electrolytic

capacitors are adopted for input filter capacitors due to their low cost per Farad and high capacitance per volume, which creates the system reliability issues since the electrolytic capacitors have a limited life span [184]. The life span of a commercial electrolytic capacitor used as a DC link capacitor for power balancing is only about 10 years, which is significantly short when compared to the typical life expectancy of a commercial PV panel (about 25 years) [250]. Therefore, the electrolytic capacitor is the main defect factor that restricts the life span of grid-tied PV systems. The total reliability of grid-tied PV systems may increase if electrolytic capacitors are replaced with film capacitors [251].

The grid power ripple with a double-line frequency inevitably produces a double-line-frequency voltage oscillation at the DC link and lead to overvoltages on the semiconductor switches in the inverter [188]. This voltage oscillation at the DC link can propagate to the input voltage of the boost converter and lead to inaccurate MPPT operation. The adoption of a DC link capacitor can mitigate the effects of the double-line-frequency voltage ripple of the grid on the DC link voltage and the PV array voltage and alleviate the stress on the IGBT switches. The amplitude of DC link voltage ripple is determined by the DC link voltage, the capacitance of the DC link capacitor and the power injected to the grid. Small DC link capacitors result in a disadvantage of the inverter output current distortion by low order harmonics when compared to large DC link capacitors [188]. The impact of large and small bulk DC link capacitors on the PV array voltage waveform is illustrated in [181].

The instantaneous charge/discharge power of the DC link capacitor (p_c) can be calculated using (4.54) by adopting an energy-balancing equation between the DC and AC sides of the grid-tied inverter [182], [252]. The energy stored in the DC-link capacitor (W_c) can be expressed in (4.55) by integrating (4.54) over a half cycle, since the stored energy is equal to the discharging electric charge of the capacitor in a half cycle of the power ripple [182].

$$p_c = p_{pv} - p_g = p_{pv}\left(1 - \cos\left(2\omega_f t\right)\right) \tag{4.54}$$

$$W_c = \int_0^{\frac{\pi}{2}} p_c dt = \frac{p_{pv}}{\omega_f} \tag{4.55}$$

where p_{pv} represents the instantaneous output power of the PV array, p_g is the instantaneous grid power, and ω_f is two times the utility grid angular frequency. Additionally, the stored energy can also be obtained from the relationship between the electric charge and voltage across the capacitor as [182]:

$$W_c = \frac{1}{2} C_{dc}(V_{max}^2 - V_{min}^2) \tag{4.56}$$

where V_{max} and V_{min} represent the upper and lower voltage limits of the DC link capacitor, respectively. C_{dc} symbolises the DC link capacitance. Thus, (4.56) can be rearranged as:

$$\frac{1}{2} C_{dc}(V_{max}^2 - V_{min}^2) = C_{dc}\Delta V \cdot V_{dc} = \frac{p_{pv}}{\omega_f} \tag{4.57}$$

$$C_{dc} = \frac{p_{pv}}{\omega_f \cdot \Delta V \cdot V_{dc}} \tag{4.58}$$

where, $\Delta V = V_{max} - V_{min}$ stands for the amplitude of the DC link voltage ripple. In this analysis, the reference DC link voltage V_{dc} is fixed at $400\ V$. To mitigate the effects of the DC link voltage ripple on the PV array voltage, a small percentage of DC link voltage ripple is selected. In this design, the DC link voltage ripple is selected as 1% of the DC link voltage, which is 4 V. Therefore, the DC link capacitance can be calculated as follows:

$$C_{dc} = \frac{3043.04}{4 \times 400 \times 2 \times \pi \times 50} = 6.054\ mF \tag{4.59}$$

To round up to the nearest standard capacitor value, the DC link capacitance value is chosen as 6.5 mF.

4.4.3.2.2 Calculation of the input filter capacitance

The input filter capacitor is used to reduce the PV array voltage ripple under normal operating conditions. It can also prevent any damages in the boost converter induced by the PV array voltage variations due to the intermittency of solar energy. The current ripple of the inductor will result in a noticeable voltage ripple in the PV array that could be attenuated by a DC input filter capacitor. Under the assumptions that the nonlinearity of the PV array output characteristics are neglected and the boost converter always operates

in continuous conduction mode (CCM), the voltage ripple of the input filter capacitance can be simply derived as follows [182]:

$$\Delta V_{pv} = \frac{DT^2 V_{pv}}{4C_{pv}L} = \frac{DV_{pv}}{4C_{pv}Lf^2} \tag{4.60}$$

Rearranging (4.60) and substituting the parameters of the boost converter, the input filter capacitance is calculated in (4.61). It is noted that the PV array voltage ripple is selected as 1% of the voltage at the MPP, which is $3.344\ V$.

$$C_{pv} = \frac{DV_{pv}}{4\Delta V_{pv} f^2 L} = \frac{0.164 \times 334.4}{4 \times 3.344 \times 2 \times 10^{-3} \times 10000^2} = 2.05 \times 10^{-5}\ F \tag{4.61}$$

For simulation purposes, the input filter capacitance is determined as $47\ \mu F$.

In summary, the parameters of the boost converter are tabulated in Table 4.2.

Table 4.2: Parameters of the boost converter.

Parameter	Value
L	$2\ mH$
C_{pv}	$47\ \mu F$
C_{dc}	$6.5\ mF$
f_s	$10\ kHz$

4.4.4 Single-phase LCL filter design

A single-phase LCL filter is used to reduce the harmonics generated by the H-bridge inverter as shown in Fig. 4.18. It provides better decoupling between the H-bridge inverter and the grid. The schematics of a single-phase LCL filter is shown in Fig. 4.19. The switching frequency of the H-bridge inverter is chosen as $10\ kHz$. Good attenuation results can be achieved with the adoption of small values of inductors and capacitors as well as a low switching frequency [253], [254]. The procedures for designing a LCL filter have been outlined in [254], [255]. The same procedures will be used in the following analysis.

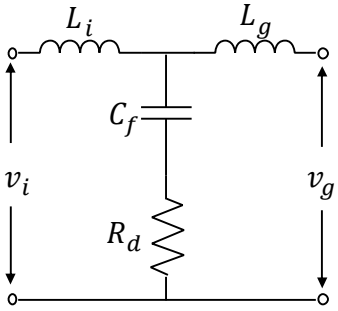

Fig. 4.19: Schematics of a single-phase LCL filter.

The base impedance and base capacitance are calculated initially since the filter capacitance is a percentage of the base values:

$$Z_b = \frac{E_n^2}{P_{pv}} = \frac{230^2}{3000} = 17.63\ \Omega \tag{4.62}$$

$$C_b = \frac{1}{\omega_g Z_b} = \frac{1}{2\pi \times 50 \times 17.63} = 1.8 \times 10^{-4}\ F \tag{4.63}$$

For the design of the filter capacitor, the new version of AS 4777 standard for *Grid connection of energy systems via inverters* stipulated that the power factor is in the range of 0.95 leading to 0.95 lagging for PV inverters with rated nominal output currents less than 20 A [256], thus the maximum reactive power absorbed by the filter capacitor is given as follows:

$$Q_{Cap} = \frac{P_{max\_array}}{0.95} \cdot \sqrt{1 - 0.95^2} = \frac{3043.04}{0.95} \times \sqrt{1 - 0.95^2} = 1\ kvar \tag{4.64}$$

Thus, the filter capacitance is calculated as follows:

$$C_f = \frac{Q_{Cap}}{\omega_g \cdot E_n^2} = \frac{1000}{2\pi \times 50 \times 230^2} = 60\ \mu F \tag{4.65}$$

The percentage of the reactive power absorbed by the filter capacitor x is calculated as follows:

$$x = \frac{C_f}{C_b} = 0.33 \tag{4.66}$$

The design of the inverter side inductance proceeds from the fact that it limits the required current ripple at the inverter side by up to 10% of the rated current [254], [255].

$$L_i = \frac{V_{dc}}{16 f_s \Delta I_{Lmax}} \tag{4.67}$$

$$\Delta I_{Lmax} = 0.1 \times \frac{\sqrt{2} P_{PV}}{E_n} \tag{4.68}$$

The inverter side inductance can be calculated as follow:

$$L_i = \frac{400}{16 \times 10000 \times 0.1 \times \frac{\sqrt{2} \times 3043.04}{230}} = 1.3\ mH \tag{4.69}$$

The relation between the inverter side inductance and grid side inductance is denoted as the index r, which is shown as follows:

$$L_g = r L_i \tag{4.70}$$

The current ripple attenuation factor k_a at the grid side can be calculated by considering the inverter as a current source at each harmonic frequency. In this design, k_a is assumed to be 20%. Equations (4.71) and (4.72) calculate the grid side inductance by eliciting the relationship between the harmonic current generated by the inverter and the one injected to the grid [255]:

$$k_a = \frac{1}{|1 + r[1 - L_{inv} C_b \omega_{sw}^2 x]|} \tag{4.71}$$

$$L_g = \frac{\sqrt{\frac{1}{k_a^2} + 1}}{C_f w_{sw}^2} \tag{4.72}$$

According to (4.71) and (4.72), L_g and r are calculated as $25.33\ \mu H$ and 0.018, respectively.

The last step is to determine the resonant frequency of the LCL filter by calculating the damping resistance R_d. The purpose of the damping resistance is to guarantee enough attenuation in the switching frequency of the inverter. The resonant frequency f_{res} and the damping resistance R_d for the LCL filter can be calculated as:

$$f_{res} = \frac{1}{2\pi} \times \sqrt{\frac{L_i + L_g}{C_f \times L_i \times L_g}} \tag{4.73}$$

$$R_d = \frac{1}{3\omega_{res}C_f} \tag{4.74}$$

Substituting all relevant values gives $f_{res} = 4.12\ kHz$ and $R_d = 0.2139\ \Omega$.

Finally, specifications of the LCL filter are tabulated Table 4.3:

Table 4.3: LCL filter specifications.

Parameter	Value
Inverter side inductance (L_i)	$1.3\ mH$
Grid side inductance (L_g)	$25.3\ \mu H$
Damping resistance (R_d)	$0.2139\ \Omega$
Filter capacitance (C_f)	$60\ \mu F$
Resonant frequency (f_{res})	$4.12\ kHz$

4.4.5 Grid modelling

After filtering out unwanted harmonics using the LCL filter, the grid-tied PV system is connected to a single-phase grid. The grid is modelled with a 230 V rms , 50 Hz equivalent Thévenin's voltage-source. The reference impedance for low voltage public supply systems that is given in [257] for electrical apparatus testing purposes is used to model the single-phase grid. Therefore, the internal impedance of the grid is (0.4+j0.25) Ω.

4.4.6 Frequency analysis of the PV system

In this section, the parameters of the boost converter presented in Section 4.4.3 and control-to-input voltage transfer functions derived in Section 4.3.4 for the four cases are used. The control-to-input voltage transfer function of the boost converter in each case are developed separately and the corresponding pole-zero and Bode plots are presented.

The control-to-input voltage transfer function in Case 1 is given as follows:

$$G_{vd,1}(s) = \frac{\hat{v}_{pv}(s)}{\hat{d}(s)} = -\frac{4.722\times10^{23}}{1.831\times10^{15}s^2+1.181\times10^{21}} \tag{4.75}$$

The corresponding pole-zero and Bode plots are shown in Fig. 4.20 and Fig. 4.21, respectively.

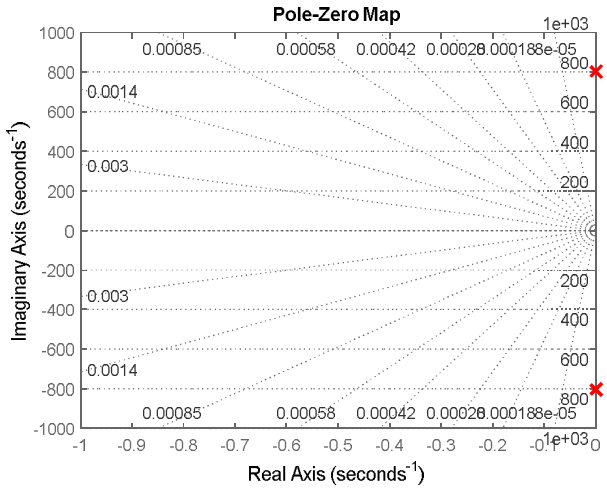

Fig. 4.20: Pole-zero diagram of the control-to-input voltage transfer function in Case 1.

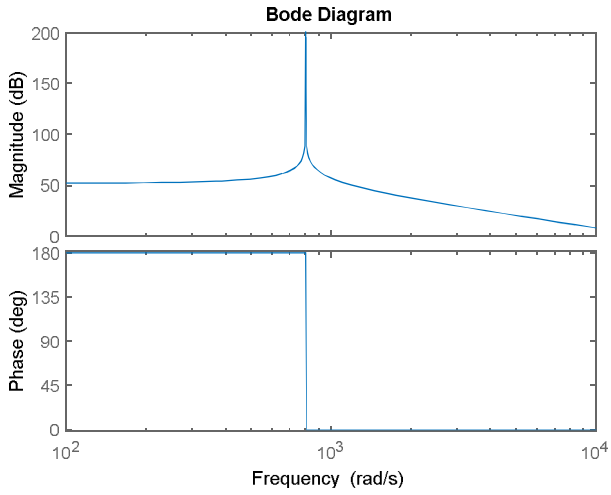

Fig. 4.21: Bode plots of the control-to-input voltage transfer function in Case 1.

The transfer function indicates a second-order system with two poles on the imaginary axis. There is a negative sign in the control-to-input voltage transfer function, which indicates that the input voltage will decrease as the duty cycle increases.

The control-to-input voltage transfer function in Case 2 is given as follows:

$$G_{vd,2} = \frac{\hat{v}_{pv}(s)}{\hat{d}(s)} = -\frac{8.298\times10^{25}}{3.218\times10^{17}s^2+1.902\times10^{19}s+2.075\times10^{23}} \tag{4.76}$$

The corresponding pole-zero and bode plots are shown in Fig. 4.22 and Fig. 4.23, respectively.

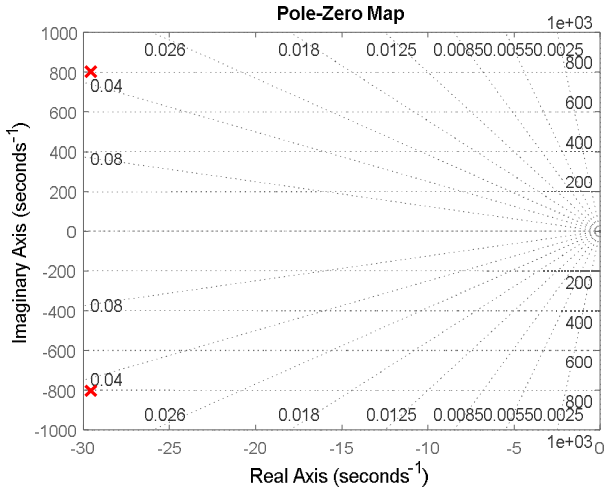

Fig. 4.22: Pole-zero diagram of the control-to-input voltage transfer function in Case 2.

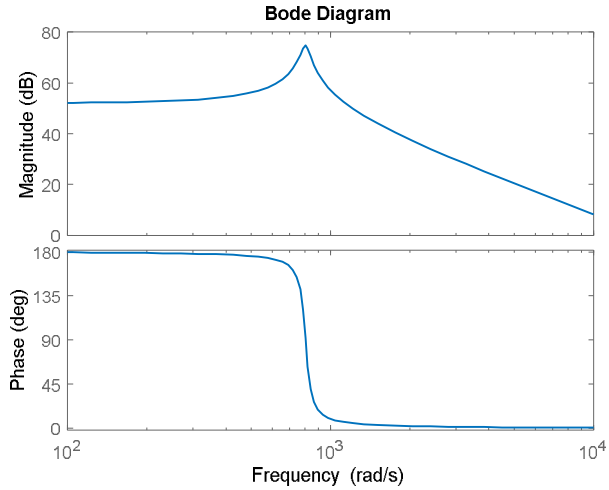

Fig. 4.23: Bode plots of the control-to-input voltage transfer function in Case 2.

The control-to-input voltage transfer function in Case 3 is given as follows:

$$G_{vd,3}(s) = \frac{\hat{v}_{pv}(s)}{\hat{d}(s)} = -\frac{1.417\times10^{28}s + 9.009\times10^{28}}{5.493\times10^{18}s^3 + 3.568\times10^{25}s} \tag{4.77}$$

The corresponding pole-zero and Bode plots are shown in Fig. 4.24 and Fig. 4.25, respectively.

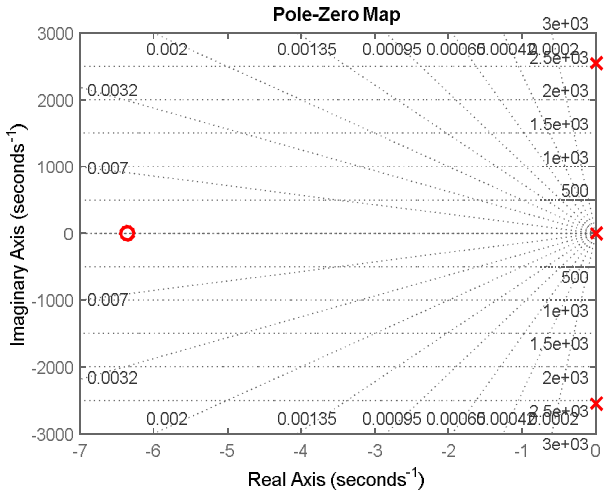

Fig. 4.24: Pole-zero diagram of the control-to-input voltage transfer function in Case 3.

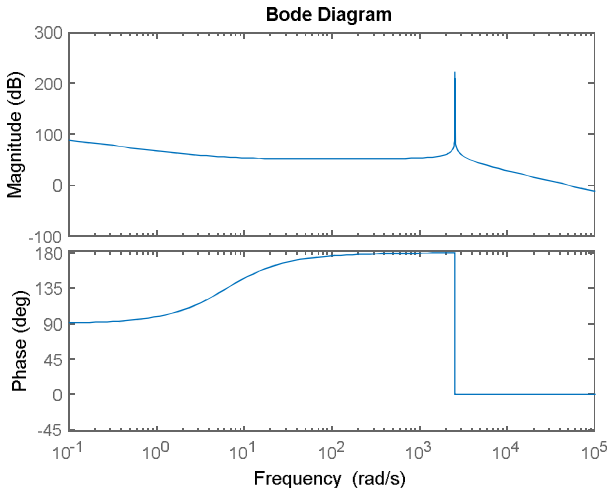

Fig. 4.25: Bode plots of the control-to-input voltage transfer function in Case 3.

The control-to-input voltage transfer function in Case 4 is given as follows:

$$G_{vd,4} = \frac{\hat{v}_{pv}(s)}{\hat{d}(s)} = -\frac{5.098\times10^{32}s+3.242\times10^{33}}{1.977\times10^{23}s^3+1.169\times10^{25}s^2+1.284\times10^{30}s+5.519\times10^{29}} \quad (4.78)$$

The corresponding pole-zero and bode plots are shown in Fig. 4.26 and Fig. 4.27, respectively.

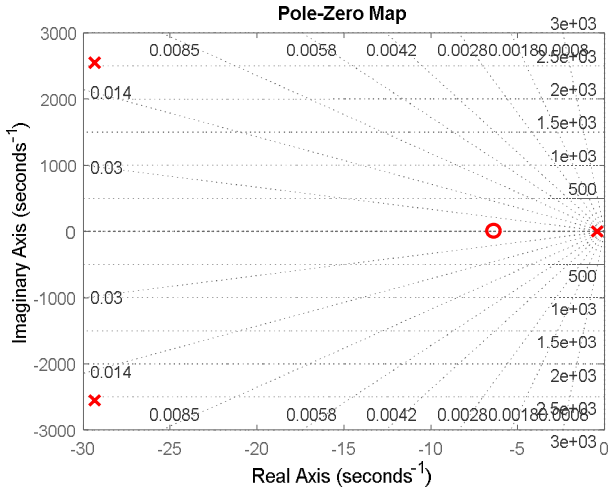

Fig. 4.26: Pole-zero diagram of the control-to-input voltage transfer function in Case 4.

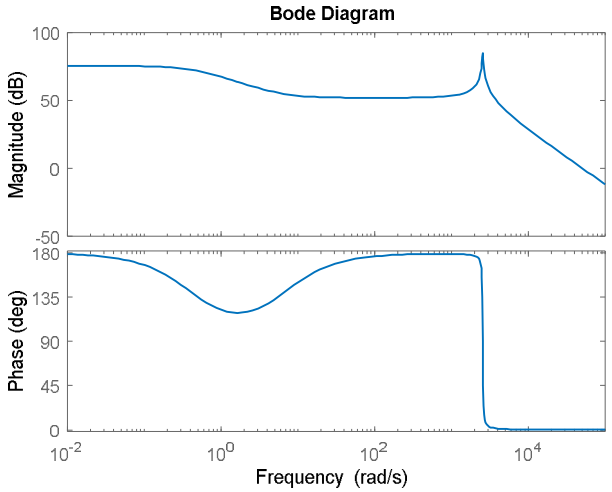

Fig. 4.27: Bode plots of the control-to-input voltage transfer function in Case 4.

Table 4.4 provides a summary of poles and zeros locations, assumptions on the small signal model, and parameters settings of the digital PID controller for the four cases. The parameters of the digital PID controller are tuned and optimized in each case using Simulink PID Tuner and Simulink Response Optimization Tool.

Table 4.4: Summary of poles and zeros locations, assumptions on the small signal model, and parameters settings of the digital PID controller for the four cases.

Case	**Poles and Zeros Locations**		**Assumptions**		**Parameters of the digital PID Controller**		
	Poles	Zeros	Equivalent Thévenin's resistance of the PV array (R_{eq})	DC link capacitor (C_{dc})	P	I	D
1	$8.0296 \times 10^2 j$, $-8.0296 \times 10^2 j$	-	Ignored	Ignored	0.02996	11.60851	1.93273×10^{-5}
2	$(-0.2956 + 8.0242j) \times 10^2$, $(-0.2956 - 8.0242j) \times 10^2$	-	Considered	Ignored	0.03282	13.41623	2.0075×10^{-5}
3	0, $2.5485 \times 10^3 j$, $-2.5485 \times 10^3 j$	-6.3589	Ignored	Considered	0.00167	1.10545	3.3344×10^{-7}
4	-0.4, $(-0.0293 + 2.5483j) \times 10^3$, $(-0.0293 - 2.5483j) \times 10^3$	-6.3589	Considered	Considered	0.00159	0.78479	5.7510×10^{-7}

It can be seen that the constants for the PID controllers are slightly different in Case 1 and Case 2, whereas the constants for the PID controllers are almost the same in the Case 3 and Case 4. This indicates the DC link capacitor has a significant effect on the parameters selection of the PID controller. The later simulation results shown in Figs. 4.33 to 4.34 will also validate this conclusion.

From the Bode plots developed in the four cases, it can be seen that the inclusion of R_{eq} in the transfer function shifts the two complex poles at the imaginary axis to the left half-plane. The inclusion of the DC link capacitor in the analysis adds a negative real zero and a negative real pole to the plant, which shifts the crossover frequency from $803\ Hz$ to $2550\ Hz$, such high frequency peak in the Bode plot requires special attention in the PID controller design.

4.5 Simulation Results

To evaluate the performance of four different parameter settings of the digital PID controller, a *Matlab/SimPowerSystems* simulation model for the PV system is constructed. This simulation model does not consider the parasitic resistances of capacitors and inductors, which is consistent with the assumptions on the PWM switch model described in Section 4.3.3. The PV array voltage responses are recorded and compared with their references under four different parameters settings of the digital PID controller. The following simulations are all conducted at constant irradiance of $1000\ W/m^2$ and temperature of $25\ ℃$. Fig. 4.28 depicts the simulation model for the single-phase grid-tied PV system. The sampling time used for the simulation model is $1\ \mu s$, while the sampling time for the digital PID controller is $100\ \mu s$, which is much longer than that for the simulation model.

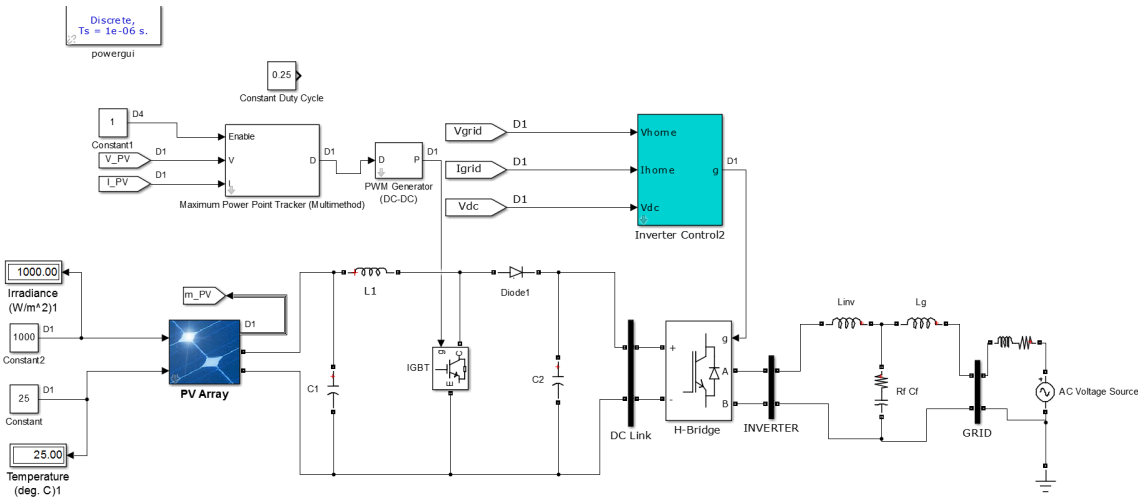

Fig. 4.28: Simulation model of the single-phase grid-tied PV system with LCL filter.

The simulation model uses a non-linear model to emulate the behaviour of the boost converter and uses the SDM to model the PV array. Simulations are carried out with the PID controllers designed based on four different control-to-input voltage transfer functions developed under four different assumptions. The parameters of the digital PID controllers under four different cases are tabulated in Table 4.5. These parameters are optimised using the automatic PID tuning algorithm in MATLAB/Simulink.

4.5.1 PV array voltage response without the controller

In this case, a constant duty cycle of 0.25 is applied to the boost converter, from the DC analysis of the boost converter, the reference voltage of the PV array is calculated by:

$$V_{pv} = (1 - D) \cdot V_{dc} = (1 - 0.25) \times 400 = 300\ V \tag{4.79}$$

The PV array voltage reference and response at steady state is displayed in Fig. 4.29. The red curve represents the voltage reference whereas the magenta curve shows the PV array voltage response. It can be seen that the PV voltage response has significant steady-state errors and deviates below the voltage reference. The PV array voltage ripple is a result of the switching of the boost converter. This voltage ripple component significantly reduces the available power extracted from the PV array [66]. The power and voltage deviations can be significantly mitigated by integrating a digital PID controller with the simulation results presented in the subsequent sections.

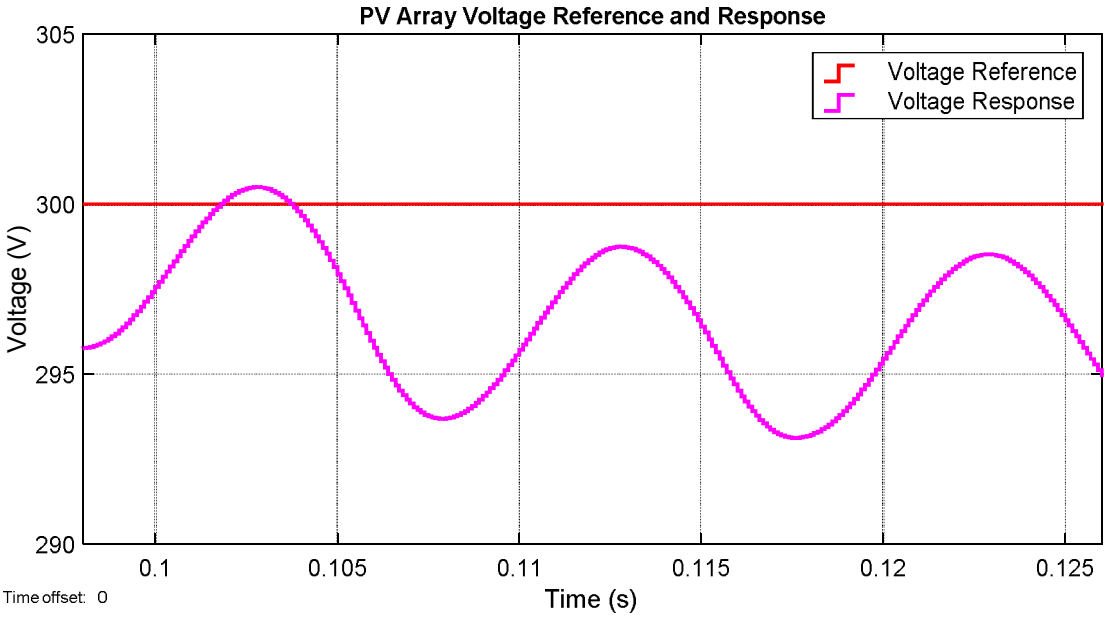

Fig. 4.29: PV array voltage performance without controller to illustrate the voltage ripple.

4.5.2 PV array voltage response with the controller designed for Case 1

In this case, the system is equipped with the digital PID controller designed in Case 1. The controller initially regulates the PV array voltage at $150\ V$. A step increase in the voltage reference from $150\ V$ to $200\ V$ is observed at $t = 0.1\ s$. It can be seen in the first subplot in Fig. 4.30 that the PV array voltage fluctuates significantly around the voltage reference, indicating that there is a large steady-state error. The PV array can track the voltage reference but with significant voltage fluctuation. The duty cycle of the boost converter fluctuates drastically from 1 to 0 that represents the saturation of the controller. This undesired effect of controller saturation leads to a fluctuating response of the PV array voltage. The reason for an oscillatory duty cycle signal is attributed to the controller windup. From Fig. 4.31, it can be observed that the PID controller output almost follows the derivative element output. The PID controller output is clamped between 0 and 1 to produce the duty cycle signal as shown in the second subplot in Fig. 4.30. This input saturation causes a steady-state oscillatory PV array voltage signal as shown in the first subplot in Fig. 4.30.

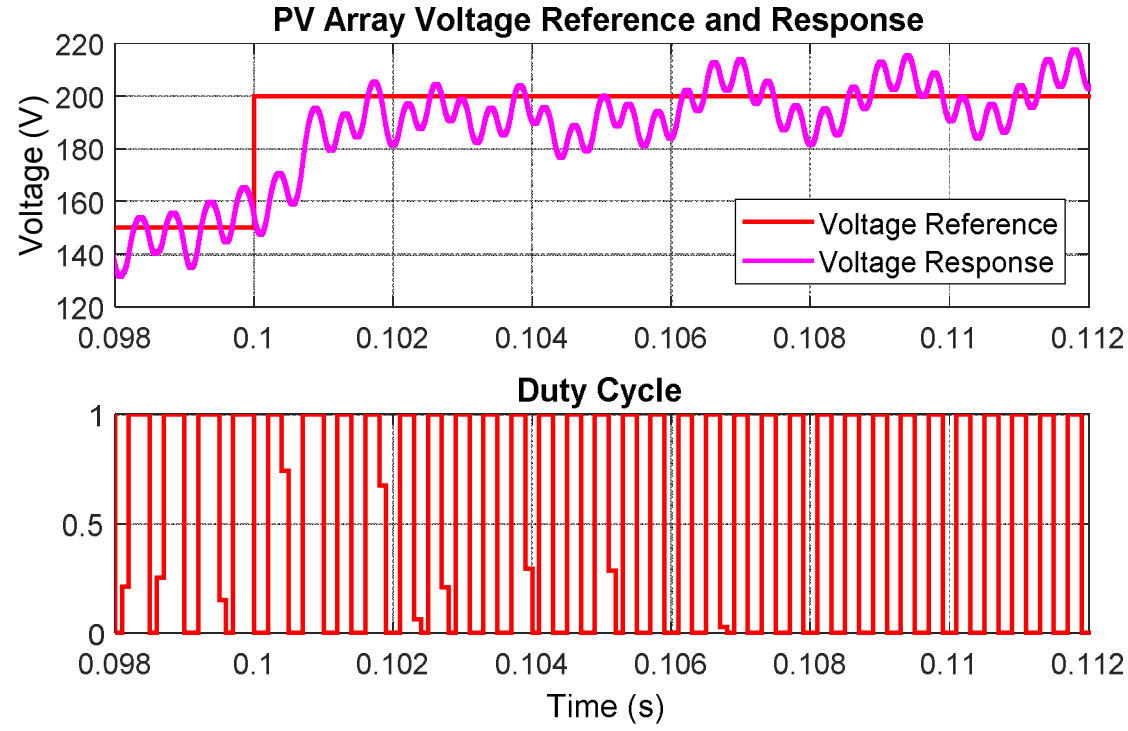

Fig. 4.30: PV array voltage performance with the controller designed for Case 1.

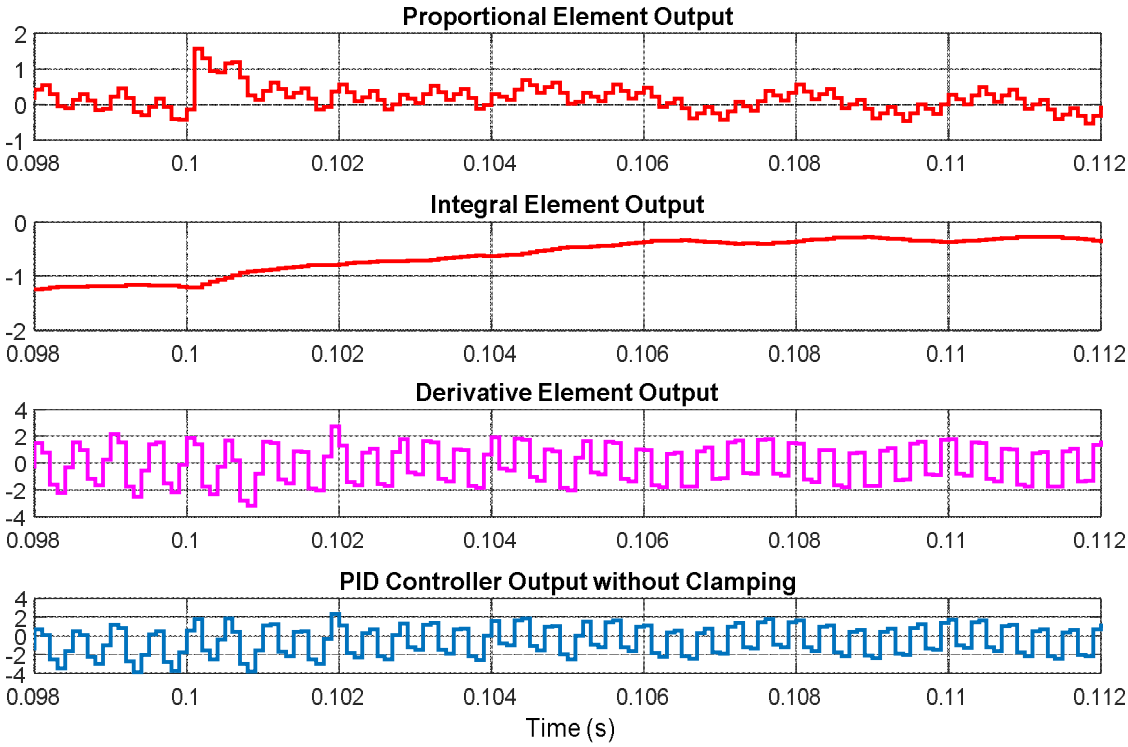

Fig. 4.31: The outputs of the proportional, the integral and the derivative modes, and the PID controller output without clamping.

4.5.3 PV array voltage response with the controller designed for Case 2

In this case, the system is equipped with the digital PID controller designed for Case 2. Similarly, a step increase in the voltage reference from 150 V to 200 V takes place at $t = 0.1\ s$. From Fig. 4.32, it can be seen that the response of the PV array voltage is similar to that in Case 1.

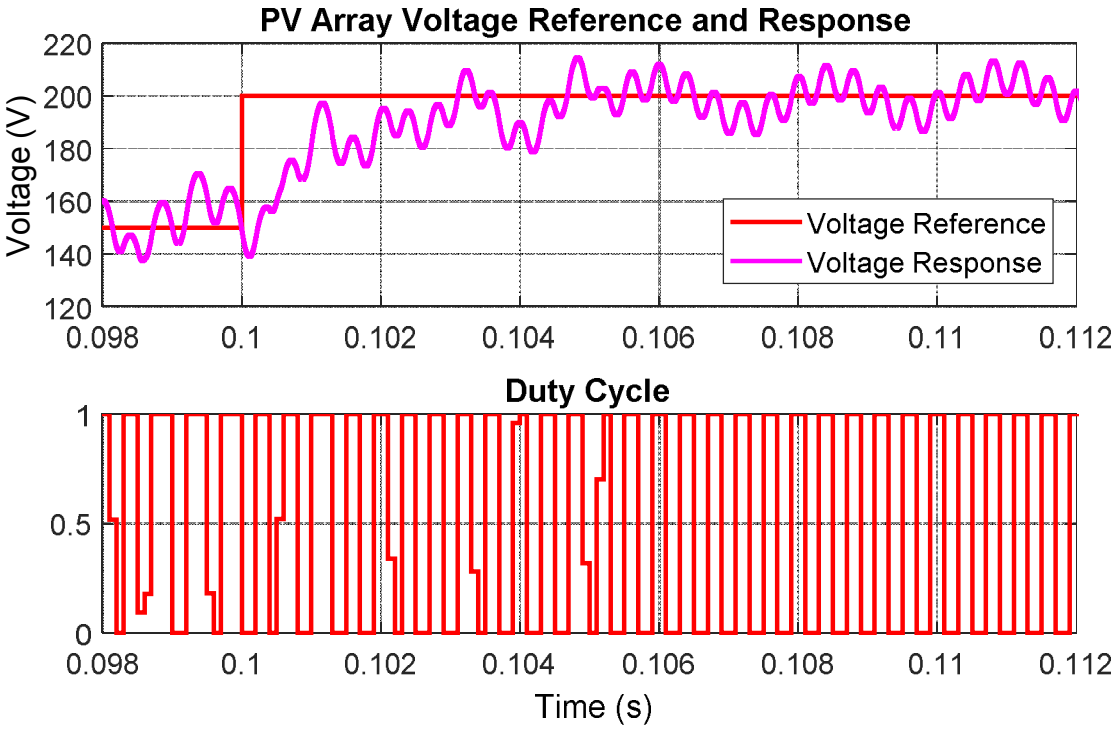

Fig. 4.32: PV array voltage performance with the controller designed for Case 2.

4.5.4 PV array voltage response with the controller designed for Case 3

In this case, the system is equipped with the digital PID controller designed in Case 3. The step increase in the voltage reference from 150 V to 200 V takes place at $t = 0.1\ s$. With the controller designed to incorporate the effect of C_{dc}, it can be seen in Fig. 4.33 that the rising time of the voltage response becomes evidently faster than the responses in Case 1 and Case 2. The steady-state voltage oscillation is significantly smaller that the responses in Case 1 and Case 2. The duty cycle of the boost converter oscillates around a fixed value approximately equal to 0.5 at the steady state.

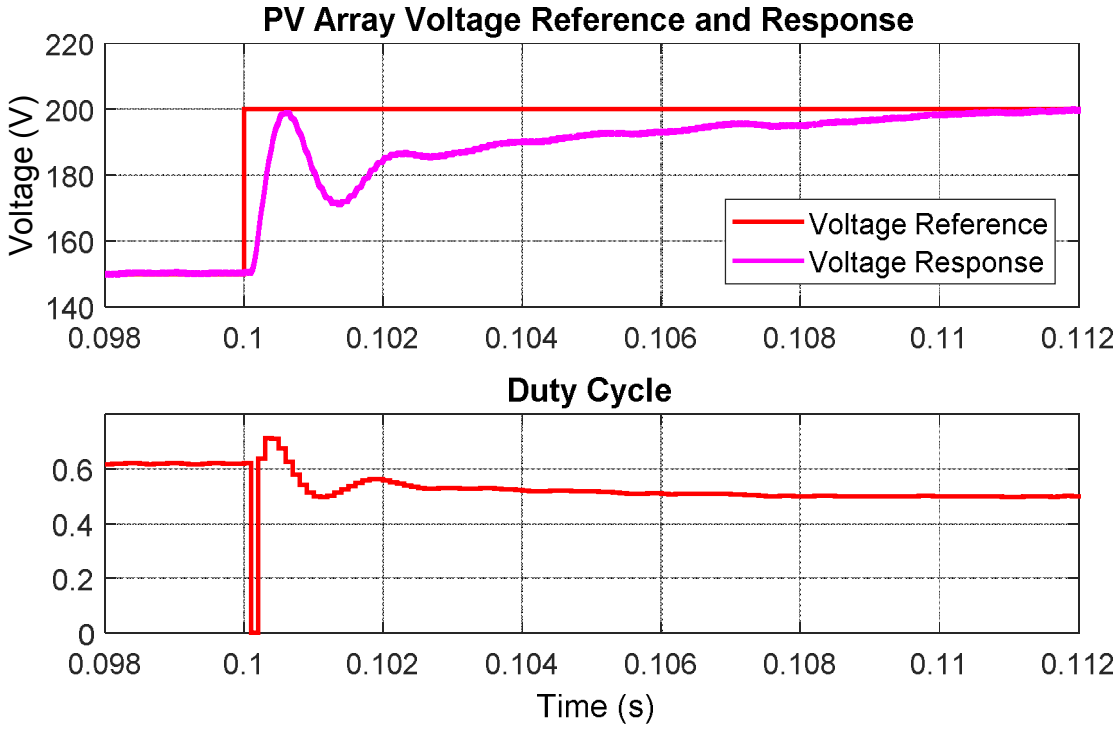

Fig. 4.33: PV array voltage performance with the controller designed for Case 3.

4.5.5 PV array voltage response with the controller designed for Case 4

In this case, the system is equipped with the digital PID controller designed for Case 4. The step increase in the voltage reference from $150\ V$ to $200\ V$ happens at $t = 0.1\ s$. It can be seen in Fig. 4.34 that the response of the PV array voltage and the duty cycle in Case 4 are similar to that in Case 3, respectively.

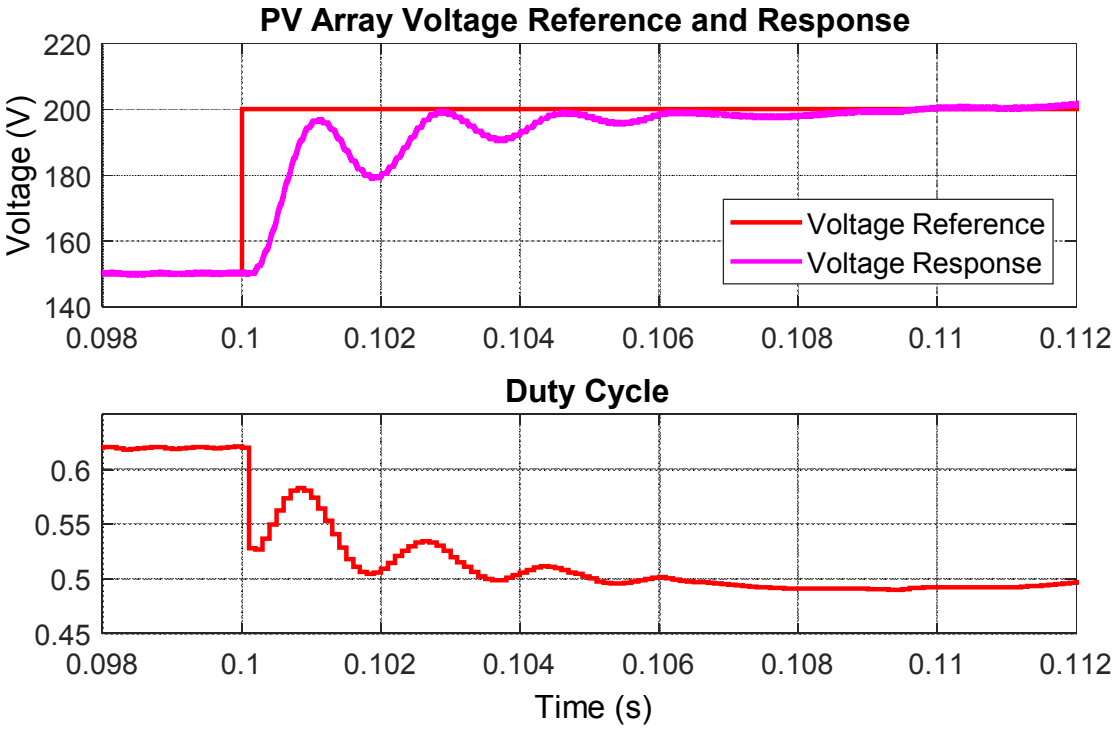

Fig. 4.34: PV array voltage performance with the controller designed for Case 4.

Table 4.5 shows the steady-state voltage and power deviations of the PV array without the PID controller and with the PID controller under four different cases. It can be noted that the voltage and power deviations without the controller are much higher than that with the controller, which also can be seen from Figs. 4.29 to 4.30. As the transfer function developed becomes more complex, the steady-state voltage and power deviations are reduced in a progressive manner from Case 1 to Case 4, which indicates a gradual improvement in the PV array voltage performance. The parameter settings of the digital PID controller designed for this case is used later in Chapter 6 to investigate the performance of the MPPT technique.

Table 4.5: Steady-state voltage and power deviations at each case.

	Steady-state Voltage Deviation (V)	Steady-state Power Deviation (W)
No Controller	5.495	284.1
Case 1	2.558	139.7
Case 2	2.553	138.2
Case 3	0.952	52.75
Case 4	0.909	51.91

4.6 Conclusion

This chapter has presented a brief review of the closed-loop control schemes for DC-DC converters input voltage control. Design of a single-phase grid-connected PV system has been covered in this chapter. A linear model for the PV array and the boost converter is developed for control system analysis. Four cases are developed based on whether the equivalent Thévenin's resistance of the PV array or the DC link capacitor is considered in the small signal model. The corresponding control-to-input voltage transfer function in each case is developed by using the PWM switch model. The DC and frequency analysis in each case is also conducted. The parameters of the digital PID controller are tuned separately according to the control-to-input voltage transfer function developed in each case. Simulation studies are conducted to illustrate the effectiveness of the four different parameter settings of the digital PID controller. High steady-state errors, slow transient responses and duty cycle saturation are observed in Case 1 and Case 2 irrespective of the effects of the DC link capacitor. The PV array voltage responses in Case 3 and Case 4 offer zero steady-state error and fast transient responses without duty cycle saturation. The optimized parameter settings of the digital PID controller in Case 4 are used to investigate the performance of the MPPT techniques that will be discussed in Chapter 6.

Chapter 5
Battery Energy Storage Systems for Plug-in Hybrid Electric Vehicles

5.1 Introduction

Plug-in hybrid electric vehicles (PHEVs) have become popular in recent years since they have advantages of low fuel cost and low carbon emissions [258] compared to conventional vehicles that use internal combustion engines. The performance of a PHEV depends highly on the on-board battery energy storage system (BESS). The choice of the BESS technology for an PHEV will depend on vehicle power and energy ratings, response time, weight, volume and operating temperature [259]. Common BESS technologies for PHEV applications include lead-acid (Pb-Acid), lithium-ion (Li-ion), nickel-cadmium (Ni-Cd), nickel-metal hydride (Ni-MH) [259] and sodium-sulphur (NaS) [5]. Among these battery technologies, Li-ion batteries have superior performance over other battery technologies and are preferably used for PHEVs applications. This is mainly attributed to several factors, like high energy density, high output current levels, flat discharge characteristics in the middle region, high energy-to-weight ratios, no memory effect, and a low self-discharge rate [260], [261]. Fig. 5.1 shows the Li-ion battery packs for a 2013 Chevrolet Volt PHEV.

One of the limitations of a Li-ion battery is that its high output current leads to a significant drop in voltage across the internal resistance. This leads to increased internal power losses and higher cell temperatures than those of a lead-acid battery. Therefore, a battery management system (BMS) is required to control the charging and discharging of the battery, and monitor the temperature of each individual cell to ensure reliable and safe operation [5]. Another functionality that an advanced BMS may have is cell balancing [261]. Cell balancing ensures that all the cells within a battery pack operate at the same voltage, and the temperature of the battery pack is well distributed among all the cells. The same operating voltage for all the cells results in an alignment in the cells' SOC [261].

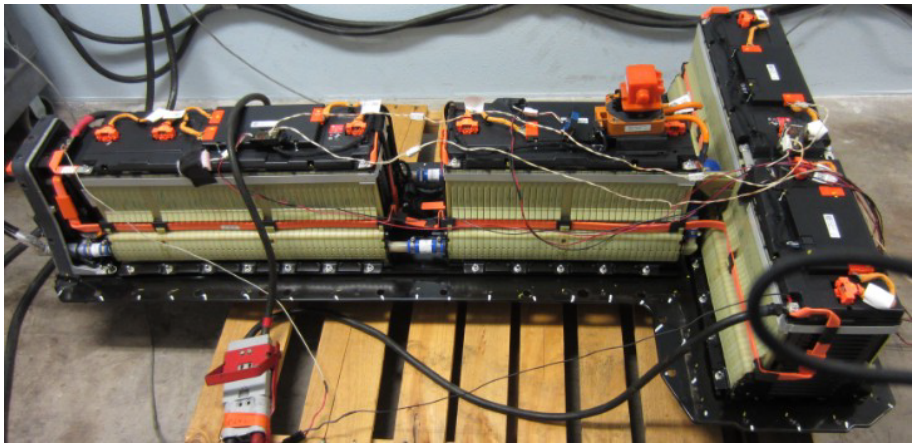

Fig. 5.1: Li-ion battery packs for a 2013 Chevrolet Volt PHEV [262].

Accurate modelling of PHEV batteries is of fundamental importance to optimize the operation strategy, extend battery life and improve vehicle performance [263]. A suitable PHEV battery model can reflect the battery's steady-state and dynamic performance. Modelling of PHEV batteries is a research area that has been studied extensively throughout the literature. Some earlier examples in this area have been demonstrated in [264]–[267]. A small subset of more recent research is described in [268]–[270]. These PHEV battery modelling approaches vary widely in terms of complexity and accuracy [269].

In [271], modelling strategies for batteries are summarized into three categories: experimental, electrochemical and electric circuit-based models [270], [271]. Experimental and electrochemical models cannot accurately represent the dynamics of vehicle batteries in terms of the SOC estimations of battery packs according to [271]. Electrochemical models emulate the static characteristics of a PHEV battery using mathematical equations that relate to the chemical reactions inside the battery [272]. These models cannot accurately simulate the battery's dynamic response [273] and require high computational power to solve the associated nonlinear partial differential equations [274]. The circuit-based models provide reasonable accuracy and robustness in simulating the dynamics of the battery [275]–[277]. Their model parameters can be estimated based on experimental data. A dedicated automated test system is used to acquire the data in [278]; these data include the responses of a battery at different discharge current levels and SOC conditions [278]. Tremblay's model is one widely used

battery model in research on battery energy storage systems [270], on-board electric vehicle batteries [269], [274] and wireless sensor networks [272]. The model incorporates both empirical and electrochemical relationships between SOC and battery terminal voltage. It is embedded into *Matlab/Simulink* as a standard library block with predefined battery model parameters [271], [279]. It has also been validated for electric vehicle applications using experimental data [269].

This chapter proposes the use of a quantum-behaved particle swarm optimisation (QPSO) parameter estimation technique to provide a more accurate estimation of Tremblay's battery model parameters. To the author's best knowledge, this approach has not yet been applied in the context of Tremblay's model parameterization. The root weighted residual sum of squares (RWRSS) between the simulated curves and the experimental discharge curves is used as the performance index to contrast different sets of results. The results obtained using the QPSO approach are compared against those obtained using the GA [267] and PSO [269] approaches. Reviews of the principles of the GA and PSO approaches have been presented in Sections 2.6.5 and 3.3.1.1, respectively. The simulated curves obtained from the GA, PSO, and QPSO parameter estimation techniques are compared to the experimental data extracted from the static capacity tests conducted by Idaho National Laboratory [280] together with the simulated curve obtained from Tremblay's parameter estimation method in [271], [279].

5.2 Tremblay's Battery Model

Tremblay's model expresses a Li-Ion battery voltage during discharging and charging processes by [271], [279]:

$$V_{discharge} = E_o - K\frac{Q}{Q-it}\cdot it - R\cdot i + Aexp(-B\cdot it) - K\frac{Q}{Q-it}\cdot i^* \qquad (5.1)$$

$$V_{charge} = E_o - K\frac{Q}{Q-it}\cdot it - R\cdot i + Aexp(-B\cdot it) - K\frac{Q}{0.1Q+it}\cdot i^* \qquad (5.2)$$

where E_o is the battery constant voltage; K is the polarization constant (V/Ah) or polarization resistance (Ω); Q is the maximum battery capacity (Ah); $it = \int idt$ is the actual battery charge (Ah); the parameter A is the exponential zone amplitude (V); i^* is

the filtered current (A); B is the exponential zone time constant inverse $(Ah)^{-1}$; R is the internal resistance (Ω); i and V_{dis} are the battery current and voltage during discharge, respectively. The current is positive for a discharging process whereas the current is negative during a charging process. The discharge voltage of the battery is decomposed into five components, which are the battery constant voltage E_o, the voltage drop across the internal resistance $R \cdot i$, the polarization voltage affected by battery charge $K \cdot \frac{Q}{Q-it} \cdot it$, the polarization voltage affected by filtered current $K \cdot \frac{Q}{Q-it} \cdot i^*$, and the exponential zone voltage $A \cdot e^{-B \cdot it}$. The filtered current i^* can be expressed as the first order step response of the battery current i, i.e., $i^* = i \cdot (1 - e^{\frac{-t}{\tau}})$, where τ is the battery response time. Fig. 5.2 shows a typical PHEV battery nominal discharge characteristic generated by Tremblay's model, where the remarkable points are clearly shown.

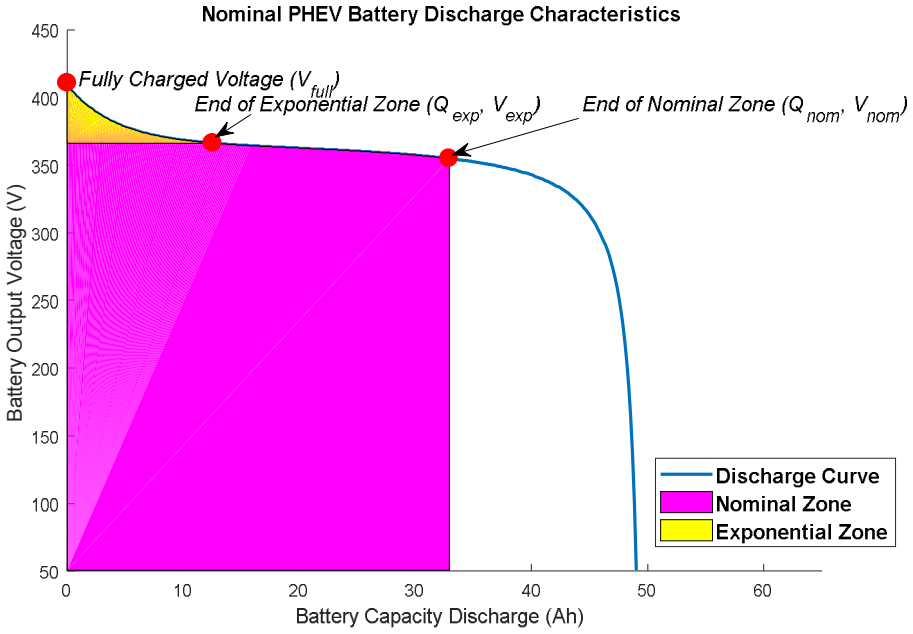

Fig. 5.2: A typical battery discharge characteristic with the three remarkable points labelled.

5.3 Parameter Estimation of Tremblay's Model

5.3.1 Introduction

Tremblay et al. [271], [279] proposed a parameter estimation method to estimate the model parameters. This method utilizes the three remarkable points (shown in Fig. 5.2), namely the fully charged voltage (V_{full}), end of exponential zone (Q_{exp},V_{exp}) and end of nominal zone (Q_{nom}, V_{nom}) that are manually sampled from the typical discharge characteristic on the manufacturer's datasheets. The parameters A, B, K, and E_o in (5.1) are determined from the three remarkable points using several approximation equations. Thus, this approach is quite subjective and error-prone in terms of locating the positions of the remarkable points [269]. The remarkable points on the extracted discharge curve may not be easily identifiable and are highly susceptible to human error. Specifically, the parameters Q_{nom}, V_{exp}, and Q_{exp} are difficult to determine from the manufacturer's discharge curve by visual analysis as indicated in [281]. The discharge characteristic obtained from the manufacturer's datasheets may not reflect the actual discharge curve of the battery since model parameters are dependent on battery life and operational environment [270]. Thus, parameter identification for PHEV batteries needs to be conducted over time and corresponding adjustments of model parameters must be made to account for changes attributed to battery aging [269].

A variety of parameter estimation techniques are proposed in the literature for the parameterization of battery models. A PSO technique is presented in [269] to estimate the model parameters of Tremblay's model. A hybrid optimization technique is proposed in [270] that utilizes a stochastic and a deterministic algorithm to identify the parameters of Tremblay's model. A GA approach is used in [267] to identify the parameters of an improved Thévenin battery model to account for the effects of electrochemical polarization and concentration polarization. A SA algorithm approach is proposed in [281] for Tremblay's model parameterization. In this technique, the discharge curves obtained from a testbed were used to validate the effectiveness of the SA algorithm. Results obtained using the SA algorithm were compared to those obtained using Tremblay's parameter estimation method.

5.3.2 Problem Formulation

The three remarkable points identified in the battery discharge curve need to be estimated to improve curve fitting to the experimental discharge characteristic. Additionally, the internal resistance R and the maximum battery capacity Q_{max} also need to be accurately estimated since R affects the shape of the battery discharge curve and Q_{max} is not provided in PHEV battery static capacity test results. In total, there are seven parameters that need to be estimated in the PHEV battery model. The objective function is defined as the root weighted residual sum of squares (RWRSS) between the model discharge curve and the discharge curve obtained from the static capacity test results in [262]. Therefore, an optimization problem is formulated as follows:

$$\underset{x}{Min}\, F(x) = \underset{x}{Min} \sqrt{\sum_{k=1}^{N} w_k [V_{Manu}(k) - V_{Mod}(k)]^2} \qquad x \in X \tag{5.3}$$

$$x = (V_{max}, V_{exp}, Q_{exp}, V_{nom}, Q_{nom}, Q_{max}, R) \tag{5.4}$$

where $F(x)$ is the objective function, k is the index of the data sample, $V_{Mod}(k)$ represents the model voltage at the k^{th} data sample, $V_{Manu}(k)$ is the manufacturer's voltage at the k^{th} data sample, N is the number of data samples, x is the vector of all estimated variables, X is the space of the solutions and w_k is the weighting factor for the k^{th} data sample. The manufacturer's voltage data are extracted from the static capacity test results at beginning of test (BOT) in [262], using a web-based tool called WebPlotDigitizer [282], which is used to extract data points from plots.

PHEV battery manufacturers usually limit the usable capacity of the battery to meet the battery life cycle requirements, vehicle drive performance and safety issues [283]. The operational range for the state-of-charge (SOC) of PHEV batteries is between 20% and 85%, i.e., the depth-of-discharge (DOD) is between 15% and 80%, as reported in [284]. To match the discharge curve in the operational range, an appropriate weighting function is needed. Many different mathematical expressions could be used to represent the weighting function. In this study, the weighting function used for parameter estimation is defined as follows [285]:

$$w = \begin{cases} 1 & , \quad \text{if } 0.15 \le DOD \le 0.8 \\ (w_{Max} - (w_{Max} - w_{Min}) \cdot \dfrac{DOD}{0.2})^{1.3} & , \quad \text{if } DOD > 0.8 \\ (w_{Max} - (w_{Max} - w_{Min}) \cdot \dfrac{DOD}{0.2})^{1.3} & , \quad \text{if } DOD < 0.15 \end{cases} \tag{5.5}$$

where w_{Max} and w_{Min} are the corresponding maximum and minimum values of the weighting function. Several other weighting functions could also be implemented to improve the accuracy of the estimated results.

5.3.3 Quantum-behaved particle swarm optimisation

A QPSO algorithm eliminates the velocity vector used by the classic PSO algorithm and its concept is inspired by quantum mechanics and physics. The global convergence of a QPSO algorithm is significantly improved when compared to the classic PSO algorithm. The equations for updating the positions of particles are presented as follows [286]:

$$\begin{cases} x_i^{k+1} = P_i^k + \beta \cdot \left| mBest^k - x_i^k \right| \cdot ln\left(\frac{1}{u}\right), \ k < 0.5 \\ x_i^{k+1} = P_i^k - \beta \cdot \left| mBest^k - x_i^k \right| \cdot ln\left(\frac{1}{u}\right), \ k \ge 0.5 \end{cases} \tag{5.6}$$

where,

$$P_i^k = (r_1 \cdot P_{best,i} + r_2 \cdot G_{best})/(r_1 + r_2) \tag{5.7}$$

$$mBest^k = \frac{1}{N}\sum_{i=1}^{N} P_{best,i} \tag{5.8}$$

where $mBest^k$ is the mean best position defined as the mean of all the personal best positions of the swarm. u, k, r_1 and r_2 are all random numbers distributed uniformly on $(0,1)$, respectively. The one and only tuning parameter β is the Contraction-Expansion coefficient. High values of β are preferred in the initial stage of optimization for global exploration, whereas low values are favored in the later stage for more accurate results in the local search [286]. In the following simulations, the parameter β decreases dynamically from 0.9 to 0.5 during the course of iterations [287].

5.3.4 Lower and upper bounds of estimated variables

The admissible lower and upper bounds of each estimated variable need to be defined prior to the parameter estimation process. An inappropriate value for one estimated variable may produce irregular or abnormal discharge curves. Thus, it is crucial to reject the values generated by the parameter estimation algorithms that have spurious physical meanings. The PHEV battery investigated in this study is the battery pack of the 2013 Chevrolet Volt – VIN 3929 [262]. The battery specifications are provided in Table 5.1.

Table 5.1: Battery specifications of the 2013 Chevrolet Volt – VIN 3929 [262].

Battery Specifications	**Value**
Manufacturer	LG Chem
Rated Pack Energy/Capacity	16.5 kWh/45.0 Ah
Battery Type	Lithium-Ion
Minimum Cell Voltage (E_{min})	3.00 V
Maximum Cell Voltage (E_{max})	4.15 V
Nominal Cell Voltage (E_{nom})	3.7 V
Number of series-connected cells (N_s)	96

According to the PHEV battery specifications given in Table 5.1, the lower and upper bounds of each estimated parameter can be derived using the relationships given in Table 5.2. Some of the symbols used in Table 5.2 can be found in Fig. 5.2 and Table 5.1. In Table 5.2, the upper and lower bounds of the internal resistance are given by the maximum and minimum values of the ten-second discharge pulse resistance dataset, denoted as R_{DOD}, as the internal resistance is dependent on DOD variation. The ten-second discharge pulse resistance dataset shows the internal resistance with respect to the DOD and is extracted from [262] using WebPlotDigitizer. It is advised in [288] that the value of Q_{max} be given by 105% of the rated battery capacity. Thus, the lower and upper bounds of Q_{max} are specified as Q_{rated} and $1.1Q_{rated}$, respectively, to include additional solutions for a better estimation of Q_{max} over a wide range.

Table 5.2: Upper and lower bounds of each model parameter.

Parameters	Upper Bound	Lower Bound
Fully Charged Voltage V_{full} (V)	$1.05E_{max} \cdot N_s$	$E_{min} \cdot N_s$
Voltage at the end of the exponential zone V_{exp} (V)	$1.05E_{max} \cdot N_s$	$E_{min} \cdot N_s$
Capacity at the end of the exponential zone Q_{exp} (Ah)	Q_{rated}	0
Voltage at the end of the nominal zone V_{nom} (V)	$1.05E_{max} \cdot N_s$	$E_{min} \cdot N_s$
Capacity at the end of the nominal zone Q_{nom} (Ah)	Q_{rated}	0
Maximum Capacity Q_{max} (Ah)	$1.1Q_{rated}$	Q_{rated}
Internal Resistance R (Ω)	MAX (R_{DOD})	MIN (R_{DOD})

As it can be seen from Table 5.2, the bounds of parameters Q_{exp} and Q_{nom} are the same, this also holds true for the parameters V_{full}, V_{exp}, and V_{nom}. Special constraints should be imposed on these parameters to ensure the algorithm rejects unreasonable values being assigned into the battery model. The constraints imposed on these parameters are expressed in the following inequalities:

$$V_{full} > V_{exp} > V_{nom} > V_{min} \; and \; 0 < Q_{exp} < Q_{nom} < Q_{rated} \tag{5.9}$$

where V_{min} is the minimum battery pack voltage that is given as $E_{min} \cdot N_s$. Some of these parameters are shown schematically in Fig. 5.2.

5.4 Simulation Results

Simulations have been conducted using 500 iterations and a population of 100 particles/chromosomes for the GA, PSO, and QPSO parameter estimation techniques. A set of PSO algorithm parameters $\omega = 0.6$, $c_1 = 1.7$ and $c_2 = 1.7$ mentioned in [289] are used in the simulations. This PSO parameters setting is shown to exhibit fast convergence and high robustness [289]. Table 5.3 compares the estimated Tremblay's model parameters generated by Tremblay's, GA, PSO, and QPSO parameter estimation

techniques. The performances of the GA, PSO, and QPSO parameter estimation techniques are assessed in terms of RWRSS value, which is also presented in Table 5.3. The performance graph of the GA, PSO, and QPSO parameter estimation techniques are presented in Fig. 5.3. The results shown in Fig. 5.4 compare the static capacity test curve and the simulated discharge curves estimated by Tremblay's, GA, PSO, and QPSO parameter estimation techniques.

Table 5.3: RWRSS and model parameters obtained using the GA, PSO and QPSO parameter estimation algorithms.

Model Parameter	**Tremblay**	**GA**	**PSO**	**QPSO**
RWRSS	172.1512	21.7588	19.1298	20.2075
Fully Charged Voltage V_{full} (V)	398.40	418.32	404.43	414.88
Voltage at the end of the exponential zone V_{exp} (V)	376.80	360.36	332.09	354.33
Capacity at the end of the exponential zone Q_{exp} (Ah)	10.67	22.39	38.42	27.13
Nominal Voltage V_{nom} (V)	331.00	317.81	300.36	319.82
Capacity at nominal voltage Q_{nom} (Ah)	42.12	41.70	43.93	41.17
Maximum Capacity Q_{max} (Ah)	47.25	49.50	46.41	47.43
Internal Resistance R (Ω)	0.1000	0.1270	0.1340	0.1344

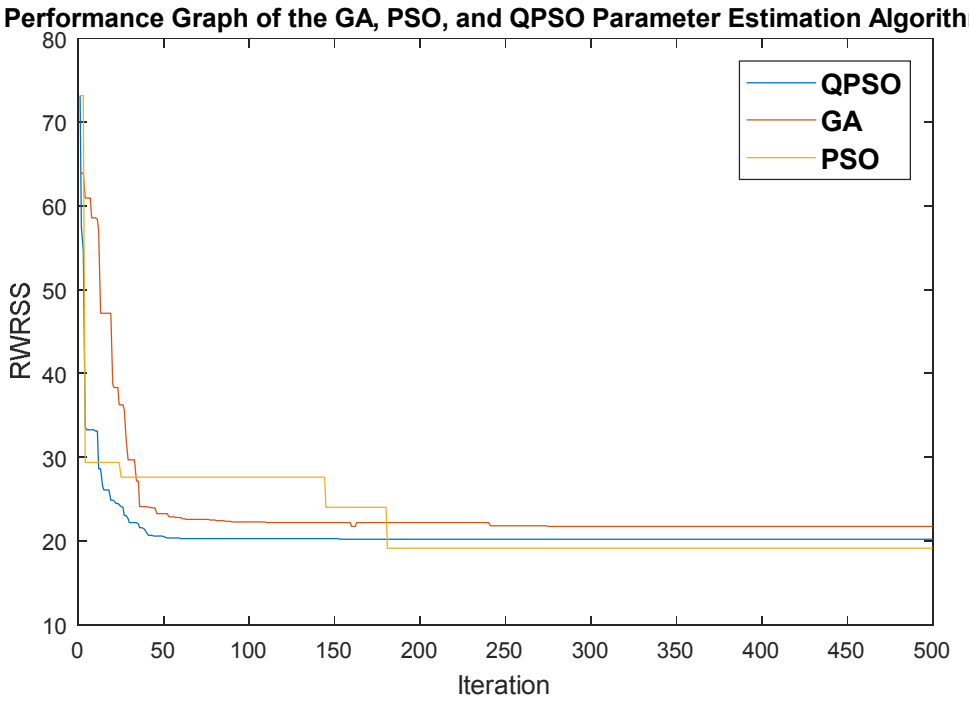

Fig. 5.3: Performance graph of the GA, PSO, and QPSO parameter estimation algorithms.

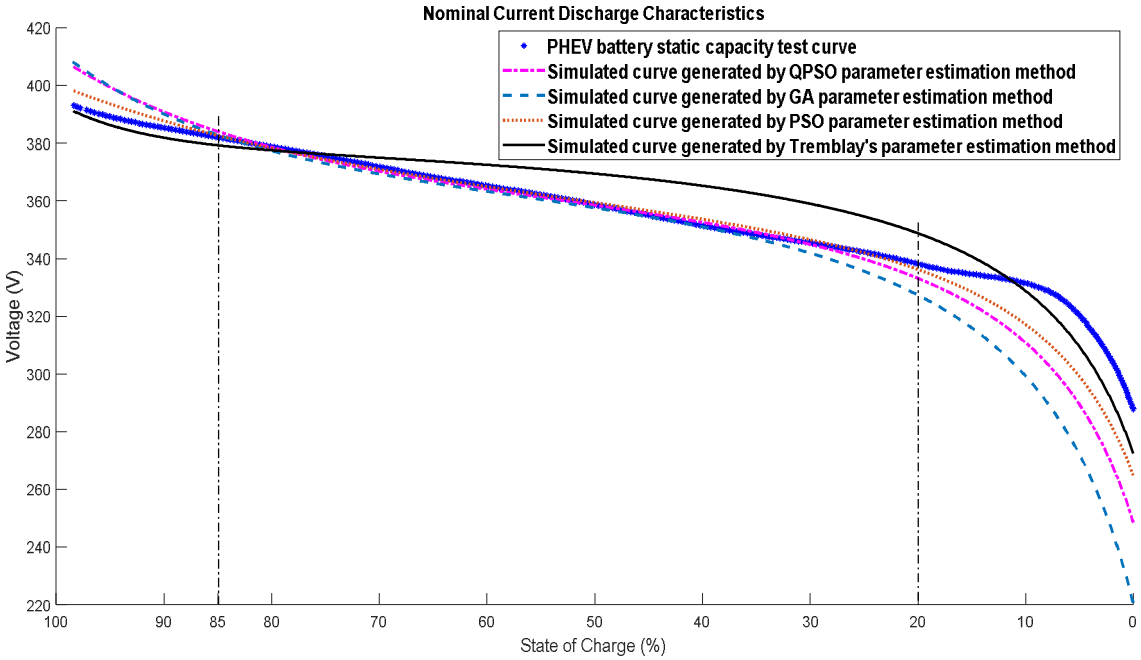

Fig. 5.4: A comparison between the static capacity test curve and the simulated curves generated by Tremblay's, GA, PSO, and QPSO parameter estimation techniques.

The results shown in Fig. 5.4 are of significance as it can be seen that the GA, PSO, and QPSO parameter estimation techniques generate similar discharge characteristics that are

almost indistinguishable in the operating SOC range for the PHEV battery. These discharge curves provide a better model fit than the discharge characteristic estimated by Tremblay's parameter estimation approach. From Table 5.3, the RWRSS values for the GA, the PSO, and the QPSO are slightly different. It can be inferred that plausible global optimal solutions have been achieved by the three methods. The beginning and the end of the static capacity test curve is not well approximated by any of the four methods. This is not a major concern since these sections are beyond the scope of interest. These sections represent a difficult operating zone for vehicle propulsion since the voltage drops quite rapidly.

From Fig. 5.3, it can be seen that the QPSO approach converges faster to its final RWRSS value with a similar accuracy level than the GA and the PSO approaches. The estimation process will accelerate using the QPSO algorithm and fewer iterations will be required to reach the final solution when compared to that obtained using the GA and the PSO methods. The QPSO approach also provides an advantage over the GA and the PSO algorithms that there is only one tuning parameter β involved in the QPSO algorithm, as shown in (5.6), thus the tuning effort is significantly reduced when compared to the GA and the PSO approaches.

5.5 Conclusion

This chapter uses the QPSO parameter estimation technique to estimate Tremblay's battery model parameters. The parameterization of Tremblay's battery model has been formulated as a multivariable optimization problem that can be solved using the QPSO parameter estimation technique. The simulated discharge curve generated by the QPSO approach is compared with those obtained using the GA and PSO approaches. The QPSO parameter estimation technique generates solutions with similar accuracy levels when compared to those obtained using the GA and PSO parameter estimation techniques, and converges to the final solution with fewer iterations than the other methods. This highlights the potential enhancement of using the QPSO algorithm to parameterize Tremblay's model as the QPSO algorithm only requires one parameter β to be tuned.

Chapter 6
Modelling of the Grid-Tied Photovoltaic System with Plug-in Hybrid Electric Vehicles as Energy Storage

6.1 Introduction

The variability and intermittency of photovoltaic (PV) generation impose some challenges on distribution networks. One challenge is that the time when peak loads happen is usually inconsistent with the period when solar energy is sufficient. This can be mitigated by integration of a battery energy storage system into the networks. The excess solar energy could be stored in a plug-in hybrid electric vehicle (PHEV) battery during the daytime, when solar power is abundant. PHEV batteries could also be charged from the grid when solar energy is not available at night. Considering these two charging scenarios, two modes of operation for the charging controller are developed, namely the SOC reference tracking and power reference tracking modes. These two modes of operation will be further illustrated in this chapter.

This chapter develops a system simulation model for the grid-connected PV system with a PHEV as energy storage. This simulation model is developed to implement the PHEV charging strategies in operation of a grid-connected PV system under different solar irradiance profiles and a certain load profile. Initially, a review of three changing levels for PHEV batteries will be presented. This is followed by the design of the grid-connected PV system. The charging strategy for the PHEV battery will be developed and explained in full detail. Finally, the simulation results under both clear sky and cloudy sky irradiance profiles are presented to validate the effectiveness of the charging strategies.

6.2 Charging Level

Charging level is an indication of charging power from a charging station or an outlet. There are three charging levels for charging EVs in Australia. Table 6.1 shows the three

charging levels in Australia. Level 1 charging is dedicated for home charging with slow charging current, where EVs are parked at a garage and charged with a conventional outlet during the night. This charging level is suitable for an EV with small battery capacity and long charging duration. Level 2 charging requires a dedicated electric vehicle supply equipment (EVSE) to connect PHEV batteries directly to the electrical power grid. The vehicle must have an On Board Charger (OBC) that communicates with the EVSE regarding when the PHEV battery starts or stops charging [290]. It is the primary charging level for both private and public charging, and the level 2 charger is also recommended by Electric Vehicles and the Environment (EVE) Australia for home installations as this charger is worth the convenience and time for charging [291]. Level 2 AC charging can be further classified into slow charging (240 V 3.3 kW-7.4 kW) and fast charging (415V 11 kW-22 kW) based on voltage level. Level 3 DC fast charging requires an off-board charger since the charging power is significantly higher than Level 1 and Level 2. Level 3 is applicable for commercial use in parking lots, shopping centres, hotels, petrol stations, and other commercial applications [292]. The charging station for Level 3 fast charging can be powered by either a power distribution grid or a solar system [293].

Table 6.1: Charging levels in Australia [291], [292], [294].

Charger Level	Energy Supply Interface	Electric Car Distance
Level 1 AC Slow 240 V 1.4 kW	Conventional outlet On-board	7.5-15 km/h
Level 2 AC Slow 240V 3.3 kW-7.4 kW	Dedicated EVSE On-board	18-40 km/h
Level 2 AC Fast 415V 11 kW-22 kW	Dedicated EVSE On-board	60-15 km/h
Level 3 DC Fast 50 kW-120 kW	Dedicated EVSE Off-board	70 km/10 mins or 420 km/h

6.3 System Design

This whole simulation model is developed by substantially modifying and extending the *Detailed Model of a 100-kW Grid-Connected PV Array* (opened by typing

'power_PVarray_grid_det') [295] and the *Supercapacitor Model* (opened by typing 'parallel_battery_SC_boost_converter') [296] in *Matlab/SimPowerSystems*. This simulation model is developed to demonstrate the performance of the PV array under varying irradiance and temperature profiles and validate the effectiveness of the charging strategies for the PHEV battery. The PHEV battery is the same as the battery investigated in Chapter 5. The battery specifications have been tabulated in Table 5.1. The parameters of battery model are modified according to the estimation results in Chapter 5 using the PSO approach. As the results obtained using the PSO approach are shown to have the smallest RWRSS value when compared to the GA and PSO parameter estimation techniques.

The grid-connected PV system consists of a 10 kW PV array with its associated SEPIC converter, a PHEV battery with its associated bidirectional buck-boost converter, a 3-level 3-phase VSI with its LC filter, and a 3-phase residential load. The residential load is designed to have a maximum power of 7 kW at 0.85 PF lagging with its power varying according to the load profile shown in Fig. 6.1.

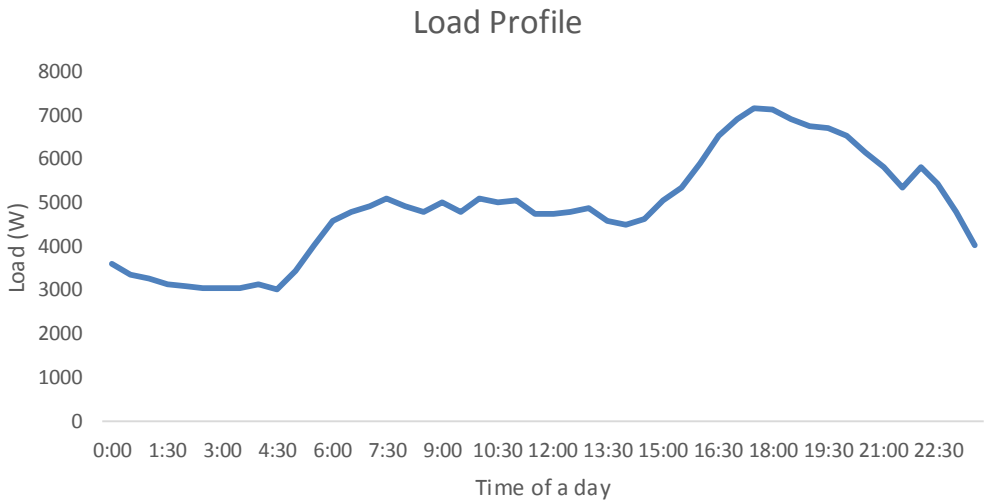

Fig. 6.1: A typical residential load profile.

The PV array model is developed by extending the PV module model for a BP 380 PV module described in Chapter 2. The PV array is constructed using the BP 380 PV panel with its datasheet parameters tabulated in Table 2.2. The parameters of the PV module model are estimated by the GA parameter estimation technique described in Section 2.6.5 and are presented in Table 2.4. A 10 kW SEPIC converter is designed to interface with

the PV array. The SEPIC converter is assumed to always operate in CCM with a switching frequency of 20 kHz. The MPPT controller implements the IC MPPT technique with a time window of 200 μs to track the MPP of the PV array in real-time. The default value of the duty cycle for the MPPT controller is 0.5. A 3 level 3-phase VSI is connected between the DC link and the AC networks to convert the 700 V DC link voltage to the 415 V AC grid voltage. The PHEV battery is connected to the DC link via a 3.3 kW bidirectional buck-boost converter. A bidirectional converter is used to boost the low PHEV battery voltage to the high DC link voltage with bidirectional power flow capabilities. A constant DC voltage source is connected at the high voltage side of the bidirectional buck-boost converter to serve as the dumb load for battery discharge. The power rating of the bidirectional buck-boost converter is limited to 3.3 kW. Fig. 6.2 shows the system architecture of the grid-connected PV system with PHEV battery energy storage.

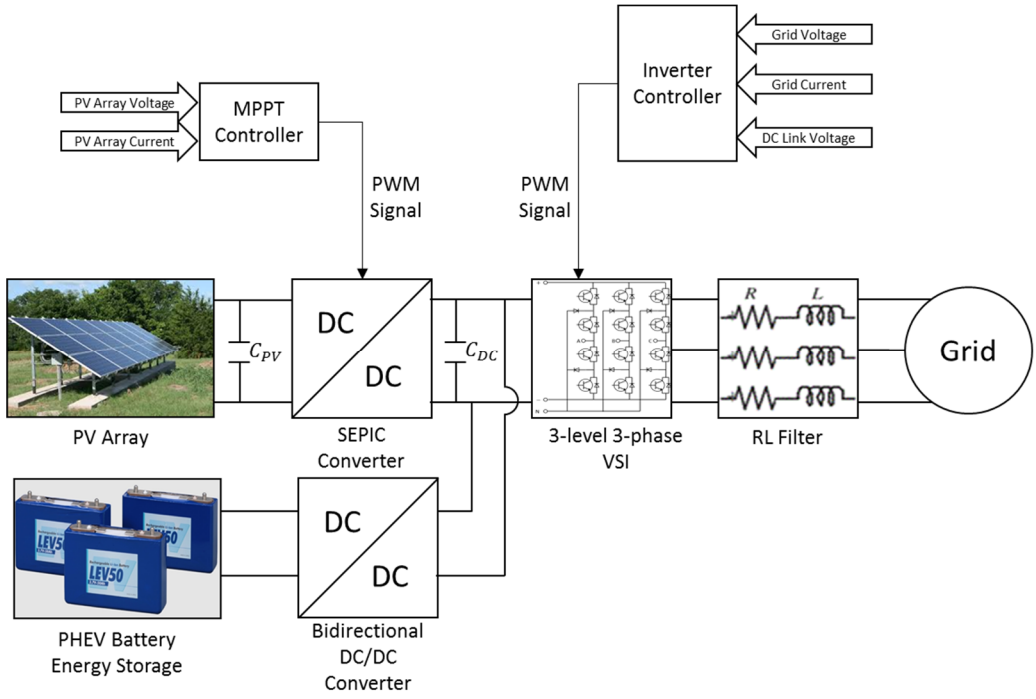

Fig. 6.2: System architecture of the grid-connected PV system with PHEV battery energy storage.

The charging controller is implemented to control the charging and discharging operation of the PHEV battery. The calculations in sizing the PV array, SEPIC converter, and bidirectional converter are attached in Appendix B.

Fig. 6.3 shows the whole simulation model for the grid-connected PV system with a PHEV as energy storage implemented in *Matlab/SimPowerSystems* environment.

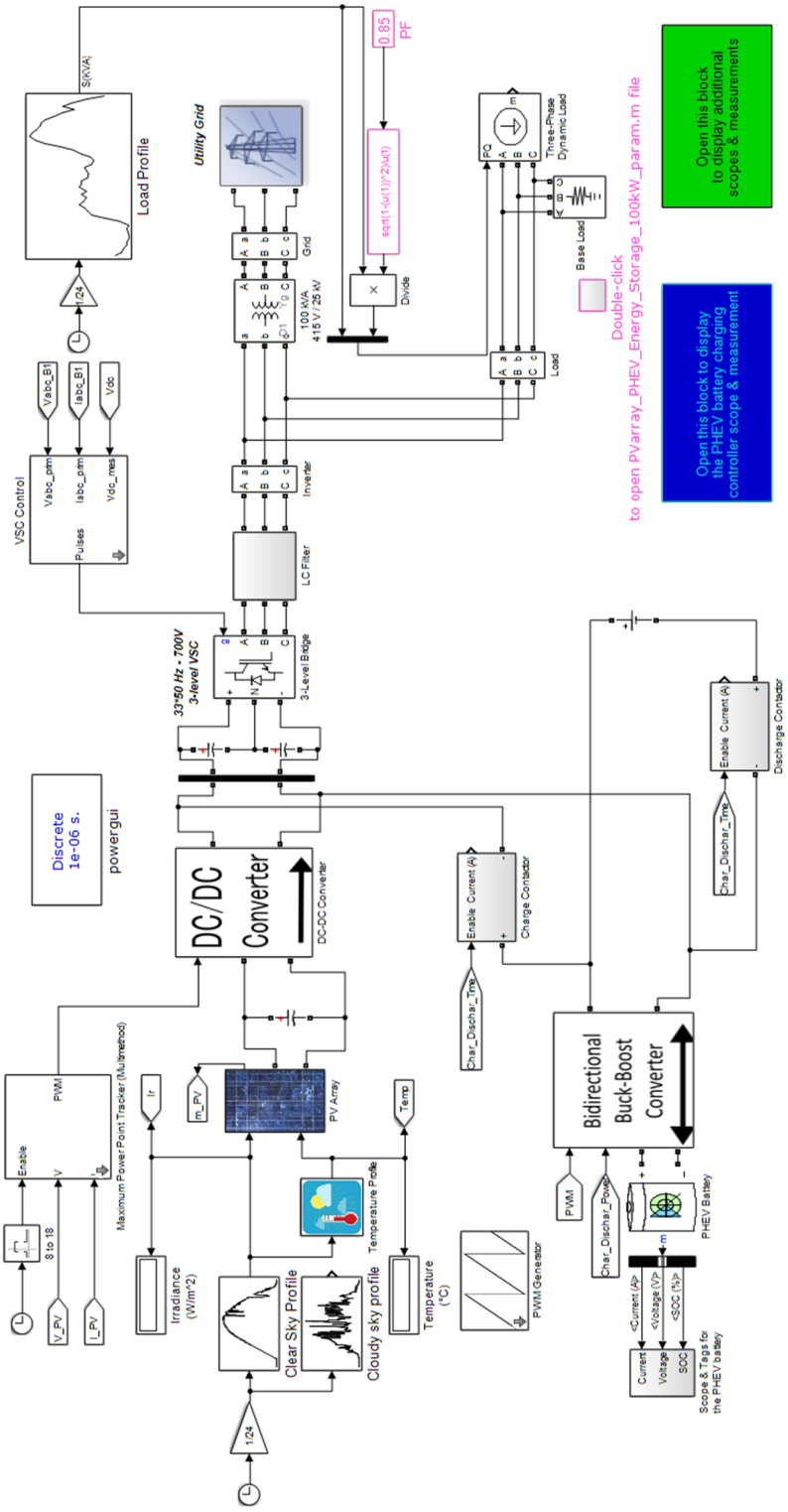

Fig. 6.3: Simulation model of the grid-connected PV system with a PHEV battery as energy storage.

6.4 Solar Irradiance and Temperature Profiles

The effects of different solar irradiance and temperature conditions on the performance of the PV array are analysed based on two different solar irradiance profiles, namely clear sky and cloudy sky profiles. These two irradiance profiles illustrate irradiance variations over the course of a day and will be used to represent the intermittent environmental conditions for the PV array. Clear sky and cloudy sky profiles are sourced from the Bureau of Meteorology (BOM) [297] at the Cape Grim station on the 1st and 3rd, May, 2015, respectively. The clear sky and cloudy sky irradiance profiles are shown in Fig. 6.4 and Fig. 6.5, respectively. The clear sky profile shows less fluctuations when compared to the cloudy sky profile, in which the irradiance varies significantly with rapid ramp rates. The highly fluctuating pattern of the cloudy sky profile is largely attributed to frequent cloud passing, because it causes drastic variations in solar insolation. From these two irradiance profiles, the solar power available period is defined as the time interval from 7:00 AM to 5:00 PM with an aggregate of 10 hours in a day in the following analyses. This solar power available period will determine the mode of operation for the charging controller, which in turns affects the charging power for the battery.

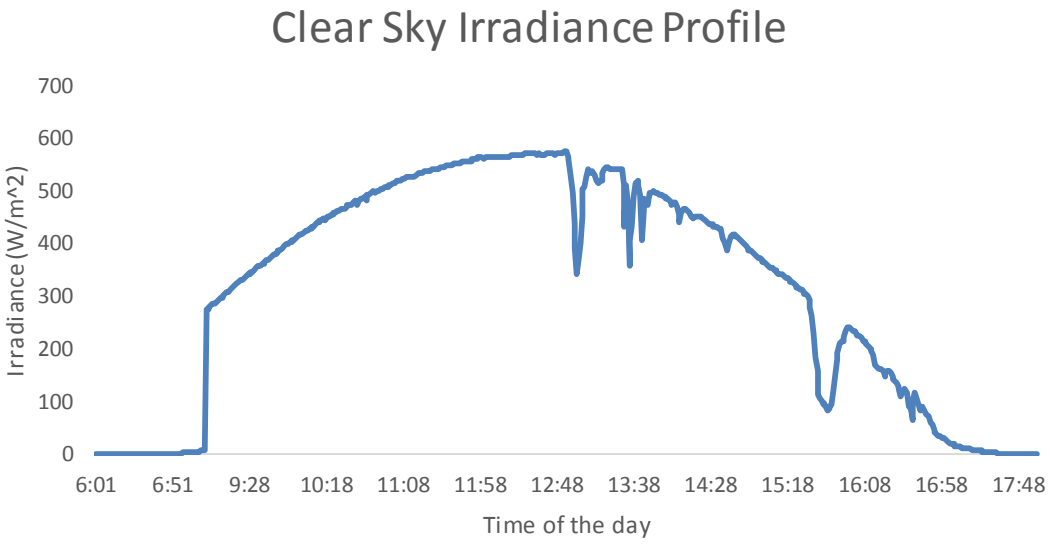

Fig. 6.4: Clear sky solar irradiance profile on 1st May 2015.

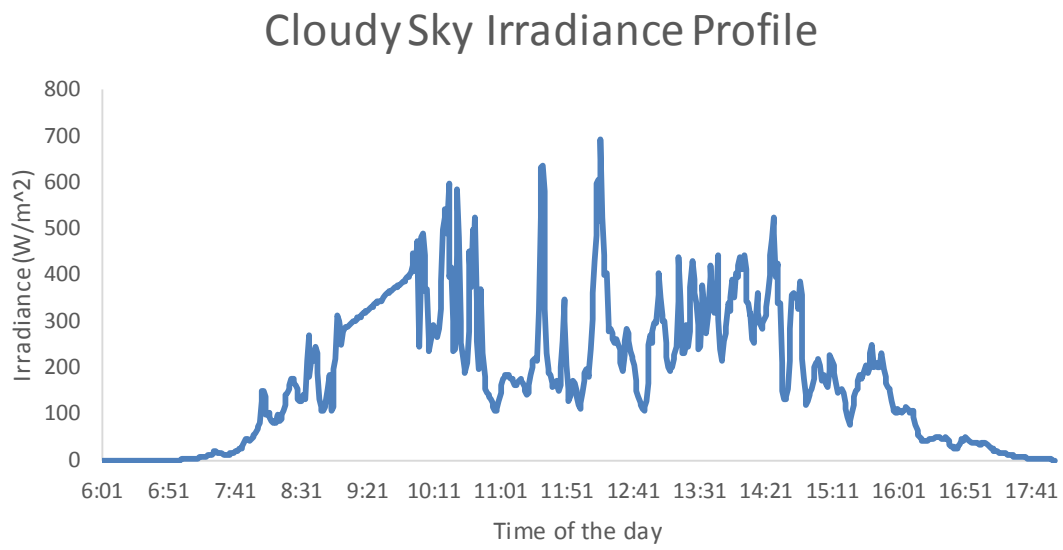

Fig. 6.5: Cloudy sky irradiance profile on 3rd May 2015.

Due to lack of real-time temperature records, real-time temperature profiles are designed to follow the same trend with the irradiance profiles using an approximate method that employs relative scaling factors. The following simulations assume that the maximum and minimum temperatures under the clear and cloudy sky profiles are 15.2 ℃ and 8 ℃, respectively. The corresponding temperature data can be calculated using the formulae as follows [13]:

$$Temp = \frac{(Ir - Ir_{\min}) \cdot (Temp_{\max} - Temp_{\min})}{Ir_{\max} - Ir_{\min}} + Temp_{\min} \tag{6.1}$$

where $Temp_{max}$ and $Temp_{min}$ are the maximum and minimum temperatures, respectively. Ir_{max} and Ir_{min} are the maximum and minimum values of solar irradiance in a solar irradiance profile, respectively. $Temp$ and Ir represent the real-time temperature and irradiance data. The calculated temperature data under clear sky and cloudy sky profiles is shown in Fig. 6.9 and Fig. 6.14, respectively.

6.5 Charging Strategies

In charging PHEV there are a number of uncertainties which must be considered such as when the PHEV will arrive home and what SOC level the battery has. Due to unavailability of SOC data about PHEV charging patterns, random SOC values in the

SOC range are assumed when the PHEV arrives and leaves home. The SOC range of the PHEV battery is limited between 20% and 85% to satisfy the battery life cycle requirements and result in a good vehicle drive performance. 30 minutes of stabilizing time is employed between each charging and discharging cycle. This stabilizing time is used for the vehicle to plug into a convenience outlet after arriving home and battery cooling after charging.

In Fig. 6.1, it can be seen that the residential load peaks from 5:30 pm to 10:00 pm in the evening each day. A study was carried out in England to investigate vehicle drivers charging behaviours [23]. This study found that private users usually charge their cars during the evening peak period, which can cause overloading and early degradation of distribution infrastructures. To avoid charging during the peak period, charging is delayed until 10:00 pm when the off-peak period starts. When the vehicle returns to the residence during the peak period, the vehicle is plugged into the network without charging. The charging power reference is set to zero and the SOC reference is the same as the actual SOC. This strategy coordinates vehicle charging to avoid coincidence with the peak period and prevent any unwanted load peaks on the distribution networks.

The following assumptions and limitations are used to develop the charging strategies:

- The PHEV battery only consumes active power when charging.
- The SOC range of the PHEV battery is between 20% and 85%.
- The solar power available time is between 7:00 AM to 5:00 PM in a day.
- A 30-minute interval is applied between each charging and discharging cycle.
- The vehicle does not charge during the evening load peak period.

Fig. 6.6 shows the flowchart of the overall control and charging strategies for the charging controller. In general terms, PHEV battery starts to charge after 30 minutes when the vehicle arrives home. In the daytime when the vehicle plug-in time is within the solar power available time, the vehicle is charged from the PV array in the power reference tracking mode. At night when solar power is unavailable, the vehicle is charged from the grid in the SOC reference tracking mode.

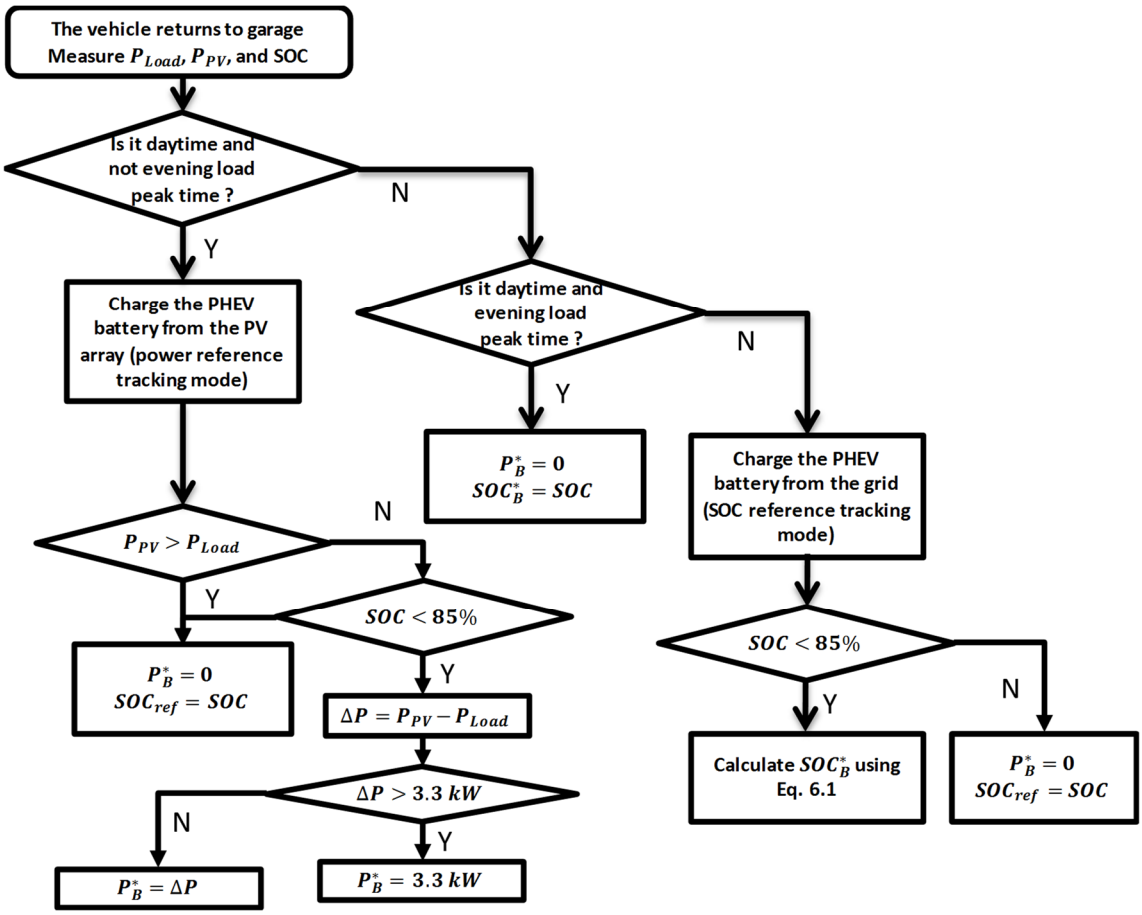

Fig. 6.6: Flowchart of the control and charging strategies for the charging controller.

6.5.1 SOC reference tracking

In the SOC reference tracking mode, the actual SOC of the battery follows a pre-set SOC reference. This charging mode is usually used for charging PHEV batteries at night using the grid power. In general, the SOC reference is a piecewise linear function that made up of several step and ramp signals with respect to the time of a day. It is assumed in the following simulations that the SOC reference is linearly increasing with respect to time while the vehicle is charging, whereas the SOC reference is linearly decreasing while the vehicle is discharging.

The actual SOC of the PHEV battery follows a linear, downward-sloping SOC reference line when discharging. The discharging SOC reference ($SOC^*_{B,\ discharge}$) can be determined using:

$$SOC^{*}_{\text{B, discharge}} = \frac{\left(t - t_{\text{end, discharge}}\right)\cdot\left(SOC_{\text{start, discharge}} - SOC_{\text{end, discharge}}\right)}{t_{\text{start, discharge}} - t_{\text{end, discharge}}} + SOC_{\text{end, discharge}} \quad (6.2)$$

where t stands for the time of a day, and $t_{start,\ discharge}$ and $t_{end,\ discharge}$ symbolise the times at the beginning and the end of a discharge cycle, respectively. $SOC_{start,\ discharge}$ and $SOC_{end,\ discharge}$ represent the SOC of the PHEV battery at the start and the end of a discharge cycle, respectively.

When the vehicle is charging from the grid, the actual SOC of the PHEV battery follows a linear, upward-sloping SOC reference line. When the vehicle is charging using the grid power, the charging SOC reference ($SOC^{*}_{B,\ charge}$) can be determined using:

$$SOC^{*}_{\text{B, charge}} = \frac{\left(t - t_{\text{end, charge}}\right)\cdot\left(SOC_{\text{arrival}} - SOC_{\text{end, charge}}\right)}{t_{\text{arrival}} - t_{\text{end, charge}}} + SOC_{\text{end, charge}} \quad (6.3)$$

where $SOC_{end,\ charge}$ and $SOC_{arrival}$ symbolises the SOC required at the end of a charge cycle and the actual SOC of the battery shortly after the vehicle returns to garage, respectively. $t_{arrival}$ and $t_{end,\ charge}$ represent the arrival time of the vehicle and the time when the vehicle finishes charging, respectively.

6.5.2 Power reference tracking

The power reference tracking strategy allows the charging power of the PHEV battery follows the power reference determined by the PV array power, load power and the SOC of the PHEV battery. The PHEV battery absorbs power under the operational range of the PHEV battery's SOC when the PV array generates more power than the load demand. If the PV array power is smaller than or equal to the load power. The charging power reference is set to 0 and the PHEV battery does not charge from the networks. If the PV array power is higher than the load power, the power difference between the PV array and local load will be calculated. If the power difference is smaller than 3.3 kW, the charging power reference will be set to the power difference. The charging power reference is limited to 3.3 kW when the power difference is higher than 3.3 kW. This is due to the factor that the rating of the on-board charger for the Chevy volt is limited to 3.3 kW to minimize the cost of the on-board charger [283].

6.6 Case Studies

Fig. 6.7 illustrates the SOC scenario for an example day used in the following simulations. This scenario could represent a retired household or a working household on the weekend. This SOC profile consists of two two-hour driving trips in the day, namely the morning and afternoon trips. The vehicle starts the morning trip at 8:00 AM with an initial SOC of 85%. Then, the driver drives the vehicle on the road until 10:00 AM. The vehicle arrives back home with 20% of its capacity remaining at 10:00 AM to start the daytime charging. The vehicle battery is charged using the PV array power in the power reference tracking mode. After that, the vehicle starts the afternoon trip and returns home again with 20% of its capacity remaining at around 5:30 PM. The charging of the vehicle is delayed until 10:00 PM to avoid the evening load peak. The night charging starts at 10:00 PM and finishes in the next day morning in the SOC reference tracking mode. The PHEV battery is required to charge up to 85% of its capacity at the end of the night charging.

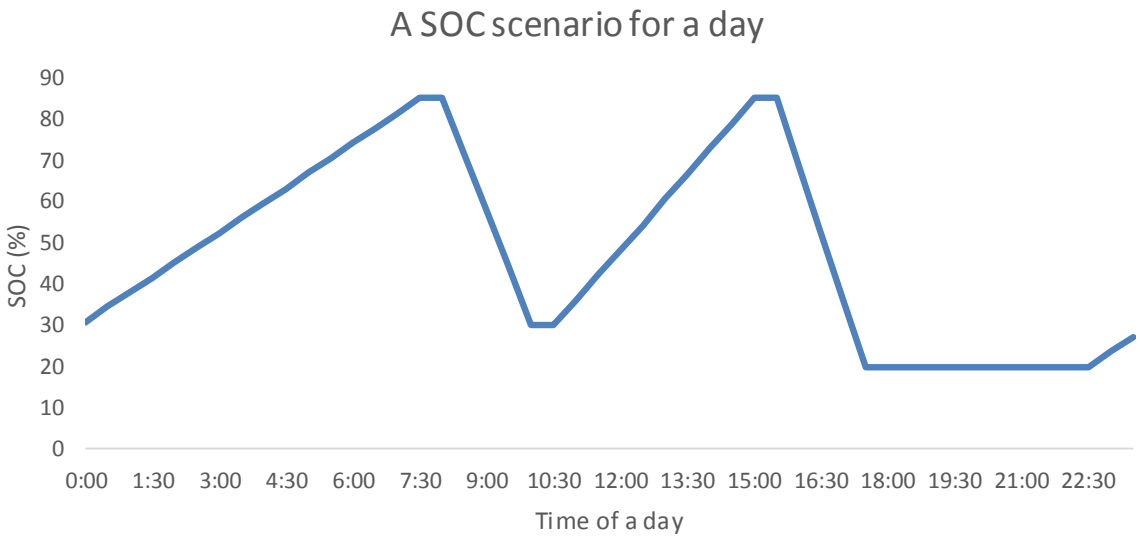

Fig. 6.7: The SOC scenario for the example day.

Fig. 6.8 shows the corresponding charging/discharging state profile for the example day used in the following simulations. The value 1 represents the battery charging whereas the value -1 represents the battery discharging. When the charging/discharging state is equal to zero, the charging controller is inactive and the battery does not charge or discharge. In other words, the reference SOC trajectory follows the actual SOC trajectory and the charging power is set to zero.

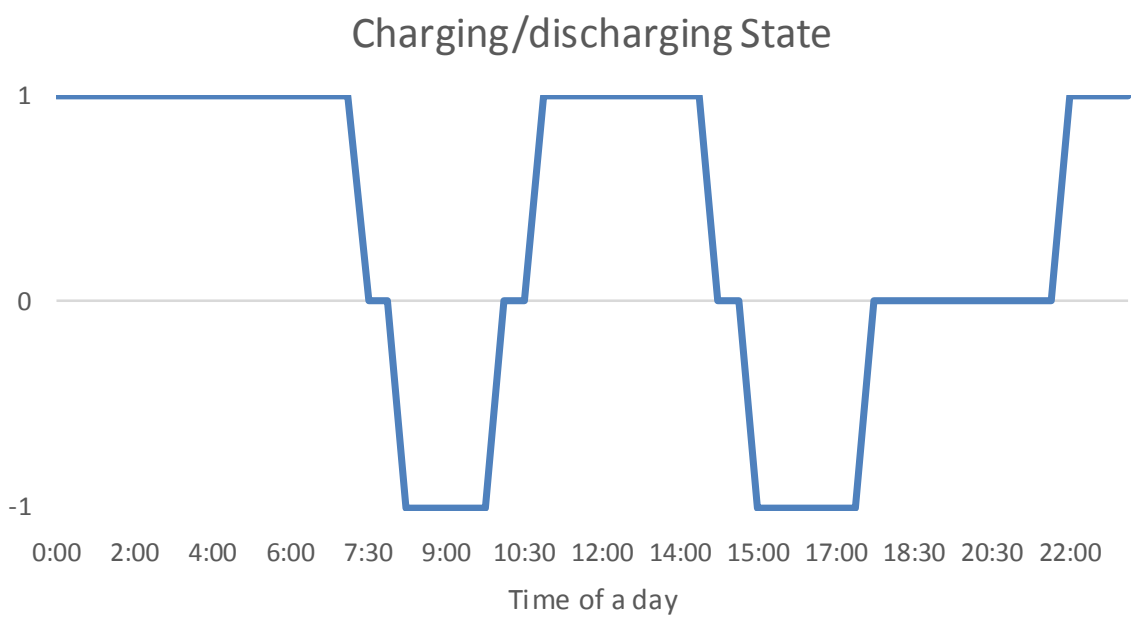

Fig. 6.8: The charging/discharging state profile for the example day.

The objectives of the charging strategy are that the PHEV battery can be charged in the power reference tracking mode when the vehicle is charging during the solar power available time. During the night time when solar power is not available, the PHEV battery is charged from the grid in the SOC reference tracking mode. The actual SOC of the PHEV battery follows a pre-set SOC reference during the night charging. The charging strategies are developed to fulfil the certain SOC level requirements required at specific times of a day under the following assumptions in the case studies:

- Two two-hour driving trips are assumed in the day.
- Fixed vehicle arrival times and SOC levels at arrival and departure are assumed.
- An initial SOC of 85% is required at the start of the morning trip.
- A minimum SOC of 50% is required before the vehicle leaves home.
- The battery is required to have at least 50% of its capacity remaining when the vehicle leaves home.

The simulations were carried out in the following two case studies. The two case studies will be described in the following two subsections and show the system performances under the clear sky and cloudy sky irradiance profiles, respectively. The simulations were conducted with a sampling time of 1 μs and a total simulation time of 24 seconds. The 24 seconds simulation time represents the full 24 hours of a day. It starts at 12 midnight

(0 hour) at the beginning of the current day and finishes at 12 midnight (24 hour) at the beginning of the next day.

6.6.1 Case A - System performance with the clear sky irradiance profile

The solar irradiance and temperature data in the clear sky profile are shown in Fig. 6.9. It can be seen that the solar irradiance available period starts from approximately 7:00 AM to 5:00 PM as shown in Fig. 6.9. The temperature data in the clear day is calculated using (6.1) according to the irradiance data. The temperature is highly unlikely to be maintained at the lowest value throughout the night and early morning. From this perspective, the temperature conditions are not well approximated using (6.1). However, as the temperature during the night and early morning has almost no impact on the PV array performance, this is not a major concern.

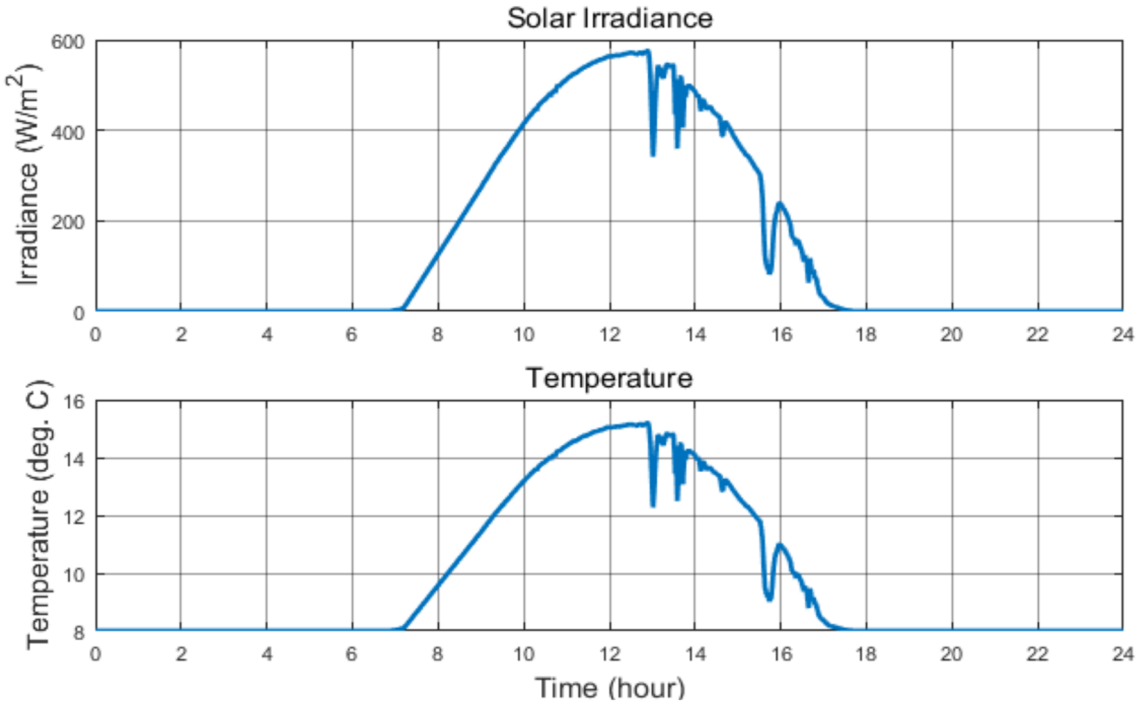

Fig. 6.9: Irradiance and temperature data in the clear sky profile.

Fig. 6.10 shows the PV array voltage, current and power and the duty cycle varying in the example day under the clear sky profile. It can be seen that the output power of the PV array is a direct correlation to the irradiance profile, but is also affected by the changes in the duty cycle. The duty cycle starts from 0.5 and gradually increases to around 0.63 in the afternoon. When the PV power reduces to approximately zero at 17:00 PM, the

duty cycle is still maintained at 0.63 in a short time, and suddenly reduces to zero at around 17:40 PM. This may be results from the delay in the response of the MPPT controller. The duty cycle is set back to 0.5 at 18:00 PM when there is no PV power generation.

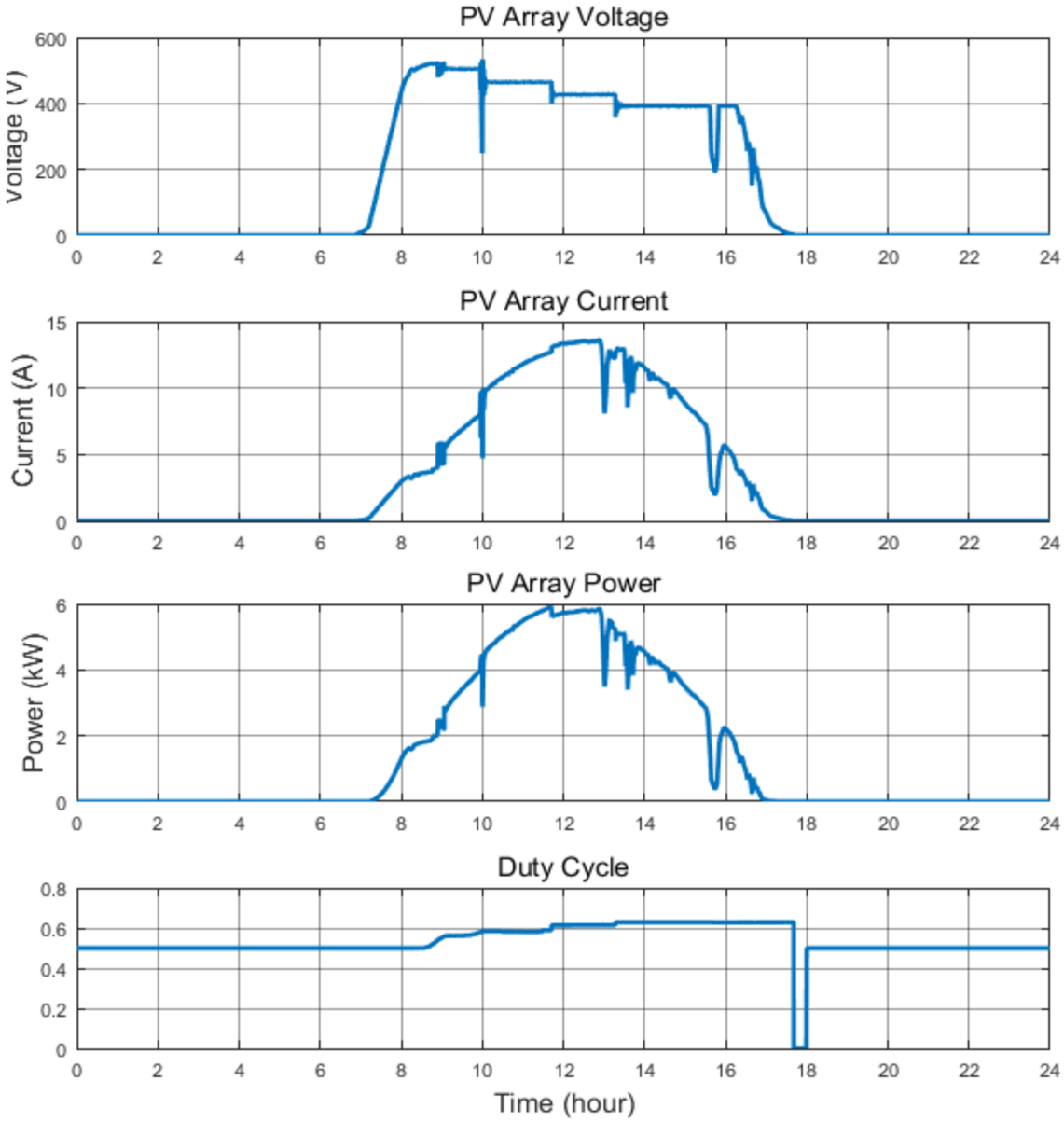

Fig. 6.10: PV array voltage, current and power and the duty cycle under the clear sky profile.

Fig. 6.11 shows the charging/discharging power and the power difference between the PV array and the local load. According to the charging/discharging state profile shown in Fig. 6.8, the discharging power is negative when the battery discharges and positive when the battery charges. The charging strategy works as expected during the night charging

when the vehicle is charged from the grid. When the charging controller works in the SOC reference mode, the battery is charged in such a way that the charging power switches rapidly between 3.3 kW and 0 to ensure that the actual SOC tracks the reference SOC with zero steady-state errors. At two specific times of the example day, which are 10:00 AM and 5:30 PM, there are power spikes happened at these time instants due to the transitions from the battery discharge to the battery charge. From 10:30 AM to 2:30 PM, the charging controller works in the power reference mode and the charging power follows the power difference between the PV array and local load.

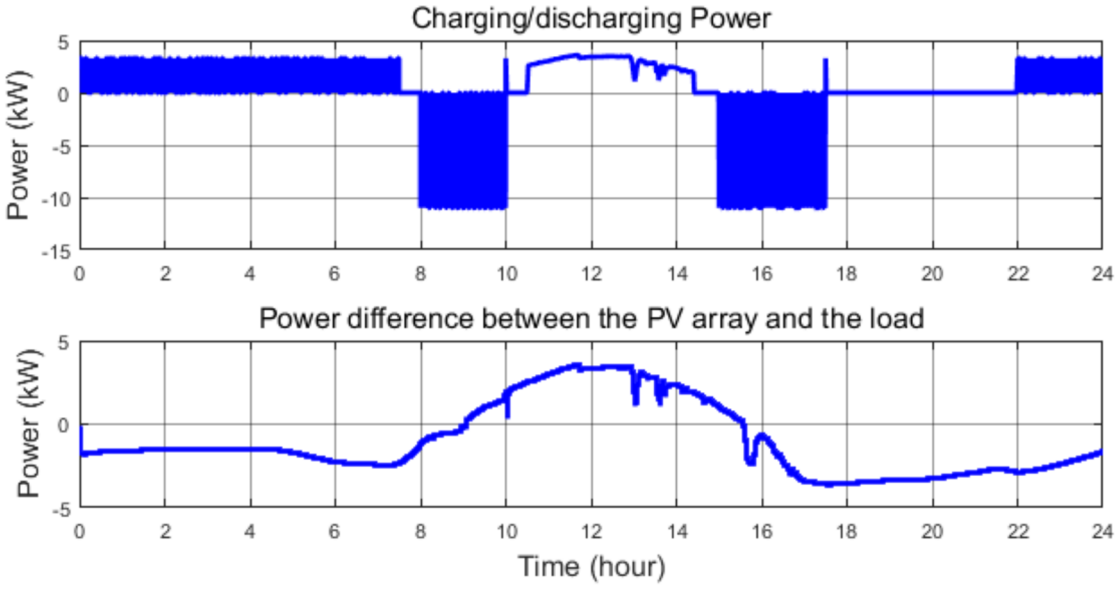

Fig. 6.11: Charging and discharging state, charging/discharging power, and the power difference between the PV array and the load under the clear sky irradiance profile.

Fig. 6.12 shows the battery current and voltage and actual SOC and reference SOC signals under the clear sky irradiance profile. It is noted that the actual SOC tracks the reference SOC well during the two battery discharging cycles. During the night charging, the actual SOC is increased to track the SOC reference with zero steady-state errors. From 10:30 AM to 2:30 PM, the actual SOC deviates slightly from the SOC reference as the charging controller works in the power reference mode and the charging power reference is set to the power difference between the PV array and local load as shown in Fig. 6.11. The battery voltage is increasing during the battery charge cycles and decreasing during the battery discharge cycles.

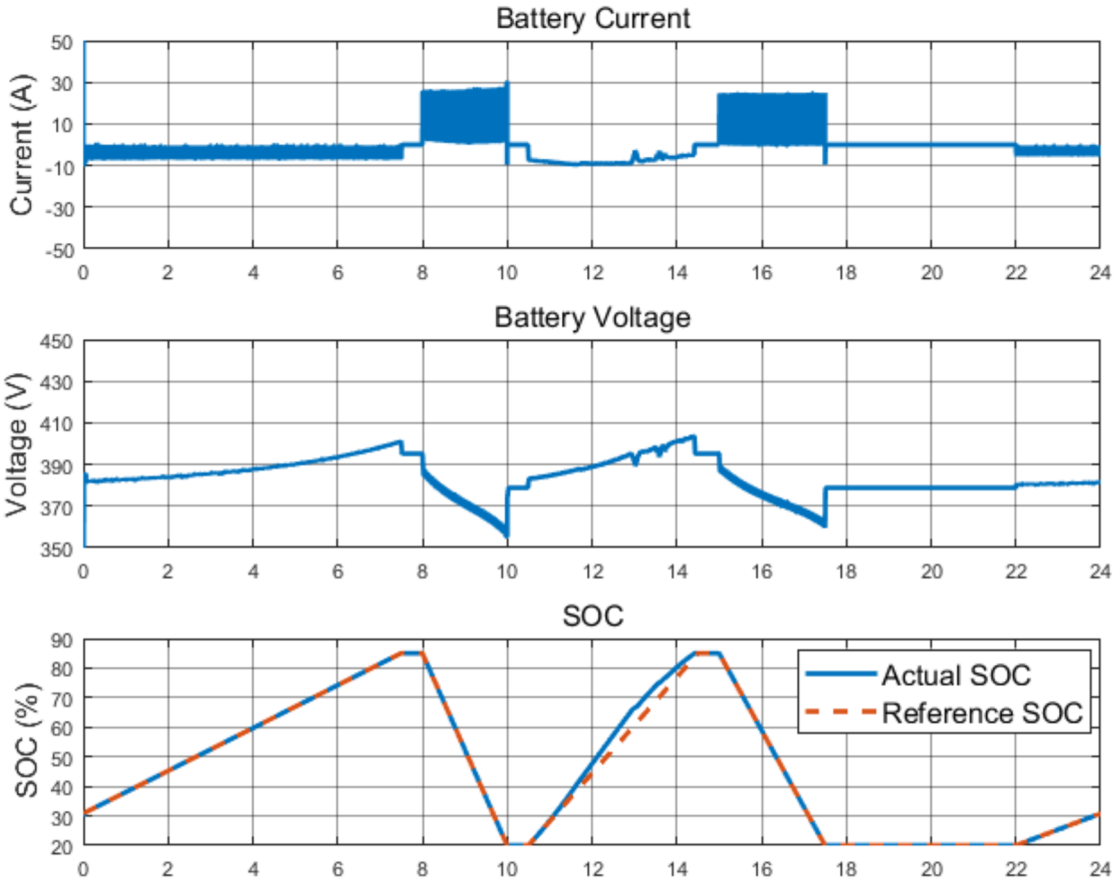

Fig. 6.12: Battery current, battery voltage, battery's actual SOC and battery's reference SOC under the clear sky profile.

Fig. 6.13 shows the DC link voltage, current and power under the clear sky irradiance profile. It can be seen that the DC link voltage is regulated at 700 V with some transients and spikes at some specific times of the example day. This is largely due to the transients between battery charging and discharging and switching on and off the MPPT controller based on the solar power available period. It is expected that the PV array current is proportional to the PV array voltage for most of the example day. The DC link current and power are larger than zero during most of the solar power available period. This is because that the PV array generates sufficient solar energy that used for charging the vehicle under the clear sky irradiance profile.

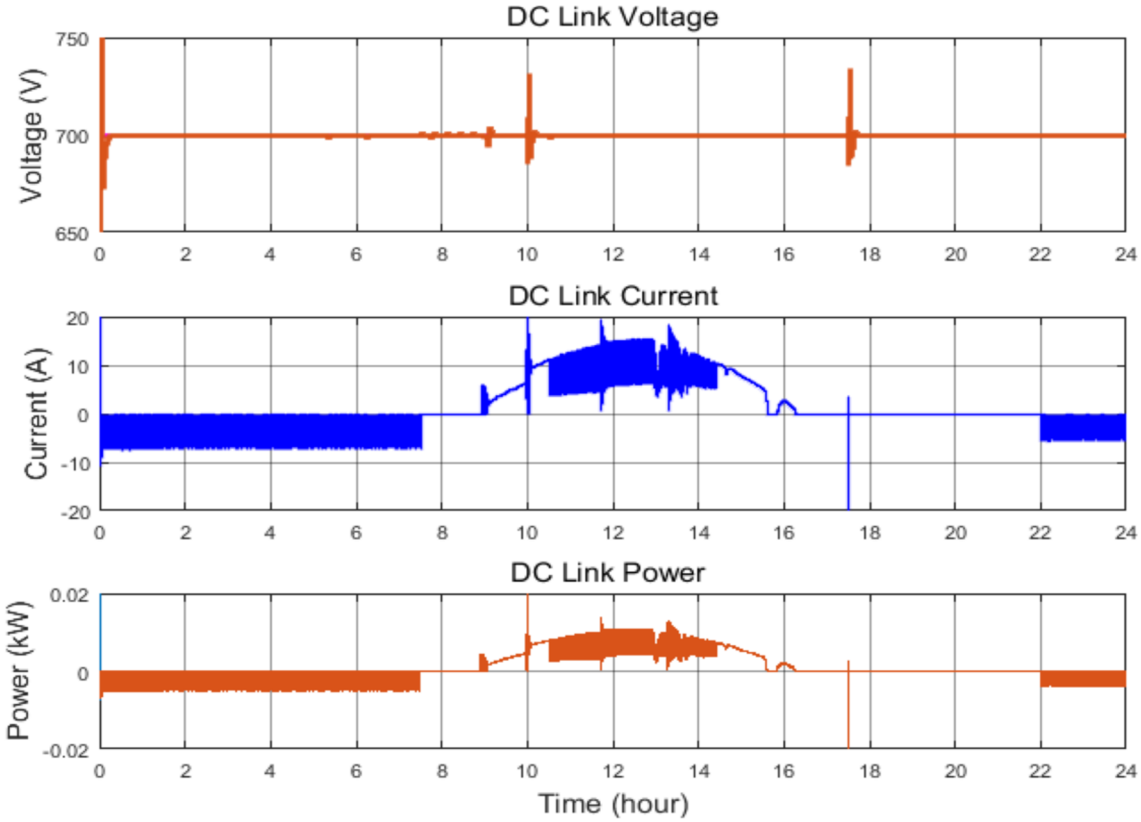

Fig. 6.13: DC link voltage, current and power under the clear sky irradiance profile.

6.6.2 Case B - System performance with the cloudy sky irradiance profile

The solar irradiance and temperature data in the cloudy sky profile are shown in Fig. 6.14.

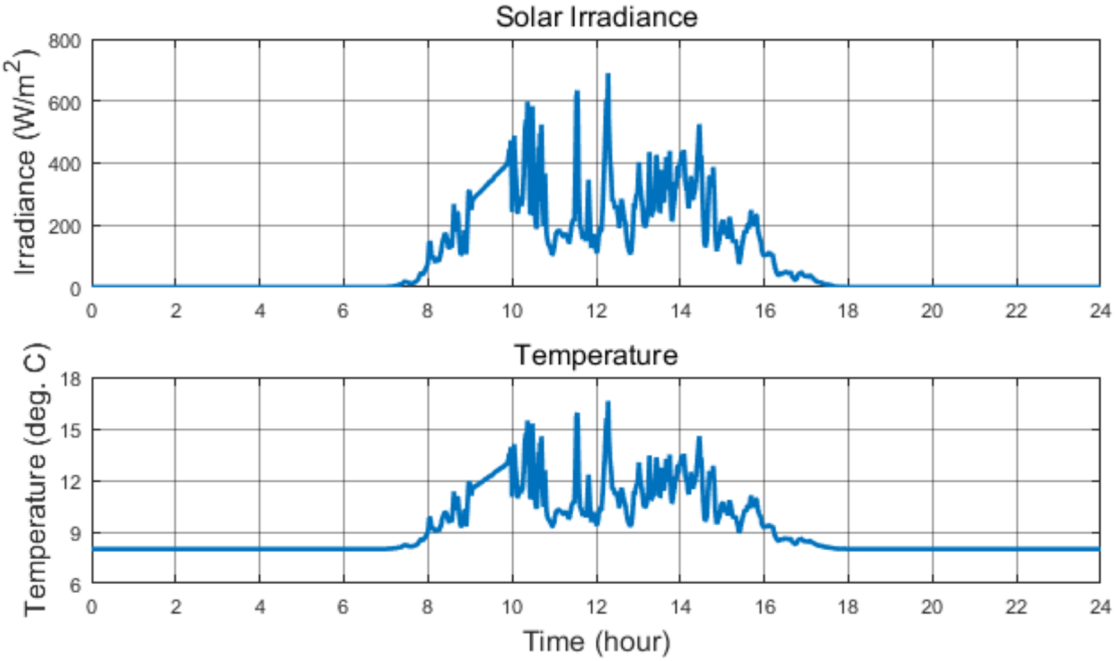

Fig. 6.14: Irradiance and temperature data in the cloudy sky profile.

The temperature data in the cloudy sky profile is calculated using (6.1) based on the cloudy sky irradiance data. It can be seen that the irradiance and temperature data in the cloudy sky profile is shown to have more fluctuations when compared to the data in the clear sky profile.

Fig. 6.15 shows the PV array voltage, current and power and the duty cycle varying in the example day under the cloudy sky profile. The PV array produces a rapid fluctuating output power when compared to the power generated under the clear sky profile. The duty cycle is maintained at around 0.58 during most of the solar power available period. There is a slight dip in the duty cycle at the midday. This is due to the sudden surges and plunges in solar irradiance that will change the PV array output power over short periods of time. The duty cycle suddenly reduces to zero at around 18:00 PM immediately prior to the switching off the MPPT controller.

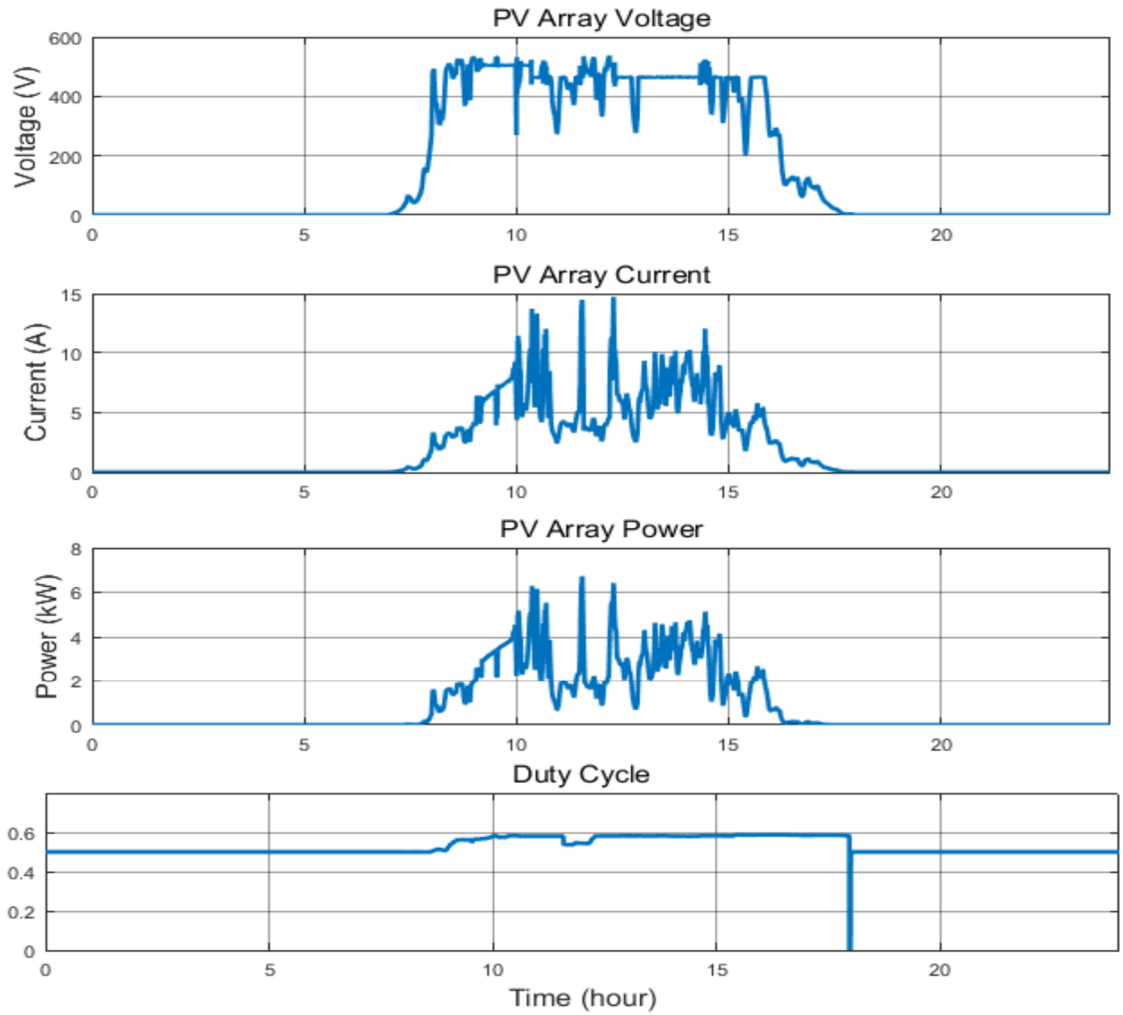

Fig. 6.15: PV array voltage, current and power, and the duty cycle under the cloudy sky profile.

Fig. 6.16 shows the charging/discharging power and the power difference between the PV array and the local loads under the cloudy sky irradiance profile. During the solar energy available period, it can be seen that the charging power is low and spiky when compared to the charging power under the clear sky profile.

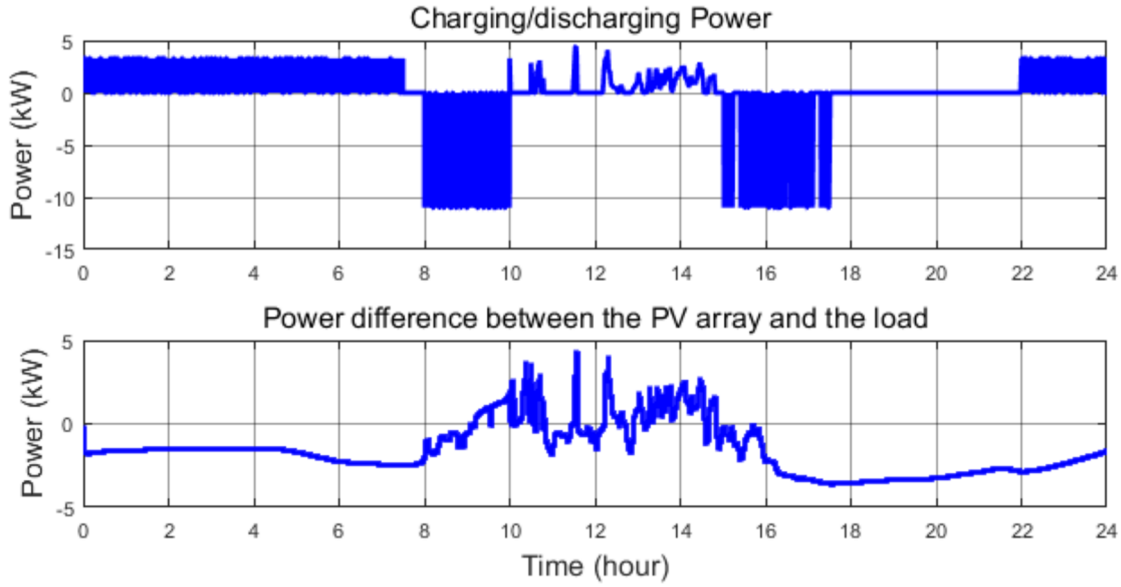

Fig. 6.16: Charging and discharging state, charging/discharging power, and the power difference between the PV array and the load under the cloudy sky irradiance profile.

Fig. 6.17 shows the battery current and voltage and actual SOC and reference SOC signals under the cloudy sky irradiance profile. At 2:30 PM when the daytime charging is about to finish, the actual SOC reaches to around 39%. This violates the SOC requirement when the vehicle leaves home. Some kinds of user overrides may be needed to charge the battery from the grid to satisfy the SOC requirements in the daytime. The charging controller may need to detect the adequacy of the solar energy during the daytime charging period. If the solar energy generated during the charging period is not enough to charge the battery to the required SOC level, charging from the grid could be initiated at some time before the daytime charging is finished. In Fig. 6.17, during the solar power available period, the actual SOC deviates significantly from the SOC reference during the time interval from 10:30 AM to 2:30 PM. This is largely due to insufficient irradiance levels during the daytime under the cloudy sky irradiance profile, which results into a low charging power in the power reference tracking mode. The battery voltage is almost kept at a constant level with some slight variations when the battery is charged from the PV

array. This may be due to the fluctuations in the charging power of the battery, which is also as result of the PV array power fluctuations.

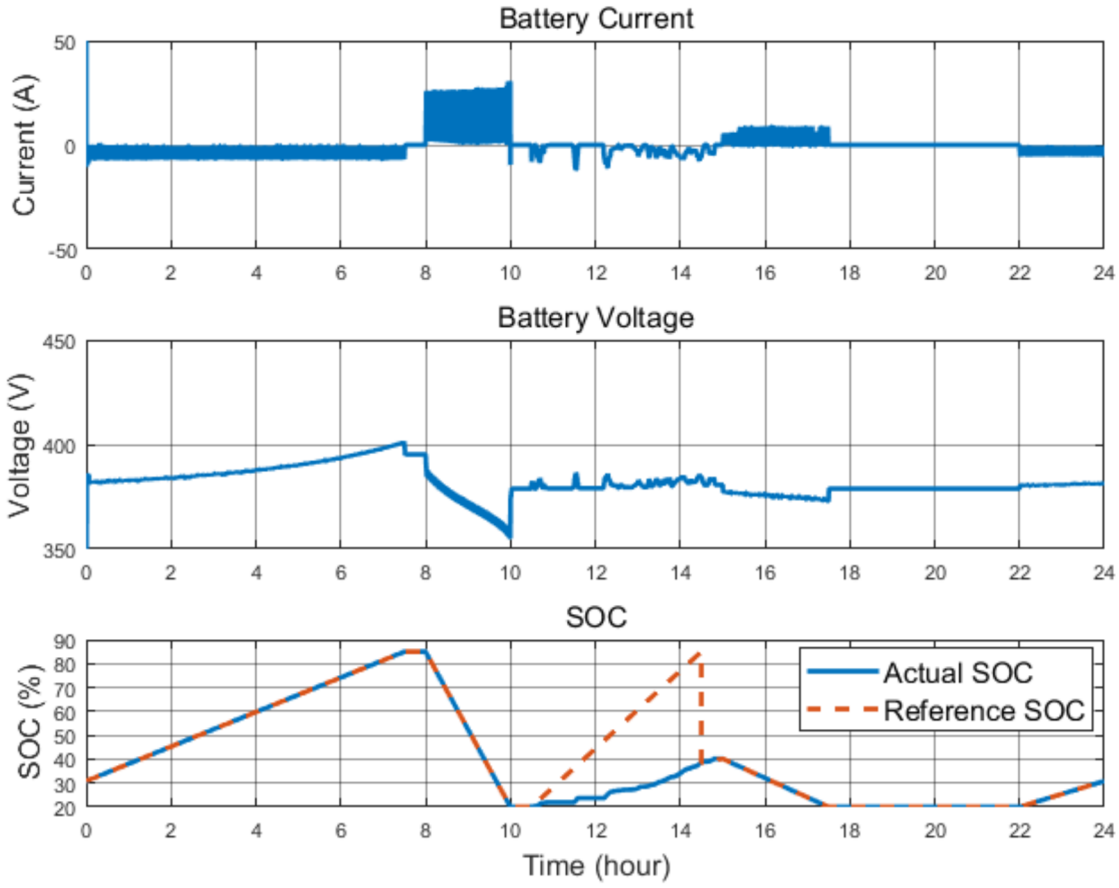

Fig. 6.17: Battery current, battery voltage, battery's actual SOC and battery's reference SOC under the cloudy sky profile.

Fig. 6.18 shows the DC link voltage, current and power under the cloudy sky irradiance profile. It can be seen that the DC link voltage behaves almost the same as the DC link voltage under the clear sky irradiance profile. During the solar power available period, there is a certain number of intervals when the DC link current and power are smaller than or equal to zero. This is because that the PV array generates not enough solar power for charging the vehicle. Potential user overrides may be applied in this case to charge the vehicle from the grid. It is noted that the PV array current is proportional to the PV array voltage during the whole day as expected.

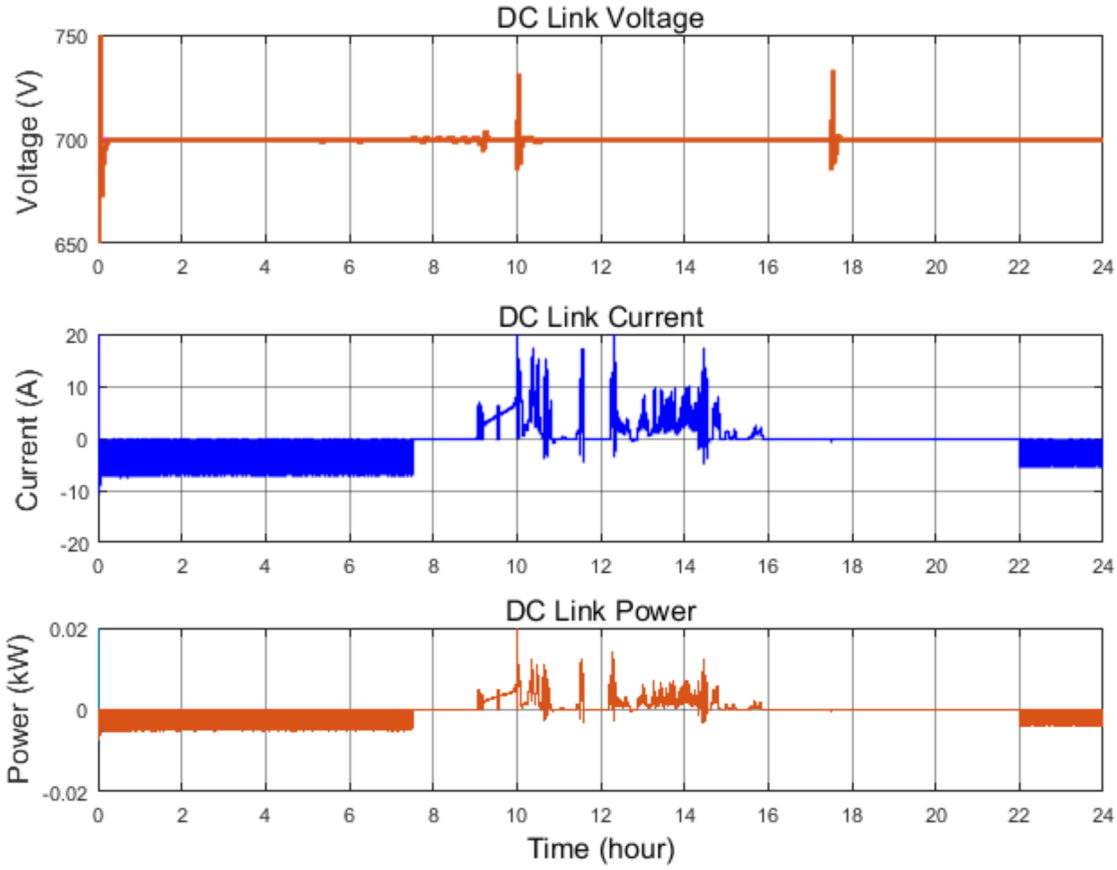

Fig. 6.18: DC link voltage, current and power under the cloudy sky irradiance profile.

6.7 Conclusion

The key objective of this chapter is to design and implement a control and charging strategy for a PHEV battery. The two modes of operation for the charging controller are well implemented based on the solar power available time. There are frequently situations where the irradiance condition is unfavourable for battery charging especially in a cloudy day, and the charging controller is required to work at the SOC reference tracking mode to follow a pre-set SOC profile. Thus, some kinds of user override may be required in some situations to ensure the battery is charged up to the required SOC levels at specific times of day when the vehicle leaves home, even if the vehicle is required to be charged from the grid during the daytime.

V2G services have not been implemented at this stage and are treated as outside the scope of the project. V2G services allow the energy stored in the batteries to be delivered to the

grid when there is a demand of reactive power in the grid. Future research could include the V2G technology to discharge the PHEV battery when faults happen in the grid or local load peaks occur.

Chapter 7
Conclusions and Recommendations for Future Research

This thesis has presented a comprehensive review and analysis of grid-connected photovoltaic (PV) systems integrated with plug-in hybrid electric vehicle (PHEV) energy storage integration in a residential environment. In order to simulate real charging scenarios for the PHEV in the day, the modelling accuracy of PV array and PHEV batteries have been improved through the parameter estimation techniques. The input voltage control of the DC-DC converter is analysed and implemented via a digital PID controller with the tuned parameters setting. This tuned parameter setting ensures that the PV array voltage tracks its reference with zero steady-state errors and fast response time. A suitable control and charging strategy has been developed to charge the vehicle from the PV array during the daytime and the grid at night. The charging controller works at the SOC reference tracking mode during the night charging to guarantee that the actual SOC of the battery satisfies the required SOC level at the end of the night charging.

The overall objectives of this thesis are modelling, control and power management of a grid-connected PV system with a PHEV battery as energy storage, parameter estimation of PV modules and PHEV batteries, experimental testing of BP 380 PV modules with validation of the PV module model and charging strategies for the PHEV batteries.

7.1 Conclusions

In summary, the major contributions have been made in the thesis are listed as follows:

- Modelling, control and power management of a grid-connected PV system with a PHEV battery as energy storage.
- A GA approach to parameter estimation for PV modules is proposed to estimate the parameters of a SDM. The relative errors at the three remarkable points are significantly reduced when compared to Villalva's iterative method.

- A novel QPSO parameter estimation technique is proposed to parameterize Tremblay's model parameters. The simulation results from Chapter 5 show that the QPSO parameter estimation technique provides similar estimation performance when compared to the GA and PSO parameter estimation techniques.
- Experimental testing of BP 380 PV modules has been conducted to validate the effectiveness of the PV module model.
- A control and charging strategy is developed to charge the vehicle from the PV array during the daytime and from the grid at night.

7.2 Suggestions for Future Research

Many future works could be done to provide a better understanding of grid-connected PV systems with a PHEV battery as energy storage. To compare the performance of the proposed system mentioned in Chapter 6, another residential PV system for PHEV loads, in addition to regular residential requirements, can be designed and implemented. This system can be a combination of two subsystems which cascade through a AC network. First subsystem consists of a PV array, a current-controlled boost converter, a MPPT controller, and an DC/AC inverter. The second subsystem can be the energy storage system with battery packs and a current-controlled bidirectional DC/AC inverter. All the current controllers can be selected as sliding mode controllers with more flexibility against conventional PID controllers. A power management algorithm can be developed to manage the power flow between the grid and the energy storage system according to load profiles. The operation and reliability of the system can be also analysed.

Future works can include:

- Development of a DC microgrid with EVs or PHEVs as energy storage and investigating whether added benefits can be achieved for future power systems.
- Utilization of intelligent controllers instead of conventional PI-controllers may give more flexibility to the control of grid-connected PV systems.
- Deployment of multiphase converters for PHEV charging interface to reduce the switching loss of the converters with minimum size inductors.

- Investigating the performance of grid-connected PV systems with PHEVs as energy storage under fault conditions
- Research on discharging strategies for PHEV batteries to supply power to the grid via the V2G technology.
- Incorporation of a supercapacitor energy storage system in the developed grid-connected PV systems to charge PHEV batteries during the daytime when the solar energy is inefficient.
- Simulation of the behaviour of an inverter controlled electric motor that serves a load during battery discharge based on the Urban Dynamometer Driving Schedule (UDDS).
- Development of a partially shaded PV array model to investigate the effects of partial shading on PV arrays.
- Incorporation of the partially shaded PV array model in the system model and development of a simple yet effective GMPPT technique to identify the GMPPT of the PV array under PSCs.

Appendix A
Script of Matlab Function Implementing the SDM for PV Modules

```
function Iout = fcn(Vin,T,Tref,G,Isc,Voc,Ns,Rs,Rp,A,Npar,Nser,Iph_n,TempC_Voc,
TempC_Isc)
%% Physical Constants
k=1.38e-23;
q=1.6e-19;
%% Change the temperature unit from Celsius to absolute scale (Kevin)
T=T+273;
Tref=Tref+273;
%% Calculate the photo-generated current at the operating condition
Iph=(Iph_n+TempC_Isc*(T-Tref))*(G/1000);
Iph=Iph*Npar;

%% Calculate the diode saturation current at STC
Io_n=Isc/(exp((q*Voc)/(Ns*A*k*T))-1);

%% Compute the diode saturation current at the operating temperature (Method 1
using the temperature coefficients)
Io_num=Isc+TempC_Isc*(T-Tref);
Io_den=exp(q*(Voc+TempC_Voc*(T-Tref))/(Ns*A*k*T))-1;
Io=Io_num./Io_den;
% Consider the temperature effect on the open circuit voltage
%% PV array diode saturation current
Io=Io*Npar;
%% Compute the thermal junction voltage
Vt=(Ns*k*T*A*Nser)/q;

Rs=Rs*Nser/Npar;   %Compute the series resistance of the PV array
Rp=Rp*Nser/Npar;   %Compute the parallel resistance of the PV array


%% Compute the PV array current using the Newton-Raphson iterative method
Iin=0;
while 1
    FL=Iph-Io*(exp((Vin+Iin*Rs)/Vt)-1)-((Vin+Iin*Rs)/Rp)-Iin;
    dFL=-Io*exp((Vin+Iin*Rs)/Vt)*(Rs./Vt)-(Rs/Rp)-1;
    I=Iin-(FL/dFL);
    if abs(I-Iin) < 10^-8
        break
    end
    Iin=I;
end
if I<0
    Iout=Iin;
else
    Iout=I;
end
```

Appendix B
System Design

To achieve a total power rating of 10 kW for the PV array, the TNM of the PV array is given as follows:

$$TNM = \frac{P_{\text{max\_array}}}{P_{\text{max\_module}}} = \frac{10\text{ kW}}{80\text{ W}} = 125 \tag{B.1}$$

The string voltage of the PV array is limited to 440 V, thus the number of series-connected modules (NM) per string is given by:

$$NM = \frac{V_{\text{mpp\_array}}}{V_{\text{mpp\_module}}} = \frac{440\text{ V}}{17.6\text{ V}} = 25 \tag{B.2}$$

The number of strings (NS) in the PV array is given as follows:

$$NS = \frac{TNM}{NM} = \frac{125}{25} = 5 \tag{B.3}$$

Thus, the output current of the PV array is calculated by:

$$I_{\text{mpp\_array}} = \frac{P_{\text{max\_array}}}{V_{\text{mpp\_array}}} = \frac{10\text{ kW}}{440\text{ V}} = 22.75\text{ A} \tag{B.4}$$

Table B.1 shows the specifications of the PV array for 10 kW generation.

Table B.1: PV array specifications for $10\ kW$ *generation.*

Parameter	Value
Rated power ($P_{mpp,\ array}$)	$10\ kW$
Number of series-connected modules (NM)	25
Number of parallel-connected strings (NS)	5
Voltage at the MPP ($V_{mpp,\ array}$)	$400\ V$
Current at the MPP ($I_{mpp,\ array}$)	$22.75\ A$

The SEPIC converter is assumed to always operate in CCM with a switching frequency of $20\ kHz$. The DC link voltage is selected as 700 V to reduce the output current ripple of the SEPIC converter, the DC link current and steady-state duty cycle of the SEPIC converter is given by:

$$I_{\mathrm{DC}} = \frac{P_{\max}}{V_{\mathrm{DC}}} = 14.3\ \mathrm{A} \tag{B.5}$$

$$D = \frac{V_{\mathrm{DC}}}{V_{\mathrm{string}} + V_{\mathrm{DC}}} = \frac{700}{440 + 700} = 0.614 \tag{B.6}$$

The ripple current flowing through the inductors L_1 and L_2 is assumed to be 30% of the input current of the DC-DC converter that is calculated in (B.4), therefore

$$\Delta i_L = 0.3 \cdot I_{in} = 6.825\ \mathrm{A} \tag{B.7}$$

The inductance of the two inductors are calculated as follows:

$$L_1 = L_2 = \frac{V_{\mathrm{string}} \cdot D}{\Delta i_L \cdot f_s} = \frac{440 \times 0.614}{6.825 \times 20000} = 1.98\ \mathrm{mH} \tag{B.8}$$

Select $2\ mH$ for the standard value for the two inductors, thus

$$L_1 = 2\ \mathrm{mH}$$
$$L_2 = 2\ \mathrm{mH}$$

Assume that the ripple voltage across the coupling capacitor is 5% of the input voltage

of the SEPIC converter, thus the coupling capacitor C_p in the SEPIC converter is given by:

$$C_p = \frac{I_{DC} \cdot D}{\Delta V_p \cdot f_s} = \frac{14.3 \times 0.614}{0.05 \times V_{\text{string}} \times 20000} = 19.96\ \mu F \tag{B.9}$$

Rounding up to a standard capacitor value, the capacitance of C_p is chosen as 20 μF.

The power rating of the bidirectional buck-boost converter is selected as 3.3 kW. The steady-state duty cycle is calculated as follows:

$$D = 1 - \frac{V_{\text{B}}}{V_{\text{DC}}} = 1 - \frac{355.2}{700} = \frac{431}{875} = 0.493 \tag{B.10}$$

The nominal battery current of the PHEV battery is calculated as follows:

$$I_{\text{B}} = \frac{P_{\text{charging}}}{V_{B,nom}} = \frac{3300}{355.2} = 9.29\ \text{A} \tag{B.11}$$

A rule of thumb is that the inductor ripple current ΔI_L is selected as 30% of the nominal battery current, which is calculated by:

$$\Delta I_L = 0.3 \cdot I_B = 0.3 \times 9.29 = 2.787\ \text{A} \tag{B.12}$$

Thus, the inductance of the bidirectional buck-boost converter is calculated as follows:

$$L = \frac{V_{\text{B}} \cdot (1 - D)}{\Delta I_L \cdot f_s} = \frac{355.2 \times (1 - D)}{2.787 \times 20000} = 3.234\ mH \tag{B.13}$$

The capacitance of the battery-side capacitor is calculated as follows [248]:

$$C_2 = \frac{1 - D}{8 \cdot L \cdot \frac{\Delta V_B}{V_B} \cdot f_s^2} = \frac{1 - 0.493}{8 \times 3.234 \times 10^{-3} \times \frac{20}{700} \times 20000^2} = 0.98\ \mu F \tag{B.14}$$

Table B.2 shows the specifications of the bidirectional buck-boost converter and SEPIC converter.

Table B.2: Specifications of the bidirectional buck-boost converter and SEPIC converter.

Parameter	**Value**
Switching frequency (f_s)	$20\ kHz$
Inductor current ripple (Δi_L)	30 %
Capacitor voltage ripple (ΔV_c)	2 %
Bidirectional Converter	
Rated power	3.3 kW
Battery voltage range ($V_{Batt,exp} - V_{Batt,nom}$)	$332.09 – 300.36\ V$
L_{Batt}	$22\ mH$
C_{Batt}	$22\ \mu F$
SEPIC Converter	
Rated power	10 kW
Input voltage (V_{in})	$400\ V$
Input current (I_{in})	$22.75\ A$
DC link voltage (V_{DC})	$700\ V$
DC link current (I_{DC})	$14.3\ A$

Bibliography

[1] S. A. Rahman, "Optimal Power Management for the UTS Plug-in Hybrid Electric Vehicle," University of Technology, Sydney, Australia, 2011.

[2] F. R. Islam, H. R. Pota, M. S. Rahman, and M. S. Ali, "Performance analysis of photovoltaic cell with dynamic PHEV loads," in *Univ. Power Eng. Conf. (AUPEC), 2012 22nd Australas.*, 2012, pp. 1–6.

[3] Australian PV Institute (APVI), "Australian PV Institute (APVI) Solar Map, funded by the Australian Renewable Energy Agency." [Online]. Available: pv-map.apvi.org.au. [Accessed: 08-Mar-2017].

[4] Global Sustainable Energy Solutions, "Standalone PV Systems : Past , Present & Future," *Global Sustainable Energy Solutions Pty Ltd.*, 2015. [Online]. Available: https://www.gses.com.au/wp-content/uploads/2016/05/GSES_Standalone-past-present-future.pdf. [Accessed: 15-May-2017].

[5] P. I. Muoka, "Control of Power Electronic Interfaces for Photovoltaic Power Systems for Maximum Power Extraction," PhD Thesis. University of Tasmania, 2014.

[6] T.-Y. Wang, "Recycling of Solar Cell Materials at the End of Life," in *Advance in Solar Photovoltaic Power Plants*, M. R. Islam, F. Rahman, and W. Xu, Eds. Springer-Verlag, 2016, pp. 287–317.

[7] V. M. Fthenakis, "End-of-life management and recycling of PV modules," *Energy Policy*, vol. 28, no. 14, pp. 1051–1058, 2000.

[8] J. Francfort, A. Briones, P. Heitmann, M. Schey, S. Schey, and J. Smart, "Power Flow Regulations and Building Codes Review by the AVTA," 2012.

[9] J. Martin, "Distributed vs. centralized electricity generation: are we witnessing a change of paradigm," *An Introduction to Distributed Generation*, 2009.

[10] N. Hadjsaid, M. C. Alvarez-Hérault, R. Caire, B. Raison, J. Descloux, and W. Bienia, "Novel architectures and operation modes of Distribution Network to increase DG integration," *IEEE PES General Meeting, PES 2010*, pp. 1–6, 2010.

[11] C. Gonzalez, R. Ramirez, R. Villafafila, A. Sumper, O. Boix, and M. Chindris, "Assess the impact of photovoltaic generation systems on low-voltage network: software analysis tool development," in *2007 9th International Conference on Electrical Power Quality and Utilisation*, 2007, pp. 1–6.

[12] A. HASHIM, TengkuJuhana TENGKU MOHAMED and H. SHAREEF, "Comparison of Decentralized Voltage Control Methods for Managing Voltage Rise in Active Distribution Networks," *Przegląd Elektrotechniczny*, vol. 89, no. 2a, pp. 214–218, 2013.

[13] M. Bester, "Voltage Management Under the Large Scale Integration of Energy Storage and Embedded Generation," Honours Thesis, University of Tasmania,

2014.

[14] S. Huang and D. Infield, "The impact of domestic Plug-in Hybrid Electric Vehicles on power distribution system loads," *Power Syst. Technol. (POWERCON), 2010 Int. Conf.*, pp. 1–7, 2010.

[15] W. Gu, H. Yu, W. Liu, J. Zhu, and X. Xu, "Demand Response and Economic Dispatch of Power Systems Considering Large-Scale Plug-in Hybrid Electric Vehicles/Electric Vehicles (PHEVs/EVs): A Review," *Energies*, vol. 6, no. 9, pp. 4394–4417, Aug. 2013.

[16] Z. Yang, Wei Xu, and X. Yu, "Optimal PHEV charge scheduling for additional power loss ratio and charging cost minimizations," in *2013 International Conference on Electrical Machines and Systems (ICEMS)*, 2013, pp. 465–469.

[17] I. Niazazari, H. A. Abyaneh, M. J. Farah, F. Safaei, and H. Nafisi, "Voltage profile and power factor improvement in PHEV charging station using a probabilistic model and flywheel," in *2014 19th Conference on Electrical Power Distribution Networks (EPDC)*, 2014, pp. 100–105.

[18] United States Environmental Protection Agency, "Sources of Greenhouse Gas Emissions," *United States Environmental Protection Agency*. [Online]. Available: https://www.epa.gov/ghgemissions/sources-greenhouse-gas-emissions. [Accessed: 19-Oct-2017].

[19] S. Pothecary, "PVMA figures show 75 GW of solar PV was installed in 2016," *PV Magazine*, 2017. [Online]. Available: https://www.pv-magazine.com/2017/01/19/pvma-figures-show-75-gw-of-solar-pv-was-installed-in-2016/. [Accessed: 16-May-2017].

[20] D. Prasad and M. Snow, *Designing with Solar Power: A Source Book for Building Integrated Photovoltaics*. Images, 2005.

[21] D. M. Soto, S. Balathandayuthapani, and C. S. Edrington, "Mitigation of PHEV charging impact on transformers via a PV-APF harmonic compensation technique: Application to V2G integration," in *2011 IEEE Vehicle Power and Propulsion Conference*, 2011, pp. 1–5.

[22] S. Lyden, "A Simulated Annealing Global Maximum Power Point Tracking Method for Photovoltaic Systems Experiencing Non-Uniform Environmental Conditions," PhD Thesis, University of Tasmania, 2015.

[23] A. P. Robinson, P. T. Blythe, M. C. Bell, Y. Hübner, and G. A. Hill, "Analysis of electric vehicle driver recharging demand profiles and subsequent impacts on the carbon content of electric vehicle trips," *Energy Policy*, vol. 61, pp. 337–348, Oct. 2013.

[24] M. G. Villalva, J. R. R. Gazoli, and E. R. R. Filho, "Comprehensive Approach to Modeling and Simulation of Photovoltaic Arrays," *IEEE Transactions on Power Electronics*, vol. 24, no. 5, pp. 1198–1208, 2009.

[25] Y. Zhang, S. Lyden, B. A. L. de la Barra, and M. E. Haque, "A genetic algorithm approach to parameter estimation for PV modules," in *2016 IEEE Power and Energy Society General Meeting (PESGM)*, 2016, pp. 1–5.

[26] T. Markvart, *Solar electricity*. Chichester, U.K.: John Wiley & Sons, 1994.

[27] S. C. W. Krauter, “Photovoltaics,” in *Solar Electric Power Generation*, Berlin, Heidelberg: Springer Berlin Heidelberg, 2006, pp. 19–48.

[28] Stion, “PV Effect - Deconstructing the elements of solar electricity.” [Online]. Available: http://www.stion.com/technology/photovoltaic-effect/. [Accessed: 22-May-2017].

[29] M. R. Islam, “Introduction,” in *Advance in Solar Photovoltaic Power Plants*, M. R. Islam, F. Rahman, and W. Xu, Eds. Springer-Verlag, 2016, pp. 1–11.

[30] M. R. Islam, F. Rahman, and W. Xu, *Advances in Solar Photovoltaic Power Plants*. Berlin, Heidelberg: Springer Berlin Heidelberg, 2016.

[31] M. A. Green *et al.*, “Solar cell efficiency tables (version 49),” *Progress in Photovoltaics: Research and Applications*, vol. 25, no. 1, pp. 3–13, Jan. 2017.

[32] M. A. Green, K. Emery, Y. Hishikawa, W. Warta, and E. D. Dunlop, “Solar cell efficiency tables (version 48),” *Progress in Photovoltaics: Research and Applications*, vol. 24, no. 7, pp. 905–913, Jul. 2016.

[33] M. Shiao, “Thin Film 2012 -2016: Technologies, Markets and Strategies for Survival,” *GTM Research*, 2012. [Online]. Available: https://www.greentechmedia.com/research/report/thin-film-2012-2016. [Accessed: 27-Nov-2016].

[34] S. Chung, “PV Power Forecasting,” Hounors Thesis, University of Tasmania, 2015.

[35] Universität Kassel, *Photovoltaic Systems Technology*. Kassel, Germany: Universität Kassel, 2003.

[36] G. M. Masters, *Renewable and Efficient Electric Power Systems*, 2nd ed. Hoboken, NJ, USA: John Wiley & Sons, Inc., 2004.

[37] A. Chatterjee, A. Keyhani, and D. Kapoor, “Identification of Photovoltaic Source Models,” *IEEE Transactions on Energy Conversion*, vol. 26, no. 3, pp. 883–889, Sep. 2011.

[38] Y. Zhang, “Photovoltaic Power System with Plug-in Hybrid Electric Vehicles as an Energy Storage,” Honours Thesis, University of Tasmania, 2014.

[39] M. C. Alonso García and J. L. Balenzategui, “Estimation of photovoltaic module yearly temperature and performance based on Nominal Operation Cell Temperature calculations,” *Renewable Energy*, vol. 29, no. 12, pp. 1997–2010, Oct. 2004.

[40] W. Xiao, W. G. Dunford, P. R. Palmer, and A. Capel, “Regulation of photovoltaic voltage,” *IEEE Transactions on Industrial Electronics*, vol. 54, no. 3, pp. 1365–1374, 2007.

[41] S. Lyden, M. E. Haque, A. Gargoom, M. Negnevitsky, and P. I. Muoka, “Modelling and Parameter Estimation of Photovoltaic Cell,” in *Univ. Power Eng. Conf. (AUPEC), 2012 22nd Australas.*, 2012, pp. 1–6.

[42] H. Patel and V. Agarwal, “MATLAB-Based Modeling to Study the Effects of Partial Shading on PV Array Characteristics,” *IEEE Trans. Energy Convers.*, vol. 23, no. 1, pp. 302–310, Mar. 2008.

[43] K. Ishaque, Z. Salam, and H. Taheri, "Accurate MATLAB Simulink PV System Simulator Based on a Two-Diode Model," *Journal of Power Electronics*, vol. 11, no. 2, pp. 179–187, Mar. 2011.

[44] G. Escobar, C. N. M. Ho, and S. Pettersson, "Maximum power point searching method for partial shaded PV strings," in *IECON 2012 - 38th Annual Conference on IEEE Industrial Electronics Society*, 2012, pp. 5726–5731.

[45] S. E. Boukebbous and D. Kerdoun, "Study, modeling and simulation of photovoltaic panels under uniform and nonuniform illumination conditions," *Revue des Energies Renouvelables*, vol. 18, no. 2, pp. 257–268, 2015.

[46] D. Sera and Y. Baghzouz, "On the Impact of Partial Shading on PV Output Power Institute of Energy Technology," *2nd WSEAS/IASME International Conference on Renewable Energy Sourses (RES'08)*, pp. 229–234, 2008.

[47] Y. Jiang, J. A. Abu Qahouq, A. Hassan, M. E. Ahmed, and M. Orabi, "Energy efficient fine-grained approach for solar photovoltaic management system," *INTELEC, International Telecommunications Energy Conference (Proceedings)*, pp. 0–3, 2011.

[48] R. C. N. Pilawa-Podgurski and D. J. Perreault, "Sub-Module integrated distributed maximum power point tracking for solar photovoltaic applications," *IEEE Transactions on Power Electronics*, vol. 28, no. 6, pp. 2957–2967, 2013.

[49] N. Femia, G. Lisi, G. Petrone, G. Spagnuolo, and M. Vitelli, "Distributed maximum power point tracking of photovoltaic arrays: Novel approach and system analysis," *IEEE Transactions on Industrial Electronics*, vol. 55, no. 7, pp. 2610–2621, Jul. 2008.

[50] R. Alonso, E. Roman, A. Sanz, V. E. M. Santos, and P. Ibanez, "Analysis of Inverter-Voltage Influence on Distributed MPPT Architecture Performance," *IEEE Trans. Ind. Electron.*, vol. 59, no. 10, pp. 3900–3907, Oct. 2012.

[51] A. Elasser, M. Agamy, J. Sabate, R. Steigerwald, R. Fisher, and M. Harfman-Todorovic, "A comparative study of central and distributed MPPT architectures for megawatt utility and large scale commercial photovoltaic plants," *IECON Proceedings (Industrial Electronics Conference)*, pp. 2753–2758, 2010.

[52] D. M. Riley and G. K. Venayagamoorthy, "Comparison of a recurrent neural network PV system model with a traditional component-based PV system model," in *2011 37th IEEE Photovoltaic Specialists Conference*, 2011, pp. 002426–002431.

[53] A. Mellit, M. Benghanem, and S. A. Kalogirou, "Modeling and simulation of a stand-alone photovoltaic system using an adaptive artificial neural network: Proposition for a new sizing procedure," *Renewable Energy*, vol. 32, no. 2, pp. 285–313, Feb. 2007.

[54] M. AbdulHadi, A. M. Al-Ibrahim, and G. S. Virk, "Neuro-Fuzzy-Based Solar Cell Model," *IEEE Transactions on Energy Conversion*, vol. 19, no. 3, pp. 619–624, Sep. 2004.

[55] M. Lundstrom, "Solar Cell Physics : recombination and generation," *Purdue University*, 2011. [Online]. Available: https://nanohub.org/resources/11942/download/2011.07.21-NCN-SC02-

Lundstrom.pdf. [Accessed: 24-May-2017].

[56] A. Sproul, "Understanding the p-n Junction," *University of New South Wales*, 2012. [Online]. Available: http://www2.pv.unsw.edu.au/nsite-files/pdfs/UNSW_Understanding_the_p-n_Junction.pdf. [Accessed: 24-May-2017].

[57] M. R. Alrashidi and M. F. Alhajri, "Parameters Estimation of Double Diode Solar Cell Model," *Engineering and Technology*, vol. 7, no. 2, pp. 93–96, 2013.

[58] K. Nishioka, N. Sakitani, Y. Uraoka, and T. Fuyuki, "Analysis of multicrystalline silicon solar cells by modified 3-diode equivalent circuit model taking leakage current through periphery into consideration," *Solar Energy Materials and Solar Cells*, vol. 91, no. 13, pp. 1222–1227, 2007.

[59] S. Liu and R. A. Dougal, "Dynamic Multi-Physics Model for Solar Array," *IEEE Power Engineering Review*, vol. 22, no. 5, p. 66, 2002.

[60] W. Xiao, W. G. Dunford, and A. Capel, "A novel modeling method for photovoltaic cells," *PESC Record - IEEE Annual Power Electronics Specialists Conference*, vol. 3, pp. 1950–1956, 2004.

[61] Y. A. Mahmoud, W. Xiao, and H. H. Zeineldin, "A parameterization approach for enhancing PV model accuracy," *IEEE Transactions on Industrial Electronics*, vol. 60, no. 12, pp. 5708–5716, 2013.

[62] A. Bellini and S. Bifaretti, "Simplified model of a photovoltaic module," *Applied Electronics*, no. 3, pp. 3–7, 2009.

[63] D. Sera, R. Teodorescu, and P. Rodriguez, "PV panel model based on datasheet values," *IEEE International Symposium on Industrial Electronics*, no. 4, pp. 2392–2396, 2007.

[64] S. Cannizzaro, M. C. Di Piazza, M. Luna, and G. Vitale, "Generalized classification of PV modules by simplified single-diode models," *IEEE International Symposium on Industrial Electronics*, pp. 2266–2273, 2014.

[65] S. B. Kjær, "Evaluation of the 'Hill Climbing' and the 'Incremental Conductance' Maximum Power Point Trackers for Photovoltaic Power Systems," *IEEE Transactions on Energy Conversion*, vol. 27, no. 4, pp. 922–929, Dec. 2012.

[66] S. B. Kjær, "Design and control of an inverter for photovoltaic applications," Aalborg University, Aalborg, Denmark, 2005.

[67] E. I. Batzelis, I. A. Routsolias, and S. A. Papathanassiou, "An explicit pv string model based on the lambert w function and simplified mpp expressions for operation under partial shading," *IEEE Transactions on Sustainable Energy*, vol. 5, no. 1, pp. 301–312, 2014.

[68] R. M. Corless, G. H. Gonnet, D. E. G. Hare, D. J. Jeffrey, and D. E. Knuth, "On the Lambert W Function," *Advances in Computational mathematics*, vol. 5, no. 1, pp. 329–359, 1996.

[69] W. Xu, C. Mu, and L. Tang, "Advanced Control Techniques for PV Maximum Power Point Tracking," in *Advance in Solar Photovoltaic Power Plants*, M. R. Islam, F. Rahman, and W. Xu, Eds. Springer-Verlag, 2016, pp. 43–78.

[70] L. Tang, Y. Zhang, W. Xu, and C. Zeng, "Novel variable step-size maximum power point tracking control strategy for PV systems based on contingence angles," *2013 IEEE Energy Conversion Congress and Exposition*, pp. 3904–3911, 2013.

[71] A. Keyhani, "Modeling of photovoltaic microgrids for bulk power grid studies," *IEEE Power Energy Soc. Gen. Meet.*, pp. 1–6, 2011.

[72] A. Keyhani, *Design of smart power grid renewable energy systems*, 2nd ed. New Jersey: John Wiley & Sons, 2011.

[73] PV Education.org, "Double Diode Model." [Online]. Available: http://pveducation.org/pvcdrom/characterisation/double-diode-model. [Accessed: 01-Dec-2016].

[74] S. Moballegh and J. Jiang, "Partial shading modeling of photovoltaic system with experimental validations," *IEEE Power Energy Soc. Gen. Meet.*, 2011.

[75] M. G. Villalva, J. R. Gazoli, and E. R. Filho, "Modeling and circuit-based simulation of photovoltaic arrays," in *2009 Brazilian Power Electronics Conference*, 2009, vol. 14, no. NOVEMBER, pp. 1244–1254.

[76] Y. Mahmoud, W. Xiao, and H. H. Zeineldin, "A Simple Approach to Modeling and Simulation of Photovoltaic Modules," *IEEE Transactions on Sustainable Energy*, vol. 3, no. 1, pp. 185–186, Jan. 2012.

[77] A. Yazdani *et al.*, "Modeling Guidelines and a Benchmark for Power System Simulation Studies of Three-Phase Single-Stage Photovoltaic Systems," *IEEE Transactions on Power Delivery*, vol. 26, no. 2, pp. 1247–1264, 2011.

[78] T. F. Elshatter, M. T. T. Elhagry, E. M. M. Abou-Elzahab, and A. a. T. Elkousy, "Fuzzy modeling of photovoltaic panel equivalent circuit," in *the Twenty-Eighth IEEE Photovoltaic Specialists Conference - 2000 (Cat. No.00CH37036)*, 2000.

[79] R. Gottschalg, M. Rommel, D. G. Infield, and M. J. Kearney, "The influence of the measurement environment on the accuracy of the extraction of the physical parameters of solar cells," *Meas. Sci. Technol.*, vol. 10, no. 9, pp. 796–804, Sep. 1999.

[80] M. A. Awadallah and B. Venkatesh, "Estimation of PV module parameters from datasheet information using optimization techniques," in *2015 IEEE International Conference on Industrial Technology (ICIT)*, 2015, vol. 2015–June, no. June, pp. 2777–2782.

[81] W. De Soto, S. A. A. Klein, and W. A. A. Beckman, "Improvement and validation of a model for photovoltaic array performance," *Solar Energy*, vol. 80, no. 1, pp. 78–88, Jan. 2006.

[82] T. Chai and R. R. Draxler, "Root mean square error (RMSE) or mean absolute error (MAE)? – Arguments against avoiding RMSE in the literature," *Geosci. Model Dev.*, vol. 7, no. 3, pp. 1247–1250, 2014.

[83] KIMO Instruments, "Technical Data Sheet for KIMO Solarimeter SL 200." [Online]. Available: http://www.kimo.fr/produits/276/sl_200.html?lang=en. [Accessed: 20-Jun-2017].

[84] S. Lyden, M. E. Haque, A. Gargoom, and M. Negnevitsky, "Modelling

photovoltaic cell: Issues and operational constraints," in *2012 IEEE International Conference on Power System Technology (POWERCON)*, 2012, pp. 1–6.

[85] S. E. Babaa, M. Armstrong, and V. Pickert, "Overview of Maximum Power Point Tracking Control Methods for PV Systems," *Journal of Power and Energy Engineering*, vol. 2, no. 8, pp. 59–72, 2014.

[86] S. Tucker, "Renewable Energy Micro-Grid Power System for Isolated Communities," Honours Thesis, University of Tasmania, 2011.

[87] A. W. Leedy, L. Guo, and K. A. Aganah, "A constant voltage MPPT method for a solar powered boost converter with DC motor load," *Conference Proceedings - IEEE SOUTHEASTCON*, 2012.

[88] S. Lyden and M. E. Haque, "Comparison of the Perturb and Observe and simulated annealing approaches for maximum power point tracking in a photovoltaic system under partial shading conditions," in *2014 IEEE Energy Conversion Congress and Exposition (ECCE)*, 2014, pp. 2517–2523.

[89] S. Lyden, M. E. Haque, and D. Xiao, "Application of a Simulated Annealing technique for global maximum power point tracking of PV modules experiencing partial shading," in *IECON 2014 - 40th Annu. Conf. IEEE Ind. Electron. Soc.*, 2014, pp. 1977–1983.

[90] S. Lyden and M. E. Haque, "Maximum Power Point Tracking techniques for photovoltaic systems: A comprehensive review and comparative analysis," *Renewable and Sustainable Energy Reviews*, vol. 52, pp. 1504–1518, Dec. 2015.

[91] Y. Fan *et al.*, "An improved simulated annealing maximum power point tracking technique for PV array under partial shading conditions," in *2016 18th European Conference on Power Electronics and Applications (EPE'16 ECCE Europe)*, 2016, pp. 1–8.

[92] K. Ishaque, Z. Salam, M. Amjad, and S. Mekhilef, "An improved particle swarm optimization (PSO)-based MPPT for PV with reduced steady-state oscillation," *IEEE Transactions on Power Electronics*, vol. 27, no. 8, pp. 3627–3638, 2012.

[93] S. Lyden, M. E. Haque, and M. A. Mahmud, "Maximum Power Point Tracking Methods for PV systems," in *Advances in Solar Photovoltaic Power Plants*, M. R. Islam, F. Rahman, and W. Xu, Eds. Berlin, Heidelberg: Springer Berlin Heidelberg, 2016, pp. 79–105.

[94] H. Patel and V. Agarwal, "MPPT scheme for a PV-fed single-phase single-stage grid-connected inverter operating in CCM with only one current sensor," *IEEE Transactions on Energy Conversion*, vol. 24, no. 1, pp. 256–263, 2009.

[95] E. Dallago, A. Liberale, D. Miotti, and G. Venchi, "Direct MPPT Algorithm for PV Sources with only Voltage Measurements," *IEEE Transactions on Power Electronics*, vol. 30, no. 12, pp. 6742–6750, 2015.

[96] H. Al-Atrash, I. Batarseh, and K. Rustom, "Statistical modeling of DSP-based hill-climbing MPPT algorithms in noisy environments," *Conference Proceedings - IEEE Applied Power Electronics Conference and Exposition - APEC*, vol. 3, pp. 1773–1777, 2005.

[97] M. Sokolov, "Small-Signal Modelling of Maximum Power Point Tracking for

Photovoltaic Systems," Imperial College London, 2013.

[98] H. Al-Atrash, I. Batarseh, and K. Rustom, "Effect of measurement noise and bias on hill-climbing MPPT algorithms," *IEEE Transactions on Aerospace and Electronic Systems*, vol. 46, no. 2, pp. 745–760, 2010.

[99] C. Ababei, S. Yuvarajan, and D. L. Schulz, "Toward integrated PV panels and power electronics using printing technologies," *Solar Energy*, vol. 84, no. 7, pp. 1111–1123, 2010.

[100] T. Takashima, T. Tanaka, M. Amano, and Y. Ando, "Maximum output control of photovoltaic (PV) array," *Collection of Technical Papers. 35th Intersociety Energy Conversion Engineering Conference and Exhibit (IECEC) (Cat. No.00CH37022)*, vol. 1, no. C, pp. 380–383, 2000.

[101] C. . Hua, J. . c Lin, and H. . Tzou, "MPP control of a photovoltaic energy system," *European Transactions on Electrical Power*, vol. 13, no. 4, pp. 239–246, 2003.

[102] K. Nishioka *et al.*, "Analysis of the Temperature Characteristics in Polycrystalline Si Solar Cells Using Modified Equivalent Circuit Model," *Japanese Journal of Applied Physics*, vol. 42, no. Part 1, No. 12, pp. 7175–7179, 2003.

[103] H. E.-S. A. Ibrahim, F. F. Houssiny, H. M. Zein El-Din, and M. A. El-Shibini, "Microcomputer controlled buck regulator for maximum power point tracker for dc pumping system operates from photovoltaic system," *IEEE International Conference on Fuzzy Systems*, vol. 1, p. I-406-I-411, 1999.

[104] H. Masoum, Mohammad A S, Dehbonei, "Design , Construction and Testing of a Voltage-based Maximum Power Point Tracker (VMPPT) for Small Satellite Power Supply," *Small*, vol. 1, 1999.

[105] M. Veerachary, T. Senjyu, and K. Uezato, "Voltage-based maximum power point tracking control of PV system," *IEEE Transactions on Aerospace and Electronic Systems*, vol. 38, no. 1, 2002.

[106] W. Issaadi, "An Improved MPPT Converter Using Current Compensation Method for PV-Applications," *INTERNATIONAL JOURNAL of RENEWABLE ENERGY RESEARCH Wassila Issaadi*, vol. 6, no. 3, 2016.

[107] A. Pandey, N. Dasgupta, and A. K. Mukerjee, "A simple single-sensor MPPT solution," *IEEE Transactions on Power Electronics*, vol. 22, no. 2, pp. 698–700, 2007.

[108] S. M. Alghuwainem, "Matching of a DC motor to a photovoltaic generator using a step-up converter with a current-locked loop," *IEEE Transactions on Energy Conversion*, vol. 9, no. 1, pp. 192–198, 1994.

[109] T. Noguchi, S. Togashi, and R. Nakamoto, "Short-current pulse-based maximum-power-point tracking method for multiple photovoltaic-and-converter module system," *IEEE Transactions on Industrial Electronics*, vol. 49, no. 1, pp. 217–223, 2002.

[110] S. Yuvarajan, D. Yu, and S. Xu, "A novel power converter for photovoltaic applications," *Journal of Power Sources*, vol. 135, no. 1–2, pp. 327–331, Sep. 2004.

[111] Z. Salameh and D. Taylor, "Step-up maximum power point tracker for

photovoltaic arrays," *Solar Energy*, vol. 44, no. 1, pp. 57–61, 1990.

[112] C. Hua, J. Lin, and C. Shen, "Implementation of a DSP-controlled PV system with peak power tracking," *IEEE Trans Ind Electron*, vol. 45, no. 1, pp. 99–107, 1998.

[113] Y. C. Kuo, T. J. Liang, and J. F. Chen, "Novel maximum-power-point-tracking controller for photovoltaic energy conversion system," *IEEE Transactions on Industrial Electronics*, vol. 48, no. 3, pp. 594–601, 2001.

[114] Y. Hsiao and C. Chen, "Maximum power tracking for photovoltaic power system," *Conference Record of the 37th 2002 IEEE Industry Applications Conference*, vol. 2, no. FEBRUARY 2002, pp. 1035–1040, 2002.

[115] Wenkai Wu, N. Pongratananukul, Weihong Qiu, K. Rustom, T. Kasparis, and I. Batarseh, "DSP-based multiple peak power tracking for expandable power system," *Eighteenth Annual IEEE Applied Power Electronics Conference and Exposition, 2003. APEC '03.*, vol. 1, no. C, pp. 525–530, 2003.

[116] X. Liu and L. A. C. Lopes, "An improved perturbation and observation maximum power point tracking algorithm for PV arrays," *PESC Record - IEEE Annual Power Electronics Specialists Conference*, vol. 3, pp. 2005–2010, 2004.

[117] N. Femia, D. Granozio, G. Petrone, G. Spagnuolo, and M. Vitelli, "Optimized one-cycle control in photovoltaic grid connected applications," *IEEE Transactions on Aerospace and Electronic Systems*, vol. 42, no. 3, pp. 954–971, 2006.

[118] I. S. Kim, M. B. Kim, and M. J. Youn, "New maximum power point tracker using sliding-mode observer for estimation of solar array current in the grid-connected photovoltaic system," *IEEE Transactions on Industrial Electronics*, vol. 53, no. 4, pp. 1027–1035, 2006.

[119] R. Leyva, C. Alonso, I. Queinnec, a Cid-Pastor, D. Lagrange, and L. Martinez-Salamero, "MPPT of photovoltaic systems using extremum-seeking control," *Ieee Transactions on Aerospace and Electronic Systems*, vol. 42, no. 1, pp. 249–258, 2006.

[120] D. Sera, T. Kerekes, R. Teodorescu, and F. Blaabjerg, "Improved MPPT method for rapidly changing environmental conditions," in *2006 IEEE International Symposium on Industrial Electronics*, 2006, no. November, pp. 1420–1425.

[121] R. I. Virgili and L. Renardieres, "Adaptive digital MPPT control for photovoltaic applications .," pp. 2414–2419, 2007.

[122] C.-C. Chu and C.-L. Chen, "Robust maximum power point tracking method for photovoltaic cells: A sliding mode control approach," *Solar Energy*, vol. 83, no. 8, pp. 1370–1378, Aug. 2009.

[123] T. P. Sahu, T. V. Dixit, and R. Kumar, "Simulation and Analysis of Perturb and Observe MPPT Algorithm for PV Array using CUK Converter," *Advance in Electronic and Electric Engineering*, vol. 4, no. 2, pp. 213–224, 2014.

[124] W. K. Francis, S. B. S., and J. Mathew, "MATLAB / Simulink PV Module Model of P&O And DC Link CDC MPPT Algorithms with Labview Real Time Monitoring And Control Over P&O Technique," in *International Journal of Advanced Research in Electrical, Electronics and Instrumentation Engineering*, 2014, pp. 92–101.

[125] I. V. Banu and M. Istrate, "Modeling of maximum power point tracking algorithm for photovoltaic systems," *2012 International Conference and Exposition on Electrical and Power Engineering*, no. 2, pp. 953–957, Oct. 2012.

[126] A. Safari and S. Mekhilef, "Incremental conductance MPPT method for PV systems," in *2011 24th Canadian Conference on Electrical and Computer Engineering(CCECE)*, 2011, pp. 345–347.

[127] G. C. Hsieh, H. I. Hsieh, C. Y. Tsai, and C. H. Wang, "Photovoltaic power-increment-aided incremental-conductance MPPT with two-phased tracking," *IEEE Transactions on Power Electronics*, vol. 28, no. 6, pp. 2895–2911, 2013.

[128] L. Zhang, W. G. Hurley, and W. H. Wölfle, "A new approach to achieve maximum power point tracking for PV system with a variable inductor," *IEEE Transactions on Power Electronics*, vol. 26, no. 4, pp. 1031–1037, 2011.

[129] Q. Mei, M. Shan, L. Liu, and J. M. Guerrero, "A novel improved variable step-size incremental-resistance MPPT method for PV systems," *IEEE Transactions on Industrial Electronics*, vol. 58, no. 6, pp. 2427–2434, 2011.

[130] J. M. Blanes, F. J. Toledo, S. Montero, and A. Garrigós, "In-Site Real-Time Photovoltaic Photovoltaic I–V Curves and Maximum Power Point Estimator," *IEEE Transactions on Power Electronics*, vol. 28, no. 3, pp. 1234–1240, Mar. 2013.

[131] W. Xiao, M. G. J. Lind, W. G. Dunford, and A. Capel, "Real-time identification of optimal operating points in photovoltaic power systems," *IEEE Transactions on Industrial Electronics*, vol. 53, no. 4, pp. 1017–1026, 2006.

[132] G. Farivar, B. Asaei, and S. Mehrnami, "An Analytical Solution for Tracking Photovoltaic Module MPP," *IEEE Journal of Photovoltaics*, vol. 3, no. 3, pp. 1053–1061, Jul. 2013.

[133] T. Esram and P. L. Chapman, "Comparison of Photovoltaic Array Maximum Power Point Tracking Techniques," *IEEE Transactions on Energy Conversion*, vol. 22, no. 2, pp. 439–449, Jun. 2007.

[134] Texas Insturments, "bq25504 Ultra Low-Power Boost Converter With Battery Management for Energy Harvester Applications," *Texas Insturments*, 2015. [Online]. Available: http://www.ti.com/lit/ds/symlink/bq25504.pdf. [Accessed: 31-May-2017].

[135] O. Lopez-Lapeña and M. T. Penella, "Low-power FOCV MPPT controller with automatic adjustment of the sample&hold," *Electronics Letters*, vol. 48, no. 20, pp. 1301 – 1303, 2012.

[136] G. W. Hart, H. M. Branz, and C. H. Cox, "Experimental tests of open loop maximum-power-point tracking techniques," *Solar Cells*, vol. 13, pp. 185–195, 1984.

[137] V. Salas, E. Olías, A. Barrado, and A. Lázaro, "Review of the maximum power point tracking algorithms for stand-alone photovoltaic systems," *Solar Energy Materials and Solar Cells*, vol. 90, no. 11, pp. 1555–1578, 2006.

[138] B. Mammano, "Current Sensing Solutions for Power Supply Designers," in *Instrument Incorporated Document*, 2001, pp. 1–38.

[139] N. Femia, G. Petrone, G. Spagnuolo, and M. Vitelli, "Optimization of Perturb and Observe Maximum Power Point Tracking Method," *IEEE Trans. Power Electron.*, vol. 20, no. 4, pp. 963–973, 2005.

[140] G. Carannante, C. Fraddanno, M. Pagano, and L. Piegari, "Experimental performance of MPPT algorithm for photovoltaic sources subject to inhomogeneous insolation," *IEEE Transactions on Industrial Electronics*, vol. 56, no. 11, pp. 4374–4380, 2009.

[141] C. W. T. C. W. Tan, T. C. Green, and C. a. Hernandez-Aramburo, "Analysis of perturb and observe maximum power point tracking algorithm for photovoltaic applications," *2008 IEEE 2nd International Power and Energy Conference*, no. PECon 08, pp. 237–242, 2008.

[142] C. W. Tan, T. C. Green, and C. a Hernandez-aramburo, "A Current-Mode Controlled Maximum Power Point Tracking Converter for Building Integrated Photovoltaics Acknowledgment Keywords Characteristic of Photovoltaic Generation BP 365U at Standard Test Condition .," *October*, pp. 1–10.

[143] M. A. Elgendy, B. Zahawi, and D. J. Atkinson, "Assessment of perturb and observe MPPT algorithm implementation techniques for PV pumping applications," *IEEE Transactions on Sustainable Energy*, vol. 3, no. 1, pp. 21–33, 2012.

[144] R. Prakash, B. Meenakshipriya, and R. Kumaravelan, "Modeling and Design of MPPT Controller Using Stepped P&O Algorithm in Solar Photovoltaic System," *World Academy of Science, Engineering and Technology, International Journal of Electrical, Computer, Energetic, Electronic and Communication Engineering*, vol. 8, no. 3, pp. 602–608, 2014.

[145] L. Qin and X. Lu, "Matlab/Simulink-Based Research on Maximum Power Point Tracking of Photovoltaic Generation," *Physics Procedia*, vol. 24, pp. 10–18, 2012.

[146] A. K. Abdelsalam, A. M. Massoud, S. Ahmed, and P. N. Enjeti, "High-performance adaptive Perturb and observe MPPT technique for photovoltaic-based microgrids," *IEEE Transactions on Power Electronics*, vol. 26, no. 4, pp. 1010–1021, 2011.

[147] M. G. Villalva, J. R. Gazoli, and E. R. Filho, "Analysis and Simulation of the P&O MPPT Algorithm Using a Linearized PV Array Model," in *2009 Brazilian Power Electronics Conference*, 2009, pp. 189–195.

[148] N. Femia, D. Granozio, G. Petrone, G. Spagnuolo, and M. Vitelli, "Predictive & adaptive MPPT perturb and observe method," *IEEE Transactions on Aerospace and Electronic Systems*, vol. 43, no. 3, pp. 934–950, 2007.

[149] D. Sera, L. Mathe, T. Kerekes, S. V. Spataru, and R. Teodorescu, "On the perturb-and-observe and incremental conductance mppt methods for PV systems," *IEEE Journal of Photovoltaics*, vol. 3, no. 3, pp. 1070–1078, 2013.

[150] K. H. Hussein, "Maximum photovoltaic power tracking: an algorithm for rapidly changing atmospheric conditions," *IEE Proceedings - Generation, Transmission and Distribution*, vol. 142, no. 1, p. 59, 1995.

[151] a. Chikh and a. Chandra, "An optimum method for maximum power point tracking in photovoltaic systems," *2011 IEEE Power and Energy Society General*

Meeting, no. 1, pp. 1–6, 2011.

[152] A. Pandey, N. Dasgupta, and A. K. Mukerjee, "High-performance algorithms for drift avoidance and fast tracking in solar MPPT system," *IEEE Transactions on Energy Conversion*, vol. 23, no. 2, pp. 681–689, 2008.

[153] R. A. Mastromauro, M. Liserre, and A. Dell'Aquila, "Control issues in single-stage photovoltaic systems: MPPT, current and voltage control," *IEEE Transactions on Industrial Informatics*, vol. 8, no. 2, pp. 241–254, 2012.

[154] D. Durgabhavani and P. S. Ratnamala, "Modeling and Analysis of Perturb & Observe and Incremental Conductance MPPT Algorithm for PV Array Using CUK Converter," *International Journal & Magazine of Engineering, Technology, Management and Research*, vol. 3, no. 2, pp. 271–278, 2016.

[155] K. S. Lee, Y. Fujii, T. Sumiya, and E. Ikawa, "Development of a 250kW PV PCS and adaptive MPPT method," in *The 2010 International Power Electronics Conference - ECCE ASIA -*, 2010, pp. 2598–2602.

[156] M. A. Elgendy, B. Zahawi, and D. J. Atkinson, "Assessment of the Incremental Conductance Maximum Power Point Tracking Algorithm," *IEEE Transactions on Sustainable Energy*, vol. 4, no. 1, pp. 108–117, Jan. 2013.

[157] R. McKercher, "Design of Power Electronic Interface for Photovoltaic Applications," Honours Thesis, University of Tasmania, 2013.

[158] T. L. Nguyen and K.-S. Low, "A Global Maximum Power Point Tracking Scheme Employing DIRECT Search Algorithm for Photovoltaic Systems," *IEEE Transactions on Industrial Electronics*, vol. 57, no. 10, pp. 3456–3467, Oct. 2010.

[159] R. Ramaprabha, B. Mathur, A. Ravi, and S. Aventhika, "Modified Fibonacci search based MPPT scheme for SPVA under partial shaded conditions," *Proceedings - 3rd International Conference on Emerging Trends in Engineering and Technology, ICETET 2010*, pp. 379–384, 2010.

[160] M. Miyatake, T. Inada, I. Hiratsuka, H. Z. H. Zhao, H. Otsuka, and M. Nakano, "Control characteristics of a fibonacci-search-based maximum power point tracker when a photovoltaic array is partially shaded," *The 4th International Power Electronics and Motion Control Conference, 2004. IPEMC 2004.*, vol. 2, no. 2, pp. 816–821, 2004.

[161] J. J. Soon and K.-S. Low, "Photovoltaic Model Identification Using Particle Swarm Optimization With Inverse Barrier Constraint," *IEEE Transactions on Power Electronics*, vol. 27, no. 9, pp. 3975–3983, 2012.

[162] R. Koad, A. F. Zobaa, and A. El Shahat, "A Novel MPPT Algorithm Based on Particle Swarm Optimisation for Photovoltaic Systems," *IEEE Transactions on Sustainable Energy*, vol. 8, no. 2, pp. 1–1, 2016.

[163] K. Ishaque, Z. Salam, H. Taheri, and A. Shamsudin, "Application of particle swarm optimization for maximum power point tracking of PV system with direct control method," *2011 IEEE Applied Power Electronics Colloquium IAPEC*, vol. 2, no. 2, pp. 1214–1219, 2011.

[164] M. Miyatake, M. Veerachary, F. Toriumi, N. Fujii, and H. Ko, "Maximum Power Point Tracking of Multiple Photovoltaic Arrays: A PSO Approach," *IEEE*

Transactions on Aerospace and Electronic Systems, vol. 47, no. 1, pp. 367–380, Jan. 2011.

[165] R. Eberhart and J. Kennedy, "A new optimizer using particle swarm theory," in *Proc. Sixth Int. Symp. Micro Mach. Hum. Sci.*, 1995, pp. 39–43.

[166] A. soufyane Benyoucef, A. Chouder, K. Kara, S. Silvestre, and O. A. sahed, "Artificial bee colony based algorithm for maximum power point tracking (MPPT) for PV systems operating under partial shaded conditions," *Applied Soft Computing*, vol. 32, no. April, pp. 38–48, 2015.

[167] M. A. Mohd Shukran, Y. Y. Chung, W.-C. Yeh, N. Wahid, and A. M. Ahmad Zaidi, "Artificial Bee Colony based Data Mining Algorithms for Classification Tasks," *Modern Applied Science*, vol. 5, no. 4, pp. 217–231, 2011.

[168] Y. H. Liu, S. C. Huang, J. W. Huang, and W. C. Liang, "A particle swarm optimization-based maximum power point tracking algorithm for PV systems operating under partially shaded conditions," *IEEE Trans. Energy Convers.*, vol. 27, no. 4, pp. 1027–1035, 2012.

[169] K. Ishaque and Z. Salam, "A Deterministic Particle Swarm Optimization Maximum Power Point Tracker for Photovoltaic System under Partial Shading Condition," *IEEE Transactions on Industrial Electronics*, vol. 60, no. 8, pp. 1–1, 2012.

[170] M. S. Ngan and C. W. Tan, "Photovoltaic Multiple Peaks Power Tracking Using Particle Swarm Optimization with Artificial Neural Network Algorithm," M. R. Islam, F. Rahman, and W. Xu, Eds. Berlin, Heidelberg: Springer Berlin Heidelberg, 2016, pp. 107–138.

[171] M. Mao, L. Zhang, Q. Duan, O. J. K. Oghorada, P. Duan, and B. Hu, "A Two-Stage Particle Swarm Optimization Algorithm for MPPT of Partially Shaded PV Arrays A Two-Stage Particle Swarm Optimization Algorithm for MPPT of Partially Shaded," *International Journal of Green Energy*, vol. 0, no. 0, pp. 1–9, 2017.

[172] W.-C. Chiang and R. A. Russell, "Simulated annealing metaheuristics for the vehicle routing problem with time windows," *Annals of Operations Research*, vol. 63, no. 1, pp. 3–27, 1996.

[173] S. Kirkpatrick, C. D. Gelatt, and M. P. Vecchi, "Optimization by Simulated Annealing," *Science*, vol. 220, no. 4598, pp. 671–680, 1983.

[174] V. Černý, "Thermodynamical approach to the traveling salesman problem: An efficient simulation algorithm," *Journal of Optimization Theory and Applications*, vol. 45, no. 1, pp. 41–51, Jan. 1985.

[175] M. A. Azam, S. Abdullah-Al-Nahid, M. A. Kabir, and S. M. H. Chowdhury, "Microcontroller based maximum power tracking of PV using stimulated annealing algorithm," in *2012 International Conference on Informatics, Electronics & Vision (ICIEV)*, 2012, pp. 298–303.

[176] B. C. McCallum, "Blind deconvolution by simulated annealing," *Optics Communications*, vol. 75, no. 2, pp. 101–105, 1990.

[177] R. E. Banchs, "Simulated Annealing," 1997. [Online]. Available:

http://www.rbanchs.com/documents/THFEL_PR15.pdf. [Accessed: 25-Jul-2017].

[178] Y.-M. Chen, C.-H. Lee, and H.-C. Wu, "Calculation of the Optimum Installation Angle for Fixed Solar-Cell Panels Based on the Genetic Algorithm and the Simulated-Annealing Method," *IEEE Transactions on Energy Conversion*, vol. 20, no. 2, pp. 467–473, Jun. 2005.

[179] S. Lyden and M. E. Haque, "A hybrid simulated annealing and perturb and observe method for maximum power point tracking in PV systems under partial shading conditions," in *2015 Australasian Universities Power Engineering Conference (AUPEC)*, 2015, pp. 1–6.

[180] M. S. ElNozahy and M. M. A. Salama, "A Comprehensive Study of the Impacts of PHEVs on Residential Distribution Networks," *IEEE Trans. Sustain. Energy*, vol. 5, no. 1, pp. 332–342, Jan. 2014.

[181] A. Trejos, D. Gonzalez, and C. A. Ramos-Paja, "Modeling of step-up grid-connected photovoltaic systems for control purposes," *Energies*, vol. 5, no. 6, pp. 1900–1926, 2012.

[182] Feng Gao, Ding Li, Poh Chiang Loh, Yi Tang, and Peng Wang, "Indirect dc-link voltage control of two-stage single-phase PV inverter," in *2009 IEEE Energy Conversion Congress and Exposition*, 2009, pp. 1166–1172.

[183] A. Abbas Elserougi, A. S. Abdel-Khalik, A. Massoud, and S. Ahmed, "Studying the effect of over-modulation on the output voltage of three-phase single-stage grid-connected boost inverter," *Alexandria Engineering Journal*, vol. 52, no. 3, pp. 347–358, 2013.

[184] H. B. Massawe, "Grid Connected Photovoltaic Systems with SmartGrid functionality," Norwegian University of Science and Technology, Trondheim, Norway, 2013.

[185] Y. L. Zhu, J. G. Yao, and D. Wu, "Comparative study of two stages and single stage topologies for grid-tie photovoltaic generation by PSCAD/EMTDC," *APAP 2011 - Proceedings: 2011 International Conference on Advanced Power System Automation and Protection*, vol. 2, pp. 1304–1309, 2011.

[186] R. M. Hudson, M. R. Behnke, R. West, S. Gonzalez, and J. Ginn, "Design considerations for three-phase grid connected photovoltaic inverters," *Conference Record of the Twenty-Ninth IEEE Photovoltaic Specialists Conference*, pp. 1396–1401, 2002.

[187] ECEN 2060, "Power Electronics and Control in Grid-Connected PV Systems Grid-Connected PV System." [Online]. Available: http://ecee.colorado.edu/~ecen2060/materials/lecture_notes/GridPVsystem.pdf. [Accessed: 01-Jun-2017].

[188] T. Kalitjuka, "Control of Voltage Source Converters for Power System Applications," Norwegian University of Science and Technology, 2011.

[189] B. Mishra and B. P. Kar, "Matlab Based Modeling of Photovoltaic Array Characteristics," National Institute of Technology, Rourkela, India, 2012.

[190] N. Mohammad, M. Quamruzzaman, M. R. T. Hossain, and M. R. Alam, "Parasitic Effects on the Performance of DC-DC SEPIC in Photovoltaic Maximum Power

Point Tracking Applications," *Smart Grid and Renewable Energy*, vol. 4, no. 1, pp. 113–121, 2013.

[191] V. C. Kotak and P. Tyagi, "DC To DC Converter in Maximum Power Point Tracker," *International Journal of Advanced Research in Electrical, Electronics and Instrumentation Engineering (An ISO Certified Organization)*, vol. 3297, no. 12, pp. 6115–6125, 2007.

[192] R. Ingudam and R. Nayak, "Modelling and Performance Analysis of DC-DC Converters for PV Grid Connected System," *International Journal of Science, Engineering and Technology Research (IJSETR)*, vol. 4, no. 5, pp. 1378–1390, 2015.

[193] W. Xiao, N. Ozog, and W. G. Dunford, "Topology Study of Photovoltaic Interface for Maximum Power Point Tracking," *IEEE Transactions on Industrial Electronics*, vol. 54, no. 3, pp. 1696–1704, Jun. 2007.

[194] A. Chini and F. Soci, "Boost-converter-based solar harvester for low power applications," *Electronics Letters*, vol. 46, no. 4, p. 296, 2010.

[195] J. Betten, "Benefits of a coupled-inductor SEPIC converter," *Analog Applications Journal, Texas Intruments*, 2011. [Online]. Available: http://www.ti.com.cn/cn/lit/an/slyt409/slyt409.pdf#page=14%5Cnwww.ti.com/aaj. [Accessed: 10-Aug-2017].

[196] S. E. Evju, "Fundamentals of Grid Connected Photo-Voltaic Power Electronic Converter Design," Norwegian University of Science and Technology, Trondheim, Norway, 2007.

[197] T. N. Thacker, "Control of Power Conversion Systems for the Intentional Islanding of Distributed Generation Units," Virginia Polytechnic Institute and State University, Blacksburg, Virginia, 2005.

[198] Fang Zheng Peng, "Z-source inverter," *IEEE Transactions on Industry Applications*, vol. 39, no. 2, pp. 504–510, 2003.

[199] O. Ellabban and H. Abu-Rub, "Z-Source Inverter: Topology Improvements Review," *IEEE Industrial Electronics Magazine*, vol. 10, no. 1, pp. 6–24, Mar. 2016.

[200] M. H. Rashid, *Power Electronics: Circuits, Devices & Applications*, 3rd ed. Upper Saddle River, NJ, USA: Pearson, 2004.

[201] Council of Standards Australia, "Grid connection of energy systems via inverters Part 2: Inverter requirements," *AS 4777.2*. 2005.

[202] S. N. M. Yusob, "Analysis of Operation Optimization and PV Output Power Optimization of Grid-Connected PV System with Energy Storage System," University of Tasmania, Hobart, 2017.

[203] Z. Rafique, "Voltage Surge & Resonance Impacts in a Grid Connected Wind Farm with Long Transmission Cables & Their Remedial Measures," Honours Thesis, University of Tasmania, 2014.

[204] M. Liserre, F. Blaabjerg, and S. Hansen, "Design and Control of an LCL-Filter-Based Three-Phase Active Rectifier," *IEEE Transactions on Industry Applications*,

vol. 41, no. 5, pp. 1281–1291, Sep. 2005.

[205] R. Teodorescu, F. Blaabjerg, M. Liserre, and a. Dell'Aquila, "A stable three-phase LCL-filter based active rectifier without damping," *38th IAS Annual Meeting on Conference Record of the Industry Applications Conference, 2003.*, vol. 3, pp. 1552–1557, 2003.

[206] R. N. Beres, X. Wang, F. Blaabjerg, M. Liserre, and C. L. Bak, "Optimal design of high-order passive-damped filters for grid-connected applications," *IEEE Transactions on Power Electronics*, vol. 31, no. 3, pp. 2083–2098, 2016.

[207] R. Teodorescu, M. Liserre, and P. Rodríguez, *Grid Converters for Photovoltaic and Wind Power Systems*. Chichester, UK: John Wiley & Sons, Ltd, 2011.

[208] H. Liu and D. Zhang, "Two-Phase Interleaved Inverse-Coupled Inductor Boost without Right Half Plane Zeros," *IEEE Transactions on Power Electronics*, vol. 32, no. 3, pp. 1–1, 2016.

[209] S. Lee, "Practical feedback loop analysis for current-mode boost converter," *Texas Instruments (Application Report, SLVA636)*, 2014. [Online]. Available: http://www.ti.com/lit/an/slva636/slva636.pdf.

[210] A. J. Forsyth and S. V. Mollov, "Modelling and control of DC-DC converters," *Power Engineering Journal*, vol. 12, no. 5, pp. 229–236, 1998.

[211] C. Batard, F. Poitiers, C. Millet, and N. Ginot, "Simulation of Power Converters Using Matlab-Simulink," in *MATLAB - A Fundamental Tool for Scientific Computing and Engineering Applications - Volume 1*, InTech, 2012, pp. 43–68.

[212] N. Kondrath and M. K. Kazimierczuk, "Unified model to derive control-to-output transfer function of peak current-mode-controlled pulse-width modulated dc–dc converters in continuous conduction mode," *IET Power Electronics*, vol. 5, no. 5, p. 582, 2012.

[213] N. Kondrath and M. K. Kazimierczuk, "Control-to-output transfer function of peak current-mode controlled PWM DC–DC boost converter in CCM," *Electronics Letters*, vol. 47, no. 17, p. 991, 2011.

[214] N. Kondrath and M. K. Kazimierczuk, "Control-to-output transfer function of peak current-mode controlled pulse-width modulated dc–dc buck converter in continuous conduction mode," *IET Power Electronics*, vol. 5, no. 5, p. 582, 2012.

[215] E. Koutroulis, K. Kalaitzakis, and N. C. Voulgaris, "Development of a microcontroller-based, photovoltaic maximum power point tracking control system," *Power Electronics, IEEE Transactions on*, vol. 16, no. 1, pp. 46–54, 2001.

[216] K. M. Tsang and W. L. Chan, "Cascade controller for DC/DC buck convertor," *IEE Proceedings - Electric Power Applications*, vol. 152, no. 4, p. 827, 2005.

[217] M. G. Villalva and E. F. Ruppert, "Input-controlled buck converter for photovoltaic applications: Modeling and design," *Power Electronics, Machines and Drives, 2008. PEMD 2008. 4th IET Conference on*, pp. 505–509, 2008.

[218] M. G. Villalva and E. Ruppert Filho, "Dynamic analysis of the input-controlled buck converter fed by a photovoltaic array," *Sba: Controle & Automação Sociedade Brasileira de Automatica*, vol. 19, no. 4, pp. 463–474, 2008.

[219] N. Mohan, T. M. Undeland, and W. P. Robbins, *Power electronics : converters, applications, and design*. John Wiley & Sons, 2003.

[220] R. Mammano, "Switching power supply topology voltage mode vs. current mode," *Elektron Journal-South African Institute of Electrical Engineers*, vol. 18, no. 6, pp. 25–27, 2001.

[221] M. E. Haque, "Lecture Note - Photovoltaic Energy System- Part II," Deakin University, 2017.

[222] G. Zhou, J. Xu, and J. Wang, "Constant-Frequency Peak-Ripple-Based Control of Buck Converter in CCM: Review, Unification, and Duality," *IEEE Transactions on Industrial Electronics*, vol. 61, no. 3, pp. 1280–1291, Mar. 2014.

[223] Texas Instruments, "Modeling, Analysis and Compensation of the Current-Mode Converter," *Texas Instruments*, 1999. [Online]. Available: http://www.ti.com/general/docs/litabsmultiplefilelist.tsp?literatureNumber=slua101. [Accessed: 14-Aug-2017].

[224] K. Lee, "Advanced Control Schemes for Voltage Regulators," Virginia Polytechnic Institute and State University, Blacksburg, Virginia, 2008.

[225] S. M. Khazraei, "Stability challenges and solutions in current-mode controlled power electronic converters," Missouri University of Science and Technology, Rolla, Missouri, USA, 2012.

[226] Steven Keeping, "Voltage- and Current-Mode Control for PWM Signal Generation in DC-to-DC Switching Regulators," *Digi-Key Electronics*, 2014. [Online]. Available: https://www.digikey.com.au/en/articles/techzone/2014/oct/voltage-and-current-mode-control-for-pwm-signal-generation-in-dc-to-dc-switching-regulators. [Accessed: 13-Aug-2017].

[227] R. W. Erickson and D. Maksimović, "Current Programmed Control," in *Fundamentals of Power Electronics*, 2nd ed., R. W. Erickson and D. Maksimovic, Eds. Boston, MA: Springer US, 2001, pp. 439–487.

[228] T. Zhao, J. Zeng, S. Bhattacharya, M. E. Baran, and A. Q. Huang, "An average model of solid state transformer for dynamic system simulation," *2009 IEEE Power and Energy Society General Meeting, PES '09*, pp. 1–8, 2009.

[229] C. Leung, S. Dutta, S. Baek, and S. Bhattacharya, "Design considerations of high voltage and high frequency three phase transformer for Solid State Transformer application," in *2010 IEEE Energy Conversion Congress and Exposition*, 2010, no. 1, pp. 1551–1558.

[230] Y. Du, S. Baek, S. Bhattacharya, and A. Q. Huang, "High-voltage high-frequency transformer design for a 7.2kV to 120V/240V 20kVA solid state transformer," in *IECON 2010 - 36th Annual Conference on IEEE Industrial Electronics Society*, 2010, pp. 493–498.

[231] M. Orabi and T. Ninomiya, "Stability investigation of the cascade two-stage PFC converter," *IEICE Transactions on Communications*, vol. E87–B, no. 12, pp. 3506–3514, 2004.

[232] J. M. Zhang, X. G. Xie, D. Z. Jiao, and Zhaoming Qian, "Stability problems and input impedance improvement for cascaded power electronic systems," in

Nineteenth Annual IEEE Applied Power Electronics Conference and Exposition, 2004. APEC '04., 2004, vol. 2, no. 1, pp. 1018–1024.

[233] W. Wei, X. Haiping, W. Xuhui, and S. Wenqing, "Dynamics and Control of Electronic Cascaded Systems," in *2006 5th International Power Electronics and Motion Control Conference*, 2006, vol. 1, pp. 1–4.

[234] W. Tang, F. C. Lee, R. B. Ridley, and I. Cohen, "Charge control: modeling, analysis, and design," *IEEE Transactions on Power Electronics*, vol. 8, no. 4, pp. 396–403, 1993.

[235] S. H. Park, H. S. Bae, J. H. Lee, and B. H. Cho, "Design of peak and charge current-mode control for parallel module solar array regulator system," *PESC Record - IEEE Annual Power Electronics Specialists Conference*, 2006.

[236] L. Dixon, "Average current mode control of switching power supplies," *Unitrode Power Supply Design Seminar Manual SEM700*, pp. 1–12, 1990.

[237] Steven Keeping, "The Role of Slope Compensation in Current-Mode-Controlled Voltage Regulators," *Digi-Key Electronics*, 2015. [Online]. Available: https://www.digikey.com.au/en/articles/techzone/2015/jan/the-role-of-slope-compensation-in-current-mode-controlled-voltage-regulators. [Accessed: 14-Aug-2017].

[238] F. Redell, R. Sheehan, and H. Anatole, "Understanding and applying current-mode control theory," in *Power Electronics Technology Exhibition and Conference*, 2007, pp. 21–26.

[239] Z. Guo, L. Wu, and Y. Liu, "Design and implementation of adaptive slope compensation in current mode DC—DC converter," *Journal of Semiconductors*, vol. 31, no. 12, p. 125004, Dec. 2010.

[240] R. Poley and A. Shirsavar, "Digital peak current mode control with slope compensation using the TMS320F2803x," *Texas Instruments*, 2012. [Online]. Available: https://www.google.com.au/url?sa=t&rct=j&q=&esrc=s&source=web&cd=1&cad=rja&uact=8&ved=0ahUKEwiZy76Oxd3VAhWIT7wKHeYRCFEQFggoMAA&url=http%3A%2F%2Fwww.ti.com%2Flit%2Fan%2Fsprabe7a%2Fsprabe7a.pdf&usg=AFQjCNHtBZOAgZYTWFntpgnuAAjXwiwWDQ. [Accessed: 17-Aug-2017].

[241] B. Novak, "Implementing peak current mode control of a switch-mode power supply with a single microcontroller," *Texas Instruments*, 2012. [Online]. Available: http://www.ti.com/lit/wp/spry205/spry205.pdf. [Accessed: 15-Aug-2015].

[242] J. Sun, "Pulse-Width Modulation," in *Dynamics and Control of Switched Electronic Systems*, 2012, pp. 25–61.

[243] D. Meeks, "Loop Stability Analysis of Voltage Mode Buck Regulator with Different Output Capacitor Types--Continuous and Discontinuous Modes," Citeseer, 2008.

[244] V. Vorpérian, "Simplified Analysis of PWM Converters Using Model of PWM Switch Part I: Continuous Conduction Mode," *IEEE Transactions on Aerospace*

and Electronic Systems, vol. 26, no. 3, pp. 490–496, 1990.

[245] R. L. Gour, "Small Signal Modelling of a Buck Converter using State Space Averaging for Magnet Load," vol. 3, no. 3, pp. 11–17, 2016.

[246] N. Femia, G. Petrone, G. Spagnuolo, and M. Vitelli, "A Technique for Improving P & O MPPT Performances of Double-Stage Grid-Connected Photovoltaic Systems," vol. 56, no. 11, pp. 4473–4482, 2009.

[247] H. Sira-Ramireza and R. Silva-Ortigoza, "Modelling of DC-to-DC Power Converters," *Control Design Techniques in Power Electronics Devices*, p. XVIII, 424, 2006.

[248] Daniel W.Hart, *Power Electronics*. New York, NY, USA: McGraw-Hill, 2011.

[249] B. J. Falin, "Designing DC / DC converters based on ZETA topology," 2010.

[250] B. Karanayil, V. G. Agelidis, and J. Pou, "Evaluation of DC-link decoupling using electrolytic or polypropylene film capacitors in three-phase grid-connected photovoltaic inverters," *IECON Proceedings (Industrial Electronics Conference)*, no. 1, pp. 6980–6986, 2013.

[251] M. E. de Oliveira Filho, J. R. Gazoli, A. J. Sguarezi Filho, and E. Ruppert Filho, "A control method for voltage source inverter without dc link capacitor," in *2008 IEEE Power Electronics Specialists Conference*, 2008, pp. 4432–4437.

[252] A. Tokumasu, H. Taki, K. Shirakawa, and K. Wada, "AC/DC converter based on instantaneous power balance control for reducing DC-link capacitance," in *2014 International Power Electronics Conference (IPEC-Hiroshima 2014 - ECCE ASIA)*, 2014, vol. 4, no. 6, pp. 1379–1385.

[253] C. S. S. D. Zammit M. Apap and C. S. S. D. Zammit M. Apap, "Comparison between PI and PR Current Controllers in Grid Connected PV Inverters," *International Journal of Electrical, Robotics, Electronics and Communications Engineering*, vol. Vol:8, no. No:2, p. 6, 2014.

[254] A. E. W. H. Kahlane, L. Hassaine, and M. Kherchi, "LCL filter design for photovoltaic grid connected systems," in *Revue des Energies Renouvelables （SIENR'14)*, 2014, vol. 8, no. 2, pp. 227–232.

[255] A. Reznik, M. G. Simoes, A. Al-Durra, and S. M. Muyeen, "LCL Filter Design and Performance Analysis for Grid Interconnected Systems," *IEEE Transactions on Industry Applications*, vol. 50, no. 2, pp. 1225–1232, Mar. 2014.

[256] Ben Noone, "PV Integration on Australian Distribution Networks Literature Review," *Australian Photovoltaic Institute*, 2013. [Online]. Available: https://apvi.org.au/wp-content/uploads/2013/12/APVA-PV-and-DNSP-Literature-review-September-2013.pdf. [Accessed: 01-Jan-2017].

[257] Council of Standards New Zealand, "Electromagnetic Compatibility (EMC) - Consideration of reference impedances and public supply network impedances for use in determining the disturbance characteristics of electrical equipment having a rated current ≤75 A per phase," *IEC Technical Report TR 60725*, 2012. [Online]. Available: https://webstore.iec.ch/publication/3092.

[258] K. Clement-Nyns, E. Haesen, and J. Driesen, "The impact of charging plug-in

hybrid electric vehicles on a residential distribution grid," *IEEE Transactions on Power Systems*, vol. 25, no. 1, pp. 371–380, Feb. 2010.

[259] S. Vazquez, S. M. Lukic, E. Galvan, L. G. Franquelo, and J. M. Carrasco, "Energy Storage Systems for Transport and Grid Applications," *IEEE Trans. Ind. Electron.*, vol. 57, no. 12, pp. 3881–3895, Dec. 2010.

[260] A. Panday and H. O. Bansal, "Temperature dependent circuit-based modeling of high power Li-ion battery for plug-in hybrid electrical vehicles," *2013 International Conference on Advances in Technology and Engineering (ICATE)*, no. 85, pp. 1–6, 2013.

[261] N. Chaturvedi, R. Klein, J. Christensen, J. Ahmed, and A. Kojic, "Algorithms for Advanced Battery-Management Systems," *IEEE Control Systems Magazine*, vol. 30, no. 3, pp. 49–68, Jun. 2010.

[262] Chevrolet Volt - VIN 3929 (2013), "Advanced Vehicle Testing Activity – Battery Pack Laboratory Testing Results," *U.S. Dept. of Energy*, 2014. [Online]. Available: https://energy.gov/sites/prod/files/2015/02/f19/batteryVolt3491.pdf. [Accessed: 24-Aug-2017].

[263] D.-H. Shin, J.-B. Jeong, T.-H. Kim, and H.-J. Kim, "Modeling of Lithium Battery Cells for Plug-In Hybrid Vehicles," *Journal of Power Electronics*, vol. 13, no. 3, pp. 429–436, May 2013.

[264] N. Omar *et al.*, "Rechargeable Energy Storage Systems for Plug-in Hybrid Electric Vehicles—Assessment of Electrical Characteristics," *Energies*, vol. 5, no. 12, pp. 2952–2988, Aug. 2012.

[265] S. Yuan, H. Wu, and C. Yin, "State of charge estimation using the extended Kalman filter for battery management systems based on the ARX battery model," *Energies*, vol. 6, no. 1, pp. 444–470, 2013.

[266] D. Aurbach, "Characterization of Batteries by Electrochemical and non-Electrochemical Techniques," in *Ind. Appl. Batter. From Cars to Aerosp. Energy Storage*, 2007, pp. 119–131.

[267] H. He, R. Xiong, and J. Fan, "Evaluation of lithium-ion battery equivalent circuit models for state of charge estimation by an experimental approach," *Energies*, vol. 4, no. 4, pp. 582–598, 2011.

[268] G. Liu, M. Ouyang, L. Lu, J. Li, and X. Han, "Online estimation of lithium-ion battery remaining discharge capacity through differential voltage analysis," *Journal of Power Sources*, vol. 274, pp. 971–989, Jan. 2015.

[269] Y. Wang and L. Li, "Li-ion battery dynamics model parameter estimation using datasheets and particle swarm optimization," *Int. J. Energy Res.*, vol. 40, no. 8, pp. 1050–1061, Jun. 2016.

[270] D. Gallo, C. Landi, M. Luiso, and R. Morello, "Optimization of Experimental Model Parameter Identification for Energy Storage Systems," *Energies*, vol. 6, no. 9, pp. 4572–4590, Sep. 2013.

[271] O. Tremblay and L.-A. A. Dessaint, "Experimental validation of a battery dynamic model for EV applications," *World Electr. Veh. J.*, vol. 3, no. 1, pp. 289–298, 2009.

[272] H. Oman, "On-board energy and power management on electric vehicles: effect of battery type," in *17th DASC. AIAA/IEEE/SAE. Digital Avionics Systems Conference. Proceedings (Cat. No.98CH36267)*, 1998, vol. 2, p. I43/1-I43/6.

[273] J. Gonder and T. Markel, "Energy management strategies for plug-in hybrid electric vehicles," in *2007 SAE World Congress*, 2007, pp. 1–5.

[274] M. Alhanouti, M. Gießler, T. Blank, and F. Gauterin, "New Electro-Thermal Battery Pack Model of an Electric Vehicle," *Energies*, vol. 9, no. 7, p. 563, 2016.

[275] H. He, R. Xiong, H. Guo, and S. Li, "Comparison study on the battery models used for the energy management of batteries in electric vehicles," *Energy Conversion and Management*, vol. 64, pp. 113–121, Dec. 2012.

[276] G. Liu *et al.*, "A comparative study of equivalent circuit models and enhanced equivalent circuit models of lithium-ion batteries with different model structures," *IEEE Transportation Electrification Conference and Expo, ITEC Asia-Pacific 2014 - Conference Proceedings*, pp. 1–6, 2014.

[277] X. Hu, S. Li, and H. Peng, "A comparative study of equivalent circuit models for Li-ion batteries," *Journal of Power Sources*, vol. 198, pp. 359–367, Jan. 2012.

[278] B. Schweighofer, K. M. Raab, and G. Brasseur, "Modeling of high power automotive batteries by the use of an automated test system," *IEEE Transactions on Instrumentation and Measurement*, vol. 52, no. 4, pp. 1087–1091, 2003.

[279] O. Tremblay, L.-A. Dessaint, and A.-I. Dekkiche, "A Generic Battery Model for the Dynamic Simulation of Hybrid Electric Vehicles," in *IEEE Veh. Power Propuls. Conf.*, 2007, pp. 284–289.

[280] J. P. Christopherson, "Battery Test Manual For Electric Vehicles Revision 3," Idaho Falls, USA, 2015.

[281] M. D. F. Brondani, A. T. Z. R. Sausen, P. S. Sausen, and M. O. Binelo, "Battery Model Parameters Estimation Using Simulated Annealing," *TEMA (São Carlos)*, vol. 18, no. 1, p. 127, May 2017.

[282] A. Rohatgi, "WebPlotDigitizer," 2016. [Online]. Available: http://arohatgi.info/WebPlotDigitizer.

[283] A. G. Boulanger, A. C. Chu, S. Maxx, and D. L. Waltz, "Vehicle electrification: Status and issues," *Proc. IEEE*, vol. 99, no. 6, pp. 1116–1138, 2011.

[284] S. Shao, M. Pipattanasomporn, and S. Rahman, "Grid Integration of Electric Vehicles and Demand Response With Customer Choice," *IEEE Transactions on Smart Grid*, vol. 3, no. 1, pp. 543–550, Mar. 2012.

[285] M. Negnevitsky, "Artificial Intelligence: A Guide to Intelligent Systems," 3rd ed., MA: Addison-Wesley, 2011, pp. 224–225.

[286] S. N. N. Omkar, R. Khandelwal, T. V. S. V. S. Ananth, G. Narayana Naik, and S. Gopalakrishnan, "Quantum behaved Particle Swarm Optimization (QPSO) for multi-objective design optimization of composite structures," *Expert Syst. Appl.*, vol. 36, no. 8, pp. 11312–11322, 2009.

[287] D. Su, W. Xu, and J. Sun, "Quantum-behaved particle swarm optimization with crossover operator," *International Conference on Wireless Networks and*

Information Systems, WNIS 2009, pp. 399–402, 2009.

[288] MathWorks, "Implement generic battery model - Simulink," *The MathWorks, Inc.*, 2017. [Online]. Available: https://au.mathworks.com/help/physmod/sps/powersys/ref/battery.html. [Accessed: 27-Jun-2016].

[289] J. L. Kuo, K. L. Chao, and L. S. Lee, "Dual mechatronic MPPT controllers with PN and OPSO control algorithms for the rotatable solar panel in PHEV system," *IEEE Transactions on Industrial Electronics*, vol. 57, no. 2, pp. 678–689, 2010.

[290] S. S. Patel, "Intelligent Direct Load Control for Electric Vehicle Charging," Honours Thesis, University of Tasmania, Hobart, TAS, 2014.

[291] EVE Australia, "Difference between Levels of Chargers," *EVE Australia*, 2016. [Online]. Available: https://www.evse.com.au/difference-between-levels-of-chargers#levelone. [Accessed: 18-Sep-2017].

[292] M. Yilmaz and P. T. Krein, "Review of Battery Charger Topologies, Charging Power Levels, and Infrastructure for Plug-In Electric and Hybrid Vehicles," *IEEE Transactions on Power Electronics*, vol. 28, no. 5, pp. 2151–2169, 2013.

[293] A. Bhattacharjee, "Design and Comparative Study of Three Photovoltaic Battery Charge Control Algorithms in MATLAB / SIMULINK Environment model and MATLAB / SIMULINK model of PV CELL AND Buck converter," *Int. J. Adv. Comput. Res.*, no. 3, 2012.

[294] "A Simple Guide to DC Fast Charging." [Online]. Available: https://www.fleetcarma.com/dc-fast-charging-guide/. [Accessed: 26-Sep-2017].

[295] The MathWorks Inc., "Detailed Model of a 100-kW Grid-Connected PV Array - MATLAB & Simulink Example - MathWorks Australia," 2014. [Online]. Available: https://au.mathworks.com/help/physmod/sps/examples/detailed-model-of-a-100-kw-grid-connected-pv-array.html. [Accessed: 19-Sep-2017].

[296] The MathWorks Inc., "Supercapacitor Model - MATLAB & Simulink Example - MathWorks Australia," 2017. [Online]. Available: https://au.mathworks.com/help/physmod/sps/examples/supercapacitor-model.html. [Accessed: 26-Sep-2017].

[297] Bureau of Meteorology, "Australia's official weather forecasts & weather radar - Bureau of Meteorology," 2017. [Online]. Available: http://www.bom.gov.au/?ref=hdr. [Accessed: 26-Sep-2017].